

# Mixing Intensification in Stirred Tank Reactors and in Small Channels

Thesis Submitted to AcSIR

*For the Award of the Degree of*

DOCTOR OF PHILOSOPHY

*In*

Engineering Sciences



By

Gunwant Mule

20EE12A26077

Under the guidance of  
Dr. Amol A. Kulkarni

CSIR-National Chemical Laboratory, Pune (India)

*Dedicated to my beloved parents.....*

## **Abstract**

*Mixing is one of the key operations in chemical and its allied industries. In most of the batch operations mixing is achieved using mechanical stirring. In recent times, fractal shapes have shown the prominent effect on hydrodynamics and hence on enhancing the mixing properties due to their edge having self-similar geometric characteristics. The fractal concept has been used to design a novel Fractal Impeller (FI) to reduce the extent of non-uniformity in mixing and in energy distribution in the stirred tank. The performance FI in terms of mixing, solid suspension and gas dispersion was better compared to conventional impellers.*

*The objective of this dissertation is to study the hydrodynamics and various aspects associated with Fractal Impeller designs. The hydrodynamics associated with a stirred tank with FI has been investigated using experimentation and computational fluid dynamics (CFD). In addition, mixing of medium viscosity liquids in a stirred tank with FI has also been studied to investigate the applicability of novel design. The variations in fractal impeller design have also been explored in a study of the effect of a number of branches (therefore the number of blades) on the performance of FI.*

*More recently, physics of flow past object found to be applicable to enhance mixing in small channels through vortex shedding. In the remaining part of the thesis, the effect of space filling nature of the object on wake dynamics has also been discussed. Objects with different shapes were considered for the study to come up with better operating conditions.*



# सीएसआयआर-राष्ट्रीय रासायनिक प्रयोगशाला

(वैज्ञानिक तथा औद्योगिक अनुसंधान परिषद)

डॉ. होमी भाभा मार्ग, पुणे - 411 008. भारत

## CSIR-NATIONAL CHEMICAL LABORATORY

(Council of Scientific & Industrial Research)

Dr. Homi Bhabha Road, Pune - 411008. India



### Thesis Certificate

This is to certify that the work incorporated in this Ph.D. thesis entitled "*Mixing Intensification in Stirred Tank Reactors and in Small Channels*" submitted by *Mr. Gunwant Mule* to Academy of Scientific and Innovative Research (AcSIR) in fulfilment of the requirements for the award of the Degree of *Doctor of Philosophy in Engineering Sciences*, embodies original research work under our supervision/guidance. We further certify that this work has not been submitted to any other University or Institution in part or full for the award of any degree or diploma. Research material obtained from other sources has been duly acknowledged in the thesis. Any text, illustration, table etc., used in the thesis from other sources, have been duly cited and acknowledged.

M. Nov 29, 2017

**Mr. Gunwant Mule**  
(Research Student)

A. Kulkarni

**Dr. Amol A. Kulkarni**  
(Research Supervisor)

Communication  
Channels

NCL Level DID : 2590  
NCL Board No. : +91-20-25902000  
EPABX : +91-20-25893300  
: +91-20-25893400



FAX

Director's Office : +91-20-25902601  
COA's Office : +91-20-25902660  
COS&P's Office : +91-20-25902664

WEBSITE

[www.ncl-india.org](http://www.ncl-india.org)

## Declaration by Research Scholar

I hereby declare that the thesis "*Mixing Intensification in Stirred Tank Reactors and in Small Channels*" submitted for the degree of Doctor of Philosophy to the AcSIR has been carried out by me at the Chemical Engineering and Process Development Division, CSIR-National Chemical Laboratory, Pune-411 008, India, under the supervision of *Dr. Amol A. Kulkarni*. Research material obtained from other sources has been duly acknowledged in the thesis. I declare that the present work has not been submitted to any other University for the award of any other degree or diploma.

M  
Nov 23, 2017

Mr. Gunwant Mule  
Senior Research Fellow,  
Chemical Engineering and Process Development Division,  
CSIR-National Chemical Laboratory,  
Dr. Homi Bhabha Road, Pune-411 008, Maharashtra, India  
& Academy of Scientific & Innovative Research (AcSIR)-CSIR, India

## Table of Contents

Acknowledgements	i
List of Tables	iii
List of Figures	iv
<b>Chapter 1 Introduction</b>	<b>1</b>
1.1 Motivation and Background	2
1.2 Outline	4
 <b>Part-I: Fractal Impeller for Stirred Tank Reactors</b>	
<b>Chapter 2 Introduction to Stirred Tank Reactors</b>	<b>9</b>
2.1 Fundamentals of Stirred Tank Reactors	10
2.1.1 Geometry of the Stirred Tank Reactor	10
2.1.1.1 <i>Radial flow impellers and flow characteristics</i>	11
2.1.1.2 <i>Axial flow impellers and flow characteristics</i>	12
2.1.1.3 <i>Close clearance impellers</i>	14
2.1.2 Dimensionless groups used in the stirred tank reactors system	15
2.1.2.1 <i>Reynolds Number, <math>Re</math></i>	15
2.1.2.2 <i>Power Number, <math>N_P</math></i>	16
2.1.2.3 <i>Flow number, <math>N_Q</math></i>	17
2.1.3 Turbulent Kinetic Energy ( $k$ )	18
2.1.4 Dissipation of turbulent kinetic energy ( $\epsilon$ )	20
2.1.5 Methods for estimation of turbulent kinetic energy dissipation	20
2.1.5.1 <i>Integral kinetic energy balance</i>	20
2.1.5.2 <i>Turbulent Kinetic energy balance</i>	21
2.1.5.3 <i>Energy Spectrum</i>	22
2.1.5.4 <i>Taylor's frozen turbulence hypothesis</i>	23
2.1.5.5 <i>Dimensional analysis</i>	24
2.1.5.6 <i>Spatial fluctuating velocity gradient measurement</i>	25
2.1.5.7 <i>Computational Fluid dynamics (CFD)</i>	25
2.1.5.8 <i>Average dissipation rate</i>	26
2.1.6 Distribution of dissipation of turbulent kinetic energy ( $\epsilon$ )	26
2.2 Recent developments in novel impellers for stirred tank reactors	36
2.2.1 Impellers for low to medium viscosity fluids	37
2.2.2 Impellers for high viscosity fluids	42
2.3 Fractals	43
2.4 Fractal Impeller (FI)	44
2.4.1 Fractal Impeller Design	45
2.4 Conclusions	46

<b>Chapter 3</b>	<b>Experimental characterization of the performance of Fractal Impeller (FI) in stirred tank</b>	<b>55</b>
3.1	Introduction	56
3.2	Ultrasonic Velocity Profiler (UVP) for flow visualization	56
3.2.1	Principles of UVP	58
3.2.2	Measurement arrangements	59
3.2.3	Data Processing	60
3.3	Power Consumption ( $P$ )	61
3.4	Mixing Time ( $\theta_{mix}$ )	62
3.5	Conclusions	63
<b>Chapter 4</b>	<b>Computational Fluid Dynamics (CFD) for Stirred Tank Reactor with Fractal Impeller</b>	<b>66</b>
4.1	Introduction	67
4.2	Governing Equations	67
4.3	Modelling Turbulent flow	68
4.3.1	Reynolds-averaged Navier-Stokes (RANS) Equations	69
4.3.2	The Standard $k-\varepsilon$ model	69
4.3.3	The $k-\omega$ Turbulence Model	71
4.3.4	Shear Stress Transport Model	71
4.4	Discretization Methods	72
4.4.1	Finite Difference Method (FDM)	72
4.4.2	Finite Volume Method (FVM)	73
4.4.3	Finite Element Method (FEM)	73
4.5	Modelling Flows in Stirred Tank	73
4.5.1	Sliding Mesh Approach	74
4.5.2	Frozen Rotor Approach	75
4.6	Conclusions	75
<b>Chapter 5</b>	<b>Analysis of Flow pattern: Experiments and CFD simulations</b>	<b>78</b>
5.1	Introduction	79
5.2	Experimental Set-up	79
5.3	Numerical Simulations	81
5.3.1	Stirred tank geometry and grid generation	81
5.3.2	Modeling approach and description	81
5.3.3	Convergence criteria, grid independence study, and grid details	83
5.3.4	Comparison of CFD models	84
5.4	Results and Discussions	88
5.4.1	Mean Velocity Profiles and Flow Patterns	88
5.4.2	Impeller Pumping Capacity	91
5.4.3	Transient flow in the stirred tank	93
5.4.4	RMS Velocities and Turbulent Kinetic Energy ( $k$ )	96
5.5	Conclusions	98

<b>Chapter 6</b>	<b>Mixing of Medium Viscosity Liquids in a Stirred Tank with Fractal Impeller</b>	101
6.1	Introduction	102
6.2	Experimental Set-up	103
6.3	Results and Discussions	104
6.3.1	Power Consumption	104
6.3.2	Mixing Time ( $\theta_{mix}$ )	106
6.3.3	Effect of viscosity on mean velocity profiles	108
6.4	Conclusions	110

<b>Chapter 7</b>	<b>Effect of Number of Branches on the Performance of Fractal Impeller: Mixing and Hydrodynamics</b>	113
7.1	Introduction	114
7.2	Experimental	114
7.2.1	Tank Geometry	114
7.2.2	Fractal Impeller	114
7.2.3	Experimental Setup	116
7.3	Results and Discussions	117
7.3.1	Flow generated by Fractal Impeller	117
7.3.1.1	<i>Effect of impeller rotation speed on mean velocity profiles</i>	117
7.3.1.2	<i>Mean Velocity and Flow Patterns</i>	118
7.3.2	Power consumption	124
7.3.3	Mixing time	126
7.4	Conclusions	129

***Part II: Exothermic reactions in stirred tank reactor***

<b>Chapter 8</b>	<b>Assessment of Usefulness of CSTRs for Exothermic Nitration: Design aspects</b>	135
8.1	Introduction	136
8.2	Nitration of by-aryl compound	137
8.2.1	Reaction	138
8.3	Experimental Section	138
8.3.1	Set up for kinetics study	138
8.3.2	Experimental Set up of Continuous Stirred Tank Reactors (CSTRs)	140
8.4	Numerical Modelling	141
8.5	Results and Discussions	143
8.5.1	Validation of numerical predictions	143
8.5.1.1	<i>Kinetic development</i>	143
8.5.1.2	<i>Comparison of numerical results with experiments</i>	143
8.5.2	Dynamics of start-up of CSTR	145
8.5.3	Effect of various parameters on the production	146
8.5.3.1	<i>Initial concentration (<math>C_{A0}</math>) and molar flow rate ratio (<math>F_{B0}/F_{A0}</math>)</i>	146



8.5.3.2	<i>Effect of volume of the reactor (<math>V</math>) and Residence time (<math>\tau</math>)</i>	147
8.5.3.3	<i>Effect of coolant inlet temperature (<math>T_{j_{in}}</math>) and coolant mass flow rate</i>	149
8.5.4	Safety aspects of the operation in CSTRs	150
8.5.5	Scale-up Strategies	151
8.5.5.1	<i>Scheme I: Thermal conductivity (<math>k_{MOC}</math>) = 1.06 W/m.K</i>	151
8.5.5.2	<i>Scheme II: Thermal conductivity (<math>k_{MOC}</math>) = 16.3 W/m.K</i>	153
8.5.5.3	<i>Scheme III: Reactors configuration with multipoint dosing</i>	155
8.5	Conclusions	158

### ***Part III: Flow Past Objects in Small Channels***

<b>Chapter 9</b>	<b>Effect of Shape of Microstructured Post on the Flow in Small Channels</b>	165
9.1	Introduction	166
9.2	Experimental Section	167
9.3	Modelling and simulations	168
9.3.1	Geometries, computational domain	168
9.3.2	Governing equations	171
9.3.3	Boundary conditions	171
9.3.4	Parameters studied	172
9.3.4.1	<i>Wake Length (<math>L_W</math>)</i>	172
9.3.4.2	<i>Drag coefficient (<math>C_D</math>) and Lift coefficient (<math>C_L</math>)</i>	172
9.3.4.3	<i>Pressure coefficient (<math>C_P</math>)</i>	173
9.3.4.4	<i>Vorticity in a channel (<math>\Omega</math>)</i>	173
9.3.4.5	<i>Critical Reynolds number (<math>Re_C</math>) for onset of vortex shedding</i>	173
9.3.5	Mesh independence	174
9.4	Results and Discussions	176
9.4.1	Validation of model	176
9.4.1.1	<i>Comparison with Experimental data</i>	176
9.4.1.2	<i>Comparison with literature data</i>	176
9.4.2	Flow patterns (streamline contour plots)	178
9.4.3	Flow-induced forces	183
9.4.4	Onset of vortex shedding	186
9.5	Effect of arrays of objects on mixing	189
9.6	Conclusions	192
<b>Chapter 10</b>	<b>Conclusions and Recommendations</b>	196
10.1	Conclusions	197
10.2	Recommendations	200

## List of Figures

Figure 2.1	Geometry of the stirred tank reactor	10
Figure 2.2	Radial flow impellers (Paul et al., 2004) <i>Reproduced with the permission from the publisher</i>	11
Figure 2.3	a) Axial profiles of mean radial velocity component (Legends specify the source of the original data) (Cooper and Wolf, 1968; Ranade and Joshi, 1990; Wu et al., 1989), b) Flow patterns generated by a Rushton turbine in a stirred tank ( <i>modified from Ng et al. (1998)</i> )	12
Figure 2.4	Axial flow impellers (Paul et al., 2004). <i>Reproduced with the permission from the publisher</i>	13
Figure 2.5	Hydrofoils with different blade angles and blade width. <i>Reproduced with the permission from the publisher</i> (Kumaresan and Joshi, 2006)	13
Figure 2.6	a) Axial velocity mean profile of pitched blade turbine and hydrofoil (modified from Kumaresan and Joshi (2006)), b) Flow generated by axial flow impellers (modified from Mishra et al. (1998))	14
Figure 2.7	Close clearance impellers a) helical ribbon, b) anchor (Paul et al., 2004). <i>Reproduced with the permission from the publisher</i>	15
Figure 2.8	Power number ( $N_p$ ) vs Reynolds number ( $Re$ ) for axial flow (Pitched blade turbine) and Radial flow impeller (Rushton turbine). <i>Modified from Literature</i> (Rushton et al., 1950)	16
Figure 2.9	a) Radial profile of dimensionless turbulent kinetic energy at impeller stream plane of Rushton turbine. ( <i>Legends specify the source of original data</i> (Baldi and Yianneskis, 2004; Cutter, 1966; Kresta and Wood, 1991; Murthy and Joshi, 2008; Wu and Patterson, 1989; Yeoh et al., 2004)). b) Axial profile of dimensionless turbulent kinetic energy across impeller tip at different radial locations (Legends specify the original data source) (Escudie and Line, 2003; Ito et al., 1975; Michelet, 1998; Wu and Patterson, 1989)	19
Figure 2.10	Radial profile of dissipation rate at impeller stream plane (Legends specify the original data source) (Baldi and Yianneskis, 2004; Lee and Yianneskis, 1998; Micheletti et al., 2004; Ng et al., 1998; Wu and Patterson, 1989; Yeoh et al., 2004; Yianneskis, 2000), b) Axial profile of dissipation rate at $r/R = 0.44$ (Legends specify the original data source) (Baldi and Yianneskis, 2004; Escudie and Line, 2003; Wang et al., 2014)	27
Figure 2.11	Radial profile of ratio of local dissipation rate to average dissipation rate at impeller stream ( <i>Legends specify the original data source</i> ) (Anandha Rao and Brodkey, 1972; Baldi and Yianneskis, 2004; Cutter, 1966; Komasaawa et al., 1974; Laufhutte and Mersmann, 1985; Okamoto et al., 1981; Sharp and Adrian, 2001; Wu and Patterson, 1989)	29
Figure 2.12	Mixed flow impeller or ARI (dimensions are in mm) ( <i>Reproduced with permission from the Publisher</i> (Ascanio et al., 2003))	37
Figure 2.13	Grid Disc Impeller (GD) (a) radial grid disc (b) square grid disc ( <i>Reproduced with permission from the Publisher</i> (Buwa et al., 2006))	38

Figure 2.14	Six blade grid disc impeller (referred to as RT-G) ( <i>Reproduced with permission from the Publisher</i> (Yang et al., 2015))	39
Figure 2.15	Rotational reciprocating plate impeller (RRPI) (a) top hub, (b) bottom hub, (c) the complete assembly (two hubs are positioned with a 30° angle relative to each other) ( <i>Reproduced with permission from the Publisher</i> (Lin et al., 2011))	40
Figure 2.16	Impeller geometries (a) Rushton turbine, (b) pitched blade turbine (PBT), (c) axial disc turbine (ADT), (d) hydrofoil (H), (e) mono axial-radial disc turbine (MARDT), (f) modified mono axial-radial disc turbine (MMARDT), (g) bi axial-radial disc turbine (BARDT), (h) modified bi axial-radial disc turbine (MBARDT) ( <i>Reproduced with permission from the Publisher</i> (Cabaret et al., 2008))	41
Figure 2.17	Schematic of Maxblend Impeller (a) Maxblend impeller design (b) tank wall (c) baffles (d) impeller grid part (e) impeller bottom paddle part (f) bottom gas region (clearance) ( <i>Reproduced with permission from the Publisher</i> (Iranshahi et al., 2007) )	43
Figure 2.18	Fractal generator and its initiator and corresponding fractal growth	44
Figure 2.19	Schematic diagram of Fractal Impeller (FI) A) front view, B) top view C) photograph of FI ( <i>modified from</i> (Kulkarni et al., 2011))	46
Figure 3.1	Velocity measurements in a stirred tank with FI by UVP (probe orientation 1 is for measurement of axial velocity, 2 for radial velocity and 3 for tangential velocity component, respectively)	60
Figure 3.2	Block diagram of data processing	61
Figure 4.1	Different zones in the modeling of stirred tank	74
Figure 5.1A	Schematic of experimental setup (1) Stirred tank, (2) electric motor, (3) UVP-Duo data acquisition system, (4) UVP probes, (5) digital torque sensor, (6) computer	80
Figure 5.1B	Photograph of Experimental Set-up	80
Figure 5.2	Grid for the fractal impeller and for the flow domain in a stirred tank A) Geometry 1 (1 rotating zone and one stationary zone), B) Geometry 2 (3 rotating zones and 1 stationary zone)	82
Figure 5.3	Effect of grid size on tangential mean velocity ( $w$ ) in the stirred tank with FI for geometry	83
Figure 5.4	(Top row) Radial mean velocity component (Middle row) Axial mean velocity component, (Bottom row) Tangential mean velocity component for experimental and CFD models at 1 <i>rps</i> . A separate comparison of CFD results with that of experimental is provided in the supporting information	87

Figure 5.5	Contour plots of normalized mean velocity components in $r$ - $z$ plane (CFD, $N = 1$ ), (A) radial ( $u/U_{Max}$ ), (B) axial ( $v/U_{Max}$ ), and (C) tangential mean velocity ( $w/U_{Max}$ ). Color scales show the maximum and minimum normalized velocity for each component	89
Figure 5.6	Mean velocity in an $r$ - $z$ plane between two baffles. Vector plot of left half plane estimated experimentally and vector plot of right half plane estimated by CFD simulations	90
Figure 5.7	Radial mean velocity profile along the $z$ -axis at $r/R = 0.677$ ( $D_{FI}/2$ ) $\diamond$ -Experiments, ---CFD	92
Figure 5.8	Schematic of fractal impeller rotation in the stirred tank	93
Figure 5.9	Radial instantaneous velocity at $r$ - $z$ mid-plane between two baffles with respect to the position of the branch. A) $\alpha=18^\circ$ , B) $\alpha=36^\circ$ , C) $\alpha=45^\circ$ , D) $\alpha=54^\circ$ , E) $\alpha=72^\circ$ , F) $\alpha=90^\circ$	94
Figure 5.10	Axial instantaneous velocity at $r$ - $z$ mid-plane between two baffles with respect to the position of the impeller branch. A) $\alpha=18^\circ$ , B) $\alpha=36^\circ$ , C) $\alpha=45^\circ$ , D) $\alpha=54^\circ$ , E) $\alpha=72^\circ$ , F) $\alpha=90^\circ$	95
Figure 5.11	Tangential instantaneous velocity at $r$ - $z$ mid-plane between two baffles with respect to the position of the branch. A) $\alpha=18^\circ$ , B) $\alpha=36^\circ$ , C) $\alpha=45^\circ$ , D) $\alpha=54^\circ$ , E) $\alpha=72^\circ$ , F) $\alpha=90^\circ$	96
Figure 5.12	Contour plot of RMS velocities A) radial ( $u_{RMS}$ ) component b) axial ( $v_{RMS}$ ) component	97
Figure 5.13	Radial profile of turbulent kinetic energy (experimental) for rps, $N$ ( $\diamond$ -1) over three axial planes. A) $z/R=0.733$ , B) $z/R=1.233$ , C) $z/R=1.733$	98
Figure 6.1	Photograph of the experimental set-up	104
Figure 6.2	Power consumption characteristics of FI, A) $P_W$ vs $N^3D^2$ , B) Slope of the energy drawn as a function of viscosity C) Power number ( $N_P$ ) vs $\log(Re)$ (points for Rushton Turbine and Pitched Blade Turbine are taken from literature [1]), D) Constant ( $\alpha$ ) as a function of viscosity for FI	105
Figure 6.2	Mixing characteristics of FI, A) response curve of normalized conductivity at different $N$ , B) mixing time ( $\theta_{mix}$ ) vs power consumption per unit mass ( $P_W$ ). $\blacksquare$ - water, $\blacktriangle$ - Liquid-3 and $\blacklozenge$ - Liquid-1	107
Figure 6.3	Mean flow patterns generated by FI in a stirred tank in an $r$ - $z$ plane between two baffles. Vector plot of left half plane and contour plot of the velocity magnitude ( $(u^2 + v^2)^{0.5}$ ) in the right half plane. In the contour plot of velocity magnitude the darkest region indicates the maximum velocity and the brightest field shows minimum velocity	109
Figure 6.4	Normalized radial profiles of mean radial velocity at different axial locations A) $z/R=0.33$ , B) $z/R=1.233$ , C) $z/R=1.7$ , D) $z/R=1.9$	110

Figure 7.1	Schematic diagram of Fractal Impeller (FI) A) top view (2 branches), B) top view (3 branches) C) top view (4 branches) D) front view (4 branches).	116
Figure 7.2	Schematic of the experimental setup (1) Stirred tank with FI (4 branches), (2) electric motor, (3) UVP-Duo data acquisition system, (4) UVP probes, (5) digital torque sensor, (6) computer	117
Figure 7.3	Radial profiles of radial mean velocity ( $u$ ) at different axial locations ( $z/R$ ) for different $N$ ( $\square = 1$ , $\Delta = 1.5$ , $\circ = 2$ ) A) $z/R=0.4$ , B) $z/R=0.833$ , C) $z/R=1.167$ . For all the plots, ordinate is $u/U_{\max}$	118
Figure 7.4	Contour plots of the measured normalized mean radial velocity in $r$ - $z$ plane for three different configurations of FI (Left) 2 branches, (Middle) 3 branches, (Right) 4 branches	119
Figure 7.5	Contour plots of the measured normalized mean axial velocity in $r$ - $z$ plane for three different configurations of FI (Left) 2 branches, (Middle) 3 branches, (Right) 4 branches	119
Figure 7.6	Radial profiles of normalized tangential mean velocity ( $w$ ) at different axial locations ( $\diamond$ -2 branches, $\Delta$ -3 branches, $\bullet$ -4 branches) A) $z/R=0.4$ , B) $z/R=0.67$ , C) $z/R=0.83$ , D) $z/R=1.167$ , E) $z/R=1.5$ , F) $z/R=1.67$	121
Figure 7.7	Tangential velocity normalized with local tip velocity at different axial locations (A) $z/R=1.667$ (region occupied by FI) (B) $z/R=1.5$ (region unoccupied by FI)	122
Figure 7.8	Flow Patterns in an $r$ - $z$ plane for three configurations of FI A) 2 branches, B) 3 branches, C) 4 branches	123
Figure 7.9	Normalized mean kinetic energy at different axial locations ( $\diamond$ -2 branches, $\Delta$ -3 branches, $\circ$ -4 branches) A) $z/R=0.4$ , B) $z/R=0.833$ , C) $z/R=0.1.16$ , D) $z/R=1.5$	124
Figure 7.10	(A) Variation of the power consumption per unit mass ( $P_w$ ) with impeller $Re$ , (B) $P_w$ vs. $N^3 D^2$ , (C) $\log[P_w]/\log[Re]$ vs. $\log(Re)$ , (D) $N_p$ vs. $\log(Re)$	126
Figure 7.11	A) Dimensionless mixing time ( $N\theta_{mix}$ ) vs $P_w$ , B) mixing time ( $\theta_{mix}$ ) vs $P_w$ , C) comparison of mixing performance of FI with Propeller and Disc Grid impeller (mixing studies by (Buwa et al., 2006) were carried out with water in 0.3m diameter tank, *Prochem Maxflow axial flow hydrofoil)	128
Figure 8.1	Experimental Set up for kinetics study	140
Figure 8.2	Experimental Set up for the production of 1-Nitro naphthalene (V-101 – stock solution naphthalene, V-102 – $HNO_3$ reservoir, P-101, 102, 103, 104 – Pumps used for the continuous operation, R-101 – CSTR1, R-102 – CSTR2, V-103 – Product container)	141
Figure 8.3	Temperature profile of CSTR1 with respect to time	145
Figure 8.4	Temperature variation in CSTR1 with respect to time	146

Figure 8.5	Reactor temperature profiles at different molar ratio A) $C_{A0}=2.1$ milimoles/ml, B) $C_{A0}=3.9$ moles/ml, C) $C_{A0}=5.7$ milimoles/ml, E) Conversion vs Molar flow ratio ( $F_{B0}/F_{A0}$ ), F) Production (kg/day) vs Molar flow ratio ( $F_{B0}/F_{A0}$ )	147
Figure 8.6	Effect of volume of the reactor and residence time on A) Temperature ( $T_{rx}$ ) in the reactor, B) Percent conversion, C) Production (kg/day)	148
Figure 8.7	Effect coolant parameters A) Multiple steady states, B) Coolant inlet temperature, C) Coolant flow rate	150
Figure 8.8	Safety aspects related to the operation of CSTRs	151
Figure 8.9	Effect of residence time and operating volume on various parameters for $k_{MOC} = 1.06$ W/m.K. A) Temperature in the reactor, B) Production, C) Conversion.	152
Figure 8.10	A) Reactor assembly for scale-up, B) Temperature in the reactors ( $k_{MOC}=1.06$ W/m.K).	153
Figure 8.11	Effect of residence time and operating volume on various parameters for $k_{MOC} = 16.3$ W/m.K. reactors A) Temperature in the reactor, B) Production, C) Conversion.	154
Figure 8.12	A) Reactor assembly for scale-up ( $k_{MOC} = 16.3$ W/m.K), B) Temperature in the reactors	155
Figure 8.13	Schematic of multipoint dosing in CSTRs in series	155
Figure 8.14	Temperature profiles of CSTRs A) Case-IIIA, B) Case-IIIB, C) Case-IIIC, D) Case-IIID, E) Case-IIIE	158
Figure 9.1	A) Schematic of experimental setup, B) Photograph of channel with square micropillar	168
Figure 9.2	A) 3D geometry for flow in a micro-channel B) 2D geometry for flow in a microchannel, C) Different conventional 2D cross-sectional geometries, D) Fractal 2D cross-sectional geometries considered in this work	170
Figure 9.3	Mesh structure in computational domain A) 2D square channel (top), B) near object (bottom left), C) at the corner of the object (bottom right)	175
Figure 9.4	A) Estimation of wake length ( $L_w$ ) from experimental data, B) Comparison of CFD results with that of experimental	176
Figure 9.5	Comparison with literature data A) drag coefficient ( $C_D$ ) vs $Re$ B) wake length ( $L_w$ ) vs $Re$ for a square cylinder at blockage ratio ( $\lambda$ ) 0.125, C) Drag coefficient ( $C_D$ ) vs blockage ratio ( $\lambda$ ), D) critical Reynolds number for flow oscillations ( $Re_C$ ) for a square cylinder [(Sharma and Eswaran, 2004) and (Patil and Tiwari, 2008) calculated $Re$ based on mean velocity at the channel inlet and hence are recalculated on the basis of maximum velocity for comparison.	177

Figure 9.6	Streamlines contour plots of elliptical cylinders of different aspect ratio (AR) at $Re=30$ A) 0.001, B) 0.1, C) 0.5, D) 1 or circular cylinder, E) 1.5, F) 2	179
Figure 9.7	Streamlines contour plots of rectangular cylinder of different aspect ratio (AR) at $Re=30$ A) 0.001 or plate, B) 0.1, C) 0.5, D) 1 or square cylinder, E) 1.5, F) 2	180
Figure 9.8	Streamlines contour plots of triangular cylinders of different aspect ratio (AR) at $Re=30$ A) $AR = 0.14$ or $\theta = 150^\circ$ , B) $AR = 0.29$ or $\theta = 120^\circ$ , C) $AR = 0.5$ or $\theta = 90^\circ$ , D) $AR = 1$ or $\theta = 53.13^\circ$ , E) $AR = 1.20$ or $\theta = 45^\circ$ , F) $AR = 1.87$ or $\theta = 30^\circ$	180
Figure 9.9	Streamline contour plots of flow around fractal objects of square initiator A) $Re=1$ , B) $Re=12$ , C) $Re=30$	182
Figure 9.10	Streamline contour plots of flow around fractal objects of triangle initiator A) $Re=1$ , B) $Re=12$ , C) $Re=30$	183
Figure 9.11	A) Drag coefficient ( $C_D$ ) vs $Re$ , B) ratio of $C_D$ for elliptical cylinders vs $Re$ , C) ratio of $C_D$ for rectangular cylinders vs $Re$ , D) ratio of $C_D$ for triangular cylinders vs $Re$ , E) ratio of $C_D$ for square cylinders fractals vs $Re$ , F) ratio of $C_D$ for triangular cylinders fractals vs $Re$	186
Figure 9.12	Critical Reynolds number ( $Re_C$ ) for the onset of vortex shedding A) with respect to the aspect ratio (AR) for different cylindrical objects, B) with respect of fractal iteration, C) with respect to cross-sectional area	187
Figure 9.13A	Symmetrical arrays with triangular cylinders (movement of the tracer)	189
Figure 9.13B	Asymmetrical arrays with triangular cylinders (movement of the tracer)	190
Figure 9.13C	Random arrays with triangular cylinders (movement of the tracer)	191
Figure 9.14	A) Residence time ( $\tau$ ) vs Reynolds number, B) Number of CSTRs vs Reynolds number. Here Reynolds number is calculated on the basis of the diameter of the channel	192

# **Chapter 1**

## **Introduction**



---

## 1.1 Motivation and Background

Mixing means the reduction of inhomogeneity of parameters like concentration, temperature or phase distribution in a reactor. The inhomogeneity in the process results in poor mass transfer, heat transfer and possibly also the selectivity of the desired product (Paul et al., 2004). The extent of mixing in different types of systems such as Liquid-Liquid, Gas-Liquid, Gas-Gas, Solid-Liquid, Solid-Solid and other multiphase combinations depends on physiochemical properties and the power consumption. Therefore, mixing is considered as an important operation in wide range of industries such as fine chemicals, pharmaceuticals, agrichemicals, petrochemicals, polymer processing, paints, food and mineral processing. Mixing can be directly related to operational cost, for example, improper mixing leads to larger batch cycles and hence operational costs.

In most of the batch operations mixing is achieved by stirring which creates inhomogeneous energy distribution in the reaction vessel. On the other hand, in small channels, shorter diffusion path and small volumes provide excellent mixing even with laminar flow. It should be noted that mixing takes place in a reacting vessel or a channel with a diffusion of the molecule. The shortest distance required for diffusion of one species to another is called as diffusion path. In case of small channels characteristics length scale is small and hence molecular diffusion is fast which results in mixing in a shorter time. In general, Mixing time (mixing time scale) is proportional to the square of the length (mixing length scale) of diffusion path. Hence it becomes important to study both the aspects for understanding the mixing in process operations. It is a known fact that most of the mixing problem arises in the scaling up the process design, where the balance between mixing time scale to mixing length scale needs to be established to get desired process results. Literature reports several correlations to establish the mixing time in a vessel for various operations with known designs ((Nienow, 1997) (Dewan et al., 2006; Kasat et al., 2008). Hence, the readily available correlations can be used to design the process. However, it is important to study each aspect of mixing for novel designs such as a novel impeller, novel reactors or novel process.

In general, mixing principles applied can be divided into two parts as active and passive mixing. In an active mixing, external energy is provided to achieve mixing, for example, use of impeller in the stirred tank or ultrasound etc. The geometry of stirred and the type of the impeller

---

can vary depending on the operation. The stirred tank can be a flat bottom or disc shape with baffles or without baffles. Additional parts such as a draft tube, heating coils can be added to the system. Conventional impellers are available in a large variety and can be utilized as per the process requirement. These include propellers, disc turbines, hydrofoils and close clearance impellers. Propellers and hydrofoils are mostly preferred for solid suspensions and homogenization (Fentiman et al., 1999; Mishra et al., 1998), disc turbines for gas-liquid operation (Paul et al., 2004; Ranade et al., 2001) and close clearance impellers are preferred for achieving mixing of highly viscous liquids (Bakker and Gates, 1995; Cabaret et al., 2008). One of the key issues with conventional impellers is that the most of the energy provided by them to the fluid is dissipated around the impeller region which is only 5-10% of the total volume of the reactor (Kresta, 1998; Kresta and Wood, 1993; Ng and Yianneskis, 2000). One of the ways to achieve the uniformity in the stirred tank is to have an impeller spread over the entire tank. In view of this, a novel impeller named ‘Fractal Impeller’ is developed at the CSIR-National Chemical Laboratory, Pune. A significant part of this thesis is based on the understanding the performance of Fractal Impeller (FI) in a stirred tank reactor.

Mixing in reactions involving multiple reactants plays a vital role in determining the rate of the reaction. For fast and exothermic reactions, it can be safely said that rate of mixing is the rate of reaction (Baldyga and Bourne, 1990; Bałdyga et al., 1997). Hence maintaining the mixing time per unit power consumptions in the stirred reactors becomes important to achieve similar results when scaling-up the reactor. Part of the thesis is based on the scale-up of the continuous stirred tank reactors for the fast and exothermic reaction using numerical simulations.

Passive mixing is achieved by the supply of pressure energy in the form of pumping and can be achieved using various methods including static mixers and other variants in small channels (Ehrfeld et al., 2000). There are different devices by which passive mixing can be achieved for example Y—type flow mixers, T—type flow mixers, split—and—recombine flow mixers, diverge—converge flow mixers etc. One of the ways to achieve mixing in small channels is by splitting and recombining the streamlines by inserting a post in a channel. Remaining part of the thesis is based on our analysis of mixing in small channels where the flow past objects of various shapes is explored.

---

## 1.2 Outline

This work aims at the improving mixing efficiency in stirred tank reactors as well as in small channels. Initial experiments and results in terms of mixing time per unit power consumed, solid handling and dispersion of gas in the liquid using a FI were much better than the standard impellers (Kulkarni et al., 2011). The results motivated us to study the flow pattern and relate it to its overall performance in terms of hydrodynamics and mixing of medium viscosity liquids. In addition to this, it was essential to study the various design aspects of the FI. The flow pattern generated by the Fractal Impeller was studied experimentally using Ultrasonic Velocity Profiler (UVP) and Computational Fluid Dynamics (CFD). The results related to this are discussed in Chapter 5. The CFD results were validated by experimental data as well as literature findings. In a view of this the thesis is outlined as follow;

### Part 1: Fractal Impeller for Stirred Tank Reactor

Chapter 2 presents the fundamentals of the stirred tank, distribution of turbulent kinetic energy ( $k$ ) and its dissipation ( $\varepsilon$ ) in a stirred tank. Recent developments in novel impellers have also been discussed briefly. In addition, the design of Fractal Impeller has been discussed in details.

In Chapter 3, experimental techniques used to study the performance of Fractal Impeller in terms of mixing; power consumption and hydrodynamics are discussed in details.

In Chapter 4, details of Computational Fluid Dynamics (CFD) such as governing equations, turbulent models, modeling approaches used in simulations of stirred tank reactors are discussed.

Chapter 5 illustrates the flow generated by Fractal Impeller in a stirred tank. The comparison of various CFD techniques with that of experimental has been presented and discussed.

Chapter 6 presents the mixing of medium viscosity liquids in a stirred tank with Fractal Impeller. The liquids used for the experimentations are 200 times more viscous than water. Results show some interesting aspects of power consumption by Fractal Impeller.

In Chapter 7, the design aspects of Fractal Impeller have been studied by evaluating the performance of various designs in terms of mixing, power consumption, and hydrodynamics.

Part 2: Exothermic reactions in stirred tank reactor: Chapter 8 presents the effectiveness of Continuous Stirred Tank Reactors (CSTRs) for exothermic nitration reactions, where complete homogenization in the reactor is assumed. In this work, numerical modeling was done for CSTRs using Matlab and results were validated using experimental data.

Part 3: Flow past objects in small channels: In Chapter 9, flow past objects in small channels is discussed in view of passive mixing. The various geometries of the objects (including fractal shapes) were selected and the flow pattern was analyzed on the basis of vortex shedding and its dynamics.

Summary of the overall work and future recommendations are discussed in Chapter 10.

---

**References**

Bakker, A., Gates, L.E., 1995. Properly choose mechanical agitators for viscous liquids. *Chemical Engineering Progress* 91, 25-34.

Baldyga, J., Bourne, J., 1990. The effect of micromixing on parallel reactions. *Chemical Engineering Science* 45, 907-916.

Baldyga, J., Bourne, J., Hearn, S., 1997. Interaction between chemical reactions and mixing on various scales. *Chemical Engineering Science* 52, 457-466.

Cabaret, F., Fradette, L., Tanguy, P.A., 2008. New turbine impellers for viscous mixing. *Chemical Engineering & Technology* 31, 1806-1815.

Dewan, A., Buwa, V., Durst, F., 2006. Performance optimizations of grid disc impellers for mixing of single-phase flows in a stirred vessel. *Chemical Engineering Research and Design* 84, 691-702.

Ehrfeld, W., Hessel, V., Haverkamp, V., 2000. *Microreactors*. Wiley Online Library.

Fentiman, N.J., Lee, K.C., Paul, G.R., Yianneskis, M., 1999. On the trailing vortices around hydrofoil impeller blades. *Chemical Engineering Research and Design* 77, 731-740.

Kasat, G.R., Khopkar, A.R., Ranade, V.V., Pandita, A.B., 2008. CFD simulation of liquid-phase mixing in solid-liquid stirred reactor. *Chemical Engineering Science* 63, 3877-3885.

Kresta, S., 1998. Turbulence in stirred tanks: Anisotropic, approximate, and applied. *The Canadian Journal of Chemical Engineering* 76, 563-576.

Kresta, S.M., Wood, P.E., 1993. The flow field produced by a pitched blade turbine: Characterization of the turbulence and estimation of the dissipation rate. *Chemical Engineering Science* 48, 1761-1774.

Kulkarni, A.A., Jha, N., Singh, A., Bhatnagar, S., Kulkarni, B.D., 2011. Fractal impeller for stirred tank reactors. *Industrial & Engineering Chemistry Research* 50, 7667-7676.

Mishra, V.P., Dyster, K.N., Nienow, A.W., Mckemmie, J., Jaworski, Z., 1998. A study of an up-and a down-pumping wide blade hydrofoil impeller: Part I. LDA measurements. *The Canadian Journal of Chemical Engineering* 76, 577-588.

Ng, K., Yianneskis, M., 2000. Observations on the distribution of energy dissipation in stirred vessels. *Chemical Engineering Research and Design* 78, 334-341.

Nienow, A.W., 1997. On impeller circulation and mixing effectiveness in the turbulent flow regime. *Chemical Engineering Science* 52, 2557-2565.

Paul, E.L., Atiemo-Obeng, V., Kresta, S.M., 2004. *Handbook of industrial mixing: science and practice*. John Wiley & Sons.

Ranade, V., Perrard, M., Le Sauze, N., Xuereb, C., Bertrand, J., 2001. Trailing vortices of Rushton turbine: PIV measurements and CFD simulations with snapshot approach. *Chemical Engineering Research and Design* 79, 3-12.

***Part-I: Fractal Impeller for Stirred Tank Reactors***

## **Chapter 2**

### **Introduction to Stirred Tank Reactors**



## 2.1 Fundamentals of Stirred Tank Reactors

The primary aim of any agitation system is to provide adequate mixing. For solid-liquid systems, an impeller should allow particles to suspend. However, in gas-liquid or gas-liquid systems bubble dispersion is necessary. Along with the main motive for the particular operation, the impeller performs several side activities. In this Chapter, all basic concepts related to impellers and stirred tank are discussed in details. These concepts and definitions form a basis for the explanation of the results in Chapters 5-8.

### 2.1.1 Geometry of the Stirred Tank Reactor

As mentioned in the previous chapter, impeller and geometry of stirred tank play an important role in performance. Stirred tank geometry involves several factors such as

- i) Impeller geometry (number of blades, inclination of the blades)
- ii) Tank diameter,  $T$
- iii) Impeller size (ratio of impeller diameter to tank diameter,  $D/T$ )
- iv) Aspect ratio (ratio of the height of the liquid in the tank to the tank diameter,  $H/T$ )
- v) Impeller clearance (ratio of the distance between the tank bottom and the impeller to the height of the vessel,  $C/T$ )
- vi) Baffle width (ratio of baffle width to the diameter of tank,  $W/T$ )

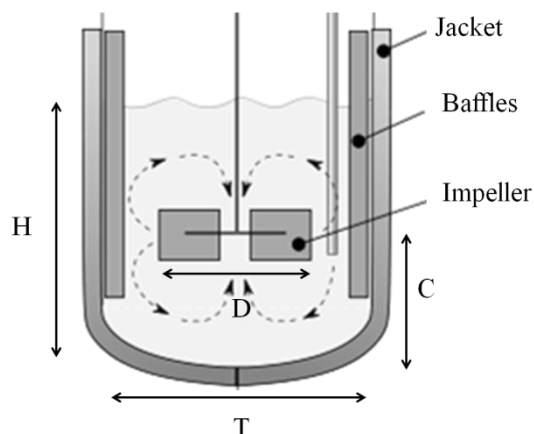


Figure 2.1: Geometry of the stirred tank reactor.

(modified from [https://en.wikipedia.org/wiki/Continuous\\_stirred-tank\\_reactor](https://en.wikipedia.org/wiki/Continuous_stirred-tank_reactor))

Impeller geometry is selected based on the process operation. However, these impellers can be broadly classified on the basis of the flow patterns they generate as axial flow impellers, radial flow impellers and tangential flow impellers (close clearance impellers).

### 2.1.1.1 Radial flow impellers and flow characteristics

Radial flow impellers are mostly used in the multiphase mixing. They are most effective for gas-liquid and liquid-liquid dispersion as they provide high shear and turbulence level (Paul et al., 2004). Radial flow impellers are further classified as Flat Blade Turbines (FBT) and Rushton Turbines (RT) (see Figure 2.2). Various other geometries can also be obtained by curving the blades (Vasconcelos et al., 2000; Zhao et al., 2011). Radial turbine induces a strong radial discharge stream towards the wall of the tank. Radial velocity is the most significant velocity in the impeller discharge stream. The maximum velocity in the stirred tank is at the tip of the impeller blade, which is referred as  $U_{tip}$ , and given by  $\pi DN$ . Here,  $D$  is an impeller diameter in meters and  $N$  is an impeller rotational speed in seconds. The global studies on the stirred tank suggest that radial mean velocity at the impeller tip is 65 to 80% of the  $U_{tip}$  (Cooper and Wolf, 1968; Escudie and Line, 2003; Lee and Yianneskis, 1998; Ranade and Joshi, 1990; Wu et al., 1989; Wu and Patterson, 1989).

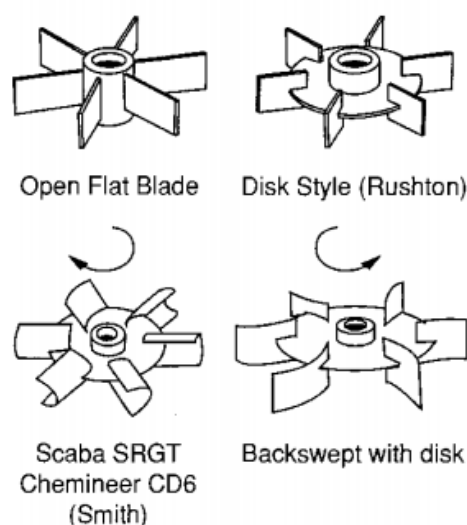


Figure 2.2: Radial flow impellers (Paul et al., 2004). *Reproduced with the permission from the publisher.*

Figure 2.3 shows the variation in the axial profile of the mean radial velocity component at different radial locations. From Figure 2.3a it can be observed that the radial component of the velocity decreases gradually as the fluid approaches to the tank wall. Near the fully baffled tank wall, the radial discharge divides into two vertical opposite streams, forming two circulation loops, one below the area of radial flow at the level of stirrer blades and other, above (Costes and Couderc, 1988a; Yianneskis et al., 1987). Baffles help the impeller discharge stream to get redirected towards the impeller axis by drawing the fluid behind them into circulation loops (Yianneskis et al., 1987), therefore two distinct circulations are formed (see Figure 2.3b).

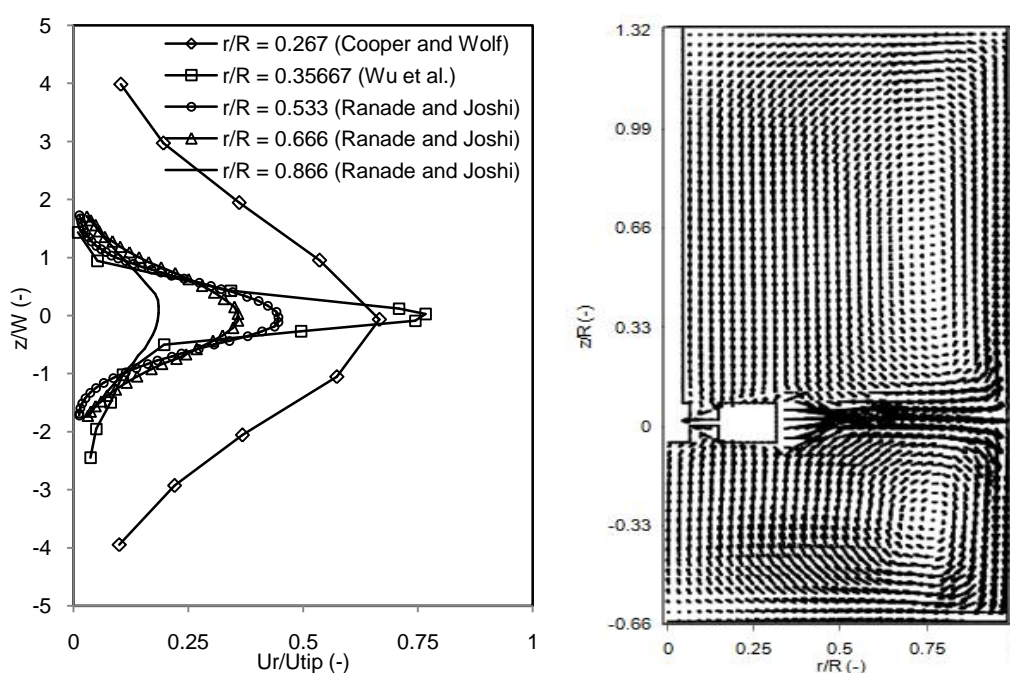


Figure 2.3: a) Axial profiles of mean radial velocity component (Legends specify the source of the original data) (Cooper and Wolf, 1968; Ranade and Joshi, 1990; Wu et al., 1989), b) Flow patterns generated by a Rushton turbine in a stirred tank (*modified from Ng et al. (1998)*)

### 2.1.1.2 Axial flow impellers and flow characteristics

Axial flow impellers are mostly preferred for solid suspensions; draw down of floating solids, mixing, however, in some cases for the gas-liquid system if operated in an up-pumping mode. These class impellers are Propellers, Pitched blade turbines (PBT), Pfudler retreat impeller, etc. Figure 2.4 gives the pictorial view of the axial flow impellers. Pitched blade turbines are widely used in the industries. Researchers have studied the effect of various design

aspects related to its geometry. The variations include the blade angle which can vary from  $10^\circ$  to  $90^\circ$  (Paul et al., 2004). However, most common blade angle is  $45^\circ$ . Kumaresan and Joshi (2006) carried out the systematic study on the effect of blade angle ( $30^\circ$ ,  $45^\circ$  and  $60^\circ$ ), number of blades, blade width and blade twist on the flow patterns generated by pitched blade turbines. Results show that the pitched blade turbines (in general, axial flow impellers) generate both radial and axial velocity components while discharging the fluid towards the tank (Aubin et al., 2004; Bugay et al., 2002; Jaworski et al., 1996; Ranade et al., 1992). Therefore, these impellers are also considered as mixed-flow impellers. In order to achieve more axial flow at low shear for particular operations, hydrofoil impellers were developed. Hydrofoils are considered more efficient than that of conventional impellers in terms of mixing achieved at same power consumption. Hydrofoil impellers are shown in Figure 2.5.

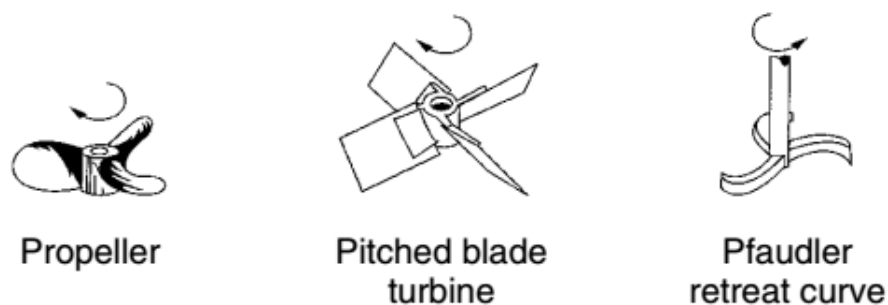


Figure 2.4: Axial flow impellers (Paul et al., 2004). *Reproduced with the permission from the publisher.*



Figure 2.5: Hydrofoils with different blade angles and blade width. *Reproduced with the permission from the publisher* (Kumaresan and Joshi, 2006).

In case of axial flow impellers (down-pumping), fluid is discharged axially downwards which hits the bottom of the tank. However, the intensity of the discharge stream is different for Hydrofoils and Pitched blade turbines (D), as can be observed in Figure 2.6a. Hydrofoils tend to produce more prominent downwards axial flow as compared to that of Pitched blade turbines (D). However, for the types, once the discharge stream hits the bottom, the fluid moves along the bottom then up the vessel wall. Due to movement of the blades low-pressure zone is created behind the impeller blades and hence fluid is drawn back to impeller zone. The entire process forms a circulation loop (see Figure 2.6b).

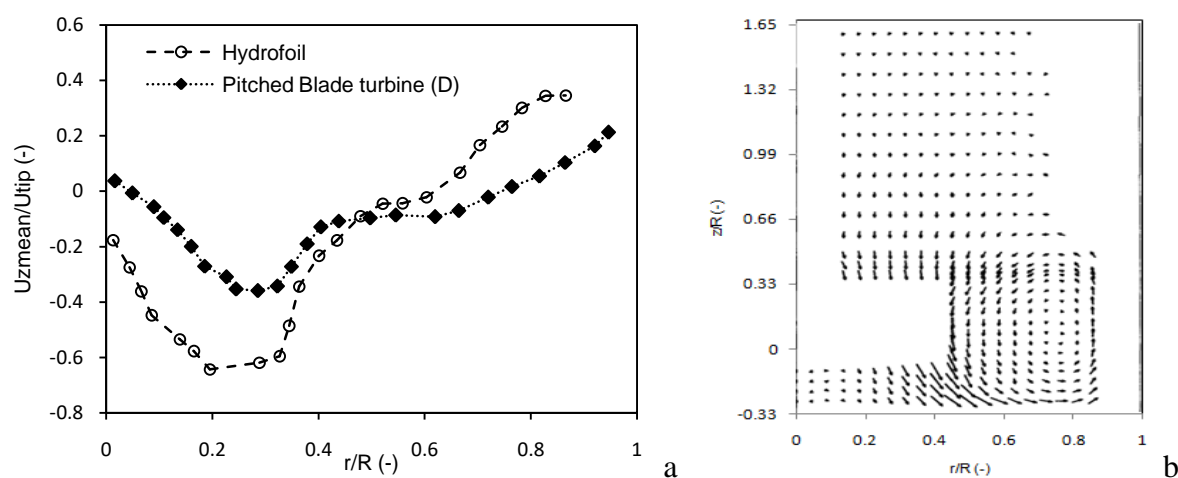


Figure 2.6: a) Axial velocity mean profile of pitched blade turbine and hydrofoil (modified from Kumaresan and Joshi (2006)), b) Flow generated by axial flow impellers (modified from Mishra et al. (1998))

### 2.1.1.3 Close clearance impellers

Highly viscous liquids (500- 50000 cPa) are difficult to pump; therefore standard impellers are not suitable for achieving mixing of highly viscous liquids. Instead, close clearance impellers are preferred for achieving mixing of highly viscous liquids. Typically, these impellers are large in size and provide top-to-bottom physical movement of the working liquid. The most common designs are the helical ribbon and the anchor (see Figure 2.7).

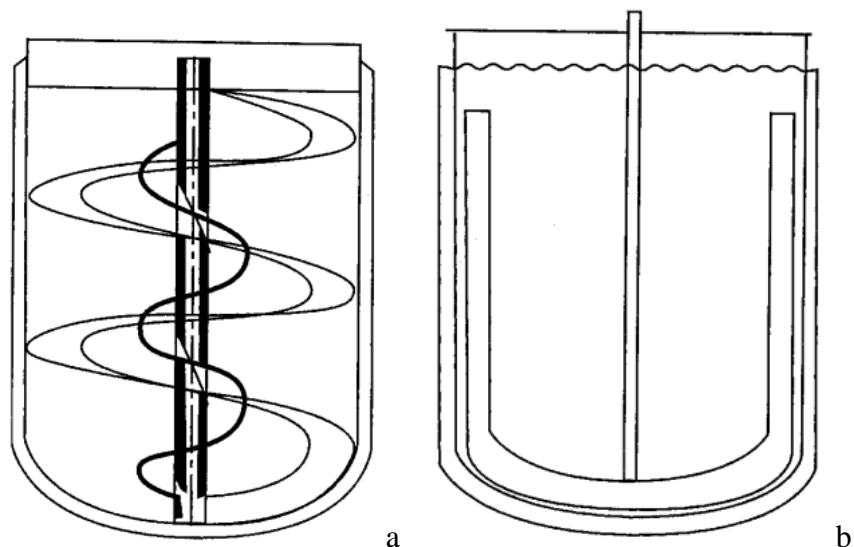


Figure 2.7: Close clearance impellers a) helical ribbon, b) anchor (Paul et al., 2004) *Reproduced with the permission from the publisher.*

### 2.1.2 Dimensionless groups used in the stirred tank reactors system

Literature reports different dimensionless number for the stirred tank reactors to evaluate the performance in terms of hydrodynamics of a given type of impeller. Listed below are the few important dimensionless numbers which are being used for evaluating the performance of fractal impeller.

#### 2.1.2.1 Reynolds Number, $Re$

Reynolds number is one of the most common dimensionless numbers used in fluid mechanics. It is defined as the ratio of inertia forces to viscous forces in a moving fluid. In the impeller system it is defined as follow;

$$Re = \frac{D^2 N \rho}{\mu} \quad 2.1$$

where  $D$  is an impeller diameter,  $N$  is the rotational speed in seconds,  $\rho$  is the density of the working fluid and  $\mu$  is the viscosity of the working fluid.

Reynolds number gives the idea about the flow regime in the system, for example when  $Re < 10-30$ , flow is termed as laminar, when  $30 < Re < 10^4 - 10^5$  flow is termed as transitional whereas for  $Re > 10^5$  it is known to be turbulent.

### 2.1.2.2 Power Number, $N_P$

Power number is considered as the significant dimensionless number in stirred tank systems as it gives an idea of the power characteristics of an impeller. It is a function of impeller type and Reynolds number, and is defined as follow;

$$N_P = \frac{P_0}{\rho N^3 D^5} \quad 2.2$$

where,  $P_0$  is the power generated by a given type of impeller.

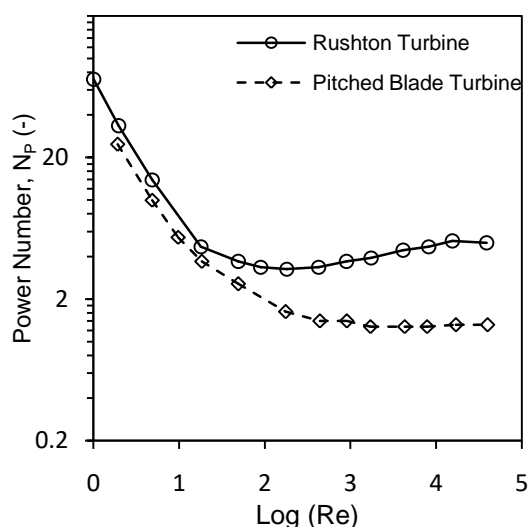


Figure 2.8: Power number ( $N_P$ ) vs Reynolds number ( $Re$ ) for axial flow (Pitched blade turbine) and Radial flow impeller (Rushton turbine). *Modified from Literature* (Rushton et al., 1950).

Power characteristics of the different impellers were first studied by Rushton et al. (1950), where authors systematically analyzed the power consumption of propellers, paddles and disc turbines by relating power number to the Reynolds number. Authors studied that for both propellers and Rushton turbines, on a logarithmic plot, power number found to decrease linearly with the Reynolds number in the laminar region. And, in a turbulent region, power number found

to be independent of Reynolds number. However, in the transition region, power number vs Reynolds number graph shows a different trend for the different impeller. For propellers, the power number decreases slowly with Reynolds number, on the other hand, for Rushton turbines power number first decreases and then increases with Reynolds number. Authors also show that power number also depends on the impeller internal designs. The power number for different impeller geometries is given in Table 2.2.

### 2.1.2.3 Flow number, $N_Q$

The flow number of an impeller is the dimensionless pumping flow rate,  $Q_{FL}$  of the impeller, here  $Q_{FL}$  refer to the flow rate from the impeller. The pumping flow rate corresponds to the fluid flow that is discharged from impeller swept volume. In general,  $Q_{FL}$  for radial and axial can be estimated as given in Eq. 2.3a in Eq. 3.2b respectively;

$$Q_{FL} = \int_{z^-}^{z^+} \pi D |u_{r,r}^0|_{r=r^+} dz \quad 2.3a$$

$$Q_{FL} = \int_0^{r^+} 2\pi r |u_{z,z}^0|_{z=z^+} dz \quad 2.3b$$

where,  $z^+$ ,  $z^-$  and  $r^+$  are the boundaries of the impeller swept volume and subscript '0' refers to fluid moving out of this volume. Calculated pumping flow can be used to estimate the flow number as;

$$N_Q = \frac{Q_{FL}}{ND^3} \quad 2.4$$

Literature reports the flow number for different impellers in the turbulent regime. For propellers, it is found to be in the range of 0.4 to 0.6. Whereas for Rushton turbines, it is 0.72 and for pitched blade turbines, it is 0.79.



### 2.1.3 Turbulent Kinetic Energy ( $k$ )

The estimation of turbulent kinetic energy induced in a stirred tank requires the knowledge of the root mean square (RMS) velocities of the three components. This can be done by measuring three separate velocity components.

$$k = \left(\frac{1}{2}\right) \overline{u'_i u'_i} \quad 2.5$$

where,  $u'_i$  is the deviation from mean velocity also known as fluctuating component. With 2D measurement technique, where the flow measurements take place on a plane, the estimation of the RMS-velocity of the third component has to be done using a pseudo-isotropic assumption. For example, if measurements are carried out in an  $r$ - $z$  plane, the tangential RMS-velocity component can be estimated from Eq. 2.6, and turbulent kinetic energy is estimated from Eq. 2.7

$$u_{\theta_{RMS}} = \left[ \left(\frac{1}{2}\right) \left( \overline{u_r'^2} + \overline{u_z'^2} \right) \right]^{0.5} \quad 2.6$$

$$k = \left(\frac{3}{4}\right) \left( \overline{u_r'^2} + \overline{u_z'^2} \right) \quad 2.7$$

here,  $u_{\theta_{RMS}}$  is the tangential RMS-velocity component. Khan et al., (2006) estimated turbulent kinetic energy ( $k$ ) by 2D Particle Image Velocimetry (PIV) (pseudo-isotropic turbulence assumption) and compared with the estimations from 3D PIV in a stirred tank with Pitched blade turbine (PBT). Authors found only a slight difference at the centre of the trailing vortex in the values of turbulent kinetic energy ( $k$ ). This approach was also adopted by some authors to estimate turbulent kinetic energy using 2D PIV for stirred tank with disc turbines (Li et al., 2011; Ranade et al., 2001; Zhao et al., 2011).

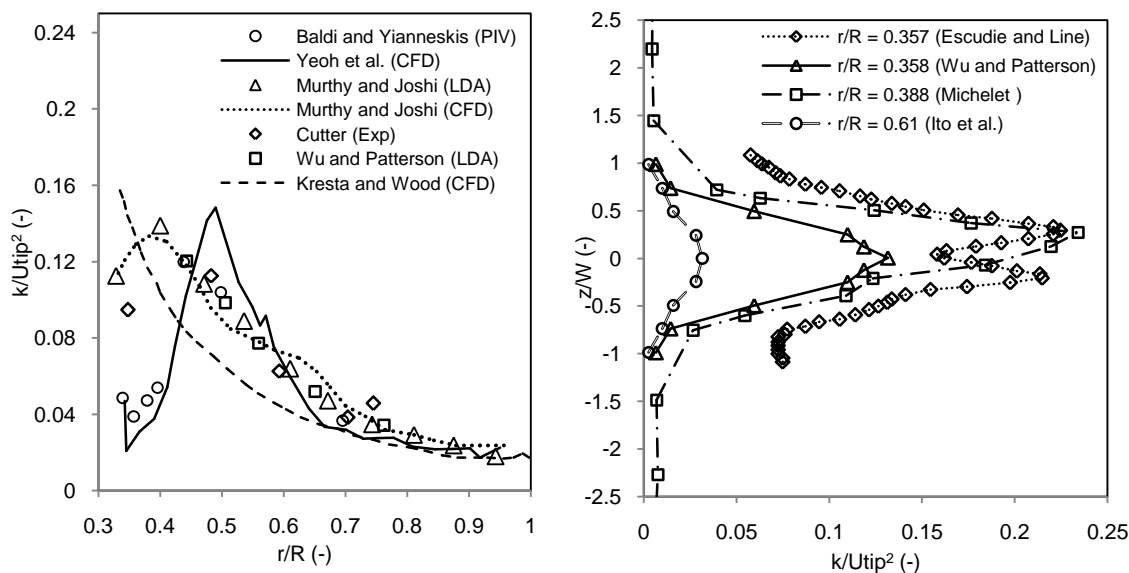


Figure 2.9: a) Radial profile of dimensionless turbulent kinetic energy at impeller stream plane of Rushton turbine. (Legends specify the source of original data (Baldi and Yianneskis, 2004; Cutter, 1966; Kresta and Wood, 1991; Murthy and Joshi, 2008; Wu and Patterson, 1989; Yeoh et al., 2004)). b) Axial profile of dimensionless turbulent kinetic energy across impeller tip at different radial locations (Legends specify the original data source) (Escudie and Line, 2003; Ito et al., 1975; Michelet, 1998; Wu and Patterson, 1989).

Usually turbulent kinetic energy is studied as a dimensionless quantity by dividing  $k$  by square of the impeller tip velocity ( $U_{tip} = \pi DN$ , where  $D$  is impeller diameter and  $N$  is impeller rotational speed). In the present study normalized turbulent kinetic energy is compared from various publications and at various locations of the stirred tank.

Most of the exchange of the energy takes place in the impeller region, therefore most of the researchers limit their studies on estimation of turbulent kinetic energy and dissipation rate in within the region (Ng and Yianneskis, 2000). Figure 2.9a shows the dimensionless kinetic energy profile in the impeller plane ( $z/R = 0$ ), whereas Figure 2.9b shows the axial profiles of dimensionless  $k$  across the impeller tip at different radial locations. The turbulent kinetic energy profile attends maxima at around  $r/R = 0.4$  to  $0.44$ . Differences in the profiles from different publications are expected and are attributed to the scaling factors in the impeller design as discussed earlier. However, all the profiles in Figure 2.9a converge nearly at  $r/R=0.65-0.70$ , which confirms the decay of the turbulent kinetic energy from impeller region to the bulk region. This also reveals the fact that the highest values of the turbulent kinetic energy ( $k$ ) are present in

the area of the outwardly flowing stream. The results compared in Figure 2.9 are either ensemble-averaged or free from periodic component.

#### 2.1.4 Dissipation of turbulent kinetic energy ( $\varepsilon$ )

The dissipation rate is calculated as the time-averaged sum of the cross-and co-correlations of the instantaneous velocity gradient, multiplied by kinematic viscosity (Kresta, 1998; Pope, 2000). Eq. 2.8 is the mathematical expression for the estimation of dissipation. The direct measurements of the gradient of the fluctuating velocities are hard to achieve with single component flow measurement techniques (Kresta and Wood, 1993a). However, with multi-point flow measurements techniques, with few approximations, it is possible to estimate fluctuating velocity gradients and hence, the dissipation (Baldi and Yianneskis, 2004; Ducci and Yianneskis, 2005; Gabriele et al., 2009; Sheng et al., 2000).

$$\varepsilon = \nu \overline{\left( \frac{\partial u'_i}{\partial x_j} + \frac{\partial u'_j}{\partial x_i} \right) \frac{\partial u'_i}{\partial x_j}} \quad 2.8$$

here,  $\nu$  is the kinematic viscosity and  $u'_j$  is the fluctuating velocity component in the  $j$ th direction. Depending on the flow measurement techniques, researchers adopted different methods to estimate the dissipation rate. All these methods are briefly reviewed.

#### 2.1.5 Methods for estimation of turbulent kinetic energy dissipation

##### 2.1.5.1 Integral kinetic energy balance

In this approach, all the velocity fluctuations are included systematically. The first study about the dissipation rate was done using this approach by Cutter (1966). The author used the photographic method in water agitated by Rushton turbine to measure the mean and fluctuating velocities. The author started with the Navier-Stokes equations and derived the Eq. 2.9 relating dissipation rate to three components of the mean and fluctuating velocities based on assumptions such as isotropic turbulence, negligible viscous stresses, and negligible axial mean velocity component.

$$2\pi r \int_{-\infty}^{\infty} \varepsilon dz = \frac{d}{dr} \left[ 2\pi r \left( \int_0^{\infty} (K^2 \bar{u}_z + 2\bar{u}_\theta \overline{u'_r u'_\theta}) dz \right) \right] \quad 2.9$$

where,  $K^2$  can be evaluated as  $\bar{u}_i^2 + u_i'^2$ . Since then, several authors (Bugay et al., 2002; Hocky and Nouri, 1996; Jaworski and Fořt, 1991; Ranade and Joshi, 1989; Wu and Patterson, 1989; Zhou and Kresta, 1996b) implemented the approach to characterize the dissipation rate over a control volume.

Khan et al., (2006) carried out the experiments with angle-resolved PIV in a stirred tank with PBT. As the flow generated by PBT have a strong axial component which was assumed to be negligible by Cutter for Rushton turbine, authors suggested a direct approach for carrying out kinetic energy balance in a microscopic region considering axial impellers. They used Eq. 2.10 to estimate the kinetic energy flow in the radial direction as;

$$KE_r = \left[ 2\pi\rho R \left( \int_{z_1}^{z_2} K_1 u_r dz \right) \right] \quad 2.10$$

here,  $K_1$  is the kinetic energy obtained from instantaneous velocities ( $K_1 = 0.5 u_i'^2$ ). This gives the average value of dissipation rate over a control volume. The control volume must be carefully defined to avoid large variations of dissipation rate and therefore, the accuracy of this method highly depends on the selection of the control volume. This method has been used to find the constant required for other methods to estimate dissipation rate (Wu and Patterson, 1989).

#### 2.1.5.2 *Turbulent Kinetic energy balance*

By carrying out the turbulent kinetic energy balance equation, the dissipation rate can be approximated. In this approach experimental evaluation of all the right-hand-term of the Eq. 2.11 is required, which involves only integral-scale turbulent quantities. The PIV or LDA experiments can be carried out to determine the Reynolds stress tensor components ( $u'_i u'_j$ ), where half-trace of the Reynolds stress tensor is called as turbulent kinetic energy ( $\frac{u'_i u'_i}{2}$ ). The accuracy of the dissipation rate in this approach is affected by the errors in the estimation of individual terms of Eq. 2.11. The estimation of pressure diffusion is not feasible by PIV and LDA methods used for flow visualization, therefore, some assumptions have to be made.

$$\varepsilon = \frac{\partial k}{\partial t} + u_j \frac{\partial k}{\partial x_j} + \frac{\partial}{\partial x_j} \left[ \left( \frac{1}{\rho} \right) (\overline{u_j p'}) + \left( \frac{1}{2} \right) \overline{u_i'^2 u_j'} + 2\nu u_j \overline{\frac{\partial u_i}{\partial x_j}} \right] + \overline{u'_i u'_j} \frac{\partial u_i}{\partial x_j} \quad 2.11$$

Bugay et al. (2002), estimated the dissipation rate for hydrofoil impeller (Lightnin A310) using this approach. Authors estimated production and advection transport of turbulent kinetic energy after the PIV experiments. The diffusion terms were neglected in comparison to those of advection and production. Escudie and Line (2003) carried out the experiments with PIV in a tank agitated by Rushton turbine. They decomposed the velocity flow field into mean, periodic and turbulent motions and solved separately the energy balance equation for each motion, they were able to estimate the kinetic pressure diffusion attributed to each motion. However, the diffusion term generated by turbulent pressure stresses was assumed to be negligible as the pressure, velocity correlation terms cannot be calculated from PIV data. They also compared the results obtained from dimensional analysis method.

### 2.1.5.3 Energy Spectrum

In homogenous turbulence, the local dissipation rate can be defined in terms of the energy spectrum,  $E(\kappa)$  (Pope, 2000);

$$\varepsilon = \int_0^{\infty} 2\nu\kappa^2 E(\kappa) d\kappa \quad 2.12$$

and for isotropic turbulence, it can be written as:

$$\varepsilon = 15\nu \int_0^{\infty} \kappa_1^2 E_1(\kappa_1) d\kappa_1 \quad 2.13$$

here  $E_1(\kappa_1)$  is the one-dimensional power spectrum,  $(\kappa_1)$  is the integral scale wavenumber and  $\kappa_1^2 E_1(\kappa_1)$  is referred as dissipation rate spectrum. In experiments by measuring power spectrum, the dissipation rate can be estimated approximately by Eq. 2.13.

The energy spectrum method has been used for estimation of dissipation rate by several authors (Anandha Rao and Brodkey, 1972; Costes and Couderc, 1988b; Komasa et al., 1974;

Lee and Yianneskis, 1998; Okamoto et al., 1981; Wernersson and Trägårdh, 1999). Different authors use different flow measurement techniques to estimate the power spectra. However, in order to fully resolve  $E_1(\kappa_1)$ , the velocity measurements must be sampled at a higher frequency. The frequency spectra obtained from Laser Doppler Velocimetry (LDV), hot-wire probe experiments do not extend to high enough wavenumbers ( $\kappa$ ) to allow an application of this method (Kresta and Wood, 1993a; Sheng et al., 2000).

#### 2.1.5.4 Taylor's frozen turbulence hypothesis

Taylor's frozen turbulence hypothesis gives the relation between spatial derivative and temporal derivative. It assumes that for a small time interval, in which the turbulent structure is frozen in space and is convected along the mean flow velocity. It means as the flow advects the turbulent eddies past sensor, the fundamental properties of the turbulent eddies remain unchanged at a small timescale. Therefore, the spatial covariance needed to estimate the turbulent dissipation rate can be obtained from the time covariance, by Eq. 2.14.

$$\overline{\left(\frac{\partial u_1'}{\partial x_1}\right)^2} = \left(\frac{1}{\bar{u}_1}\right)^2 \overline{\left(\frac{\partial u_1'}{\partial t}\right)^2} \quad 2.14$$

And for isotropic homogeneous turbulence, the dissipation rate can be expressed in terms of time covariance.

$$\varepsilon = \frac{15\nu}{(\bar{u}_1)^2} \overline{\left(\frac{\partial u_1'}{\partial t}\right)^2} \quad 2.15$$

The above relation holds well if the principal direction of the flow is with the flow measuring coordinate axis, and for low turbulent intensity. This indicates that measuring velocity component should be significant (for example, pipe flows). In reality, flow in the stirred tank is very complex and therefore, this approach can't be applied (Kresta and Wood, 1993a). Care must be taken to validate this method when applying for the estimation of dissipation rate ( $\varepsilon$ ).

### 2.1.5.5 Dimensional analysis

This method is being used by several authors to estimate the dissipation rate in a stirred tank. In an isotropic turbulence, dissipation rate can be expressed in terms of a micro-scale and turbulence velocity fluctuations.

$$\varepsilon = 15\nu \left( \frac{u'}{\lambda} \right)^2 \quad 2.16$$

Here  $\lambda$  is the Taylor micro-scale. Rao and Brodkey (1972) used Eq. 2.16 to estimate the dissipation rate. Using equilibrium turbulence argument Eq. 2.16 can be modified as:

$$\varepsilon = A \frac{u'^3}{l} \quad 2.17$$

here,  $A$  is proportionality constant,  $u'$  is a characteristic turbulent velocity, and  $l$  is a characteristic length. Eq. 2.17 is based on the assumptions such as i) most energy enters the turbulent flow at the largest scale of motion, ii) most of the energy is carried by larger eddies, iii) and some constant fraction of the total kinetic energy is dissipated every time scale. The basis of the above argument is that the energy content can be characterized by  $u'^2$ , and that the rate of transfer of energy can be characterized by velocity fluctuations  $u'$  over some length scale ( $l$ ). There can be different ways in which the turbulent quantities can be estimated in Eq. 2j. For instance,  $u'$  can be taken as RMS velocity (Anandha Rao and Brodkey, 1972; Kresta and Wood, 1993a; Zhou and Kresta, 1996a, b), it can also be taken as square root of turbulent kinetic energy (Costes and Couderc, 1988b; Gabriele et al., 2009; Kresta and Wood, 1993a; Lee and Yianneskis, 1998; Wu et al., 1989; Wu and Patterson, 1989). And  $l$  can be calculated from autocorrelations function (Anandha Rao and Brodkey, 1972; Escudie and Line, 2003; Gabriele et al., 2009; Kresta and Wood, 1993a, b; Wu et al., 1989; Wu and Patterson, 1989) or can be taken as some fraction of impeller diameter (Bhattacharya et al., 2007; Costes and Couderc, 1988b; Kresta and Wood, 1993a, b; Wu et al., 1989; Zhou and Kresta, 1996a, b) or can be Taylor micro scale (Anandha Rao and Brodkey, 1972) or can be estimated via energy balance calculations throughout the total volume of the stirred tank ( $V$ ) (Schäfer et al., 1997) or can be estimated by the method suggested by Luk and Lee (1986).

---

Kresta and Wood (1993a) compared several methods used for estimation of dissipation rate from single point measurements. Several methods of estimating the dissipation rate from single-point measurement were not recommended for future calculations, including the application of Taylor's hypothesis. The authors recommended the use of  $D/10$  as a length scale and traverse RMS velocity as a velocity scale for the estimation of the dissipation rate by dimensional analysis, where constant 'A' can be set to unity.

#### **2.1.5.6 *Spatial fluctuating velocity gradient measurements***

The spatial fluctuating velocity gradient can be estimated from 2D or 3D flow measurement techniques. More recently, PIV (2D and 3D) and LDV techniques showed promising results to estimate the dissipation rate by spatial fluctuating velocity gradients. Information on PIV, LDA and several other flow visualization technique can be found in the review by Mavros (2001). Sharp and Adrian (2001) estimated 5 out of 12 terms of the Eq. 2.8 whereas Ducci and Yianneskis (2005) estimated 9 out of 12 using such 2D or 3D flow measurement techniques. Depending on the flow measurement techniques, assumptions like isotropic turbulence can be minimized and estimation of dissipation rate can be improved. Several authors used this approach to estimate the dissipation rate with minimal assumptions (Baldi and Yianneskis, 2004; Lee and Yianneskis, 1998; Micheletti et al., 2004). To overcome PIV resolution limitations, Sheng et al. (2000) estimated dissipation rate in a stirred tank with PBT employing large-eddy PIV method. The energy dissipated at the small scales was approximated by the sub-grid energy flux using this approach. This method was implemented by Zhao et al. (2011) to study the dissipation rate in a stirred tank with disc turbines.

#### **2.1.5.7 *Computational Fluid dynamics (CFD)***

Computational approaches offer more insight into the physics of the flow field in the stirred tank. Researchers have found CFD as a reliable tool for understanding the mean flow and turbulent quantities. There are different computational approaches to model the effect of turbulence such as Reynolds-average (RANS), Large Eddy Simulations (LES) and Direct Numerical Simulations (DNS). Depending on the computational cost and the accuracy needed



the computational approach can be selected. There exists a huge literature on computation approaches for stirred tank simulations. All the simulation approaches are capable of providing the mean flow field and turbulent quantities such as turbulent kinetic energy and dissipation and can be used to compare the performances of different types of the impeller.

### 2.1.5.8 *Average dissipation rate*

The dissipation rate in the stirred tank is also commonly given in terms of average dissipation rate. The average dissipation rate can be measured from the power input.

$$\bar{\varepsilon} = \frac{P}{\rho V} \quad 2.18$$

here,  $P$  is power input through the impeller in the stirred tank.  $V$  is the total volume of the tank and  $\rho$  is the density. However, it does not reflect local flow characteristics.

### 2.1.6 **Distribution of dissipation of turbulent kinetic energy ( $\varepsilon$ )**

From the scale-up point of view, the general practice has been to study  $\varepsilon/\bar{\varepsilon}$  as normalized dissipation, where  $\bar{\varepsilon}$  estimated from Eq. 2.18. The success of  $\bar{\varepsilon}$  as a scaling factor is restricted to cases where exact geometric similarity is maintained (Paul et al., 2004). But in reality it is hard to achieve. Whereas, use of  $N^3 D^2$  as a dimensional variable allows exact scale-up, over the asymmetric region, from  $D = T/2$  to  $D = T/3$  (Baldi and Yianneskis, 2004; Zhou and Kresta, 1996b) and separates the effect of other variables on local dissipation rate. In the present study, dissipation rate is studied as a dimensionless quantity by dividing  $\varepsilon$  by  $N^3 D^2$  and normalized dissipation rate is compared at various locations of the stirred tank from the various publications.

The local turbulent kinetic energy dissipation rate in the stirred tank gives the idea about the distribution of the energy provided by the impeller in the stirred tank. Several authors studied the dissipation rate in the stirred tank. In the first-ever study on dissipation rate in a stirred tank with Rushton turbine by Cutter (1966). Like turbulent kinetic energy, it is important to look at the distribution of the dissipation rate in the impeller region. As pointed out earlier, the contribution of periodic and mean kinetic energy dissipation rate is negligible in comparison with the dissipation rate of turbulent kinetic energy (Escudie and Line, 2003; Sharp and Adrian,

2001). Baldi et al. (2004) also concluded that at a distance  $r/R=0.45$ , contributions of mean and periodic dissipation rate are near zero. This is because at viscous scales the periodic kinetic energy transfers the energy to turbulence and gets dissipated. However, they mentioned considering the contribution of periodic and mean dissipation rate in their future studies. The radial and axial profiles of the dissipation rate compared here are taken as phase-averaged or ensemble-averaged. Figure 2.10 shows the radial and axial profiles of the dissipation rate of the turbulent kinetic energy. At nearly  $r/R = 0.4$  to  $0.44$  dissipation rate is observed to be maximum in the impeller stream (Baldi and Yianneskis, 2004; Hartmann et al., 2004; Yianneskis, 2000), therefore, it is more intuitive to study the axial profile of dissipation rate at  $r/R=0.44$ .

The general trend can be observed in Figure 2.10a, the normalized dissipation rate first increases and then decreases as the radial distance increases. The variation in the dissipation rate profiles is expected due to the different approaches used for the estimation of dissipation rate. The equilibrium and isotropy is applicable in most of the part of the tank except for the impeller discharge stream (Sharp and Adrian, 2001; Yeoh et al., 2004), and hence, the estimation of dissipation rate assuming isotropic turbulence by dimensional analysis leads to underestimating the dissipation rate in impeller region and overestimates in bulk region (Baldi et al., 2004). In the vicinity of the impeller, dissipation rate estimation by dimensional analysis leads to 50% underestimation when compared to estimation by direct measurements (Micheletti et al., 2004). Also, the estimated value of dissipation rate by dimensional analysis near the impeller tip is actually a local maximum which differs from global maxima by a factor of 2 (Escudie and Line, 2003). In addition, the maximum of normalized dissipation rate varies at least 30% depending on a number of terms directly measured (Ducci and Yianneskis, 2005). The difference in the comparison may also be due to the different  $Re$  or flow measurement technique used (earlier works utilizing photographic methods exhibits greater deviation from the more recent LDA and PIV studies) (Baldi and Yianneskis, 2004). It must also be noted that to fully resolve the velocity scales in a turbulent flow, the measurement technique must be capable of resolving velocities down to small multiple of Kolmogorov length scale,  $\eta = (v^3/\varepsilon)^{0.25}$  (Sharp and Adrian, 2001). Moreover, the scaling and design of the impeller contributes to the variation in the distribution of the dissipation (Yianneskis, 2000).

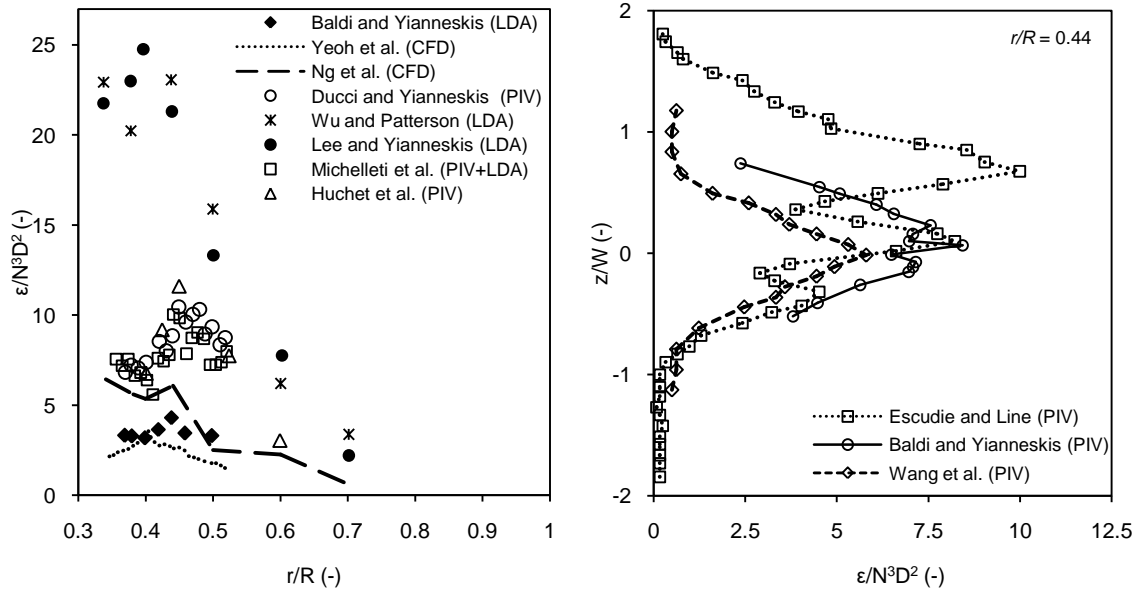


Figure 2.10: a) Radial profile of dissipation rate at impeller stream plane (Legends specify the original data source) (Baldi and Yianneskis, 2004; Lee and Yianneskis, 1998; Micheletti et al., 2004; Ng et al., 1998; Wu and Patterson, 1989; Yeoh et al., 2004; Yianneskis, 2000), b) Axial profile of dissipation rate at  $r/R = 0.44$  (Legends specify the original data source) (Baldi and Yianneskis, 2004; Escudie and Line, 2003; Wang et al., 2014).

The magnitude of normalized dissipation rate is observed to be highest in impeller region. Micheletti et al. (2004) compared the dissipation rate profiles obtained at different phase-resolved angles and found variations in dissipation rate profiles in the range of  $0.34 \leq r/R \leq 0.52$ . The variations are due to trailing vortices, therefore, the distribution of dissipation rate ( $\varepsilon$ ) is expected to have similar to those of turbulent kinetic energy ( $k$ ) (refer Figure 2.9) and indeed, it reflects a source of energy. The CFD predictions suggest that substantial amount of energy is also dissipated along the baffles and tank wall (Micheletti et al., 2004; Ng and Yianneskis, 2000), this is expected as energy containing eddy breaks down at boundaries and dissipates the energy at small scales.

Dissipation rate in the stirred tank is also commonly given in terms of average dissipation rate ( $\bar{\varepsilon}$ ). The average dissipation rate can be measured from the power input (refer to Eq. 2.18). Okamoto et al. (1981) used this phenomenon to correlate the local dissipation rate in the impeller stream ( $\varepsilon_i$ ) and circulation region ( $\varepsilon_c$ ) for a stirred tank with the six-bladed impeller. Authors reported the following correlations to account for the effect of impeller diameter on  $\varepsilon$  ( $0.25 \leq D/T \leq 0.70$ ):

$$\frac{\varepsilon_i}{\bar{\varepsilon}} = 7.8 \left(\frac{D}{T}\right)^{-1.38} \exp\left(-\frac{2.46D}{T}\right) \quad 2.19$$

$$\frac{\varepsilon_c}{\bar{\varepsilon}} = 0.90 \left(\frac{D}{T}\right)^{1.10} \quad 2.20$$

These equations give a basic idea about the effect of impeller diameter on local dissipation rate, however, does not provide maximum, minimum or average dissipation rate in the region (Zhou and Kresta, 1996b). Since  $\varepsilon$  varies from point to point, these correlations are not reliable especially in the impeller stream. Zhou and Kresta (1996b) also reported the shortcoming of these correlations, precisely. To come out with the possible correlations from the literature data, we normalized local dissipation rate in the impeller stream region with average dissipation rate. From Figure 2.11, it can be observed that the normalized dissipation rate ( $\varepsilon/\bar{\varepsilon}$ ) is the order of 5–35; thus, it can be concluded that the magnitude of the dissipation rate in the impeller region corresponds to 10–50 times the averaged volumetric dissipation rate in the tank. The variation in the comparison is huge which might be due to measurement technique, tank geometry, etc. therefore the distribution of dissipation rate varies from report to report. The comparison of  $\varepsilon/\bar{\varepsilon}$  is scattered and it is not as appropriate as  $\varepsilon/N^3D^2$ , is attributed to scaling rules.

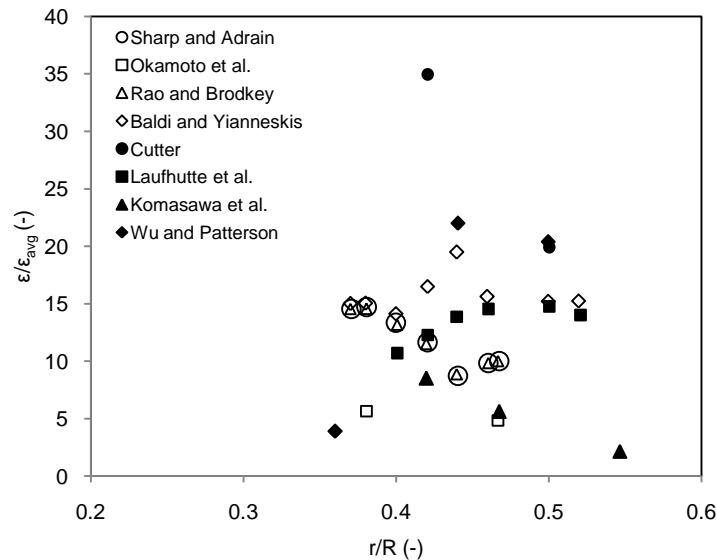


Figure 2.11: Radial profile of ratio of local dissipation rate to average dissipation rate at impeller stream (*Legends specify the original data source*) (Anandha Rao and Brodkey, 1972; Baldi and Yianneskis, 2004; Cutter, 1966; Komasawa et al., 1974; Laufhutte and Mersmann, 1985; Okamoto et al., 1981; Sharp and Adrian, 2001; Wu and Patterson, 1989).

To investigate the energy distribution in the stirred tank with radial flow impeller further, we compare the distribution of dissipation rate in the stirred tank from several publications. These reports are mostly for Rushton turbines. The percentages of the total energy dissipated in regions in the tank were taken directly from articles or calculated from volume integration as follow;

$$P_v = \int_0^{2\pi} \int_r^{r+r'} \int_h^{h+h'} r \rho \varepsilon dh dr d\theta \quad 2.21$$

$$\% \text{ Energy Dissipated} = \frac{P_v}{P} \times 100 \quad 2.22$$

Table 2.1 illustrates such distribution of energy distribution (dissipation rate) in the stirred tank. First ever study of Cutter (1966) on dissipation reported that the most of the energy supplied to the impeller is dissipated in the impeller region (~70%), with only 30% being dissipated in bulk region. However, Gunkel and Weber (1975) proposed different results when they measured the flow parameters in the baffled tank with Rushton turbine by hot-wire anemometer. They found the most of the energy supplied to the impeller was dissipated in the bulk region. It is clearly evident that the most of the energy is dissipated in the impeller region ranging from 20 to 70%. It must be noted that the small differences in the impeller geometries can lead to differences in the dissipation rate. Various other reasons which lead to differences in the distribution of dissipation have already been discussed. It must be noted that the flow measurement area and regions specified by the different authors also slightly vary from each other. From Table 2.1, it is clear that the energy dissipated in the impeller region varies from 11 to 78% in different studies. Similarly, in the bulk region, it varies from 11 to 57%. Experimental estimations are often carried out in impeller stream region, which compromises a relatively small part of the volume of the stirred tank and estimates from CFD predictions subject to the accuracy of CFD model. Therefore, the analysis needs to be carefully done when comparing.



Table 2.1: Distribution of dissipation rate in the stirred tank with radial flow impellers

Reference	Experimental Set-up details (Dimensions in 'm') Working Fluid: Water	Key Parameter Studied	Flow Measurement Technique	Method used for estimation of dissipation	Distribution of dissipation rate in Stirred Tank		Conclusion and Remark
					Impeller Region	Bulk Region	
Cutter (1966)	T=0.292, H = 0.304, D=T/3, B=T/10 (RPM: 200, 400, 600)	Mean and fluctuating Velocity components	Photographic measurements	Integral kinetic energy balance (section 2.1.5.1)	70%	30%	The value of $\varepsilon/\bar{\varepsilon}$ varies from 0.25 outside the impeller stream to 70 inside.
Günkel and Weber (1975)	T=0.457, H=T, D=0.228, C=T/2, B=T/10 (RPM: 400, 600, 800)	Fluctuating Velocities, Energy Spectra ( $E(\kappa)$ )	Hot-wire anemometer	Energy Spectra (section 2.1.5.3)	38% (Impeller stream)	-	Most of the energy supplied to the impeller is dissipated in the bulk region.
Wu and Patterson (1989)	T=0.270, H=T, D=0.93, C=T/3, B=T/10, (RPM: 200, Re=27000)	Mean and fluctuating Velocity components	Laser Doppler Velocimetry (LDV)	Integral kinetic energy balance (section 2.1.5.1)	60%	40%	Periodic fluctuations dominate the turbulence field close to the impeller.

Wu et al. (1989)	T=0.270, H=T, D=0.93, C=T/3, B=T/10, (RPM: 200, Re=27000)	Mean and fluctuating Velocity Dissipation rate ( $\epsilon$ )	Laser Doppler Velocimetry (LDV)	Dimensional analysis $A = 1, l = t \times u$ (section 2.1.5.5)	20% (Impeller stream)	-	The method used provides a valid way to estimate dissipation.
Ranade and Joshi (1990)	T=0.3, D=T/3, C=T/3, B=T/10 (Re = 32000)	Mean and RMS velocities, turbulent kinetic energy	CFD ( $k$ - $\epsilon$ )	CFD Predictions (section 2.1.5.7)	64%	36%	Mean velocities are predicted correctly, but turbulent kinetic energy is under- predicted at various locations
Kresta and Wood (1991)	T=0.456, H=T, D=T/3, B=T/10, W=D/5, C=T/3, (RPM: 950)	Mean Velocities, turbulent kinetic energy ( $k$ ), dissipation rate ( $\epsilon$ )	CFD (SRJ*) with FDM code	CFD Predictions (section 2.1.5.7)	89%	11%	Turbulent SRJ* model can be applied to the modeling of flow in stirred tank with Rushton Turbine.
Zhou and Kresta (1996a)	T=0.240, H=T, D=T/2, C=T/2, B=T/10 (RPM: 221, Re=52200)	Dissipation rate ( $\epsilon$ )	Laser Doppler Velocimetry (LDV)	Dimensional Analysis (section 2.1.5.5) $A = 1, l = D/10,$ $u = q^{0.5}, q =$ $1.5u^2$	43.5%	-	Rushton turbines generate the most turbulent kinetic energy compare to other impellers (PBTD, A310)



Ranade (1997)	T=0.3, D=T/3, C=T/3, B=T/10 (Re = 32000)	Mean Velocities, turbulent kinetic energy ( $k$ ), dissipation rate ( $\epsilon$ )	CFD ( $k$ - $\epsilon$ )	CFD Predictions (section 2.1.5.7)	22% (Impeller swept volume)	-	The $k$ - $\epsilon$ model leads to adequate representation of dissipation.
Ng and Yianneskis (2000)	T=0.1, H=T, D=T/3, C=T/3, W=D/5 (RPM: 2165, Re=40000)	Turbulent kinetic energy ( $k$ ) and dissipation rate ( $\epsilon$ )	Laser Doppler Velocimetry (LDV) and CFD ( $k$ - $\epsilon$ )	CFD Predictions (section 2.1.5.7)	43%	57%	Around 50% of the energy dissipated in a region of close to the tank wall.
Escudie and Line (2003)	T=0.45, H=T, D=T/3, C=T/3, W=D/5, B=T/10 (RPM:150, Re=56256)	Turbulent kinetic energy ( $k$ ) and dissipation rate ( $\epsilon$ )	Particle Image Velocimetry (PIV)	Turbulent kinetic energy balance (section 2.1.5.2)	15% (Impeller stream)**	-	The dissipation rate of mean and periodic kinetic energy is found to be negligible in the impeller stream.
Sharp and Adrian (2001)	T=0.1524, H=T, D=T/3, C=T/3, W=D/5, B=T/10 (Re=4580, $N_p$ =4.5)	Turbulent kinetic energy ( $k$ ) and dissipation rate ( $\epsilon$ )	Particle Image Velocimetry (PIV)	Spatial fluctuating velocity gradient measurements (5 out of 12 terms) (section 2.1.5.6)	11% (Impeller stream)***	-	The deviation from isotropy is up to 80%.

Derksen and Van den Akker, (1999)	T=0.27, H=T, D=0.344T, C=T/3, W=D/5, B=T/10 (Re=29000)	Mean velocities, Turbulent kinetic energy ( $k$ ) and dissipation rate ( $\epsilon$ )	Laser Doppler Velocimetry (LDV) and CFD (LES)	CFD Predictions (section 2.1.5.7)	78%****	22%	Dissipation rate is heterogeneously distributed throughout the tank.
Present work (Fractal Impeller)	T=0.3, H=T, D=0.67T	Mean velocities, Turbulent kinetic energy ( $k$ )	Ultrasonic Velocity Profiler (UVP)	CFD Predictions			

\*SRJ – Swirling Radial Jet, \*\*Measurement area ( $-0.5 \leq z/W \leq 0.5$  and  $0.356 \leq r/R \leq 0.54$ ), \*\*\* Measurement area ( $-0.5 \leq z/W \leq 0.5$  and

## 2.2 Recent developments in novel impellers for stirred tank reactors

Depending upon the physicochemical properties of the fluids and the time scales of specific operation, the corresponding impellers are different. Rushton turbine is one of the most common impellers used in the industry for gas dispersion. However, it is known that power consumption suddenly falls (nearly 50%) when gas is introduced in the system due to the trailing vortices (Nienow, 1996; Paul et al., 2004) and hence it limits the potential heat and mass transfer. Therefore, several improved impeller designs have been reported for enhancement of the quality, capacity, and energy efficiency of an impeller or a combination of impellers. For example, concave-blade disk turbines and the up-pumping wide-blade hydrofoils designs maintain more than 70% of their ungassed power draw on gassing and therefore have been suggested for the gas dispersion (Paul et al., 2004). Similarly, recent developments in the improvement of axial flow impellers focus on increasing axial flow at a reduced shear rate, (Fentiman et al., 1998; Paul et al., 2004) which helps to facilitate mixing in shear sensitive systems. Even the twist angle or blade width of the Pitched Blade Turbines (PBT) can lead to different flow characteristics and hence the efficiency (Kumaresan and Joshi, 2006; Ranade et al., 1992). Various improved axial flow impellers design has been studied and compared by many researchers from which authors drew some noticeable conclusions. For example, Jaworski et al. (1996) have compared Chemineer HE-3 (CHE3) and Prochem Maxflo T (PMT) hydrofoil impellers at equal power input and observed that the mean axial and radial profiles for both the impellers show the similar trend, however, differs in magnitude. Similarly, Kumaresan and Joshi (2006) studied the various impeller designs and concluded that the power number and the flow numbers decrease with a decrease in  $W/D$  ratio and also with blade twist.

Literature reports some efficient operation protocols to improve the performance of impellers such as co-reverse periodic rotation, (Yao et al., 1998) time-dependent fluctuating rotational speed, (Lamberto et al., 1996; Yao et al., 1998) off centre impeller positions, (Ascanio et al., 2002) unconventional configurations (Ascanio et al., 2002) and use of conical vessel (Rielly et al., 2007). All such designs showed promising results in terms of mixing, however, such designs have limited practical applications. However, with increasing complexity of fluid properties and the corresponding variations with shear or temperature, it is necessary to evolve newer impellers that overcome some of the limitations of the conventional impellers. In the

recent time, a few very novel impeller designs are reported in the literature, with the focus on improving the performance for specific kind of systems.

### 2.2.1 Impellers for low to medium viscosity fluids

Axial flow impellers, radial flow impellers, and hydrofoils are mostly used for the liquid with low to medium viscosity (Paul et al., 2004). These impellers are broadly classified on the basis of flow patterns they generate in the stirred tank. It is known that axial flow impellers show low power consumption as compared to radial flow impellers and hence they are considered as the first choice in the industries for stirring. On the other hand, radial flow impellers are used for efficient gas dispersion in liquid. To account for both axial flow impeller and radial flow impeller characteristics Ascanio et al. (2003) introduced a new Mixed Flow Impeller which is also referred as the new hybrid axial/radial flow impeller (ARI) for mixing and dispersion of Newtonian and non-Newtonian fluids. Figure 2.12 illustrates the design of the Mixed flow impeller (or ARI). As it can be observed from the figure the straight blades are attached to the pitched blades making it the hybrid impeller. Authors studied the performance in terms of power input data, mixing time and compared with those of standard pitched blade turbine (PBT) downflow and Rushton turbine (RT). In terms of power number ( $N_p$ ) ARI performed as the combination of PBT and RT. From the mixing time analysis done by the authors, it was observed that, ARI showed better mixing efficiency than RT. ARI showed some promising results in terms of mixing however further studies are required especially in terms of flow characterization, gas dispersion and scale-up as to consider it as an option in the industries for mixing and dispersion.

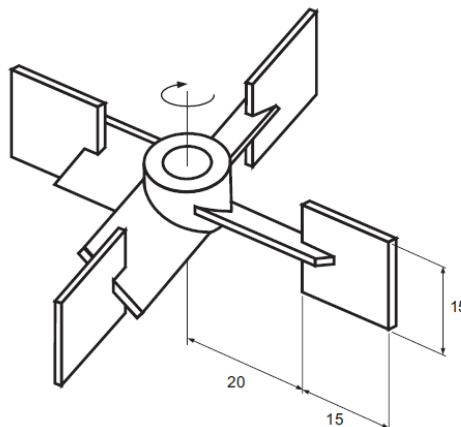


Figure 2.12: Mixed flow impeller or ARI (dimensions are in mm) (*Reproduced with permission from the Publisher* (Ascanio et al., 2003)).

Along the same line, Buwa et al. (2006) have proposed a Grid Disc Impeller (GD) (see Figure 2.13) for mixing of single-phase flow in a stirred tank. Authors studied the flow generated by grid disc impeller in a stirred tank using LDA. They also performed the power measurement calculations and mixing experiment for the grid disc impeller and compared the results with standard propellers and a solid disc. Based on the analysis, authors performed the numerical simulations to predict the mean profiles, mixing time and power consumption. After validation authors used their validated model to study the effect of grid configuration on the performance of the grid disc impeller and extended their study (Dewan et al., 2006).

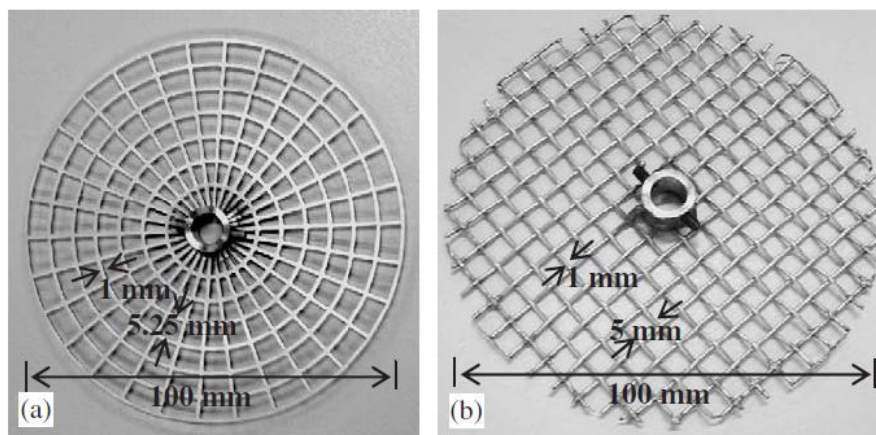


Figure 2.13: Grid Disc Impeller (GD) (a) radial grid disc (b) square grid disc (*Reproduced with permission from the Publisher (Buwa et al., 2006)*).

Results show that the Grid Disc impeller develops two distinct circulation loops same as the standard RT does, however, its performance in terms of mixing efficiency per unit power is as comparable as a standard propeller (Buwa et al., 2006). By studying the effect of grid authors compared the flow generated by radial grid disc impeller and square grid disc impeller and found to be similar. Dewan et al. (2006) extended the study through numerical studies in which they studied the effect of diameter, grid opening size and a number of impellers on the performance of GD. Authors mentioned that an increase in disc size opening resulted in a decrease in power and mixing time and therefore in improved overall performance. They also mentioned that the overall mixing performance per unit power consumed of the dual impeller configuration was better than that of the single impeller.

Yang et al. (2015) designed the impeller having a similar concept as that of Grid Disc (GD) Impeller. However, the design has six flat blades attached to grid disc giving it a look

similar to Rushton turbine (RT/6, six blades attached to solid disc). Due to design similarity authors referred to the new design as RT-G (see Figure 2.14) and compared the performance with that of RT through experimental and numerical investigations. Authors concluded that the axial velocities of RT-G have a higher magnitude than those of RT which mean RT-G can improve the uniformity of the axial velocity distributions and hence can improve the circulations in the stirred tank. Authors have also found the magnitude of radial profiles increased, however, the increase was not significant (Yang et al., 2015). Moreover, about 20-30% increase in the turbulent kinetic energy ( $k$ ) due to impeller design was observed at approximately same power consumption ( $P_0$  of RT-G is 1.3% lower than that of RT) (Yang et al., 2015). Authors concluded that RT-G can achieve homogeneous mixing faster than the RT under the same operating condition. However, more experimental work should be provided to support the statement, also the experiments of gas dispersion in a stirred tank with RT-G need to be carried out to check Relative Power Demand (RPD) on gassing as to consider RT-G as an option for industrial applications.



Figure 2.14: Six blade grid disc impeller (referred to as RT-G) (*Reproduced with permission from the Publisher* (Yang et al., 2015)).

Handling of a fermentation broth in a bioreactor is one of the key issues in the industries due to its rheological property. Recently, several approaches have been reported to solve the problem of viscous fermentation. Literature reports that the axial reciprocating plate impeller (APRI) is mostly preferred design due to its unique characteristics of axial movement (Lin et al., 2011). However, to meet the sterilization requirement as the APRI impeller shaft moves in and out of the bioreactor. Lin et al. (2011) proposed a new Rotational Reciprocating Plate Impeller

(RRPI) (see Figure 2.15) with an idea similar to APRI. Authors studied the power consumption and overall mass transfer coefficient (water-oxygen system) and compared the results with those of triple Rushton turbine (TRP, three Rushton turbine mounted on the single shaft) and an axial reciprocating plate impeller (APRI) in a 22-liter laboratory scale bioreactor. They concluded that the RRPI performed similar as that of TRT in water, whereas the ARPI provided lower oxygen mass transfer rate (due to the higher coalescence of the bubble (Lin et al., 2011)). Whereas, in a viscous medium (10 g/L CMC solution), the oxygen mass transfer rate was observed as good as that of ARPI. Therefore the proposed designs of rotational reciprocating plate impeller (RRPI) can be considered as a good alternative to handle fermentation having rheologically evolving broth.

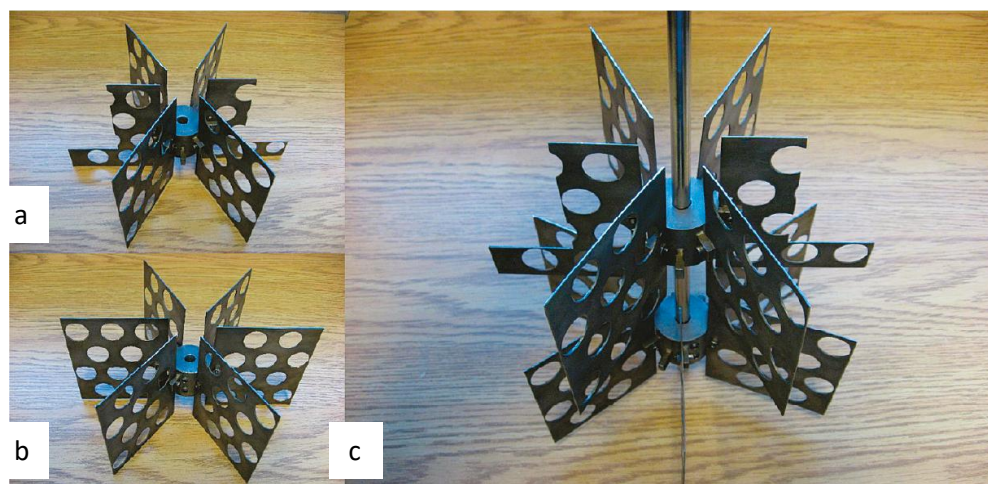


Figure 2.15: Rotational reciprocating plate impeller (RRPI) (a) top hub, (b) bottom hub, (c) the complete assembly (two hubs are positioned with a  $30^\circ$  angle relative to each other) (*Reproduced with permission from the Publisher (Lin et al., 2011)*).

It is believed that the standard impellers (axial flow and radial flow) are not suitable for viscous mixing. Recent studies (Lamberto et al., 1996; Lamberto et al., 1999) show some promising results to achieve viscous mixing and avoid segregated regions. Adopting to same concepts, Cabaret et al. (2008) have recently proposed new impeller designs to eliminate the segregated region. Figure 2.16 shows all the new designs along with standard impellers (RT, PBT, etc.). Figure 2.16e shows the impellers which have asymmetry in the blades as two of the blades are twisted (mono axial-radial disc turbine, MARDT). Figure 2.16g shows the same design except it has four blades twisted in an asymmetric way (bi axial-radial disc turbine, BARDT). Above mentioned impellers were modified by attaching counter blades on the axial

blades in order to force the fluid go axially (modified mono axial-radial disc turbine, MMARDT and modified bi axial-radial disc turbine, MBARDT). The performance (in terms of power consumption and mixing evolution) of the new modified impellers mentioned in the Figure 2.16 was compared with those of standard impellers. Authors reported that the mixing efficiency in laminar flow can be better achieved by new mixed flow impellers than standard impellers. Authors also reported that the MARDT impellers operating in down-pumping mode are the best operating condition for viscous (laminar) mixing.

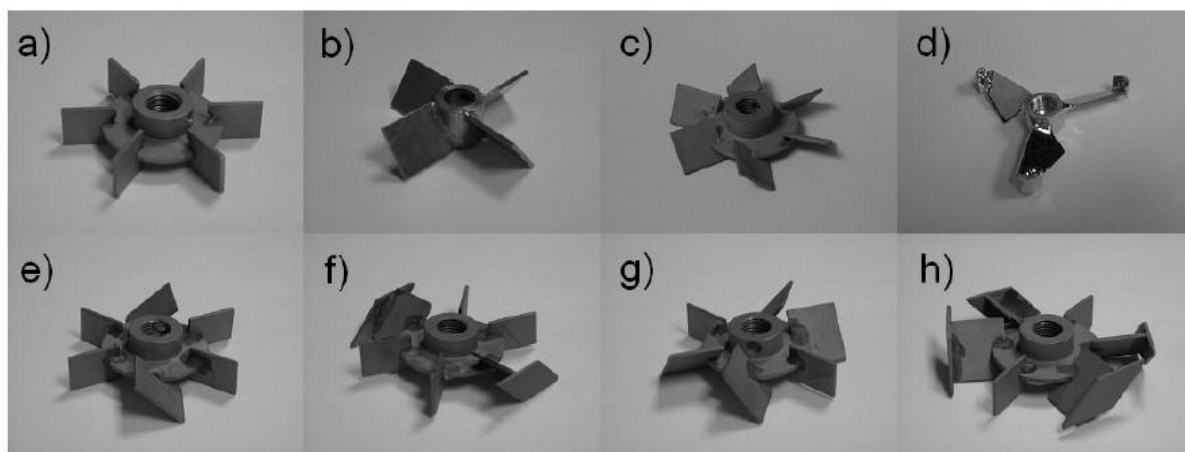


Figure 2.16: Impeller geometries (a) Rushton turbine, (b) pitched blade turbine (PBT), (c) axial disc turbine (ADT), (d) hydrofoil (H), (e) mono axial-radial disc turbine (MARDT), (f) modified mono axial-radial disc turbine (MMARDT), (g) bi axial-radial disc turbine (BARDT), (h) modified bi axial-radial disc turbine (MBARDT) (*Reproduced with permission from the Publisher (Cabaret et al., 2008)*)

The power number for standard and new impeller designs have been listed in Table 2.2. From the Table 2.2, it can be observed that some of the new designs have lower power number ( $P_0$ ) compared to that of standard impellers. However, power number ( $P_0$ ) alone should not be considered as the performance evaluation criterion for selecting the impeller for mixing and dispersion.



Table 2.2: Power number for various impeller designs

Impeller Design (reference)	D/T	Power Number ( $P_0$ )
Rushton turbine (RT) (Rushton et al., 1950)	0.33	5.95
Rushton turbine (RT) (Zhou and Kresta, 1996b)	0.33	5.4
Rushton turbine (RT) (Yang et al., 2015)	0.33	5.42
PBT/6 blades, 30° (Ranade et al., 1992)	0.33	0.87
PBT/6 blades, 45° (Ranade et al., 1992)	0.33	2.10
PBT/6 blades, 45° (Kumaresan and Joshi, 2006)	0.33	1.8
PBT/6 blades, 60° (Ranade et al., 1992)	0.33	3.33
PBT/6 blades, 60° (Kumaresan and Joshi, 2006)	0.33	3.32
Standard Propeller (Ranade et al., 1992)	0.33	0.89
Standard Propeller (Buwa et al., 2006)	0.39	0.41
Lightnin A310 (Zhou and Kresta, 1996b)	0.475	0.30
Chemineer HE3 (Jaworski et al., 1996)	0.46	0.305
Prochem Maxflo T (Jaworski et al., 1996)	0.35	1.58
Square Grid Disc Impeller (Buwa et al., 2006)	0.33	0.67
Radial Grid Disc Impeller (Buwa et al., 2006)	0.33	0.466
Six blade grid disc Impeller (RT-G) (Yang et al., 2015)	0.33	5.35
Axial/Radial flow impeller (ARI) (Ascanio et al., 2003)	0.21	1.43

### 2.2.2 Impellers for high viscosity fluids

Viscous mixing mostly carried out in a stirred tank with standard open impellers such as anchor blades, helical ribbons, etc. Viscous mixing is obtained by a sequence of the stretching-folding-breaking mechanism. Therefore the design of impeller for viscous mixing is considered a formidable task. However, researchers have reported some of the new impeller designs for high viscosity fluid.

Maxblend impeller (SHI Mechanical & Equipment Inc.) is one of the designs used for viscous mixing especially in Japan. Figure 2.17 illustrates the schematic of the Maxblend impeller in a stirred tank. Maxblend impeller showed good mixing performance at relatively low power consumption, therefore, it is considered as the most promising impeller for viscous mixing (Iranshahi et al., 2007). Many researchers have studied the performance of Maxblend impeller through experimental and numerical investigation. Literature reports that the Maxblend and Double Helical Ribbon (DHR, one of the standard impeller used for viscous mixing) consume same power when operated at same conditions, however, Maxblend has a longer mixing time when  $Re < 10$  and a shorter mixing time when  $Re > 10$  (Takahashi et al., 2006). Further investigation on the performance of Maxblend impeller was carried out by Iranshahi et al.

(2007). Authors studied the flow and mixing in a stirred tank with the Maxblend impeller in a laminar region. Authors found the segregation zones at the bottom of the tank at low  $Re$ . However at higher  $Re$  fast and homogeneous mixing was achieved (Iranshahi et al., 2007).

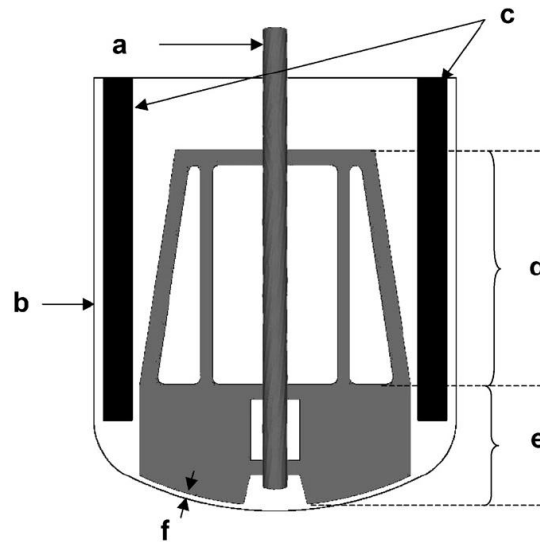


Figure 2.17: Schematic of Maxblend Impeller (a) Maxblend impeller design (b) tank wall (c) baffles (d) impeller grid part (e) impeller bottom paddle part (f) bottom gas region (clearance) (Reproduced with permission from the Publisher (Iranshahi et al., 2007) ).

Few more designs such as Fullzone (FZ) impeller and Large Double Blade (LDB) impeller have also been reported for the mixing of viscous liquid in the stirred tank. Fullzone (FZ) impeller and Large Double Blade (LDB) impeller have the same configuration as that of the Maxblend impeller. Their performance in terms of micro-mixing was compared by Liu et al. (2015). In general, LDB impeller has the advantage of both Fullzone impeller and Maxblend impeller and has good adaptability in the different viscous system.

### 2.3 Fractals

Fractals are a mathematical concept originally proposed by Mandelbrot (1983) and is used in explaining the complex phenomena in natural sciences and engineering. Fractals are characterized by its dimensions. For fractal with between 1 to 2 dimensions, one considers the relation between the endpoints. The simplest of all is the generator which has a fractional dimension of 1 i.e. a line. In the present case, as shown in the Figure 2.18, as the segments within the generator are equal unit lengths, one can determine the fractional dimension by dividing the

logarithm of the number of unit length in the generator by logarithm of the number of unit length across the initiator. Since there are five segments in this generator and three unit lengths across the initiator, the fractional dimension (Cutting and Garvin, 1987) is  $\log(5)/\log(3)$  or about 1.47. Another fascinating property of fractal is self-similarity at all the scales. Excellent description of fractals has been given in a paper by Cutting and Garvin (1987). Fractal nature in flow and turbulence has been studied in detail by Sreenivasan (1991).

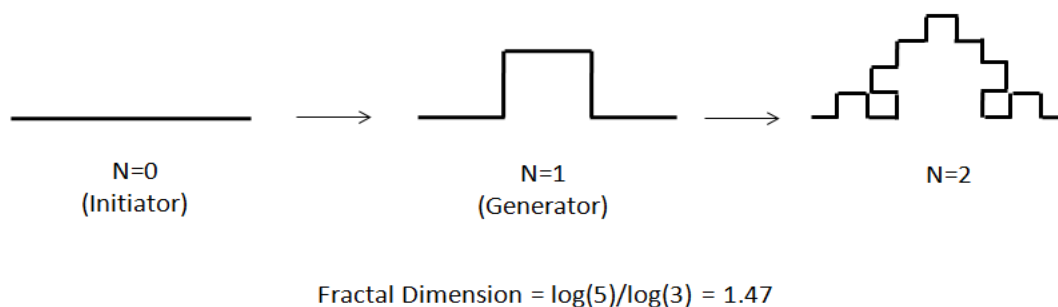


Figure 2.18: Fractal generator and its initiator and corresponding fractal growth.

## 2.4 Fractal Impeller (FI)

As highlighted in section 2.1.6, most of the energy supplied by the impeller to the fluid is dissipated in the impeller region and impeller stream which is nearly 5-10% of the total volume (Wu and Patterson, 1989; Zhou and Kresta, 1996b). Therefore it is believed that the hydrodynamic uniformity is difficult to achieve in the stirred tank with standard impellers. More recently Trivellato (2011) has addressed the same issue and proposed a design of Perforated Paddle Impeller. On the basis of the numerical simulation for various combinations (2, 4, 8, 16 paddles having 0, 6, 12, 20 and 30 holes) as to overcome energy distribution related issues, the configuration with 4 paddles and 30 holes found to be the best among all. However, authors reported that no combination was capable of avoiding the formation of a central slow motion zone close to impeller shaft (Trivellato, 2011). Hence the non-homogeneity in the stirred tank forces to operate the stirred tank at higher revolution speed to achieve the level of homogeneity.

Along the same line, a group of the researcher in CSIR-National Chemical Laboratory, Pune, India, also addressed the same issue and proposed the use of Fractal Impeller (FI) for mixing and dispersion. The purpose of selecting a fractal geometry is very clear. The fractal

designs are self-similar and therefore are expected to deliver power in a self-similar manner in the entire stirred tank. Fractal Impeller (see Figure 2.19) is designed in such way that it occupies almost the same volume (approximately 0.4% of a stirred tank) as standard impellers however it is spread over an entire reactor and hence covers almost 95% of the total volume. Since most of the blades simply cut the fluid in different planes it reduces overall friction and hence the power consumption. The performance of Fractal Impeller in terms of mixing time, power consumption, gas dispersion and solid handling was studied and compared with those of standard impellers (RT and PBTD). The mixing efficiency per unit power consumed was seen lower than that of PBTD (Kulkarni et al., 2011). Moreover, Fractal Impeller showed promising results in lifting the solid particles and suspending them at relatively low rotational speed. In addition, gas dispersion in the liquid was seen better with narrow bubble size distribution throughout the stirred tank (Kulkarni et al., 2011).

Due to its structural complexity, it would be difficult to imagine the flow generated by Fractal Impeller, therefore more work in terms of flow visualization was needed to examine the mixing behavior. Hence, the overwhelming performance of the Fractal Impeller motivated us to study hydrodynamics, mixing, power consumption and design aspects of the new impeller design.

#### 2.4.1 Fractal Impeller Design

The fractal impeller is designed in such a way that it retains the self-similar structure even at small scales. The overall structure of the fractal impeller signifies the growth of the fractal from the square initiator (see Figure 2.18). The schematic of the impeller is shown in Figure 2.19. The impeller has four main branches referred as  $B_I$ , where I refers to 1, 2, 3, 4; each of further gets split in three sub-branches, referred as  $B_{Ik}$ , where  $k \sim 1, 2, 3$ . On each such sub-branch, we have four blades. Of which two blades are horizontal and the remaining two are vertical. An additional sub-branch at the bottom of the impeller referred as  $B_S$ , is designed to generate the necessary tangential flow in the region close to the tank bottom. As mentioned earlier, in the entire design, the orientation of the blades is kept such that most of the blades actually do not sweep any fluids with them but simply fragment the fluid as they pass through it. Also, at a given impeller rotation speed ( $N$ , 1/s), the angular distance covered by different blades

varies and thus yields different blade tip velocities ( $2\pi lN$ , where  $l$  is the distance of the blade from the centre).

The distance of the additional sub-branch ( $B_5$ ) from the bottom of the tank was set to 85 mm ( $z/R=0.567$ ). And, the distance of  $B_{II}$  branch from the bottom of the tank was 110 mm ( $z/R=0.733$ ), of  $B_{I2}$  was 185 mm ( $z/R=1.233$ ) and of  $B_{I3}$  was 260 mm ( $z/R=1.733$ ).

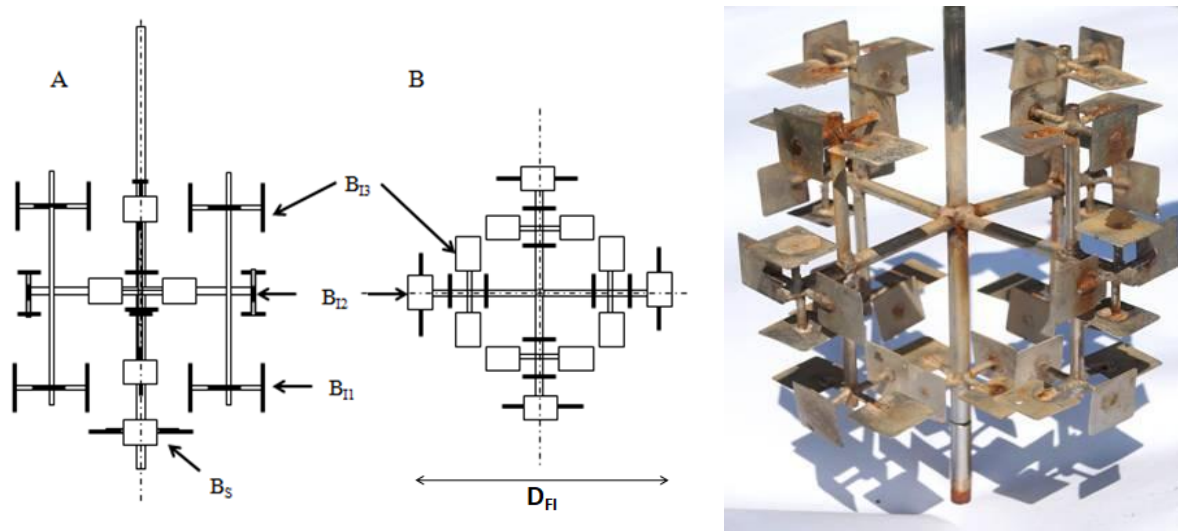


Figure 2.19: Schematic diagram of Fractal Impeller (FI) A) front view, B) top view C) photograph of FI (*modified from Kulkarni et al. (2011)*).

As mentioned earlier, the branches of the FI are spread over the entire tank. Since the blades are placed at different radial distances the farthest distance between the two blades was considered as an effective diameter of FI ( $D_{FI}$ ).

Other designs were also considered while designing, however, fabrication point of view those were not possible. Hence above mentioned design was fabricated.

## 2.5 Conclusions

Achieving good quality mixing, dispersion and suspension in the stirred tanks is conventionally done using a combination of known impellers. A variety of thumb rules exist for their selection and scale-up.

In this chapter, basics of stirred tank reactors have been discussed briefly, which will be the basis for the part of the thesis. Research work carried out over many decades using

experimental, as well as computational fluid dynamics (CFD), has successfully helped several reliable designs to see the industrial stirred tanks. The distribution of turbulent kinetic energy, as well as dissipation rate in the stirred tank comparison, showed that the energy dissipated in the impeller region varies from 11 to 78% in different studies. Similarly, in the bulk region, it varies from 11 to 57%. This clarifies the fact that the impeller region is the most active region in the entire stirred tank which has only 3% of the total volume. Hence, this area can be explored for development of new impellers to address these issues.

New impeller designs reported in this chapter are based on the developments of new methods of measurements, new concepts, and improved knowledge of flow past objects and probably for specific kind of applications. However, at this moment these impellers need to be studied more in terms of their scalability, design approach, positioning in the stirred tank, sizing, numbers, etc. While a lot of new areas of mixing are opening and a few need mixing at sub-micron scales, scale-up may be economical using the stirred tanks only. This implies that readers need to wait and watch for the applicability of these new designs and new ones that would come in the near future. The promising observations from these designs indicate a potential in new concepts in a traditionally old area of the stirred tank.

This chapter also gives the basic design aspects of Fractal Impeller and its applicability for carrying out various operations in stirred tank reactors.

---

**References**

Anandha Rao, M., Brodkey, R., 1972. Continuous flow stirred tank turbulence parameters in the impeller stream. *Chemical Engineering Science* 27, 137-156.

Ascanio, G., Brito-Bazán, M., Carreau, P.J., Tanguy, P.A., 2002. Unconventional configuration studies to improve mixing times in stirred tanks. *The Canadian Journal of Chemical Engineering* 80, 558-565.

Ascanio, G., Foucault, S., Tanguy, P.A., 2003. Performance of a new mixed down pumping impeller. *Chemical Engineering & Technology* 26, 908-911.

Aubin, J., Le Sauze, N., Bertrand, J., Fletcher, D.F., Xuereb, C., 2004. PIV measurements of flow in an aerated tank stirred by a down- and an up-pumping axial flow impeller. *Experimental Thermal and Fluid Science* 28, 447-456.

Baldi, S., Ducci, A., Yianneskis, M., 2004. Determination of dissipation rate in stirred vessels through direct measurement of fluctuating velocity gradients. *Chemical Engineering & Technology* 27, 275-281.

Baldi, S., Yianneskis, M., 2004. On the quantification of energy dissipation in the impeller stream of a stirred vessel from fluctuating velocity gradient measurements. *Chemical Engineering Science* 59, 2659-2671.

Bhattacharya, S., Hebert, D., Kresta, S.M., 2007. Air Entrainment in Baffled Stirred Tanks. *Chemical Engineering Research and Design* 85, 654-664.

Bugay, S., Escudie, R., Line, A., 2002. Experimental analysis of hydrodynamics in axially agitated tank. *AIChE Journal* 48, 463-475.

Buwa, V., Dewan, A., Nassar, A.F., Durst, F., 2006. Fluid dynamics and mixing of single-phase flow in a stirred vessel with a grid disc impeller: Experimental and numerical investigations. *Chemical Engineering Science* 61, 2815-2822.

Cabaret, F., Fradette, L., Tanguy, P.A., 2008. New Turbine Impellers for Viscous Mixing. *Chemical Engineering & Technology* 31, 1806-1815.

Cooper, R.G., Wolf, D., 1968. Velocity profiles and pumping capacities for turbine type impellers. *The Canadian Journal of Chemical Engineering* 46, 94-100.

Costes, J., Couderc, J., 1988a. Study by laser Doppler anemometry of the turbulent flow induced by a Rushton turbine in a stirred tank: influence of the size of the units—I. Mean flow and turbulence. *Chemical Engineering Science* 43, 2751-2764.

Costes, J., Couderc, J., 1988b. Study by laser Doppler anemometry of the turbulent flow induced by a Rushton turbine in a stirred tank: influence of the size of the units—II. Spectral analysis and scales of turbulence. *Chemical Engineering Science* 43, 2765-2772.

Cutter, L.A., 1966. Flow and turbulence in a stirred tank. *AIChE Journal* 12, 35-45.

Cutting, J.E., Garvin, J.J., 1987. Fractal curves and complexity. *Perception & Psychophysics* 42, 365-370.

Derksen, J., Van den Akker, H.E., 1999. Large eddy simulations on the flow driven by a Rushton turbine. *AIChE Journal* 45, 209-221.

Dewan, A., Buwa, V., Durst, F., 2006. Performance Optimizations of Grid Disc Impellers for Mixing of Single-Phase Flows in a Stirred Vessel. *Chemical Engineering Research and Design* 84, 691-702.

Ducci, A., Yianneskis, M., 2005. Direct determination of energy dissipation in stirred vessels with two-point LDA. *AIChE Journal* 51, 2133-2149.

Escudie, R., Line, A., 2003. Experimental analysis of hydrodynamics in a radially agitated tank. *AIChE Journal* 49, 585-603.

Fentiman, N.J., St.Hill, N., Lee, K.C., Paul, G.R., Yianneskis, M., 1998. A Novel Profiled Blade Impeller for Homogenization of Miscible Liquids in Stirred Vessels. *Chemical Engineering Research and Design* 76, 835-842.

Gabriele, A., Nienow, A.W., Simmons, M.J.H., 2009. Use of angle resolved PIV to estimate local specific energy dissipation rates for up- and down-pumping pitched blade agitators in a stirred tank. *Chemical Engineering Science* 64, 126-143.

Günkel, A.A., Weber, M.E., 1975. Flow phenomena in stirred tanks. Part II. The bulk of the tank. *AIChE Journal* 21, 939-949.

Hartmann, H., Derksen, J.J., Montavon, C., Pearson, J., Hamill, I.S., van den Akker, H.E.A., 2004. Assessment of large eddy and RANS stirred tank simulations by means of LDA. *Chemical Engineering Science* 59, 2419-2432.

Hockey, R., Nouri, J., 1996. Turbulent flow in a baffled vessel stirred by a 60 pitched blade impeller. *Chemical Engineering Science* 51, 4405-4421.

Iranshahi, A., Devals, C., Heniche, M., Fradette, L., Tanguy, P.A., Takenaka, K., 2007. Hydrodynamics characterization of the Maxblend impeller. *Chemical Engineering Science* 62, 3641-3653.



Ito, S., Ogawa, K., Yoshida, N., 1975. Turbulence in impeller stream in a stirred vessel. *Journal Chemical Engineering of Japan* 8, 206-209.

Jaworski, Z., Fořt, I., 1991. Energy dissipation rate in a baffled vessel with pitched blade turbine impeller. *Collection of Czechoslovak Chemical Communications* 56, 1856-1867.

Jaworski, Z., Nienow, A.W., Dyster, K.N., 1996. An LDA study of the turbulent flow field in a baffled vessel agitated by an axial, down-pumping hydrofoil impeller. *The Canadian Journal of Chemical Engineering* 74, 3-15.

Khan, F., Rielly, C., Brown, D., 2006. Angle-resolved stereo-PIV measurements close to a down-pumping pitched-blade turbine. *Chemical Engineering Science* 61, 2799-2806.

Komasawa, I., Kuboi, R., Otake, T., 1974. Fluid and particle motion in turbulent dispersion—I: Measurement of turbulence of liquid by continual pursuit of tracer particle motion. *Chemical Engineering Science* 29, 641-650.

Kresta, S., 1998. Turbulence in stirred tanks: Anisotropic, approximate, and applied. *The Canadian Journal of Chemical Engineering* 76, 563-576.

Kresta, S.M., Wood, P.E., 1991. Prediction of the three-dimensional turbulent flow in stirred tanks. *AIChE Journal* 37, 448-460.

Kresta, S.M., Wood, P.E., 1993a. The flow field produced by a pitched blade turbine: Characterization of the turbulence and estimation of the dissipation rate. *Chemical Engineering Science* 48, 1761-1774.

Kresta, S.M., Wood, P.E., 1993b. The mean flow field produced by a 45° pitched blade turbine: Changes in the circulation pattern due to off bottom clearance. *The Canadian Journal of Chemical Engineering* 71, 42-53.

Kulkarni, A.A., Jha, N., Singh, A., Bhatnagar, S., Kulkarni, B.D., 2011. Fractal Impeller for Stirred Tank Reactors. *Industrial & Engineering Chemistry Research* 50, 7667-7676.

Kumaresan, T., Joshi, J.B., 2006. Effect of impeller design on the flow pattern and mixing in stirred tanks. *Chemical Engineering Journal* 115, 173-193.

Lamberto, D., Muzzio, F., Swanson, P., Tonkovich, A., 1996. Using time-dependent RPM to enhance mixing in stirred vessels. *Chemical Engineering Science* 51, 733-741.

Lamberto, D.J., Alvarez, M.M., Muzzio, F.J., 1999. Experimental and computational investigation of the laminar flow structure in a stirred tank. *Chemical Engineering Science* 54, 919-942.

Laufhutte, H., Mersmann, A., 1985. Dissipation of power in stirred vessels, Proceedings of the 5th European Conference on Mixing, pp. 331-340.

Lee, K.C., Yianneskis, M., 1998. Turbulence properties of the impeller stream of a Rushton turbine. *AIChE Journal* 44, 13-24.

Li, Z., Bao, Y., Gao, Z., 2011. PIV experiments and large eddy simulations of single-loop flow fields in Rushton turbine stirred tanks. *Chemical Engineering Science* 66, 1219-1231.

Lin, Y., Zhang, Z., Thibault, J., 2011. New Impeller for Viscous Fermentation: Power Input and Mass Transfer Coefficient Correlations. *Industrial & Engineering Chemistry Research* 50, 3510-3516.

Liu, B., Wang, M., Liu, J., Qian, L., Jin, Z., 2015. Experimental study on micromixing characteristics of novel large-double-blade impeller. *Chemical Engineering Science* 123, 641-647.

Luk, S., Lee, Y., 1986. Mass transfer in eddies close to air-water interface. *AIChE Journal* 32, 1546-1554.

Mandelbrot, B.B., 1983. *The fractal geometry of nature*. Macmillan.

Mavros, P., 2001. Flow visualization in stirred vessels: A review of experimental techniques. *Chemical Engineering Research and Design* 79, 113-127.

Michelet, S., 1998. Turbulence et dissipation au sein d'un réacteur agité par une turbine Rushton-*vélocimétrie laser Doppler à deux volumes de mesure*.

Micheletti, M., Baldi, S., Yeoh, S.L., Ducci, A., Papadakis, G., Lee, K.C., Yianneskis, M., 2004. On spatial and temporal variations and estimates of energy dissipation in stirred reactors. *Chemical Engineering Research and Design* 82, 1188-1198.

Mishra, V.P., Dyster, K.N., Nienow, A.W., Mckemmie, J., Jaworski, Z., 1998. A study of an up-and a down-pumping wide blade hydrofoil impeller: Part I. LDA measurements. *The Canadian Journal of Chemical Engineering* 76, 577-588.

Murthy, B., Joshi, J., 2008. Assessment of standard  $k-\epsilon$ , RSM and LES turbulence models in a baffled stirred vessel agitated by various impeller designs. *Chemical Engineering Science* 63, 5468-5495.

Ng, K., Fentiman, N., Lee, K., Yianneskis, M., 1998. Assessment of sliding mesh CFD predictions and LDA measurements of the flow in a tank stirred by a Rushton impeller. *Chemical Engineering Research and Design* 76, 737-747.

Ng, K., Yianneskis, M., 2000. Observations on the distribution of energy dissipation in stirred vessels. *Chemical Engineering Research and Design* 78, 334-341.

Nienow, A., 1996. Gas-liquid mixing studies: A comparison of Rushton turbines with some modern impellers. *Chemical Engineering Research & Design* 74, 417-423.

Okamoto, Y., Nishikawa, M., Hashimoto, K., 1981. Energy dissipation rate distribution in mixing vessels and its effects on liquid-liquid dispersion and solid-liquid mass transfer. *International Chemical Engineering* 21, 88-94.

Paul, E.L., Atiemo-Obeng, V., Kresta, S.M., 2004. *Handbook of industrial mixing: science and practice*. John Wiley & Sons.

Pope, S.B., 2000. *Turbulent flows*. Cambridge University Press.

Ranade, V., Joshi, J., 1990. Flow generated by a disc turbine. II: Mathematical modelling and comparison with experimental data. *Chemical Engineering Research and Design* 68, 34-50.

Ranade, V., Perrard, M., Le Sauze, N., Xuereb, C., Bertrand, J., 2001. Trailing vortices of Rushton turbine: PIV measurements and CFD simulations with snapshot approach. *Chemical Engineering Research and Design* 79, 3-12.

Ranade, V.V., 1997. An efficient computational model for simulating flow in stirred vessels: a case of Rushton turbine. *Chemical Engineering Science* 52, 4473-4484.

Ranade, V.V., Joshi, J.B., 1989. Flow generated by pitched blade turbines I: Measurements using laser doppler anemometer. *Chemical Engineering Communications* 81, 197-224.

Ranade, V.V., Mishra, V.P., Saraph, V.S., Deshpande, G.B., Joshi, J.B., 1992. Comparison of axial-flow impellers using a laser doppler anemometer. *Industrial & Engineering Chemistry Research* 31, 2370-2379.

Rielly, C.D., Habib, M., Sherlock, J.P., 2007. Flow and mixing characteristics of a retreat curve impeller in a conical-based vessel. *Chemical Engineering Research and Design* 85, 953-962.

Rushton, J., Costich, E., Everett, H., 1950. Power characteristics of mixing impellers. 2. *Chemical Engineering Progress* 46, 467-476.

Schäfer, M., Höfken, M., Durst, F., 1997. Detailed LDV measurements for visualization of the flow field within a stirred-tank reactor equipped with a Rushton turbine. *Chemical Engineering Research and Design* 75, 729-736.

Sharp, K., Adrian, R., 2001. PIV study of small-scale flow structure around a Rushton turbine. *AIChE Journal* 47, 766-778.

Sheng, J., Meng, H., Fox, R.O., 2000. A large eddy PIV method for turbulence dissipation rate estimation. *Chemical Engineering Science* 55, 4423-4434.

Sreenivasan, K.R., 1991. Fractals and multifractals in fluid turbulence. *Annual Review of Fluid Mechanics* 23, 539-+.

Takahashi, K., Horiguchi, H., Mishima, M., Yatomi, R., 2006. Mixing characteristics in a vessel agitated by large paddle impeller Maxblend, 12th Euro. Conf. on Mixing, pp. 696-701.

Trivellato, F., 2011. On the efficiency of turbulent mixing in rotating stirrers. *Chemical Engineering and Processing: Process Intensification* 50, 799-809.

Vasconcelos, J.M., Orvalho, S.C., Rodrigues, A.M., Alves, S.S., 2000. Effect of blade shape on the performance of six-bladed disk turbine impellers. *Industrial & Engineering Chemistry Research* 39, 203-213.

Wang, X., Feng, X., Yang, C., Mao, Z.S., 2014. Energy dissipation rates of newtonian and non-newtonian fluids in a stirred vessel. *Chemical Engineering & Technology* 37, 1575-1582.

Wernersson, E.S., Trägårdh, C., 1999. Turbulence characteristics in turbine-agitated tanks of different sizes and geometries. *Chemical Engineering Journal* 72, 97-107.

Wu, H., Patterson, G., Van Doorn, M., 1989. Distribution of turbulence energy dissipation rates in a Rushton turbine stirred mixer. *Experiments in Fluids* 8, 153-160.

Wu, H., Patterson, G.K., 1989. Laser-Doppler measurements of turbulent-flow parameters in a stirred mixer. *Chemical Engineering Science* 44, 2207-2221.

Yang, F.L., Zhou, S.J., Zhang, C.X., 2015. Turbulent flow and mixing performance of a novel six-blade grid disc impeller. *Korean Journal of Chemical Engineering* 32, 816-825.

Yao, W., Sato, H., Takahashi, K., Koyama, K., 1998. Mixing performance experiments in impeller stirred tanks subjected to unsteady rotational speeds. *Chemical Engineering Science* 53, 3031-3040.

Yeoh, S., Papadakis, G., Yianneskis, M., 2004. Numerical simulation of turbulent flow characteristics in a stirred vessel using the LES and RANS approaches with the sliding/deforming mesh methodology. *Chemical Engineering Research and Design* 82, 834-848.

Yianneskis, M., 2000. Trailing vortex, mean flow and turbulence modification through impeller blade design in stirred reactor. . Proc. Euro. Conf. on Mixing, Delft, The Netherlands, 1.

Yianneskis, M., Popiolek, Z., Whitelaw, J., 1987. An experimental study of the steady and unsteady flow characteristics of stirred reactors. *Journal of Fluid Mechanics* 175, 537-555.

Zhao, J., Gao, Z.M., Bao, Y.Y., 2011. Effects of the blade shape on the trailing vortices in liquid flow generated by disc turbines. *Chinese Journal of Chemical Engineering* 19, 232-242.

Zhou, G., Kresta, S.M., 1996a. Distribution of energy between convective and turbulent flow for three frequently used impellers. *Chemical engineering research & design* 74, 379-389.

Zhou, G., Kresta, S.M., 1996b. Impact of tank geometry on the maximum turbulence energy dissipation rate for impellers. *AIChE Journal* 42, 2476-2490.

## **Chapter 3**

### **Experimental characterization of the performance of Fractal Impeller (FI) in stirred tank**

### 3.1 Introduction

Comparison of a novel impeller with that of the conventional impeller in terms of performance is essential to prove the usefulness of the novel concept. In recent times, a large number of experimental techniques have been adopted to study the performance of the given type of impeller. The performance of an impeller is evaluated on the basis of power consumption, mixing per unit per consumption, flow characteristics, heat transfer, and mass transfer (gas-liquid, solid-liquid, and liquid-liquid) per unit power consumption. Therefore, it is important to discuss the experimental techniques in details as possible. In this chapter, the experimental techniques related to power draw, mixing and flow visualization are discussed.

### 3.2 Ultrasonic Velocity Profiler (UVP) for flow visualization

Flow patterns analysis for any given impeller is important for studying the mixing time efficiency effectively as it gives the detailed analysis of dead zones, circulation loops, and maximum velocities in the stirred tank. The local velocities can be determined using several widely used flow measurement techniques such as light sheet visualization (reflective tracer particle is traced), Pitot tube, Hot-wire anemometry, Laser-Doppler Velocimetry (LDV), Particle Image Velocimetry (PIV), Ultrasonic Velocity Profiler (UVP), etc (Mavros, 2001). The design of Fractal Impeller is such that it covers most of the tank volume with its blades, therefore, the techniques with optical resolutions and intrusive nature cannot be adopted for flow visualization. The more details are given in Table 3.1. Based on the applicability, Ultrasonic Velocity Profiler (UVP) was chosen as the flow measurement technique. Therefore, neutrally buoyant solid particles ( $\rho_s = 1060 \text{ kg/m}^3$ ) of diameter ( $d_{NB}$ )  $350 \mu\text{m}$  were used to measure liquid velocities. 1% (v/v) solid loading of neutrally buoyant particles was used to carry out the experiments.

Table 3.1: Different flow measurement techniques and analysis of their its applicability for fractal impeller in a stirred tank

Sr. No.	Flow measurement techniques (Reference)	Working principle	Remark
1	Pitot tube (Jaworski and Fořt, 1991; Mavros, 2001)	Tube facing the flow generates pressure by the velocity of the fluid. This generated pressure is compared with reference pressure and velocity is calculated using Bernoulli's principle.	It is an intrusive technique and cannot be adopted for the present system as impeller covers the whole tank.
2	Hot-wire Anemometry (Cooper and Wolf, 1968; Mavros, 2001)	It uses the concept of convective heat transfer to measure the velocities in the vessel.	It is also an intrusive technique and measures the velocities and temperature at a point in a flow.
3	Laser-Doppler Velocimetry (Ducci and Yianneskis, 2005; Hartmann et al., 2004; Jaworski et al., 1996)	In a selected control volume, when a small particle passes through it, it scatters light. This light is captured by the photodetector. The analysis of change in the intensity fluctuations on the photodetector gives the local velocities.	In LDV, probe lies outside the tank, however, with multiple blades spread over the entire tank, as outermost blades will not allow the measurement in the inner part of the tank. Therefore, it is difficult to measure the velocity by optical constraints,
4.	Particle Image Velocimetry (Aubin et al., 2004; Baldi and Yianneskis, 2004; Ranade et al., 2001; Zhao et al., 2011)	It works on the principle of simple photographic recording of a particle moving in a control volume. A careful comparison of the two consecutive frames gives the local velocity information.	It is a very accurate method for measuring the flow in the stirred tank. It is based on optical measurements, hence the flow measurement in the entire tank is not possible and hence ruled out.
5.	Ultrasonic Velocity Profiler (Bouillard et al., 2001; Sardeshpande et al.; Takeda, 1995a, b)	This measures the velocity in a control volume by the detection of Doppler shift in the ultrasound frequency.	This is less accurate as compared to LDA, PIV, HWA. However, it is perfectly suitable for present system as it does not intervene the flow in the system.



### 3.2.1 Principles of UVP

The ultrasound velocity profiler (UVP) method is based on pulsed ultrasound echography (MET-FLOW, 2002; Takeda, 1995a, b). An ultrasound pulse is emitted from the transducer along the measuring line. The same transducer receives the echo frequencies reflected from the surface of solid suspended in the liquid. Information on the position from which the ultrasound is reflected can be measured from time delay ( $t$ ) between the start of the pulse burst and its reception as:

$$X = \frac{c \times t}{2} \quad 3.1$$

at the same time, the velocity information is derived from the Doppler shift frequencies at that moment:

$$V = 0.5 (c \times f_D) / f_o \quad 3.2$$

If UVP succeeds to measure the delay ( $t$ ) and Doppler shift ( $f_D$ ) it is possible to calculate both position and velocity of a particle in a measuring axis. Figure 3.1 gives the pictorial view of velocity measurements in a stirred tank by UVP. Doppler frequency shift can be negative, positive or zero (depending on the movement of the solid particles), and it can be used for identifying the circulation zones/patterns in the stirred tank. However, the information is available only periodically; therefore, following the Nyquist theorem the measurable velocity range of UVP is limited. This means that a maximum velocity ( $V_{Max}$ ) exists for each reception frequency. In addition, the maximum penetration depth ( $P_{Max}$ ) is fixed by the velocity of sound in the medium ( $c$ ) over the time period of the pulse ( $t_{prf}$ ):

$$P_{Max} = 0.5 (c \times t_{prf}) \quad 3.3$$

similarly, with multiplying  $V_{Max}$  and  $P_{Max}$  yields:

$$P_{Max} V_{Max} = c^2 / 8 f_o \quad 3.4$$

from the above two equations, it can be concluded that increasing the time between the pulses ( $t_{prf}$ ) will increase the maximum measurable depth, but will also reduce the maximum velocity which can be measured.

UVP is a unique measurement technique that can be used even for opaque systems and hence acts more like a stethoscope for the measurement of hydrodynamics inside the system (Takeda, 1995b). However, it also has a few limitations. One of major limitation comes from the winding intensity lobe, which is related to the wavelength of the emitted wave and the radius of the transducer. This means that the more the distance from the transducer, the width of the measurement region increases (Bouillard et al., 2001; Mavros, 2001). This indicates that before using UVP one must have some idea about the possible minimum and maximum velocity in the system. Also, because it measures an average velocity over a bin (an expanding cylindrical section of the diameter of probe and length decided by the user), UVP results are intrinsically relatively less accurate than the laser Doppler methods (LDA or PIV). Hence the probe selection plays an important role in defining the accuracy of the measurements and it is also controlled by the maximum velocity range and the maximum measuring distance. UVP needs neutrally buoyant particles to be used in the system to track the flow in a given spatial domain. If the size of the particle used for the experiment is bigger than the wavelength, the ultrasonic waves are reflected and refracted by the particle. In such a case the direction of propagation and intensity of ultrasonic wave are affected and it will give erroneous velocity profiles. Therefore the selection of particles as well as the UVP probe for measuring the velocity profiles must be done carefully. More details on UVP and the measurement approach can be found in the literature (Bouillard et al., 2001; MET-FLOW, 2002; Sardeshpande et al.).

### 3.2.2 Measurement arrangements

UVP measurements were carried out for all the three velocity components. The time duration for each UVP measurement was set to 100 seconds. UVP measures the velocity profile along the measuring axis; therefore, radial ( $u$ ) and axial ( $v$ ) profiles can be obtained by pointing the probe at respective directions on a plane midway between two consecutive baffles. A zone between two consecutive baffles of the stirred tank was considered for measuring the tangential ( $w$ ) component.

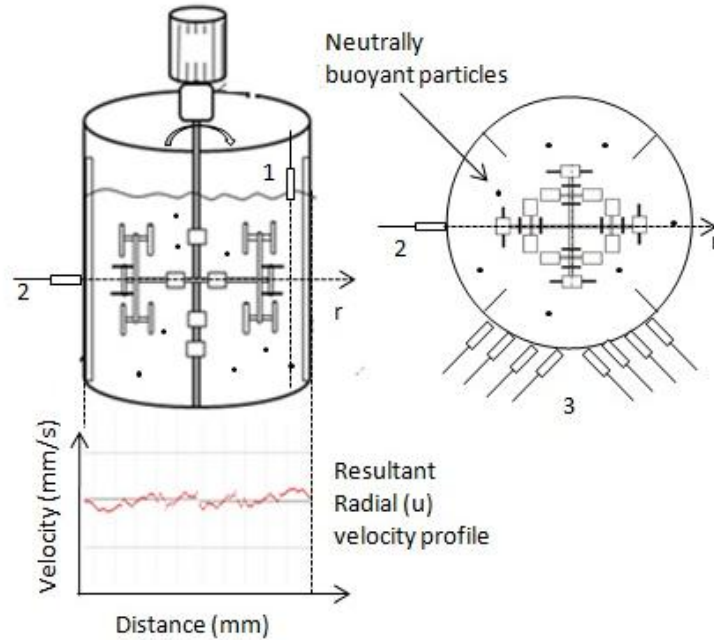


Figure 3.1: Velocity measurements in a stirred tank with FI by UVP (probe orientation 1 is for measurement of axial velocity, 2 for radial velocity and 3 for tangential velocity component, respectively).

### 3.2.3 Data Processing

All the measured profiles were collected and analyzed using MATLAB code and the figures were plotted. Figure 3.2 gives the details of data processing and its implication in calculating the flow characteristics. Once the raw velocity data is generated from the experiments for a particular velocity component, the data is imported into MATLAB code and mean and fluctuating component are separated using statistical analysis. The mean component of each velocity component is used for calculating the flow patterns and impeller flow number, whereas fluctuating component is used for calculating the turbulent kinetic energy ( $k$ ). The instantaneous velocity data measured in a two-dimensional plane was resolved in resultant vectors and the tangential ( $w$ ) component (along with an angle of  $45^\circ$ ) was obtained by solving Eq. (3.5) and Eq. (3.6) simultaneously.

$$u_x = u \cos \theta - w \sin \theta \quad 3.5$$

$$u_y = u \sin \theta + w \cos \theta \quad 3.6$$

All the components of the velocity were studied as dimensionless parameters by dividing velocity by maximum velocity in the tank ( $U_{Max} = \pi D_{FI} N$ , where  $D_{FI}$  is impeller diameter and  $N$  is impeller speed in 1/s). As mentioned in the block diagram, the time averaged velocity data obtained from 500 transient profiles was used to determine the 2D radial-axial velocity vector field and corresponding contour maps. The RMS velocity data was used for the estimation of the local turbulent kinetic energy ( $k$ ).

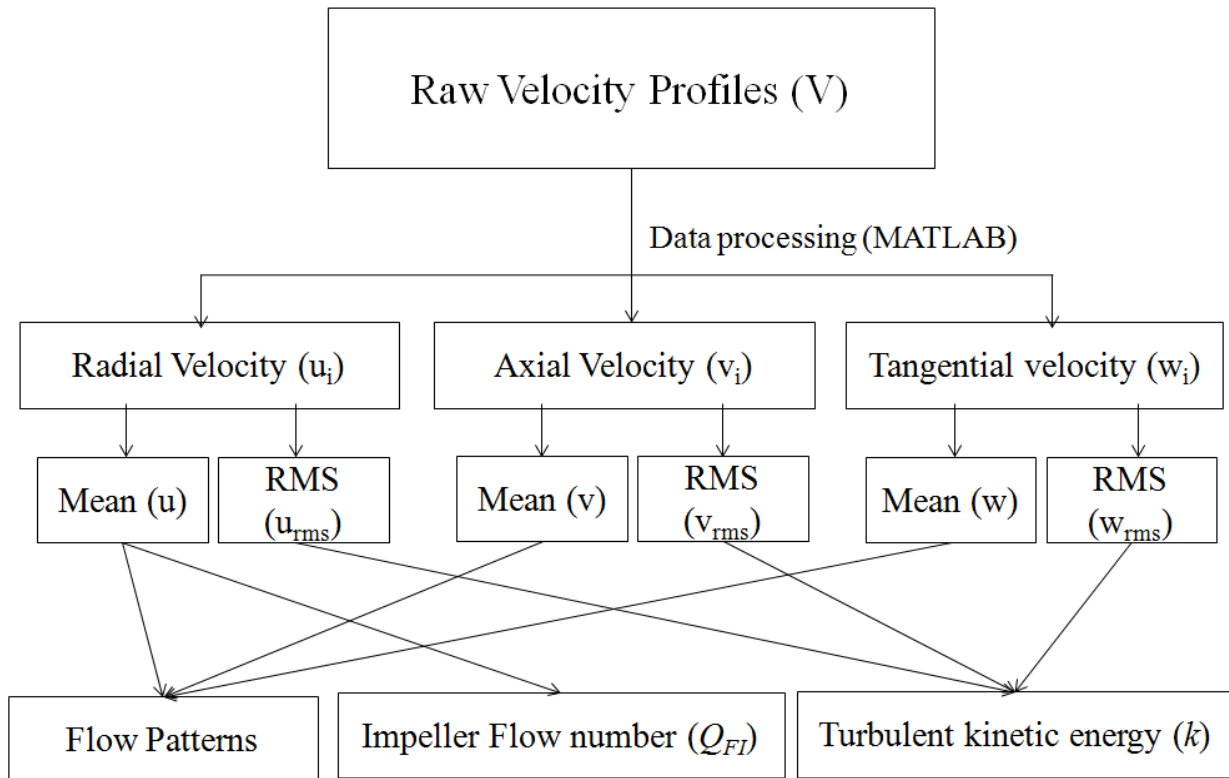


Figure 3.2: Block diagram of a data processing

### 3.3 Power Consumption ( $P$ )

The most common in fundamental measurement in the stirred tank operations is power drawn by an impeller. Many scale-up rules heavily rely on the power consumption per unit volume. Moreover, in the introduction part, impellers are identified on the basis of their power number ( $N_p$ ). Power consumption by the impeller can be measured by several techniques such as Electricals measurements, Calorimetric measurements, Dynamometers, Torquemeters, Strain Gauges etc. Each method has its own advantages and disadvantages, the details on this are

already discussed by Ascanio et al. (2004). In this work, a rotary torque transducer (CTimeSync Ltd., UK) was used to measure the torque experienced by the impeller at different impeller rotation speeds. This is a non-contact optical device, which functions on the displacement principle causing a variation of the volume of light generated using a laser source inside the device. A proportional volume of light gets generated by the low power demand solid-state laser depending on upon the extent of torsion experienced by the impeller shaft during its motion. This volume of light is captured by the optical components attached to the transducer torsion shaft, and the value helps the user know the torque experienced for a given impeller rotation speed. The torque data was taken online on a PC using data acquisition system. The steel ball placed at bottom of the tank supports the shaft and thus ensures that the weight of the impeller is not on the torque sensor and the measured torque was entirely due to friction experienced by the impeller blades. The power consumption ( $P$ ) the fractal impeller configuration was estimated using the torque data ( $\tau_r$ ) at different rotational speeds as  $P = 2\pi N\tau_r$ , where  $N$  is the impeller rotational speed per second. Subsequently power consumption per unit mass  $P_W$  (W/kg) was also estimated.

### 3.4 Mixing Time ( $\theta_{mix}$ )

Literature reports indicate various ways to measure the mixing time, viz. decolorization, off-line sampling, thermocouple technique, conductivity probe technique etc. (Paul et al., 2004). One of the simplest and most widely used techniques is conductivity probe technique. In the entire work, conductivity probe technique was used to estimate the mixing time, where a tracer (0.5% of the total volume) pulse was given in the form of a concentrated salt solution at the top liquid surface. The position of tracer input was maintained unchanged for all the experiments. The tracer concentration was monitored using the conductivity probe fixed at a location behind one of the baffle. All the signals were normalized using Eq. (3.7).

$$C'_i = \frac{C_i - C_0}{C_\infty - C_0} \quad 3.7$$

where  $C_0$  is the concentration measured before addition of tracer,  $C_\infty$  is the final stable value after the test is complete,  $C_i$  is the probe output and  $C'_i$  is the corresponding normalized probe output. The mixing time, in general, is defined as the time required for the normalized

concentration of the tracer reaches within 95 and 105% of the final value ( $C_{\infty}$ ). Separate set of experiments was carried out to measure the mixing time at a fixed impeller rotation speed by changing the location of tracer injection. In such experiments, the variation in the estimated mixing time was less than 5%.

### **3.5 Conclusions**

Various methods used for investigating the performance of fractal impeller in terms of flow analysis, power consumption and mixing time have been discussed in details. As the fractal impeller has space filling nature an intrusive and optical method for flow visualization cannot be adopted. Therefore, Ultrasonic Velocity Profiler (UVP) has been considered to measure the local velocities in a stirred tank with the fractal impeller. Power consumption measurements were done using torque sensor as it helps in measuring the power drawn by the impeller with accuracy at lab scale. Mixing time measurements were done using conductivity probe technique as it is widely accepted. Based on the results of power consumption and mixing time, the efficiency of the fractal impeller is discussed in the subsequent chapter.

---

## References

- Ascanio, G., Castro, B., Galindo, E., 2004. Measurement of power consumption in stirred vessels—a review. *Chemical Engineering Research and Design* 82, 1282-1290.
- Aubin, J., Le Sauze, N., Bertrand, J., Fletcher, D.F., Xuereb, C., 2004. PIV measurements of flow in an aerated tank stirred by a down- and an up-pumping axial flow impeller. *Experimental Thermal and Fluid Science* 28, 447-456.
- Baldi, S., Yianneskis, M., 2004. On the quantification of energy dissipation in the impeller stream of a stirred vessel from fluctuating velocity gradient measurements. *Chemical Engineering Science* 59, 2659-2671.
- Bouillard, J., Alban, B., Jacques, P., Xuereb, C., 2001. Liquid flow velocity measurements in stirred tanks by ultra-sound Doppler velocimetry. *Chemical Engineering Science* 56, 747-754.
- Cooper, R.G., Wolf, D., 1968. Velocity profiles and pumping capacities for turbine type impellers. *The Canadian Journal of Chemical Engineering* 46, 94-100.
- Ducci, A., Yianneskis, M., 2005. Direct determination of energy dissipation in stirred vessels with two-point LDA. *AIChE Journal* 51, 2133-2149.
- Hartmann, H., Derksen, J.J., Montavon, C., Pearson, J., Hamill, I.S., van den Akker, H.E.A., 2004. Assessment of large eddy and RANS stirred tank simulations by means of LDA. *Chemical Engineering Science* 59, 2419-2432.
- Jaworski, Z., Fořt, I., 1991. Energy dissipation rate in a baffled vessel with pitched blade turbine impeller. *Collection of Czechoslovak Chemical Communications* 56, 1856-1867.
- Jaworski, Z., Nienow, A.W., Dyster, K.N., 1996. An LDA study of the turbulent flow field in a baffled vessel agitated by an axial, down-pumping hydrofoil impeller. *The Canadian Journal of Chemical Engineering* 74, 3-15.
- Mavros, P., 2001. Flow visualization in stirred vessels: A review of experimental techniques. *Chemical Engineering Research and Design* 79, 113-127.
- MET-FLOW, 2002. UVP Monitor Model UVP-DUO with Software Version 3 - User's Guide
- Paul, E.L., Atiemo-Obeng, V., Kresta, S.M., 2004. Handbook of industrial mixing: science and practice. John Wiley & Sons.

Ranade, V., Perrard, M., Le Sauze, N., Xuereb, C., Bertrand, J., 2001. Trailing vortices of Rushton turbine: PIV measurements and CFD simulations with snapshot approach. *Chemical Engineering Research and Design* 79, 3-12.

Sardeshpande, M.V., Juvekar, V.A., Ranade, V.V., Solid suspension in stirred tanks: UVP measurements and CFD simulations. *Canadian Journal of Chemical Engineering* 89, 1112-1121.

Takeda, Y., 1995a. Instantaneous velocity profile measurement by ultrasonic Doppler method. *JSME International Journal Series B* 38, 8-16.

Takeda, Y., 1995b. Velocity profile measurement by ultrasonic doppler method. *Experimental Thermal and Fluid Science* 10, 444-453.

Zhao, J., Gao, Z.M., Bao, Y.Y., 2011. Effects of the blade shape on the trailing vortices in liquid flow generated by disc turbines. *Chinese Journal of Chemical Engineering* 19, 232-242.



**Chapter 4**  
**Computational Fluid Dynamics (CFD) for Stirred Tank Reactor  
with Fractal Impeller**

## 4.1 Introduction

Computational Fluid Dynamics (CFD) has gained popularity in recent time for flow predictions. With the recent development of computational fluid dynamics (CFD), numerical simulations are employed as a reliable tool for analyzing the flow field and local velocities. In a stirred tank with baffles, the flow around the impeller blades interacts with stationary baffles and generates a three-dimensional, rotary turbulent flow. Prediction of such a complex flow using numerical methods is always challenging. Therefore, CFD has become an effective tool for understanding the flow patterns in a stirred tank and thereby design a suitable impeller configuration to achieve the desired flow pattern. The performance of novel impeller design or blade design can also be studied effectively using CFD simulations without actually fabricating it. Buwa et al. (2006) successfully employed a similar approach to analyze the flow generated by novel 'grid disc' impeller. Similarly, Ge et al. (2014) adopted the CFD simulations for studying the hydrodynamics of modified pitched blade turbines. In one of the recent article, Ri et al. (2017), adopted CFD for studying horizontal stirred tank reactor for the biohydrogen production.

In the view of this, in this Chapter, different CFD models and CFD approaches used to model the stirred tank have been discussed in details. In the next section, governing equations have been discussed, followed by different numerical discretization methods have been discussed in section 4.3. In section 4.4, different turbulent models used to simulate flow have been discussed. Section 4.5 presents the modeling approaches.

## 4.2 Governing Equations

Basics of Computational Fluid Dynamics (CFD) lie in solving fluid dynamics fundamental equations. These fundamental equations are conservation of mass and momentum (Bird, 2002). These equations are non-linear differential equations and serve as the basis for predicting the transient or steady state fluid flow. The conservation of mass equation, commonly known as the continuity equation in vector notation is given as follow;

$$\frac{\partial \rho}{\partial t} + \frac{\partial(\rho u_i)}{\partial x_i} = 0 \quad 4.1$$

where  $\rho$  is density,  $u_i$  is the velocity in  $x_i$  direction. For an incompressible flow, where it is assumed that density is constant because for an incompressible fluid pressure and temperature does not affect the density, therefore, Eq. 4.1 can be simplified as;

$$\frac{\partial u_i}{\partial x_i} = 0 \quad 4.2$$

Similarly, momentum equation is expressed as given below;

$$\frac{\partial(\rho u_i)}{\partial t} + u_j \frac{\partial(\rho u_i)}{\partial x_j} = \frac{\partial \tau_{ij}}{\partial x_j} + B \quad 4.3$$

where,  $\tau_{ij}$  is the stress tensor and B is the body force vector. Stress tensor is resolved and it takes the form of the Eq. 4.4. This equation is also known as Navier-Stokes equations.

$$\rho \frac{\partial u_i}{\partial t} + \rho u_j \frac{\partial u_i}{\partial x_j} = - \frac{\partial P}{\partial x_i} + \mu \frac{\partial^2 u_i}{\partial x_j^2} + \rho g_i \quad 4.4$$

### 4.3 Modelling Turbulent flow

As it is known that, the flow generated in the stirred tank is transient and three dimensional. Therefore, various approximations have been established to study the turbulent flow. Different approaches that are used for simulating turbulent flows in a stirred tank include: (i) Reynolds-averaged Navier-Stokes (RANS) model (Deglon and Meyer, 2006; Hartmann et al., 2004; Murthy and Joshi, 2008), (ii) large eddy simulations (LES) (Li et al., 2011; Yeoh et al., 2004), and (iii) direct numerical simulations (DNS)(Sbrizzai et al., 2006). In DNS, Navier-Stokes equations are numerically solved without any turbulent model. This implies that the whole range of spatial and temporal scales needs to be resolved in the computational mesh and in time difference respectively. The resolution of smallest dissipative scale (Kolmogorov scale) up to the largest scale is associated with the motions of eddies containing most of the kinetic energy. Since the resolution needs to be finest, the computational cost of the DNS is very high (Joshi et al.; Sbrizzai et al., 2006). On the other hand, in LES, the large scales are resolved and small eddies are modeled using subgrid-scale model (SGS model). This is because the large eddies of the flow are dependent on the geometry while the smaller scales are universal. Although LES is

computationally cheaper than DNS, the computational cost of LES remains still high for complicated process equipment (Montante et al., 2001). RANS approach is used to predict the mean flow properties and it needs a suitable turbulent model to get closure for the governing equations. This method is computationally less expensive than the DNS and LES and hence is a widely used approach (Joshi et al., 2011b, Murthy and Joshi, 2008). Several models have been developed to close the governing equations, among which the standard  $k-\varepsilon$  turbulence model has been widely applied to study practical flows. The standard  $k-\varepsilon$  model is known to be slightly inaccurate for non-isotropic flow and turbulent flow in the vicinity of solid walls. However, the use of variations in RANS models such as low Reynolds number  $k-\varepsilon$ ,  $k-\omega$ , Reynolds stress model (RSM) etc. improve the predictions to some extent although at additional computational time (Aubin et al., 2004; Buwa et al., 2006; Jenne and Reuss, 1999; Jones et al., 2001; Khopkar et al., 2004; Montante et al., 2001). In this work, Reynolds-averaged Navier-Stokes models have been used to study the flow generated by Fractal Impeller and the details about them are discussed in sub-section.

#### 4.3.1 Reynolds-averaged Navier-Stokes (RANS) Equations

As described, the RANS equations are time-averaged equations of motion for fluid flow, where the instantaneous quantity is decomposed into its time-averaged and fluctuating quantities. These equations are as follow;

$$\rho \bar{u}_j \frac{\partial \bar{u}_i}{\partial x_j} = \rho \bar{B}_i + \left[ -\bar{p} \delta_{ij} + \mu \left( \frac{\partial \bar{u}_i}{\partial x_j} + \frac{\partial \bar{u}_j}{\partial x_i} \right) - \rho \overline{u_i u_j} \right] \quad 4.5$$

where,  $-\rho \overline{u_i u_j}$  is apparent stress which is widely referred as Reynolds stress.

#### 4.3.2 The Standard $k-\varepsilon$ model

It is one of the commonly used turbulence models in CFD. The standard  $k-\varepsilon$  model is a two-equation, first-order closure model. This model uses eddy-viscosity hypothesis for turbulence. Eddy-viscosity hypothesis states that the Reynolds stresses can be linearly related to the mean velocity gradients in a manner analogous to the relationship between the stress and strain tensors in laminar Newtonian flow (Boussinesq, 1877). This can be expressed mathematically as follow;

$$\tau_{ij} = 2\mu_t S_{ij}^* - \frac{2}{3}\rho k \delta_{ij} \quad 4.6$$

where,  $\mu_t$  is a scalar property and called as eddy viscosity and  $k$  is turbulent kinetic energy. The above equation can be written as follow;

$$-\rho \overline{u_i u_j} = \mu_t \left( \frac{\partial U_i}{\partial x_j} + \frac{\partial U_j}{\partial x_i} + \frac{2}{3} \frac{\partial U_k}{\partial x_k} \delta_{ij} \right) - \frac{2}{3} \rho k \delta_{ij} \quad 4.7$$

for an incompressible flow;

$$\frac{\partial U_k}{\partial x_k} = 0 \quad 4.8$$

The  $k$ - $\varepsilon$  model assumes that the turbulent viscosity can be determined using Eq. 4.9

$$\mu_t = C_\mu \rho \frac{k^2}{\varepsilon} \quad 4.9$$

where,  $C_\mu$  is a constant and given in Table 4.1. Whereas, turbulent kinetic energy ( $k$ ) and its dissipation ( $\varepsilon$ ) are calculated using Eqs. 4.10 and 4.11 as follow;

$$\frac{\partial(\rho k)}{\partial t} + \frac{\partial(\rho k u_i)}{\partial x_i} = \frac{\partial}{\partial x_j} \left[ \frac{\mu_t}{\sigma_k} \frac{\partial k}{\partial x_j} \right] + 2\mu_t E_{ij} E_{ij} - \rho \varepsilon \quad 4.10$$

$$\frac{\partial(\rho \varepsilon)}{\partial t} + \frac{\partial(\rho \varepsilon u_i)}{\partial x_i} = \frac{\partial}{\partial x_j} \left[ \frac{\mu_t}{\sigma_\varepsilon} \frac{\partial \varepsilon}{\partial x_j} \right] + C_{1\varepsilon} \frac{\varepsilon}{k} 2\mu_t E_{ij} E_{ij} - C_{2\varepsilon} \rho \frac{\varepsilon^2}{k} \quad 4.11$$

where,  $E_{ij}$  represents the component of the rate of deformation, and  $C_{1\varepsilon}$ ,  $C_{2\varepsilon}$ ,  $\sigma_k$ , and  $\sigma_\varepsilon$  are constants and given in the table below. It should be noted that this model is a high Reynolds number model and does not apply in the region close to the wall. In this scenario, wall functions are usually employed.

Table 4.1: Parameters of the standard  $k$ - $\varepsilon$  turbulence model.

$C_\mu$	$C_{1\varepsilon}$	$C_{2\varepsilon}$	$\sigma_k$	$\sigma_\varepsilon$
0.09	1.44	1.92	1.0	1.3

### 4.3.3 The $k$ - $\omega$ Turbulence Model

Similar to  $k$ - $\varepsilon$ , the  $k$ - $\omega$  turbulence model is two equation closure model. Where eddy viscosity is given by Eq. 4.12

$$\mu_t = \rho \frac{k}{\omega} \quad 4.12$$

And turbulent kinetic energy ( $k$ ) and its specific rate of dissipation ( $\omega$ ) are calculated using Eqs. 4.13 and 4.14 as follow (Wilcox, 2008);

$$\frac{\partial(\rho k)}{\partial t} + \frac{\partial(\rho k u_j)}{\partial x_j} = \rho \tau_{ij} \frac{\partial u_i}{\partial x_j} - \beta_0^* \rho \omega k + \frac{\partial}{\partial x_j} \left[ \left( \mu + \sigma_k \frac{\rho k}{\omega} \right) \frac{\partial k}{\partial x_j} \right] \quad 4.13$$

$$\frac{\partial(\rho \omega)}{\partial t} + \frac{\partial(\rho \omega u_i)}{\partial x_j} = \frac{\gamma \omega}{k} \tau_{ij} \frac{\partial u_i}{\partial x_j} - \beta_0 \rho \omega^2 + \frac{\partial}{\partial x_j} \left[ \left( \mu + \sigma_\omega \frac{\rho k}{\omega} \right) \frac{\partial \omega}{\partial x_j} \right] + \frac{\rho \sigma_d}{\omega} \frac{\partial k}{\partial x_j} \frac{\partial \omega}{\partial x_j} \quad 4.14$$

Closure coefficients of these above equations are given as;

$$\gamma = \frac{13}{25}, \quad \beta_0^* = \frac{9}{100}, \quad \sigma_k = \frac{1}{2}, \quad \sigma_\omega = \frac{3}{5} \quad 4.15$$

$$\sigma_d = \begin{cases} 0, & \frac{\partial k}{\partial x_j} \frac{\partial \omega}{\partial x_j} \leq 0 \\ \sigma_{do}, & \frac{\partial k}{\partial x_j} \frac{\partial \omega}{\partial x_j} > 0 \end{cases} \quad \sigma_{do} = \frac{1}{8} \quad 4.16$$

### 4.3.4 Shear Stress Transport Model

This model is the extension of  $k$ - $\omega$  model. This model directly can be used all the way down to the wall through viscous sub-layers due to the  $k$ - $\omega$  formulation in the inner parts of the boundary layer. Therefore, the SST model can be used as low Reynolds number turbulence model. The SST model formulation also adapts to a  $k$ - $\varepsilon$  behavior in the free-stream region and hence avoids the common  $k$ - $\omega$  problem that the model is too sensitive to the inlet free stream turbulence properties. Moreover, the SST model produces a bit too large turbulence levels in regions with large normal strain, like stagnation regions and regions with strong acceleration.

The governing equation for calculating eddy viscosity is given by Eq. 4.17,  $k$  is given by Eq. 4.18 and modified  $\omega$  is given by Eq. 4.19 as follow;

$$\mu_t = \rho \frac{a_1 k}{\max(a_1 \omega, SF_2)} \quad 4.17$$

$$\frac{\partial(\rho k)}{\partial t} + \frac{\partial(\rho k j)}{\partial x_j} = \rho(\min(\tau_{ij} \frac{\partial u_i}{\partial x_j}, 10\beta_0^* k \omega)) - \beta_0^* \rho \omega k + \frac{\partial}{\partial x_j} \left[ (\mu + \sigma_k \mu_t) \frac{\partial k}{\partial x_j} \right] \quad 4.18$$

$$\frac{\partial(\rho \omega)}{\partial t} + \frac{\partial(\rho \omega u_j)}{\partial x_j} = \gamma S^2 - \beta_0 \rho \omega^2 + \frac{\partial}{\partial x_j} \left[ (\mu + \sigma_\omega \mu_t) \frac{\partial \omega}{\partial x_j} \right] + 2(1 - F_1) \sigma_{\omega 2} \frac{1}{\omega} \frac{\partial k}{\partial x_j} \frac{\partial \omega}{\partial x_j} \quad 4.19$$

Closure coefficients and auxiliary relations are given as follow;

$$S = \sqrt{2S:S}, S = \frac{1}{2} \left( \frac{\partial u_i}{\partial x_j} + \frac{\partial u_j}{\partial x_i} \right) \quad 4.20$$

$$F_2 = \tanh \left\{ \left[ \max \left( \frac{2\sqrt{k}}{\beta_0^* \omega y}, \frac{500\mu}{y^2 \omega} \right) \right]^2 \right\} \quad 4.21$$

$$F_1 = \tanh \left\{ \left\{ \min \left[ \max \left( \frac{2\sqrt{k}}{\beta_0^* \omega y}, \frac{500\mu}{y^2 \omega} \right), \frac{4\sigma_{\omega 2} k}{CD_{k\omega} y^2} \right] \right\}^4 \right\} \quad 4.22$$

$$CD_{k\omega} = \max \left( 2\rho \sigma_{\omega 2} \frac{1}{\omega} \frac{\partial k}{\partial x_j} \frac{\partial \omega}{\partial x_j}, 10^{-10} \right) \quad 4.23$$

$$\varphi = \varphi_1 F_1 + \varphi_2 (1 - F_1), \quad \alpha_1 = \frac{5}{9}, \alpha_2 = 0.44, \quad \beta_{01} = \frac{3}{40}, \beta_{02} = 0.0828, \quad \beta_0^* = \frac{9}{100}$$

$$\sigma_{k1} = 0.85, \quad \sigma_{k2} = 1, \quad \sigma_{\omega 1} = 0.5, \quad \sigma_{\omega 2} = 0.856$$

#### 4.4 Discretization Methods

Finding a general or analytical solution for Navier-Stokes equation for most of the industrial problems becomes difficult. Hence, numerical method analysis is used to provide an

alternative and suitable solution. Numerical methods typically transform differential equations into a set of algebraic equations using some approximations. These algebraic equations are solved on a given mesh for a domain to get a solution of the original differential equations. Transformation of differential methods into algebraic equations can be done by several methods which are known as discretization methods. Most commonly used three discretization methods are i) Finite Difference Method (FDM), ii) Finite Volume Method (FVM) and iii) Finite Element Method (FEM). These methods are discussed briefly in the sub-section.

#### **4.4.1 Finite Difference Method (FDM)**

In this method, an approximation of differential equations is done by Taylor series expansion. In this flow field is discretized by setting up the structured grid. The structured grid consists of multiple mesh points. The resulting algebraic equations are solved for the values of the discrete mesh points of the domain or grid. This is one of the oldest and simplest discretization methods. More details on this can be found in Anderson and Wendt (1995) and Chapra and Canale (1988).

#### **4.4.2 Finite Volume Method (FVM)**

In this method, the grid subdivides into a number of volumes and computational nodes for calculation of variables which lie at the centroid of each control volume. For each control volume, the transformed algebraic equations of the partial differential equations are solved. The Finite Volume Method (FVM) is conservative, as the flux entering a given volume is identical to that leaving the adjacent volume. The advantage of this method is that it is suitable for any type of mesh using the direct discretization of the conservation laws. Therefore, the conservation of mass, momentum, and energy take place at the discrete level (Ferziger and Peric, 2012, Moukalled et al., 2016).

#### **4.4.3 Finite Element Method (FEM)**

In this discretization method, the domain is divided into elements of arbitrary shape and sizes. For each such element, a number of nodes (points) are defined on its edges. At all these points the transformed algebraic equations of the partial differential equations are solved. In this case, the differential equations are firstly multiplied by a weight function before being integrated



over the entire computation domain. These weight functions are generally linear, quadratic or cubic. The role of the weight function is to obtain a best numerical solution by ensuring that some weighted average of the residual error over the entire domain is zero. This method has come of age for computational fluid dynamics. COMSOL Multiphysics<sup>(R)</sup> uses finite element method for flow modeling.

#### 4.5 Modelling Flows in Stirred Tank

In any rotating machinery such as a stirred tank, requires the use of moving cell zones. One zone is defined as modeling domain that contains an impeller and the other one is outside this which has baffles. Conservation of mass and momentum should be established to account for the integration between two domains (Figure 4.1). This can be addressed by two approaches, i) Sliding mesh approach, ii) Frozen rotor approach. In the present work, the flow is defined as turbulent and three dimensional and various strategies need to establish to come up with better results. Therefore, both the approaches have been adopted. COMSOL Multiphysics® enables the use of these two modeling approaches for performing CFD simulations of the stirred tank.

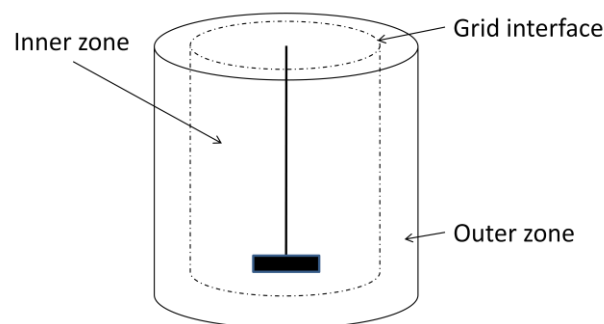


Figure 4.1: Different zones in the modeling of stirred tank

##### 4.5.1 Sliding Mesh Approach

In sliding mesh approach, two or more different moving zones are used. The stirred tank domain is subdivided. These subdivided zones are separated by an interface (Figure 4.1). The grid structure of the separated zones does not have to match with each other. These two zones slide to each other along the grid interface in discrete time steps. In the inner zone, the mesh is moving whereas in outer zone mesh is stationary. These interfaces boundary is also known as

coupling boundary between two zones. The interface establishes the conservation of mass and momentum across the domain.

This model is used extensively to investigate the start-up conditions of the impeller. Hence, the accuracy becomes a necessity. However, this method is computationally expensive when the desired result is to simulate how the mixer will perform after a period of time, and during normal operation under pseudo steady-state conditions.

#### **4.5.2 Frozen Rotor Approach**

In this approach, the model simulates rotating flow by assuming that the topology of the system relative to the rotating reference frame is frozen. This means the equations are solved in a rotating reference in inner zone and a stationary frame in the outer region. This approach assumes a pseudo steady-state condition, which means the topology is not changing with time. Hence, it significantly reduces the computational resources required to simulate the flow in the stirred tank. Using this feature is equivalent to solving for the stationary Navier-Stokes equations where centrifugal and Coriolis forces have been added to the rotating domains. This approach is a reasonable model of time-averaged flow when the rotor-stator interactions are relatively weak and requires much less computational resources than transient modeling techniques.

#### **4.6 Conclusions**

In this Chapter, the numerical methods used in this thesis to simulate the flow generated by the fractal impeller in a stirred tank have been discussed in details. Governing equations of different turbulence models and their approximations and shortcomings have also been discussed. Along with the different turbulence models, different simulating approaches have been discussed. The sliding mesh approach and frozen rotor approach both have been adopted in the thesis to come up with better CFD strategies. The results based on numerical studies are discussed in Chapter 5.

---

## References

- Anderson JD, Wendt J., 1995, Computational fluid dynamics. New York: McGraw-Hill.
- Aubin, J., Fletcher, D.F., Xuereb, C., 2004. Modeling turbulent flow in stirred tanks with CFD: the influence of the modeling approach, turbulence model and numerical scheme. *Experimental Thermal and Fluid Science* 28, 431-445.
- Bird, R.B., 2002. Transport phenomena. *Applied Mechanics Reviews* 55, R1-R4.
- Boussinesq, J., 1877. *Essai sur la théorie des eaux courantes*. Imprimerie nationale.
- Buwa, V., Dewan, A., Nassar, A., Durst, F., 2006. Fluid dynamics and mixing of single-phase flow in a stirred vessel with a grid disc impeller: experimental and numerical investigations. *Chemical Engineering Science* 61, 2815-2822.
- Chapra, S.C., Canale, R.P., 1988. *Numerical methods for engineers*. McGraw-Hill New York.
- Deglon, D., Meyer, C., 2006. CFD modelling of stirred tanks: Numerical considerations. *Minerals Engineering* 19, 1059-1068.
- Ferziger JH, Peric M., 2012 *Computational methods for fluid dynamics*. Springer Science & Business Media..
- Ge, C.-Y., Wang, J.-J., Gu, X.-P., Feng, L.-F., 2014. CFD simulation and PIV measurement of the flow field generated by modified pitched blade turbine impellers. *Chemical Engineering Research and Design* 92, 1027-1036.
- Hartmann, H., Derksen, J.J., Montavon, C., Pearson, J., Hamill, I.S., van den Akker, H.E.A., 2004. Assessment of large eddy and RANS stirred tank simulations by means of LDA. *Chemical Engineering Science* 59, 2419-2432.
- Jenne, M., Reuss, M., 1999. A critical assessment on the use of  $k-\epsilon$  turbulence models for simulation of the turbulent liquid flow induced by a Rushton-turbine in baffled stirred-tank reactors. *Chemical Engineering Science* 54, 3921-3941.
- Jones, R.M., Harvey, A.D., Acharya, S., 2001. Two-equation turbulence modeling for impeller stirred tanks. *Journal of fluids engineering* 123, 640-648.
- Joshi, J.B., Nere, N.K., Rane, C.V., Murthy, B.N., Mathpati, C.S., Patwardhan, A.W., Ranade, V.V., 2011a. CFD simulation of stirred tanks: Comparison of turbulence models (Part II: Axial flow impellers, multiple impellers and multiphase Dispersions). *Canadian Journal of Chemical Engineering* 89, 754-816.

Joshi, J.B., Nere, N.K., Rane, C.V., Murthy, B.N., Mathpati, C.S., Patwardhan, A.W., Ranade, V.V., 2011b. CFD simulation of stirred tanks: Comparison of turbulence models. Part I: Radial flow impellers. *Canadian Journal of Chemical Engineering* 89, 23-82.

Khopkar, A.R., Mavros, P., Ranade, V.V., Bertrand, J., 2004. Simulation of flow generated by an axial-flow impeller: Batch and continuous operation. *Chemical Engineering Research and Design* 82, 737-751.

Li, Z., Bao, Y., Gao, Z., 2011. PIV experiments and large eddy simulations of single-loop flow fields in Rushton turbine stirred tanks. *Chemical Engineering Science* 66, 1219-1231.

Montante, G., Lee, K., Brucato, A., Yianneskis, M., 2001. Experiments and predictions of the transition of the flow pattern with impeller clearance in stirred tanks. *Computers & Chemical Engineering* 25, 729-735.

Moukalled, F., Mangani, L., Darwish, M., 2016. The finite volume method in computational fluid dynamics.

Murthy, B., Joshi, J., 2008. Assessment of standard  $k-\epsilon$ , RSM and LES turbulence models in a baffled stirred vessel agitated by various impeller designs. *Chemical Engineering Science* 63, 5468-5495.

Ri, P.-C., Ren, N.-Q., Ding, J., Kim, J.-S., Guo, W.-Q., CFD optimization of horizontal continuous stirred-tank (HCSTR) reactor for bio-hydrogen production. *International Journal of Hydrogen Energy*.

Sbrizzai, F., Lavezzo, V., Verzicco, R., Campolo, M., Soldati, A., 2006. Direct numerical simulation of turbulent particle dispersion in an unbaffled stirred-tank reactor. *Chemical Engineering Science* 61, 2843-2851.

Wilcox, D.C., 2008. Formulation of the  $k-x$  turbulence model revisited. *AIAA J* 46, 2823-2838.

Yeoh, S., Papadakis, G., Yianneskis, M., 2004. Numerical simulation of turbulent flow characteristics in a stirred vessel using the LES and RANS approaches with the sliding/deforming mesh methodology. *Chemical Engineering Research and Design* 82, 834-848.

## **Chapter 5**

### **Analysis of Flow pattern: Experiments and CFD simulations**

## 5.1 Introduction

Over last few decades the development of our understanding of mixing in a stirred tank reactor comprising of one or more number of impellers has led to certain standard protocols in terms of geometric ratios, impeller positioning and impeller numbers for achieving specific performance in terms of power consumption, mixing, heat transfer and mass transfer (Paul et al., 2004). These protocols are highly influenced by flow patterns and turbulence generated by an impeller in the stirred tank (Joshi et al., 1982; Khopkar et al., 2004; Kumaresan and Joshi, 2006; Machado et al.; Patwardhan et al., 2003; Paul et al., 2004). In the literature extensive information is available on the flow generated by various types of impellers (Aiba, 1958; Aubin et al., 2001; Kresta and Wood, 1993a; Ranade and Joshi, 1989; Wu and Patterson, 1989). In a given stirred tank a combination of different types of impellers can be used to generate the desired flow pattern (Kresta and Wood, 1993b; Kumaresan and Joshi, 2006; Kumaresan et al., 2005; Montante et al., 2001; Ranade and Joshi, 1989). Recent advancements in terms of giving a fractal shape to the blades (Steiros et al., 2016), or using impellers with large perforated blades (Trivellato, 2011) or geometrical modification of pitched blade turbines for improving mixing Ge et al. (2014) show that change in the impeller design or blade design can alter the flow field and hence the mixing efficiency.

In view of this, in this chapter, the detailed flow patterns analysis in a stirred tank with FI by experimentation and numerical modeling has been done. Moreover, the finer aspects of flow near the impeller zone have been explored using CFD simulations.

## 5.2 Experimental Set-up

Experiments were carried out in an acrylic flat bottom cylindrical tank ( $T=H=0.3\text{m}$ ) having four baffles ( $W=T/10$ ) with FI of a diameter ( $D_{FI}$ ) of 0.19 m ( $D_{FI}/T=0.63$ ). The schematic of the experimental setup is shown in Figure 5.1. The impeller shaft was connected to a DC motor via a shaft-mounted torque transducer (CTimeSync Ltd., UK). FI was supported from the bottom with a steel ball of 6 mm diameter. Tap water was used as a working fluid ( $\rho = 998 \text{ kg/m}^3$ ). UVP measurements were carried out as described in Chapter 3 in midplane between two baffles for three different rps ( $N$ , 1/s) i.e. 1, 1.5 and 2.5 which corresponds to  $Re = 36100$ , 54150 and 90250 respectively.  $Re$  was calculated using the maximum diameter  $D_{FI}$ , of the FI.

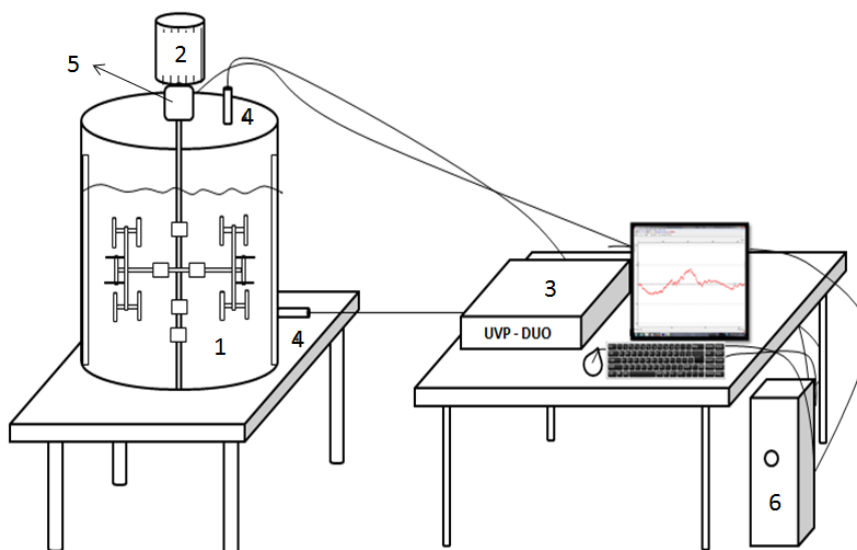


Figure 5.1A: Schematic of experimental setup (1) Stirred tank, (2) electric motor, (3) UVP-Duo data acquisition system, (4) UVP probes, (5) digital torque sensor, (6) computer

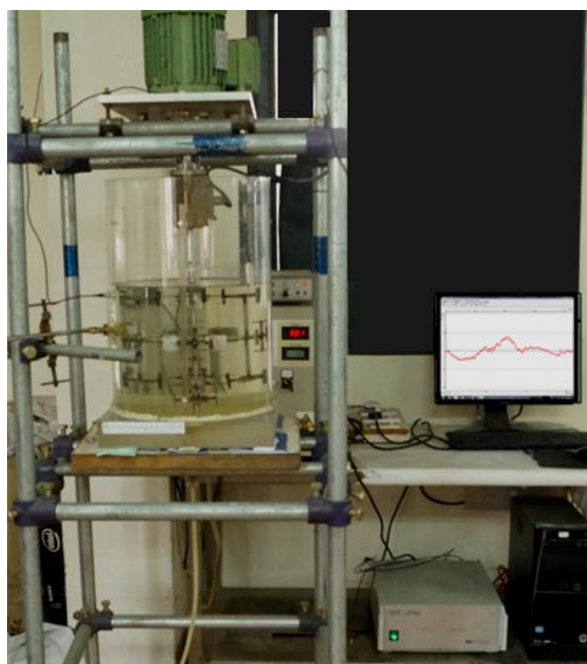


Figure 5.1B: Photograph of Experimental Set-up

### 5.3 Numerical Simulations

The tank geometry considered for the CFD simulations is the same as that used for experimental work. In this work, we have simulated the flow pattern in a stirred tank with FI and compared the outcome from different simulation strategies with experimental data. These simulation strategies are discussed subsequently.

#### 5.3.1 Stirred tank geometry and grid generation

In the present work, two different geometries have been used to predict the flow in the stirred tank. In the first case, two zones were created (stationary and rotary) and the inner and outer zones were separated in order to enable the use of sliding mesh technique. In the second case, four zones (i.e. one stationary and three rotary) were created so as to capture the turbulent flow more precisely near the blades. In order to make three rotating zones, connecting rods between branches were removed from the geometry (see Figure 5.2B). Aubin et al. (2004) have reported the effect of modeling approaches (i.e. Multiple Reference Frame and Sliding Mesh) on flow pattern in a stirred tank, where authors found slight effects on the mean velocity profiles for up-pumping and down-pumping axial flow impellers in impeller discharge region. In the present case, since most of the vessel is occupied by fractal impeller it becomes necessary to study the effect of both the approaches. Therefore, for both the geometries, Multiple Reference Frame (MRF) and Sliding Mesh (SM) techniques have been adopted. Details of the element number are given in the next sub-section. All the results were compared with experimental data for the validation of different approaches. COMSOL Multiphysics<sup>®</sup> was used to create a grid as shown in Figure 5.2.

#### 5.3.2 Modeling approach and description

As mentioned in the earlier chapter, CFD simulations carried out using COMSOL Multiphysics<sup>®</sup> use finite element methods for solving the continuity equation, Navier-Stokes equations, and the equations for turbulence in the flow (discussed in Chapter 4). In this application, the blades of the impeller and baffles are modeled as a wall with zero thickness. The standard wall function is imposed to specify the wall boundary condition and water was chosen as the operating fluid. The free surface is modeled with zero-flux and zero stress condition.



Figure 5.2 shows the grid structure for the tank as well as for impeller for two different approaches.

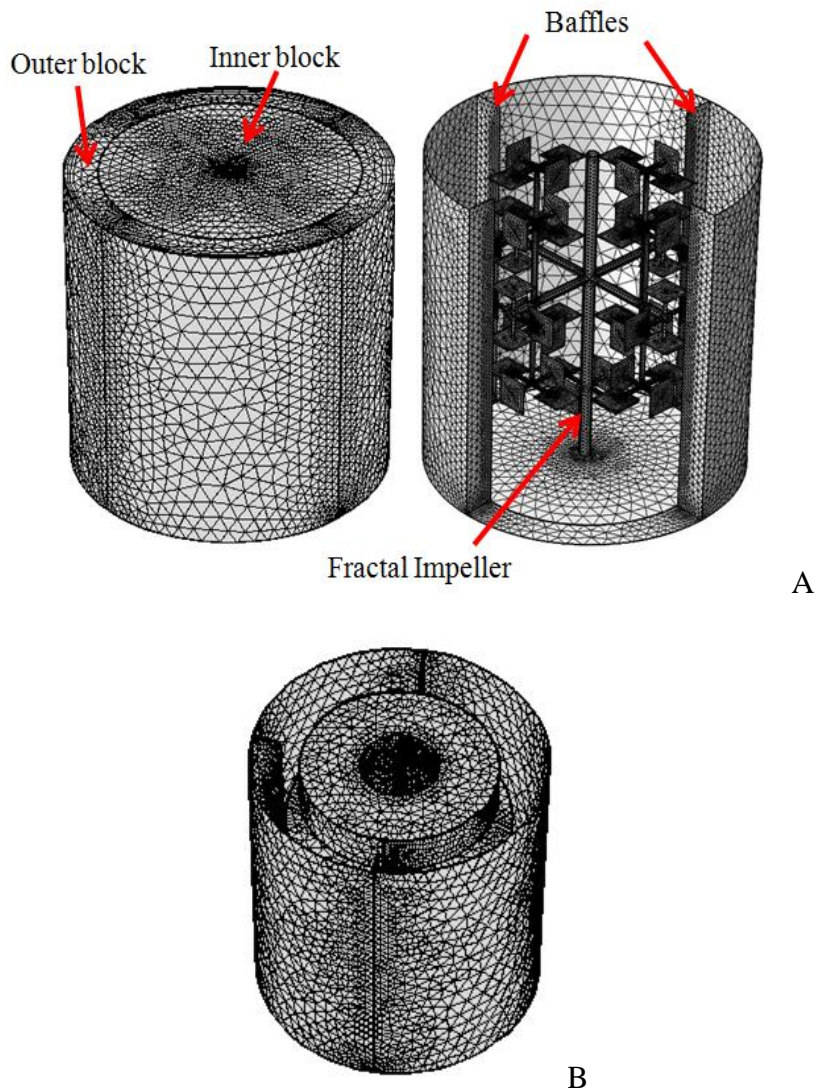
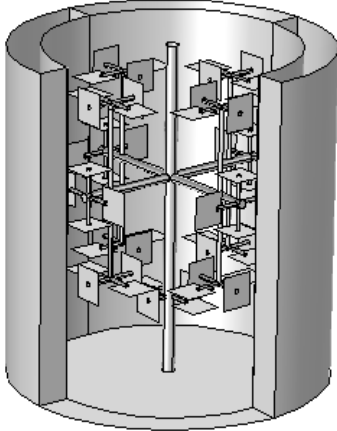
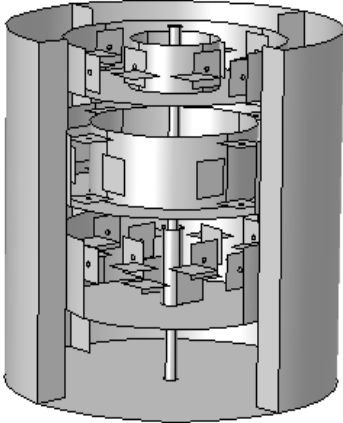


Figure 5.2: Grid for the fractal impeller and for the flow domain in a stirred tank A) Geometry 1 (1 rotating zone and one stationary zone), B) Geometry 2 (3 rotating zones and 1 stationary zone).

As mentioned before, since the blades of an FI are spread throughout the stirred tank the farthest distance between two blades is considered as impeller diameter. This implies that the  $Re$  calculated based on this diameter is high even at low impeller rotation speed ( $N$ , rps). However, considering voids at different levels in the stirred tank, the flow can still remain laminar.

Therefore, the laminar model found to be the best choice to initialize the simulation studies. However since the laminar viscosity model does not solve for the turbulence in the stirred tank, therefore, some of the RANS models were also used to for the simulations. Different variations of the RANS models available in COMSOL® were used in the present study as to come up with certain guidelines about the CFD simulations of Fractal Impeller. Table 5.1, gives the detail information about the CFD simulation strategies. Velocity profiles from all these simulations were compared with that of experimental measurements at  $N = 1$  rps (i.e. 60 rpm). Results are discussed subsequently.

Table 5.1: CFD simulation strategies used for simulations of the stirred tank with Fractal Impeller

Stirred Tank Geometry	Simulation Approach	Models used
	Multiple Reference Frame (MRF)	<i>Laminar, <math>k-\varepsilon</math>, <math>k-\omega</math>, and Shear Stress Transport (SST)</i>
	Sliding Mesh (SM)	<i>Laminar, and <math>k-\varepsilon</math></i>
	Multiple Reference Frame (MRF)	<i>Laminar, <math>k-\varepsilon</math>, <math>k-\omega</math>, and Shear Stress Transport (SST)</i>

### 5.3.3 Convergence criteria, grid independence study, and grid details

In order to set the convergence criteria, simulations for each time interval were performed until the residuals of the mean velocity and turbulent quantities are less than  $10^{-5}$ . For sliding mesh simulations, initially, each simulation was carried out for 10 revolutions to achieve converged solutions. The detailed transient analysis showed that the results do not change after 5-6 revolutions. In order to reduce the computation time, grid independent study for three mesh sizes (element numbers are given in the bracket), i) coarse mesh (0.57 M), normal grid (2 M) and fine grid (6.7 M) were carried out.

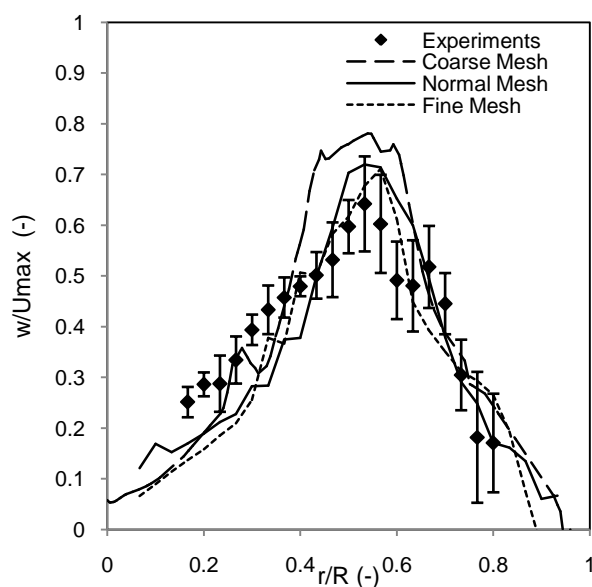


Figure 5.3: Effect of grid size on tangential mean velocity ( $w$ ) in the stirred tank with FI for geometry 1.

From Figure 5.3 it is evident that fine mesh and normal mesh are predicting approximate similar results and are comparable with that of experimental. However, the coarse mesh was found to tend to over-predict the results. Therefore, in a view of keeping the computational time in the mind normal mesh found to be the best option for further simulations. Details on the specifications of the elements and grid can be found in Table 5.2. Separate grid independent study was also carried out for geometry 2 as well.

Table 5.2: Details of the element type in the grid structure

Element type	Coarse grid	Normal grid	Fine grid
	Number of elements	Number of elements	Number of elements
Tetrahedral	415359	1796422	6400248
Pyramid	7830	26944	30436
Prism	30090	149544	324880
Number of boundary layer	2	5	6
Total	453279	1972910	6755564

### 5.3.4 Comparison of CFD models

The CFD simulation carried out using various simulation strategies were compared with the experimental results for  $N = 1$  rps. Velocity profiles obtained from UVP measurements at different locations of the stirred tank are ensemble averaged profiles; therefore, for the comparison with CFD data, the velocity profiles from sliding mesh simulation are also considered as ensemble averaged. Figure 5.4 shows the comparison of radial, axial and tangential velocities at different locations in the stirred tank. From the Figures, it can be observed that the MRF approach using different models over-predicts the radial component and underpredicts the tangential flow due to impeller baffle interaction. The distance between the impeller blades and baffles is less in the present case (when compared to the conventional impellers) and therefore, sliding mesh technique found the best choice for the simulations. Among all the geometrical approaches and models used to predict the flow, Laminar viscosity model and the  $k-\varepsilon$  model with sliding mesh technique showed a better comparison with the experimentally measured velocity profiles in most of the part of the stirred tank, except in the middle part. This deviation in the middle part can be attributed to the slight geometrical differences in the impeller geometry (actual and simulated). Moreover, in the experimental section, the bin size in UVP measurements can also lead to some errors. At the BI2 branch location ( $z/R=1.233$ ), model under-predicts or over-predicts the tangential, radial or axial mean profiles. Careful observation of the design of fractal impeller suggests that this region is occupied by connecting sections which probably does not allow the measurement correctly,

which can also be justified by the RMS profiles in this region. Figure 5.12A suggests the region where the deviation from mean velocity is higher. Since the fractal impeller has a larger diameter, tangential mean velocities are expected to be larger (Figure 5.4C), which was also evident from the experimentally measured tangential velocity data in the stirred tank. The maximum tangential velocity is close to the region having vertical blades parallel to the tank wall and it decreases sharply beyond the vicinity of these blades. Therefore, prediction of the tangential component becomes important in deciding the simulation approaches. A careful observation suggests that laminar model gives better predictions of tangential velocity profiles than that of  $k-\varepsilon$ . Moreover, it also captures the trends of all the velocity profiles in all the part of the vessel. Axial velocities predicted by CFD simulations were found higher in the near shaft region (see Figure 5.4B). This can be attributed to the vortex formation near the shaft, which does not allow UPV probe to measure local velocities precisely and accurately near the shaft region that forms a vortex. This can be justified by axial RMS profiles near the shaft (see Figure 5.12). The mean flow generated by the fractal impeller in a stirred tank is discussed subsequently. Based on these observations, simulation with both *Laminar* and  $k-\varepsilon$  were carried out.  $k-\varepsilon$  model, however, found to under-predict the turbulent kinetic energy for the present system, which can be attributed to the small scale turbulent eddies generated at a different section of the tank due to rotation of the fractal impeller.

It should be noted that, based on the results, comparison of CFD results with that of experimental is limited to mean profiles and that too at low rps (1 rps). Different viscosity models (laminar and turbulent) are considered for simulations only to bring out the extent of variation in predictions. The simulations for 1.5 rps and 2.5 rps were not carried out. The small-scale turbulent eddies in the stirred tank with FI can be resolved using DNS and relevant work is in progress and not presented here.

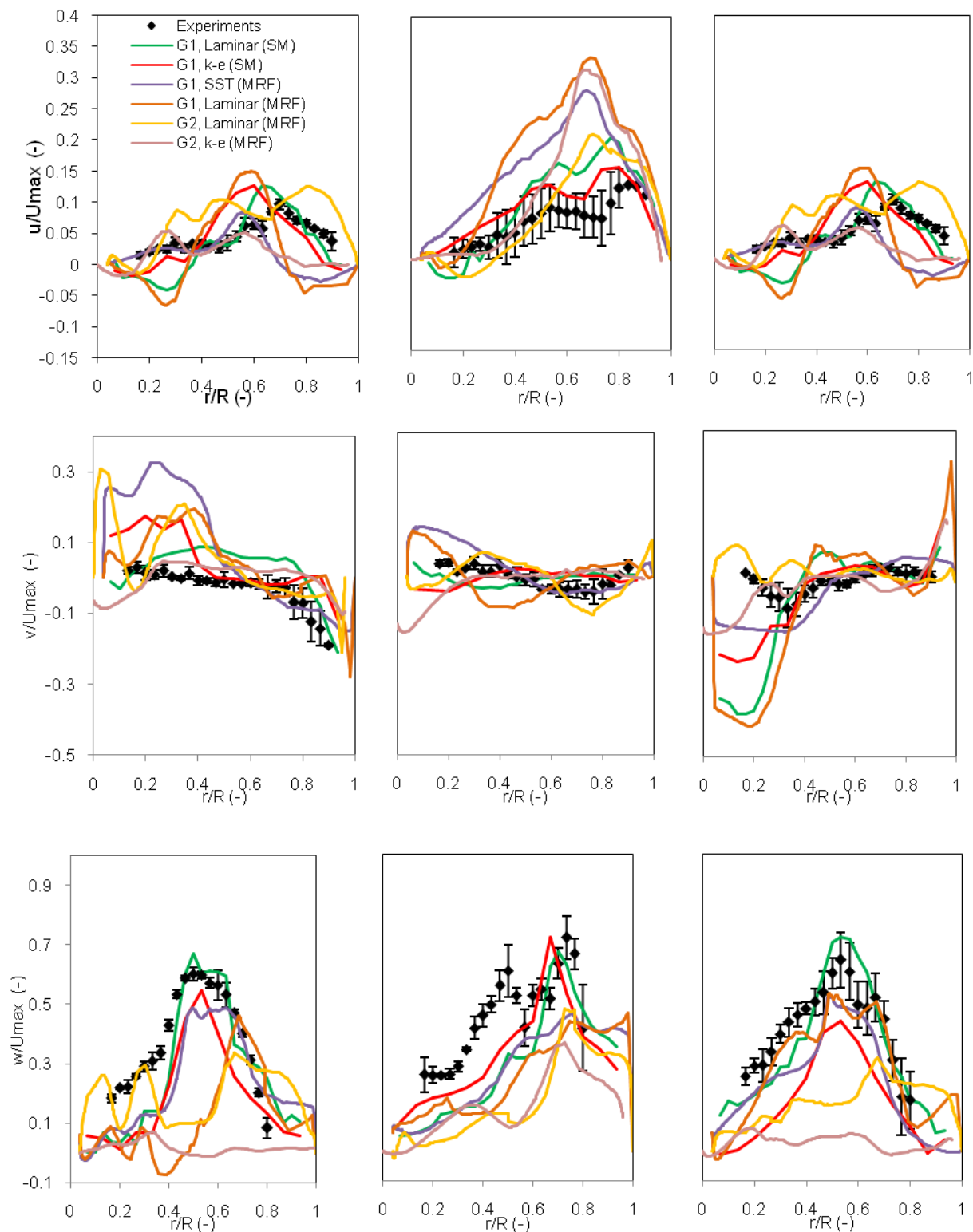


Figure 5.4: (Top row) Radial mean velocity component (Middle row) Axial mean velocity component, (Bottom row) Tangential mean velocity component for experimental and CFD models at 1 rps.

## 5.4 Results and Discussions

### 5.4.1 Mean Velocity Profiles and Flow Patterns

From the comparison of the normalized mean velocities, it was evident that the normalized velocity profiles (i.e. the flow pattern) at different  $N$  (rps) is identical. Figure 5.5A shows a gradual change in the radial velocities along the axial direction confirming the existence of two primary circulation loops. The perpendicular blades of the  $B_{12}$  branch discharge the fluid radially outward and the analysis of discharge flow rate ( $Q_{FI}$ ) is given in a separate section. The fluid discharged near the tank wall gets redirected in the upward and downward direction in the form of axial velocity (see Figure 5.5B).

Among all the velocity components, the tangential component is significantly predominant (almost by a factor of 6) when compared with the radial and axial velocity components. In order to further understand the relative variation in the tangential velocity component in the blade regions, it was normalized by local tip velocity of the blades ( $2\pi lN$ , where  $l$  is the distance of the blade from the centre). The contribution of the tangential velocity component in the flow generated by FI in the stirred tank almost 60 to 80% of the local tip velocity in the region of blades and can be attributed entirely to the movement of vertical blades that throws the fluid in its vicinity in the outward direction by centrifugal force. The design of FI does not allow recirculation region to be formed behind the blades, which helps in reducing the form drag and the energy consumption. Since the blades only chop the fluid layers, such design would yield streamlines that would follow the flow separation over the blades.

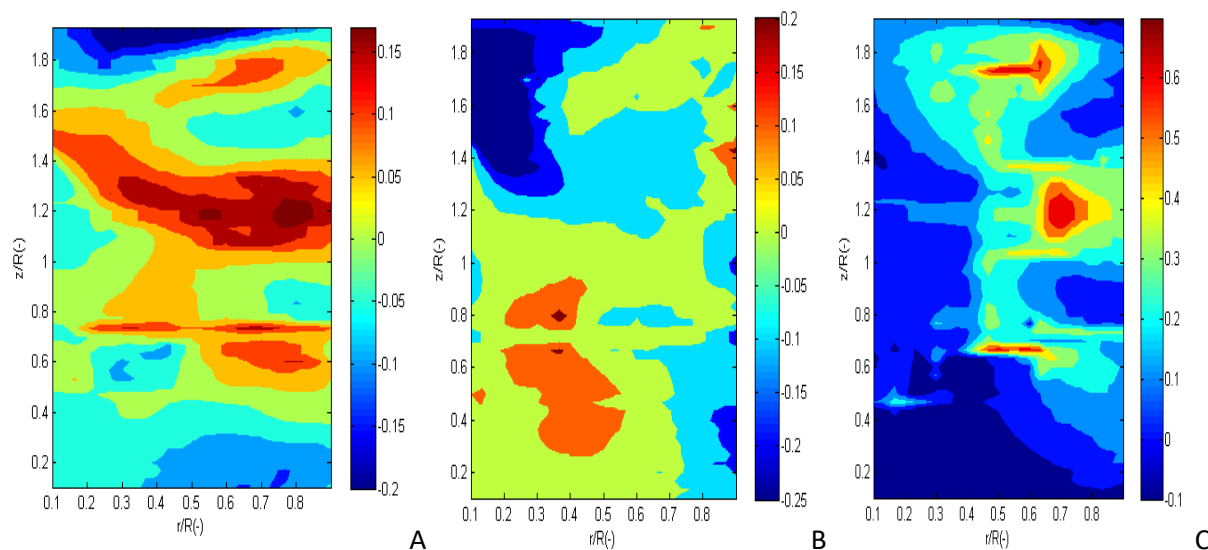


Figure 5.5: Contour plots of normalized mean velocity components in  $r$ - $z$  plane (CFD,  $N = 1$ ), (A) radial ( $u/U_{Max}$ ), (B) axial ( $v/U_{Max}$ ), and (C) tangential mean velocity ( $w/U_{Max}$ ). Color scales show the maximum and minimum normalized velocity for each component.

The velocity profiles at the level of  $B_{I2}$  branch (i.e at  $z/R=1.233$ ) showed much higher radial and tangential velocity components in the horizontal plane. These are the only blades which were found to be strongly pushing the fluid towards vessel wall. The discharge flow rate was estimated for three different impeller rotation speeds ( $N$ ) and the pumping capacity of the FI is explained in the subsequent section (5.4.2). From Figure 5.6, it can be distinctly observed that near the tank wall the radial discharge due to movement of vertical blades of  $B_{I2}$  gets divided into two vertically opposite streams. Similarly, the vertical blades of  $B_{II}$  and  $B_{I3}$  branches also help in generating and maintaining such flows near the vessel wall. Once the down-flowing jet along the wall encounters the vessel bottom, the fluid moves along the bottom and re-enters the circulation loop close to tank axis.



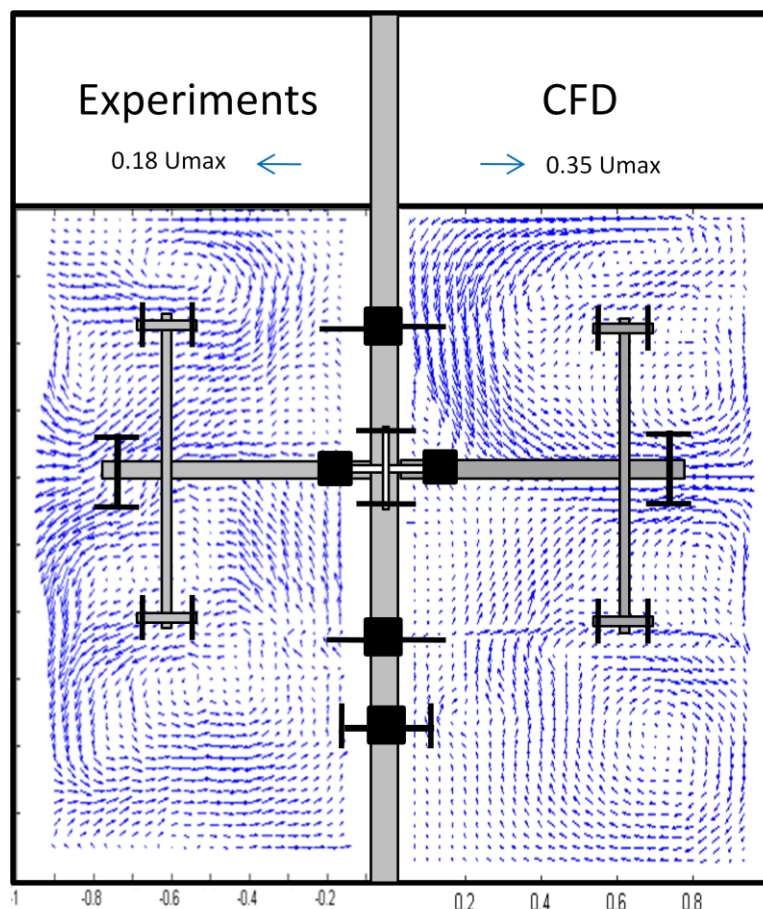


Figure 5.6: Mean velocity in an  $r$ - $z$  plane between two baffles. Vector plot of left half plane estimated experimentally and vector plot of right half plane estimated by CFD simulations.

Similarly, up-flowing jet along the wall encounters the free surface, loses significant energy and then gets pooled towards the impeller axis. This generates and strengthens a low-pressure zone near the shaft, where the fluid coming from the bottom and the top surface is drawn in the axial region and redirected again. This sets a two-loop circulation in the tank. The strength of this circulation was seen to increase with increasing impeller rotation speed. This continuous transport of fluid leads to the formation of two primary and two secondary circulation loops (can be observed in Figure 5.6). The primary circulation loops, one each is located at the top and at the bottom of the tank, while the secondary loops were found in between the three sub-branches ( $B_{11}$ ,  $B_{12}$ , and  $B_{13}$ ). The movement of horizontal blades and additional sub-branch at the bottom ( $B_s$ ) helps in generating and maintaining the upward and downward flow in various planes, while the vertical blades prominently generate the radial and the tangential flow. Overall

flow patterns in an  $r$ - $z$  plane for  $N = 1$  is shown in Figure 5.6. The axial velocities in the upper left part of the plain found to be higher from the CFD predictions than that of experimental. This can be due to vortex formation near the shaft region, which does not allow the accurate measurement of velocity profiles.

#### 5.4.2 Impeller Pumping Capacity

The vertical blades of  $B_{I1}$ ,  $B_{I2}$  and  $B_{I3}$  branch discharge the fluid towards the vessel wall with certain flow rate proportional to the impeller rotation speed (see Figure 5.7). In the case of an FI, pumping is radially outward and can be estimated by Eq. (5.1) for each branch,

$$Q_{B_{I1}} = \int_{z1^-}^{z1^+} \pi D_{FI} |u_{r=r^+}| dz \quad 5.1a$$

$$Q_{B_{I2}} = \int_{z2^-}^{z2^+} \pi D_{FI} |u_{r=r^+}| dz \quad 5.1b$$

$$Q_{B_{I3}} = \int_{z3^-}^{z3^+} \pi D_{FI} |u_{r=r^+}| dz \quad 5.1c$$

$$Q_{FI} = Q_{B_{I1}} + Q_{B_{I2}} + Q_{B_{I3}} \quad 5.1d$$

where,  $z^-$ ,  $z^+$  and  $r^+$  are the boundaries of the control volume. This expression considers radial pumping flow rates and can be directly used for the calculation of discharge flow rate of the FI. The control volume for FI was selected on the basis of flow patterns and Figure 5.7. It should be noted that, predicted profiles have higher magnitude in discharge region than that of experimental. Therefore, the predicted flow rate is expected to be higher. The boundaries of the control volume for  $B_{I1}$  is  $z1^- = 0.095$  m ( $z/R=0.633$ ),  $z1^+ = 0.125$ m ( $z/R=0.833$ ),  $r^+ = 0.095$ m ( $r/R=0.67$ ) for  $B_{I2}$  is  $z2^- = 0.15$ m ( $z/R=1$ ),  $z2^+ = 0.21$ m ( $z/R=1.4$ ),  $r^+ = 0.095$ m ( $r/R=0.67$ ) and for  $B_{I3}$  is  $z3^- = 0.245$ m ( $z/R=1.633$ ),  $z3^+ = 0.275$ m ( $z/R=1.833$ ), and  $r^+ = 0.095$ m ( $r/R=0.67$ ).

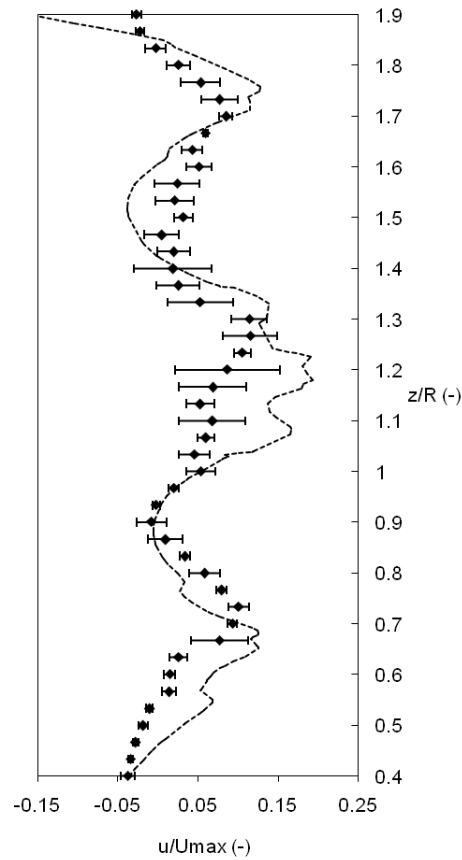


Figure 5.7: Radial mean velocity profile along the z-axis at  $r/R = 0.677 (D_{FI}/2)$   $\diamond$ -Experiments, -- - CFD

Table 5.3: Discharge flow rate (pumping capacity) of the fractal impeller

RPS ( $N, 1/s$ )	Discharge flow rate ( $Q_{FI}$ ), $m^3/s$						Flow Number ( $Fl = Q_{FI}/ND^3$ )	
	Experiments			CFD			Experiments	CFD
	$Q_{BI1}$	$Q_{BI2}$	$Q_{BI3}$	$Q_{BI1}$	$Q_{BI2}$	$Q_{BI3}$	$Q_{FI}/ND^3$	
1 (60 r.p.m.)	0.0006	0.0017	0.0006	0.0008	0.0025	0.0009	0.419	0.61
1.5 (90 r.p.m.)	0.00072	0.0028	0.00073	-	-	-	0.414	-
2.5 (150 r.p.m.)	0.0018	0.0034	0.0019	-	-	-	0.414	-

The measured and simulated discharge flow rates induced due to the movement of vertical blades of the  $B_{12}$  branch are given in Table 5.3. It is quite intuitive that with the increase of  $N$  discharge flow rate increases and hence the circulation velocities in the tank also increase. However, the flow number remains constant. Almost identical flow rates from CFD simulation at different rps reflects the identical velocity profiles. With the details analysis of flow it can be concluded that, with the flow patterns supporting the dispersion due to circulation loops, this impeller can be used for gas-liquid operations. Similar studies are in progress and will be reported separately.

### 5.4.3 Transient flow in the stirred tank

The flow generated in the tank has an unsteady nature depending upon the location of the impeller branches from the observation plane. The flow at the  $r$ - $z$  mid-plane between two baffles was analyzed at different time instants, which gives the nature of the transient flow generated by the FI. It should be noted that in Figure 5.8, the impeller branch is moving and flow field is captured on the  $r$ - $z$  mid-plane between two baffles. The transient variation in the radial velocity in the tank at different times is shown in Figure 5.9. Negative radial velocities in the lower and upper part of the vessel confirm the existence of the two primary circulation loops in the stirred tank. Similar features were observed even for the instantaneous axial velocities (see Figure 5.10).

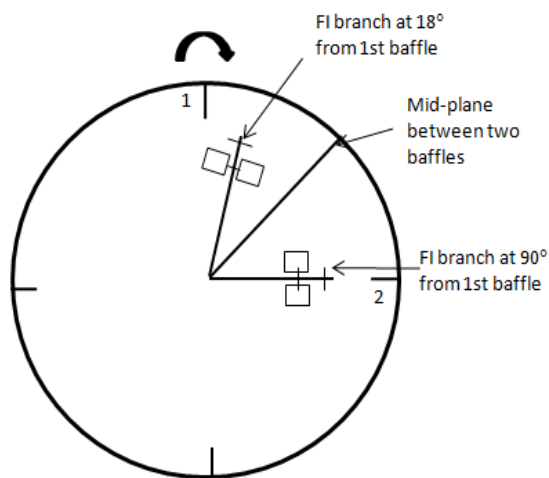


Figure 5.8: Schematic of fractal impeller rotation in the stirred tank.

Moreover, the extent of variation in the axial velocities is minimal and therefore strengthens the circulation loops. The tangential velocities in the stirred tank were seen to have the maximum effect of the movement of the blades, mainly because of the strong discharge of fluid from the vertical branches of the impeller.

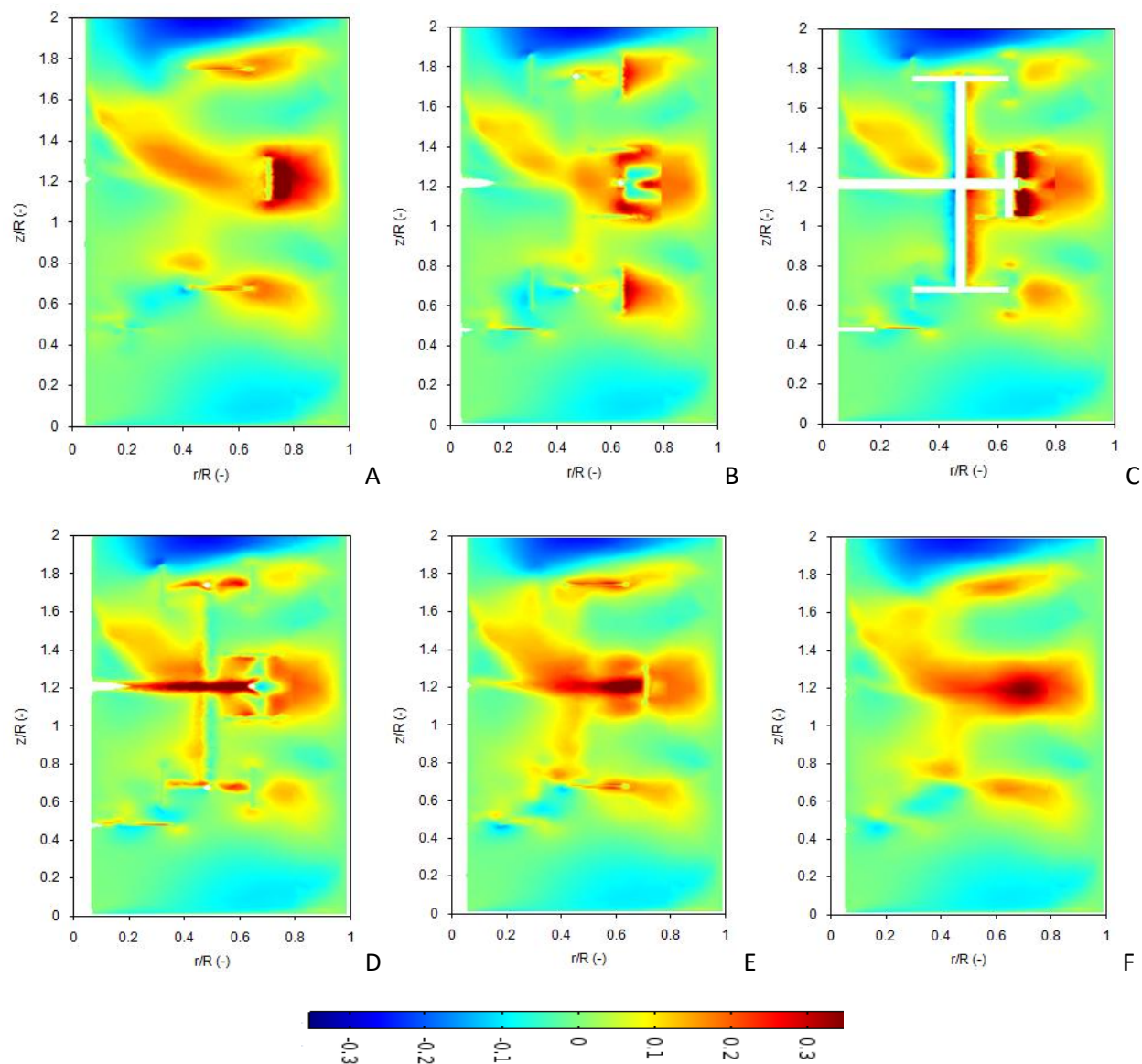


Figure 5.9: Radial instantaneous velocity at r-z mid-plane between two baffles with respect to the position of the branch. A)  $\alpha=18^\circ$ , B)  $\alpha=36^\circ$ , C)  $\alpha=45^\circ$ , D)  $\alpha=54^\circ$ , E)  $\alpha=72^\circ$ , F)  $\alpha=90^\circ$ .

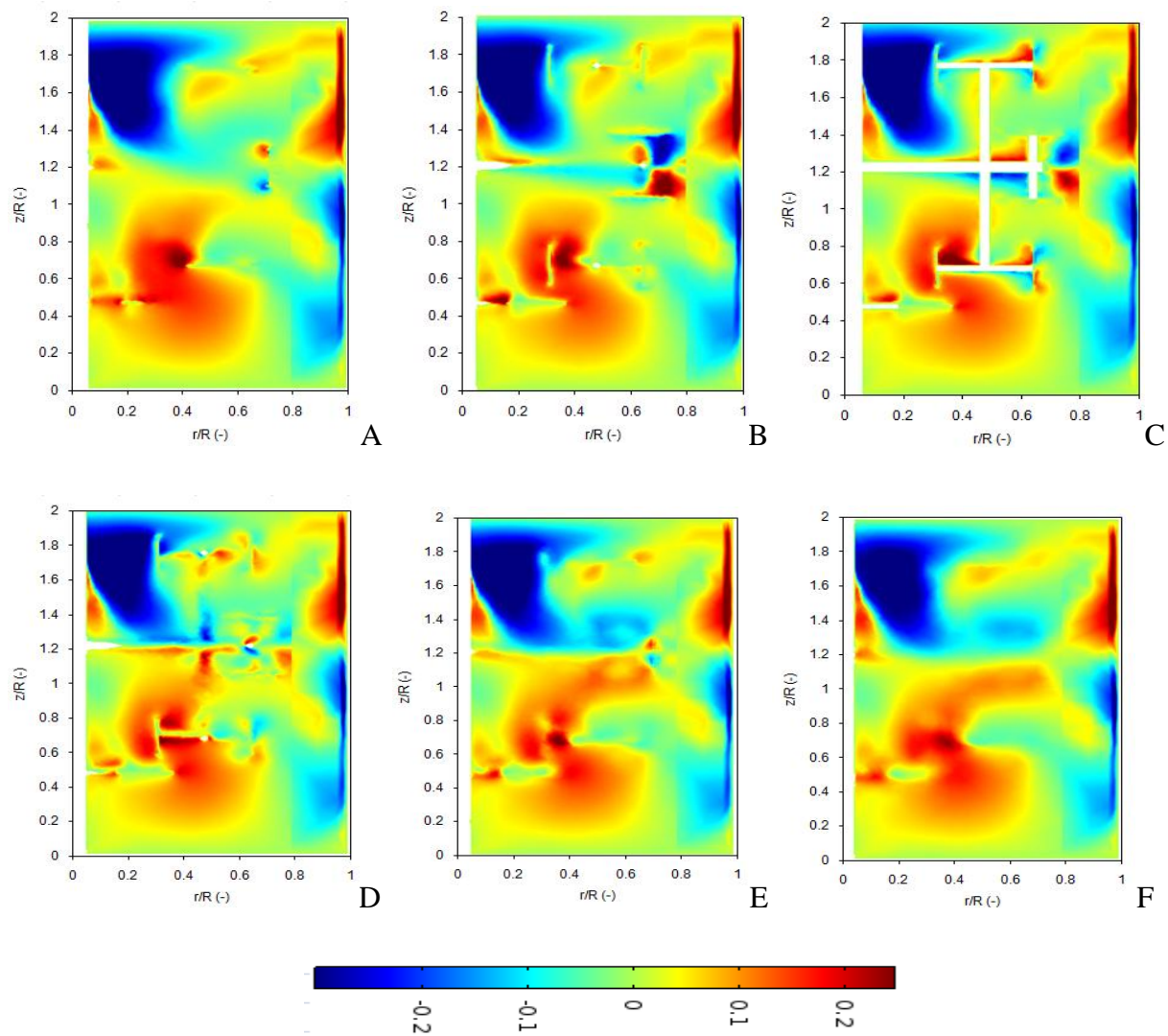


Figure 5.10: Axial instantaneous velocity at r-z mid-plane between two baffles with respect to the position of the impeller branch. A)  $\alpha=18^\circ$ , B)  $\alpha=36^\circ$ , C)  $\alpha=45^\circ$ , D)  $\alpha=54^\circ$ , E)  $\alpha=72^\circ$ , F)  $\alpha=90^\circ$ .

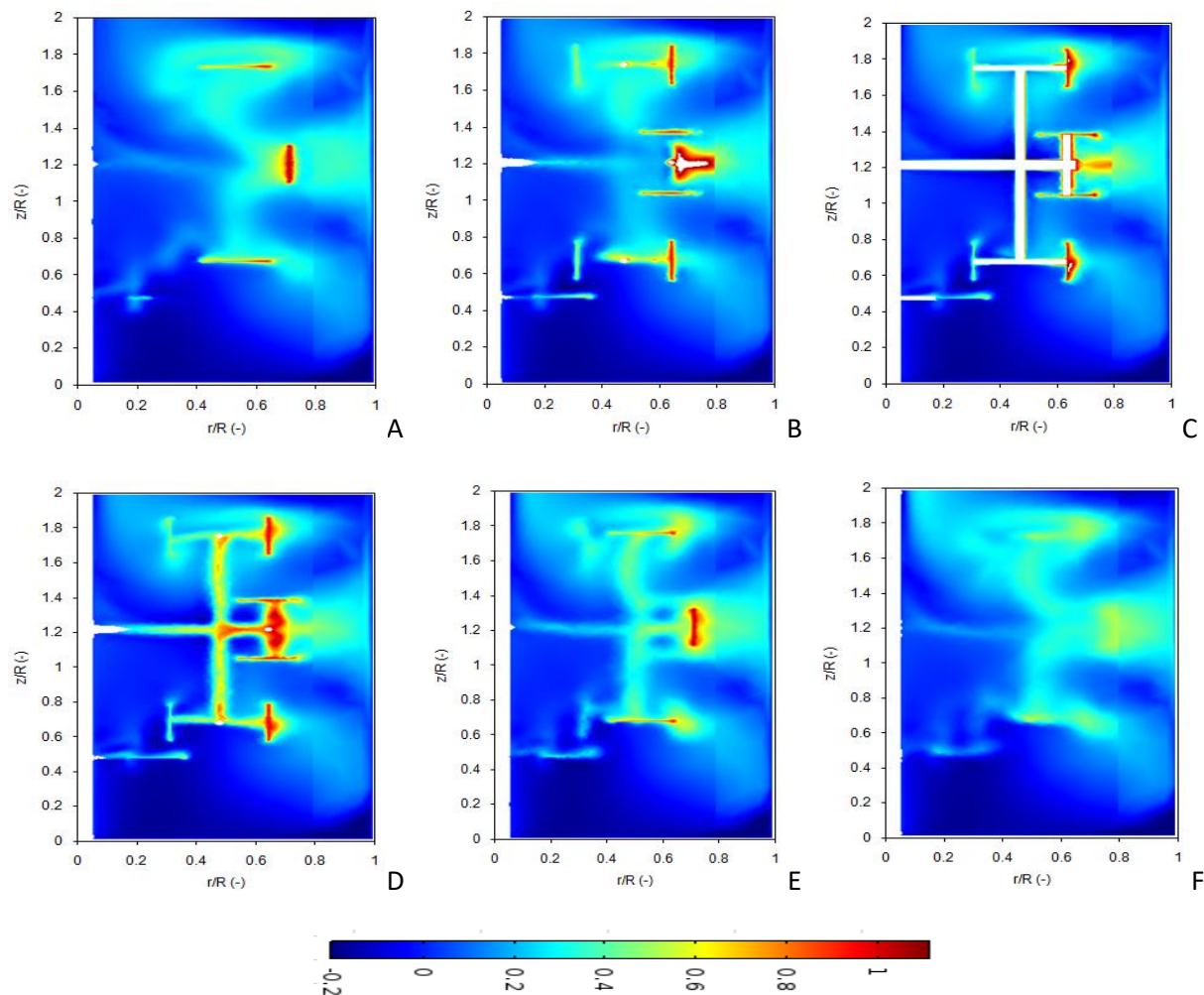


Figure 5.11: Tangential instantaneous velocity at r-z mid-plane between two baffles with respect to the position of the branch. A)  $\alpha=18^\circ$ , B)  $\alpha=36^\circ$ , C)  $\alpha=45^\circ$ , D)  $\alpha=54^\circ$ , E)  $\alpha=72^\circ$ , F)  $\alpha=90^\circ$ .

#### 5.4.4 RMS Velocities and Turbulent Kinetic Energy (k)

Micro-mixing in the stirred tank gets significantly enhanced by turbulence (Paul et al., 2004). In order to understand the nature of turbulence in the stirred tank with FI, the spatial variation of root mean square (RMS) velocities and turbulent kinetic energy was monitored. The time series analysis of the spatiotemporal UVP velocity data was carried out to find out the existence of periodic frequencies to see if the trailing vortices behind the blades of FI exist. However, no such observations were found. RMS velocity data were used to calculate turbulent kinetic energy using Eq. (5.2). The simulated values of the turbulent kinetic energy based on  $k-\varepsilon$  model were seen to be always lower than the experimental data (not shown here). The turbulent

kinetic energy variation is monitored in terms of a dimensionless quantity (ratio of  $k$  to the square of maximum velocity ( $U_{Max}$ ) at the farthest tip of the impeller).

$$k = \left(\frac{1}{2}\right) (u_{RMS}^2 + v_{RMS}^2 + w_{RMS}^2) \quad 5.2$$

Figure 5.12A and Figure 5.12B show the contour maps of the RMS velocities at  $N = 2.5$  for radial and axial velocity component respectively. The radial RMS velocity component was considerably higher in the region occupied by FI. The RMS velocity profiles for all the three components were different, which indicated that the turbulence generated by the FI is non-homogeneous and non-isotropic. This finding is important in a view of selecting turbulent models for CFD predictions as most of the RANS models work on the principle of isotropic turbulence.

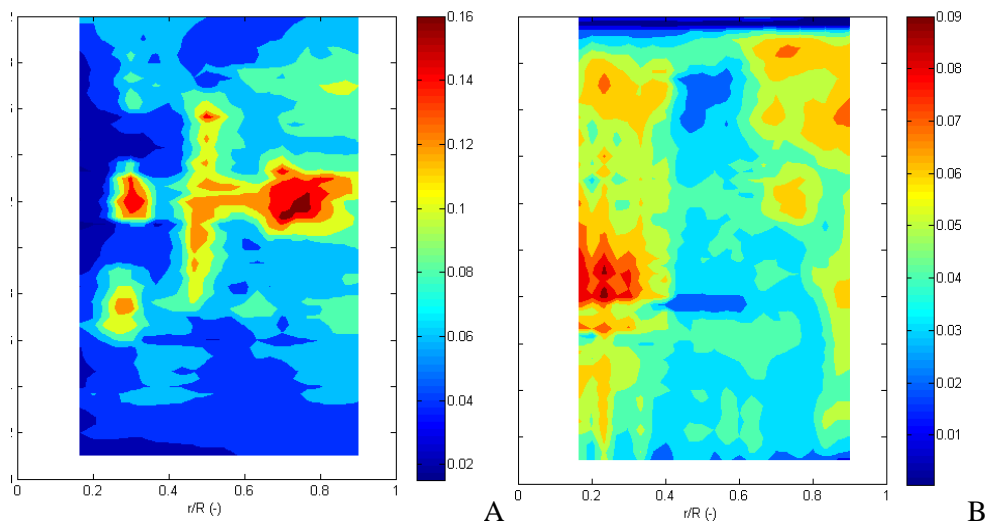


Figure 5.12: Contour plot of RMS velocities A) radial ( $u_{RMS}$ ) component b) axial ( $v_{RMS}$ ) component.

With the help of RMS velocity components, turbulent kinetic energy ( $k$ ) was calculated by using Eq. (5.2). The values of kinetic energy increase with increasing rps and the values were higher in the regions where the overall convective mean flow was stronger. Variation in turbulent kinetic energy for three different rps (normalized with the square of maximum tip speed) is almost identical. The normalized turbulent kinetic energy at different rps almost overlapped indicating that the amount of energy dissipated in the tank scales almost linearly with the impeller rotation speed. Since the FI covers larger volume in the stirred tank than any other conventional impellers, the distribution of  $k$  throughout the tank was better with an FI.



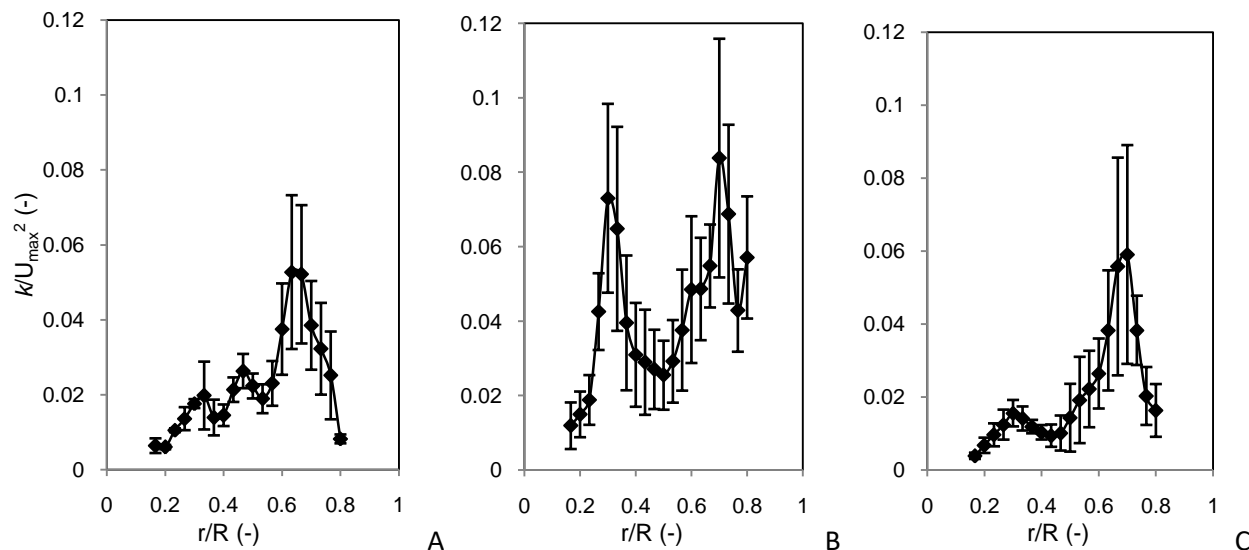


Figure 5.13: Radial profile of turbulent kinetic energy (experimental) for rps,  $N (\hat{\diamond}-1)$  over three axial planes. A)  $z/R=0.733$ , B)  $z/R=1.233$ , C)  $z/R=1.733$ .

## 5.5 Conclusions

The flow generated by Fractal impeller (FI) in the stirred tank was measured experimentally using Ultrasonic velocity profiler (UVP) for a range of impeller rotation speeds and compared with the flow pattern generated from CFD simulations. Various simulation strategies were adopted to come up with better comparison with that of experimental results. Among all, a laminar model with sliding mesh approach found to be the best choice for CFD simulation of stirred tank with the fractal impeller. All the three velocity components were mapped in the entire stirred tank. Mean flow obtained from CFD simulations found to be comparable with experimental, however, turbulent kinetic energy was under-predicted by various RANS models. The flow generated by the fractal impeller in a stirred tank was found to have a very large tangential velocity component. Several interacting mixing zones were observed in the  $r$ - $z$  plane, which gets generated from two primary and a few secondary circulation loops. Strong tangential flow is seen to enhance the interaction of different mixing zones thereby achieving better mixing characteristics. Large deviations in the RMS velocity components were found in the most of the region in the tank which suggests the non-isotropic nature of the turbulence. Based on the experimental evidence, the distribution of turbulent kinetic energy throughout the stirred tank was seen to be better than in the stirred tank with conventional impellers.

## References

- Aiba, S., 1958. Flow patterns of liquids in agitated vessels. *AIChE Journal* 4, 485-489.
- Aubin, J., Fletcher, D.F., Xuereb, C., 2004. Modeling turbulent flow in stirred tanks with CFD: the influence of the modeling approach, turbulence model and numerical scheme. *Experimental Thermal and Fluid Science* 28, 431-445.
- Aubin, J., Mavros, P., Fletcher, D.F., Bertrand, J., Xuereb, C., 2001. Effect of axial agitator configuration (Up-Pumping, Down-Pumping, Reverse Rotation) on flow patterns generated in stirred vessels. *Chemical Engineering Research and Design* 79, 845-856.
- Buwa, V., Dewan, A., Nassar, A., Durst, F., 2006. Fluid dynamics and mixing of single-phase flow in a stirred vessel with a grid disc impeller: experimental and numerical investigations. *Chemical Engineering Science* 61, 2815-2822.
- Ge, C.-Y., Wang, J.-J., Gu, X.-P., Feng, L.-F., 2014. CFD simulation and PIV measurement of the flow field generated by modified pitched blade turbine impellers. *Chemical Engineering Research and Design* 92, 1027-1036.
- Hartmann, H., Derksen, J.J., Montavon, C., Pearson, J., Hamill, I.S., van den Akker, H.E.A., 2004. Assessment of large eddy and RANS stirred tank simulations by means of LDA. *Chemical Engineering Science* 59, 2419-2432.
- Joshi, J.B., Nere, N.K., Rane, C.V., Murthy, B.N., Mathpati, C.S., Patwardhan, A.W., Ranade, V.V., 2011a. CFD simulation of stirred tanks: Comparison of turbulence models (Part II: Axial flow impellers, multiple impellers and multiphase dispersions). *Canadian Journal of Chemical Engineering* 89, 754-816.
- Joshi, J.B., Nere, N.K., Rane, C.V., Murthy, B.N., Mathpati, C.S., Patwardhan, A.W., Ranade, V.V., 2011b. CFD simulation of stirred tanks: Comparison of turbulence models. Part I: Radial flow impellers. *Canadian Journal of Chemical Engineering* 89, 23-82.
- Joshi, J.B., Pandit, A.B., Sharma, M.M., 1982. Mechanically agitated gas-liquid reactors. *Chemical Engineering Science* 37, 813-844.
- Khopkar, A.R., Mavros, P., Ranade, V.V., Bertrand, J., 2004. Simulation of flow generated by an Axial-Flow impeller: Batch and continuous operation. *Chemical Engineering Research and Design* 82, 737-751.
- Kresta, S.M., Wood, P.E., 1993a. The flow field produced by a pitched blade turbine: Characterization of the turbulence and estimation of the dissipation rate. *Chemical Engineering Science* 48, 1761-1774.

Kresta, S.M., Wood, P.E., 1993b. The mean flow field produced by a 45° pitched blade turbine: Changes in the circulation pattern due to off bottom clearance. *The Canadian Journal of Chemical Engineering* 71, 42-53.

Kumaresan, T., Joshi, J.B., 2006. Effect of impeller design on the flow pattern and mixing in stirred tanks. *Chemical engineering journal* 115, 173-193.

Kumaresan, T., Nere, N.K., Joshi, J.B., 2005. Effect of internals on the flow pattern and mixing in stirred tanks. *Industrial & Engineering Chemistry Research* 44, 9951-9961.

Machado, M.B., Nunhez, J.R., Nobes, D., Kresta, S.M., Impeller characterization and selection: Balancing efficient hydrodynamics with process mixing requirements. *AIChE Journal* 58, 2573-2588.

Montante, G., Lee, K., Brucato, A., Yianneskis, M., 2001. Experiments and predictions of the transition of the flow pattern with impeller clearance in stirred tanks. *Computers & Chemical Engineering* 25, 729-735.

Patwardhan, A.W., Pandit, A.B., Joshi, J.B., 2003. The role of convection and turbulent dispersion in blending. *Chemical Engineering Science* 58, 2951-2962.

Paul, E.L., Atiemo-Obeng, V., Kresta, S.M., 2004. *Handbook of industrial mixing: science and practice*. John Wiley & Sons.

Ranade, V.V., Joshi, J.B., 1989. Flow generated by pitched blade turbines I: Measurements using laser Doppler anemometer. *Chemical Engineering Communications* 81, 197-224.

Ri, P.-C., Ren, N.-Q., Ding, J., Kim, J.-S., Guo, W.-Q., CFD optimization of horizontal continuous stirred-tank (HCSTR) reactor for bio-hydrogen production. *International Journal of Hydrogen Energy*.

Steiros, K., Bruce, P., Buxton, O., Vassilicos, J., 2016. Power consumption and form drag of regular and fractal-shaped turbines in a stirred tank. *AIChE Journal*.

Trivellato, F., 2011. On the efficiency of turbulent mixing in rotating stirrers. *Chemical Engineering and Processing: Process Intensification* 50, 799-809.

Wu, H., Patterson, G.K., 1989. Laser-Doppler measurements of turbulent-flow parameters in a stirred mixer. *Chemical Engineering Science* 44, 2207-2221.

## **Chapter 6**

### **Mixing of Medium Viscosity Liquids in a Stirred Tank with Fractal Impeller**

## 6.1 Introduction

Mixing in a stirred tank is a common unit operation in chemical and allied industries. In general, axial flow and radial flow impellers are preferred for the mixing of liquids having low to moderate viscosity (Paul et al., 2004). However, these conventional impellers are found to be inefficient for laminar mixing or mixing of viscous liquids (Ascanio et al., 2002; Cabaret et al., 2008). It is known that laminar mixing is achieved by stretching and folding of streamlined as well as through the chaotic advection (Paul et al., 2004) and therefore it is hard to achieve such phenomena in a stirred tank. Upon applying the conventional impellers for viscous fluids, various dead zones and segregated regions get formed during mixing. Recently, various new alternatives such as time-dependent rotational speed (Lamberto et al., 1996; Yao et al., 1998), off-centre impellers (Alvarez et al., 2002; Ascanio et al., 2002), unconventional configurations (Ascanio et al., 2002), asymmetry in the impeller designs etc. have been reported to minimize the segregated regions. Literature also reports a few new turbine impellers for viscous mixing (Cabaret et al., 2008). However, these methods are less practiced in the industries for a variety of reasons (Paul et al., 2004). In industries, for mixing of higher viscosity liquids (5 to 50 Pa.s), close clearance impellers such as Helical blade mixer, Anchor mixer etc. are mostly preferred as turbines do not cause any motion at the vessel walls.

Motion in the entire stirred tank can be well achieved with the local advection if impeller blades spread are over an entire tank. Moreover, any sweeping action by the impeller blades is detrimental to overall power demand during mixing of viscous fluids. In view of this, we propose to see the applicability of a Fractal Impeller (FI) for mixing of medium viscosity liquids. Since the blades are distributed radially over the entire tank, at any impeller rotation speed there would be increasing tangential velocity along the tank radius. However, the number of vertically aligned blades at any radial location would decide the overall flux in that radial plane. On the other hand, in the absence of any strong wakes in the entire tank, the horizontal blades would simply cut the fluid thereby generating bidirectional motion throughout the tank. Thus, the interaction of different types of fluid movements is expected to achieve higher energy dissipation and hence better performance.

In this Chapter, mixing of medium viscosity liquids using Fractal Impeller has been discussed in details.

## 6.2 Experimental Set-up

Experiments were carried out in an acrylic flat bottom cylindrical tank ( $T=H=0.3\text{m}$ ) having four baffles ( $W=T/10$ ) with FI of a diameter ( $D_{FI}$ ) of 0.19 m ( $D_{FI}/T=0.63$ ). The schematic of the experimental setup is shown in Figure 5.1. The impeller shaft was connected to a DC motor via a shaft-mounted torque transducer (CTimeSync Ltd., UK). FI was supported from the bottom with a steel ball of 6 mm diameter. Liquids having different viscosities were prepared by adding tap water to a viscous liquid and were used as working fluids. The details on the physical properties are given in Table 6.1. Neutrally buoyant solid particles ( $\rho_s = 1060 \text{ kg/m}^3$ ) of diameter ( $d_{NB}$ ) 350  $\mu\text{m}$  were used to measure liquid velocities. 1% (v/v) solid loading of neutrally buoyant particles was used to carry out the experiments. UVP measurements were carried out in midplane between two baffles for different liquids.  $Re$  was calculated on the basis of diameter  $D_{FI}$ , of the FI.

The experiments were carried out to study the power consumption, mixing, and hydrodynamics of medium viscosity liquids (see Table 6.1) in the stirred tank with FI. Liquids of different viscosity were prepared by mixing water in UCON liquid of viscosity 1.33 Pa.s and density 1015  $\text{kg/m}^3$ . The details on the measurement techniques are discussed in Chapter 3.

Table 6.1: Physical properties of the fluids used in the present work

Liquids/Properties	Density ( $\rho$ ), $\text{kg/m}^3$	Viscosity ( $\mu$ ), Pa.s
Liquid 1	1010 $\pm$ 2	0.192
Liquid 2	1005 $\pm$ 2	0.154
Liquid 3	1005 $\pm$ 2	0.058
Liquid 4	1004 $\pm$ 2	0.008
Water	997	0.001

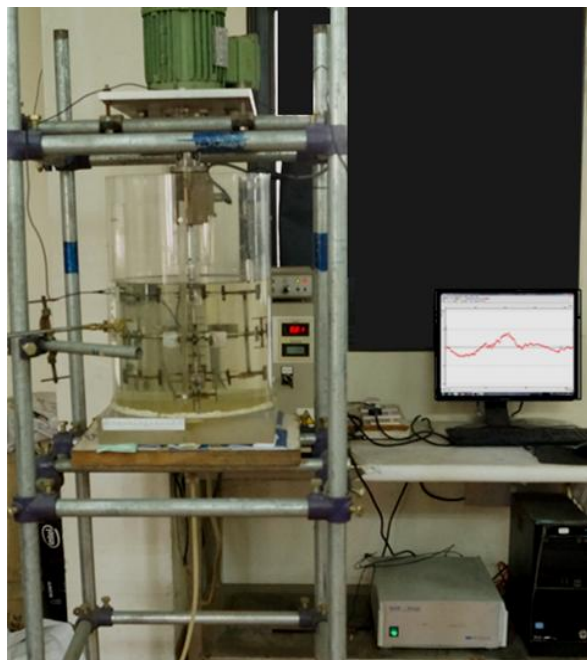


Figure 6.1: Photograph of the experimental set-up.

## 6.3 Results and Discussions

### 6.3.1 Power Consumption

Power consumption measurements were carried out as outlined in the experimental section. The power consumption ( $P$ ) for all the liquids mentioned in Table 1 was estimated using the torque data ( $\tau$ ) at different impeller rotational speeds as  $P = 2\pi N\tau$ , where  $N$  is the impeller rotational speed per second. Subsequently power consumption per unit mass  $P_W$  (W/kg) and Power number  $N_p$  were estimated. Figure 6.2A shows the variation in  $P_W$  as a function of power draw scale ( $N^3 D^2$ ). For different viscosity liquids, the plot shows a first order relation over the entire range of  $N$ . However, the slope of Liquid 1 (which has highest the viscosity among five) found to be greater than the rest. This shows that the overall energy drawn is proportional to the fluid viscosity. We also analyzed the dependence of energy drawn on the respective fluid viscosities (Figure 6.2B), which showed a second order relation. To get further insights, power number ( $N_p$ ) was plotted with respect to impeller  $Re$  and results are given in the Figure 6.2C. From the Figure 6.2C, clearly shows that, unlike conventional impellers,  $N_p$  vs  $Re$  plot for FI shows different curves for each fluid having different viscosity. However individual curves followed the trend of  $N_p$  decreasing with increasing  $N$ . This is an interesting observation and

indicates that the approach of analysis and design of stirred tank with conventional impellers may not be suitable for a stirred tank with FI. Since, there are multiple blades spread over a stirred tank at different radial and axial locations the local Reynolds number ( $Re_L$ ) is different in various regions. Systematic studies on the contribution of various blades (vertical as well as horizontal) towards power consumption and the scale up studies are in progress to establish a universal power characteristic curve and design guidelines.

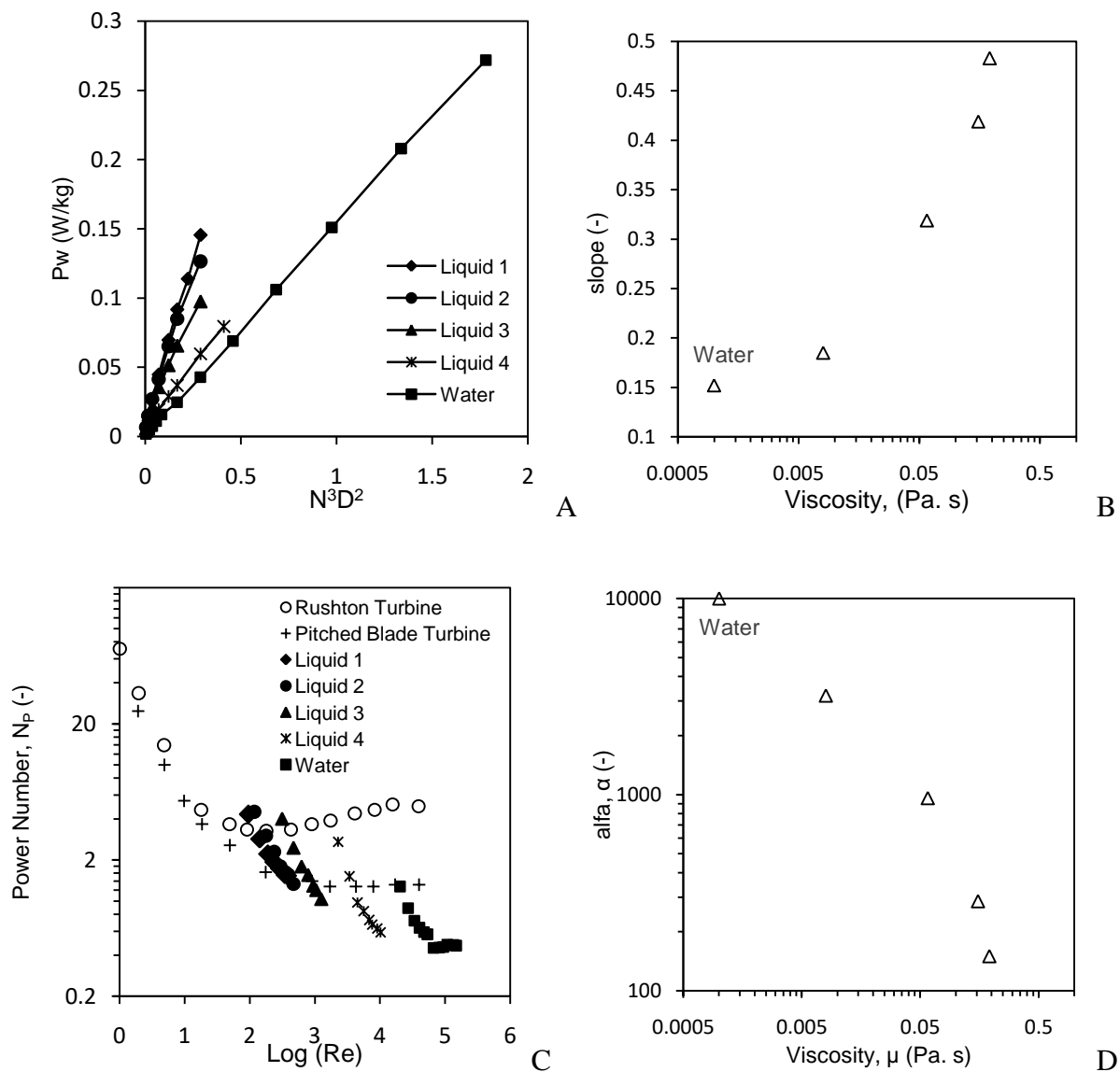


Figure 6.2: Power consumption characteristics of FI, A)  $P_w$  vs  $N^3D^2$ , B) Slope of the energy drawn as a function of viscosity C) Power number ( $N_p$ ) vs  $\log(Re)$  (points for Rushton Turbine and Pitched Blade Turbine are taken from literature (Paul et al. (2004))), D) Constant ( $\alpha$ ) as a function of viscosity for FI.



It is known that at low  $Re$ , the power number is inversely proportional to  $Re$  ( $N_p = \alpha Re^{-1}$ ) (Paul et al., 2004; Rushton et al., 1950). For all the liquids studied in the present work, this trend was observed over a range of  $Re$ . The proportionality constant ( $\alpha$ ), however, was found to be inversely proportional to viscosity (Figure 6.2D). For the viscous liquids (i.e. Liquid-1, Liquid-2, and Liquid-3), the FI could not be rotated beyond  $N = 2$  due to mechanical vibrations of the impeller and hence further measurements were not possible. For Liquid-4, variation in the slope of  $N_p$  vs  $Re$  curve can be observed at  $Re \cong 6800$ , suggesting a transition region. And, for water as fluid, the plot of  $N_p$  vs  $Re$  goes through a minimum and becomes constant at 0.4 beyond  $Re > 90000$ , which possibly indicates the fully turbulent flow in a stirred tank with FI.

From above discussions, it is clear that power consumption characteristics of FI are different from that of conventional impellers. However, for an individual fluid, it follows the trends similar to that of the conventional impellers. Hence broadly, it can be said that the laminar region was observed for Liquid-1, Liquid-2, and Liquid-3 at all the rotational speeds. However, transition region was observed for Liquid-4. Whereas, a turbulent region at which  $N_p$  becomes constant was found to be from  $Re \cong 90000$  ( $N=2$ ,  $\mu=0.001$ ). This further implies that for the liquids under consideration, to achieve  $N_p$  independent of  $Re$ , the impeller rotation speeds need to be in the range of  $143\text{ s}^{-1}$  to  $473\text{ s}^{-1}$  with a relative increase in the viscosity from 0.058 to 0.192 Pas. Such conditions are not practical and for individual fluids, it may not be necessary to operate the FI in the turbulent regime. Unlike the conventional impellers, the primary reason for not needing such a high  $Re$  for FI is the efficacy of the flow that can still yield reasonably good mixing in a short time. In order to validate this hypothesis, the mixing time measurements were carried out for these viscous liquids.

### 6.3.2 Mixing Time ( $\theta_{mix}$ )

Mixing is the primary role of an impeller in a stirred tank reactor. A lot of literature is available on mixing of highly viscous liquids to lowest viscosity liquids (such as water). Many researchers have proposed correlations for mixing time ( $\theta_{mix}$ ) in the stirred tank in terms of  $D/T$  ratio, impeller rotation speed ( $N$ ), power per unit mass ( $P_w$ ) etc. (Nienow, 1997; Patwardhan and Joshi, 1999). However, most of the correlations are found in the turbulent regime. In general, it is known that impeller with larger  $D/T$  ratio and lower  $N_p$  are a good choice for mixing of miscible

liquids. However, mixing complexities increases with increase in fluid viscosities as mixing of viscous liquids entirely depends on bulk velocities and stretching and folding of streamlines. Here we present our observations on mixing characteristics of FI for such viscous liquids. Mixing time was measured in the experimental section and the response curves were normalized. For all the cases the locations of tracer injection and probe as well as the quantity of injected tracer were retained the same. The normalized response curves (Chapter 3) for various impeller rotational speeds are given in Figure 6.2A. The response curves show similar behavior for all the rotational speed, which further confirmed that the geometric factors were kept unchanged.

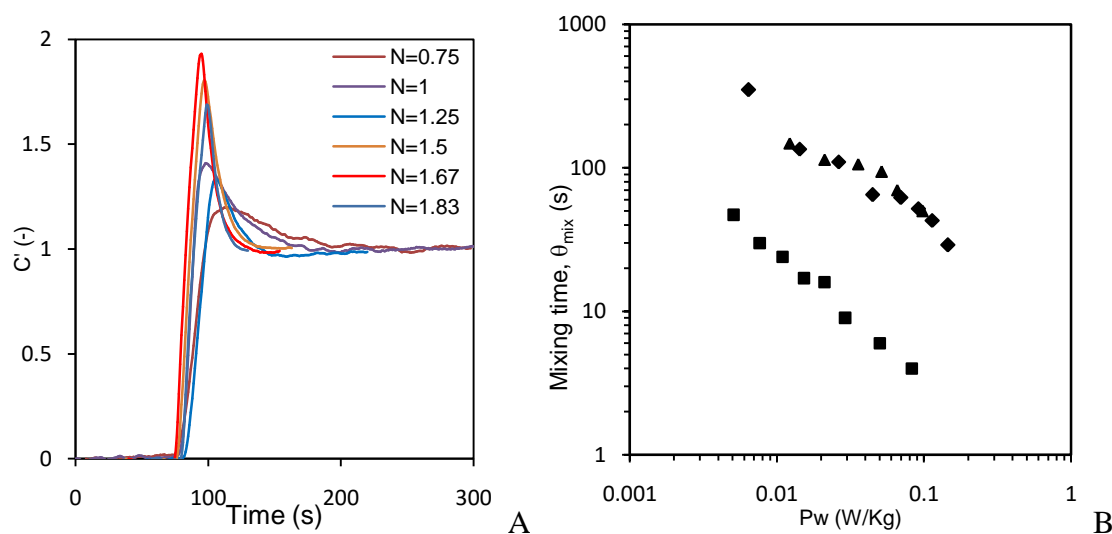


Figure 6.2: Mixing characteristics of FI, A) response curve of normalized conductivity at different  $N$ , B) mixing time ( $\theta_{mix}$ ) vs power consumption per unit mass ( $P_w$ ). ■ - water, ▲ – Liquid-3 and ♦ - Liquid-1

In order to evaluate the performance of FI for mixing of viscous fluids, mixing time ( $\theta_{mix}$ ) was plotted against the power consumption per unit mass (see Figure 6.2B). From Figure 4B, it can be clearly seen that, at identical power consumption, the time required for homogenization is the lowest in case of water. However, for Liquid 1 and Liquid 3, which are 58 times and 192 times more, viscous than water the mixing time vs. power consumption showed identical and overlapping features. For water, the plot was linear while for viscous liquids it showed power law behavior having two trends depending upon the value of  $P_w$ . Mixing time for medium viscosity liquids was found to be the function of power per unit mass only and can be given as:

$$\theta_{mix} = 0.835P_W^{-0.70} \quad 6.1$$

This shows that mixing of medium viscosity liquids in the stirred tank with FI depends only on power consumption and hence can be entirely attributed to the micro-mixing associated with it. As the FI is spread over the entire tank, it distributes the mechanical energy to the fluid in a more uniform manner. This further implies that in the limit of mechanically stable and tolerable impeller rotation speed the mixing time increases drastically with increase in viscosity. As a result, accurate correlations are not available in the literature (Bakker and Gates, 1995). Ascanio et al. (2002) reported the unconventional methods to improve mixing in laminar flow conditions and compared with conventional single-impeller configuration for viscous fluids (0.15 and 0.5 Pa s). These authors have reported mixing time of 87 and 20 seconds for Rushton turbine in a stirred tank ( $T=0.165$  m,  $\mu=0.15$  Pa s) at  $N=1.67$  and  $6.67$  (100 and 400 r.p.m.) respectively. Whereas, in our case, the homogenization was achieved in 52 seconds at  $N=1.67$  (100 r.p.m.). Although this is a very qualitative comparison, it explains the superiority of the FI over conventional impellers. In order to get further insight into the effect of space filling nature and viscosities on the mixing, the flow patterns in the tank were studied.

### 6.3.3 Effect of viscosity on mean velocity profiles

The flow generated by FI has been broadly discussed in the previous chapter. The flow was found to be more tangential in most of the part of the vessel due to space filling nature of the impeller. The vertical blades of  $B_{12}$  branch found to discharge volume of fluid towards the tank wall. The discharge stream was found to get divided into two vertically opposite streams. This overall transport develops two distinct circulation loops (one at the bottom and one at the top) in the  $r$ - $z$  plane. The observations for the flow of water are shown in Figure 6.3. Due to strong tangential flow, the interaction between  $r$ - $z$  planes would be stronger and hence the mixing can be achieved more vigorously.

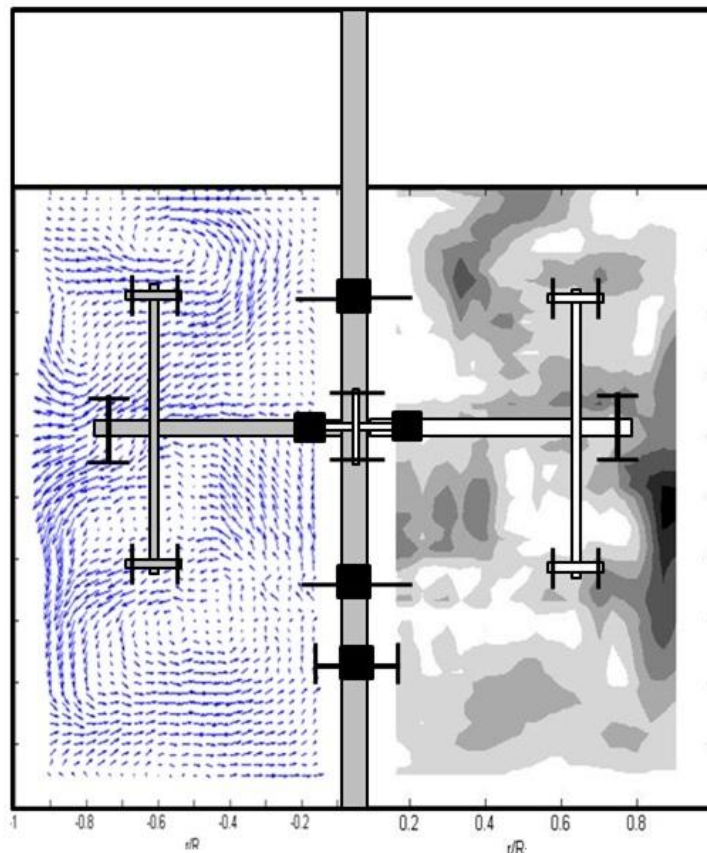


Figure 6.3: Mean flow patterns generated by FI in a stirred tank in an  $r$ - $z$  plane between two baffles. Vector plot of left half plane and contour plot of the velocity magnitude  $((u^2 + v^2)^{0.5})$  in the right half plane. In the contour plot of velocity magnitude the darkest region indicates the maximum velocity and the brightest field shows minimum velocity.

The effect of fluid viscosities on normalized velocity profiles was studied. The normalized radial mean velocity profiles at various axial locations were compared for Liquid-1 and Liquid-3 over a range of impeller rotation speeds. The results are given in Figure 6.4. From the given plots it can be observed that the normalized mean radial velocity profiles are almost similar for two different liquids. Thus the nature of radial velocity profile is not affected by the choice of viscosity, which might be the reason for mixing time to be a function of only  $P_w$ . The other velocity components would also show similar feature.

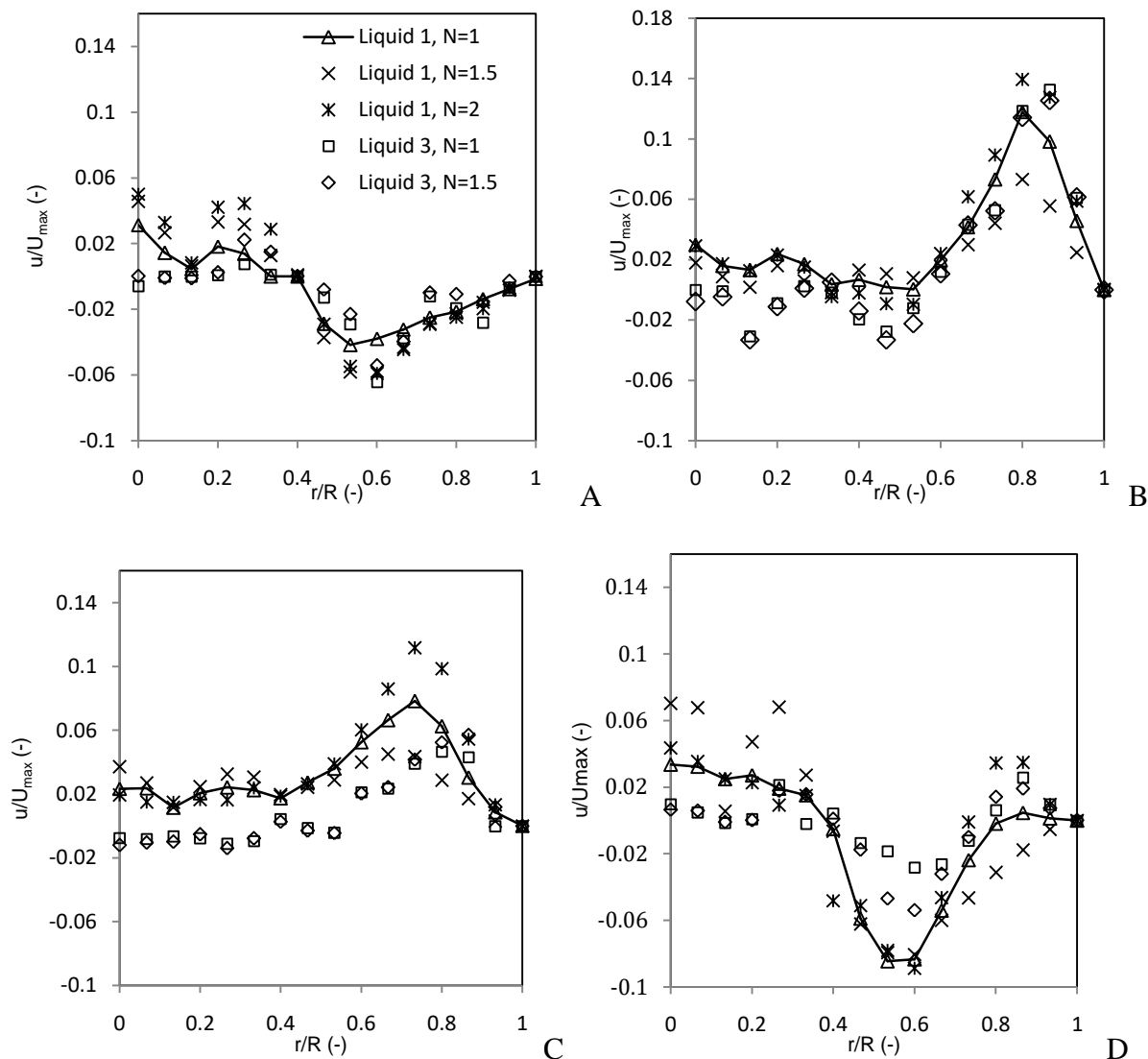


Figure 6.4: Normalized radial profiles of mean radial velocity at different axial locations A)  $z/R=0.33$ , B)  $z/R=1.233$ , C)  $z/R=1.7$ , D)  $z/R=1.9$

## 6.4. Conclusions

In this work power consumption, mixing time and velocity measurements were performed in a stirred tank filled with fluids of different viscosities. The power consumption per unit mass measured at different impeller rotation speeds of the FI showed trends similar to the conventional impellers. However, it was not necessary as well as possible to operate the impeller at high  $Re$  to achieve  $N_P$  independent of  $Re$ . Mixing time for the viscous liquids was found to be

a function of power consumption per unit mass and showed power law dependence. The measured mixing time was significantly lower than the conventional impellers and hence the Fractal Impeller can be a good option for mixing of viscous liquids. Mean radial velocity profiles were found to be unaffected by the fluid viscosities in the laminar region.

---

**References**

Alvarez, M.M., Arratia, P.E., Muzzio, F.J., 2002. Laminar mixing in eccentric stirred tank systems. *The Canadian Journal of Chemical Engineering* 80, 546-557.

Ascanio, G., Brito-Bazán, M., Carreau, P.J., Tanguy, P.A., 2002. Unconventional configuration studies to improve mixing times in stirred tanks. *The Canadian Journal of Chemical Engineering* 80, 558-565.

Bakker, A., Gates, L.E., 1995. Properly choose mechanical agitators for viscous liquids. *Chemical Engineering Progress* 91, 25-34.

Cabaret, F., Fradette, L., Tanguy, P.A., 2008. New turbine impellers for viscous mixing. *Chemical Engineering & Technology* 31, 1806-1815.

Lamberto, D., Muzzio, F., Swanson, P., Tonkovich, A., 1996. Using time-dependent RPM to enhance mixing in stirred vessels. *Chemical Engineering Science* 51, 733-741.

Nienow, A.W., 1997. On impeller circulation and mixing effectiveness in the turbulent flow regime. *Chemical Engineering Science* 52, 2557-2565.

Patwardhan, A.W., Joshi, J.B., 1999. Relation between flow pattern and blending in stirred tanks. *Industrial & Engineering Chemistry Research* 38, 3131-3143.

Paul, E.L., Atiemo-Obeng, V., Kresta, S.M., 2004. *Handbook of industrial mixing: science and practice*. John Wiley & Sons.

Rushton, J., Costich, E., Everett, H., 1950. Power Characteristics of mixing impellers, 2. *Chemical Engineering Progress* 46, 467-476.

Yao, W., Sato, H., Takahashi, K., Koyama, K., 1998. Mixing performance experiments in impeller stirred tanks subjected to unsteady rotational speeds. *Chemical Engineering Science* 53, 3031-3040.

## **Chapter 7**

### **Effect of Number of Branches on the Performance of Fractal Impeller: Mixing and Hydrodynamics**



## 7.1 Introduction

In general, the design of a stirred tank reactor is optimized on the basis of power consumption, heat transfer, mass transfer, and mixing. Mixing in the stirred tank mainly depends on the bulk flow induced by the impeller (Nere et al., 2003; Nienow, 1997; Patwardhan and Joshi, 1999) as well as the turbulent fluctuations. Depending upon the application, in addition to the type of impeller, various other factors such as vessel type, clearance from the bottom, impeller diameter etc. also affect the mixing efficiency (Houcine et al., 2000; Kumaresan et al., 2005). It is known that the most of the energy provided by impeller to the fluid is dissipated around the impeller region which is only 5-10% of the total volume of the reactor (Kresta, 1998; Kresta and Wood, 1993; Ng and Yianneskis, 2000). And therefore, Fractal Impeller found to be a good choice to achieve uniformity. The Fractal Impeller showed some promising results in terms of mixing, solid suspension, gas dispersion and hydrodynamics has now motivated us to study its various design aspects, which include: fractal structure, number of branches, blade configuration, dimensions of blades, the orientation of blades etc. This study explores the effect of a number of branches on the performance of FI. The performance is measured in terms of power consumption, mixing time and flow pattern so as to choose the right configuration for further studies.

In view of the above discussion, this Chapter is organized as follows: After the Introduction, we have given the details on experimental set-up, impeller configurations Section 3 gives the results and discussions in details.

## 7.2 Experimental

### 7.2.1 Tank Geometry

Experiments were carried out in an acrylic tank of diameter ( $T$ ) 0.3 m having four baffles (baffle width  $W = T/12$ ). The tank had a dished shaped bottom with a bottom outlet for removing liquid. The liquid height ( $H$ ) was maintained at 0.31m as to minimize the air entrainment at higher rotational speeds.

### 7.2.2 Fractal Impeller

Fractal Impeller has self-similar geometrical features at different scales. It has multiple blades placed at different axial and radial locations, of which half of the blades are vertically oriented and the remaining are horizontal. These blades are attached to the sub-branches ( $B_{IK}$ )

that are attached to the main branch ( $B_I$ ), which are attached to the impeller shaft. The details on the design are as follows;

- 1) Each sub-branch ( $B_{IK}$ ) has square shaped four blades (30 mm x 30 mm x 1 mm), two are horizontal and two are vertical (see Figure 7.1).
- 2) Three sub-branches of the above design are attached to the main branch ( $B_I$ ). The sub-branches are attached in such a manner that one is co-axial to the main branch while the other two ( $B_{I1}$  and  $B_{I3}$ ) are parallel to the shaft and perpendicular to the main branch. These sub-branches are arranged in a such a way that the  $B_{I1}$  and  $B_{I3}$  branches are placed equidistance from the perpendicular branch ( $B_{I2}$ ).
- 3) The main branch ( $B_I$ ) having three sub-branches is attached to the impeller shaft at a fixed plane for creating local advection through rotational movement. The number of main branches that are attached to the shaft can be changed using a small hub.
- 4) An additional sub-branch ( $B_S$ ) with four blades (two vertical and two horizontal) was attached to the impeller shaft to create sufficient flow at the bottom of the tank.

With this concept, different configurations of Fractal Impeller were assembled. It is necessary to mention that, with the specific dimensions of blades and branches, FI with 5 branches was not found feasible as blades of two different branches were found overlapping in the same plane. Hence the experiments were performed only with 2, 3 and 4 branched FI, separated by  $180^\circ$ ,  $120^\circ$ , and  $90^\circ$ , respectively. The separation angle between the two successive branches ensures the symmetry in the design. The schematics of the configurations are given in Figure 7.1. The orientation of the vertical, as well as the horizontal blades, helps to avoid sweeping of any fluids but enhances the fragmentation of fluid in the vicinity of the blades as the impeller rotates. Moreover, at a given impeller rotation speed ( $N$ , 1/s), the angular distance covered by different blades varies and thus yields different blade tip velocities ( $2\pi lN$ , where  $l$  is the distance of the blade from the centre) over the plane of rotation.

The sub-branch ( $B_S$ ) at the bottom of the tank was at a distance of 60 mm ( $z/R=0.4$ ). And, the distance of  $B_{I1}$  branch from the bottom of the tank was 125 mm ( $z/R=0.833$ ), of  $B_{I2}$  was 175 mm ( $z/R=1.167$ ) and of  $B_{I3}$  was 225 mm ( $z/R=1.5$ ). Due to geometrical complexities, the farthest

distance between two blades is considered as the diameter of the FI. For FI with 2 and 4 branches, the  $D_{FI}$  was measured to be 0.23m ( $D_{FI}/T=0.77$ ), whereas, for 3 branches it was 0.24m ( $D_{FI}/T=0.8$ ).

### 7.2.3 Experimental Setup

The schematic diagram of the experimental setup is shown in Figure 7.2. The impeller shaft was connected to a DC motor via a shaft mounted torque transducer (CTimeSync Ltd., UK). FI was supported from the bottom with a steel ball of 6 mm diameter. Tap water was used as a working fluid ( $\rho = 998 \text{ kg/m}^3$ ) and neutrally buoyant solid particles ( $\rho_s = 1060 \text{ kg/m}^3$ ) of diameter ( $d_{NB}$ )  $350 \mu\text{m}$  were used to measure liquid velocities. 1% (v/v) solid loading of neutrally buoyant particles was used to carry out the experiments. UVP measurements were carried out in a midplane between two baffles for a range of rotational speeds ( $N$ ) for three different configurations of FI.

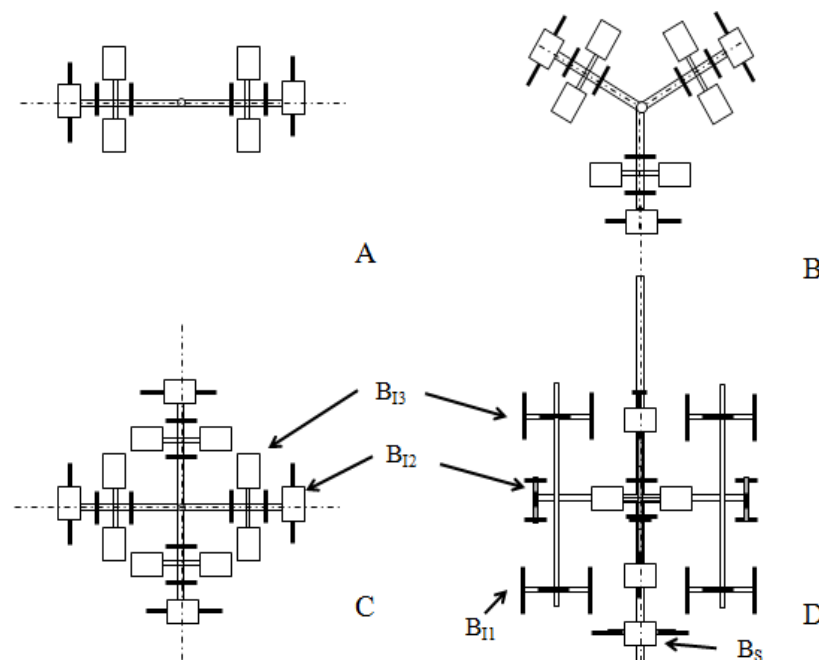


Figure 7.1: Schematic diagram of Fractal Impeller (FI) A) top view (2 branches), B) top view (3 branches) C) top view (4 branches) D) front view (4 branches).

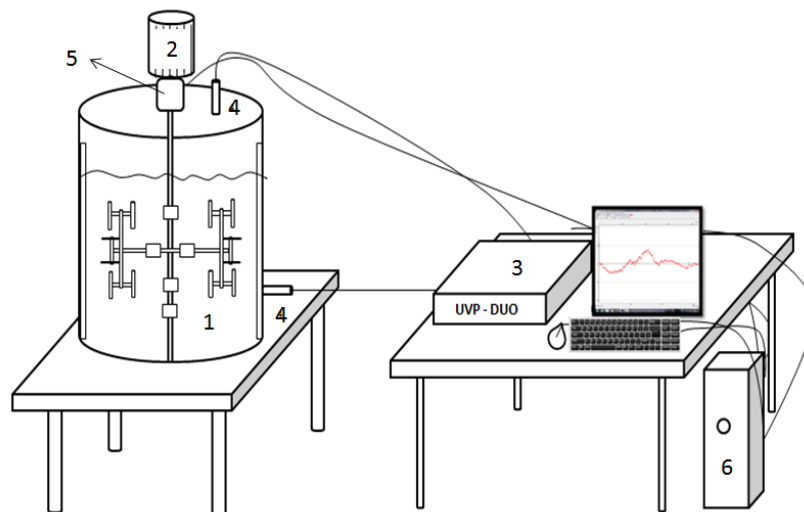


Figure 7.2: Schematic of the experimental setup (1) Stirred tank with FI (4 branches), (2) electric motor, (3) UVP-Duo data acquisition system, (4) UVP probes, (5) digital torque sensor, (6) computer.

## 7.3 Results and Discussions

### 7.3.1 Flow generated by Fractal Impeller

In order to understand the superior mixing characteristics from the Fractal Impeller, the flow pattern in the stirred tank was measured. Local velocity measurements were carried out at different impeller rotational speeds and the data is presented in terms of normalized velocity profiles. After checking the consistency in the data for one design configuration, the mean velocities of all the three components for all three configurations were compared at  $N=2$ .

#### 7.3.1.1 *Effect of impeller rotation speed on mean velocity profiles*

All the local velocities were normalized with maximum velocity in the tank ( $U_{Max}$ ) to have consistency in the comparison. Figure 7.3 shows the normalized radial mean velocity ( $u$ ) profiles in an  $r$ - $z$  plane between two consecutive baffles at different axial locations for FI with 4 branches. The figure indicates that the nature of the radial mean velocity component for three different rotational speed ( $N$ ) was almost identical. Since the normalized mean velocity data at different planes showed consistent behavior, further measurements were carried out to explore the variation in different velocity components in the flow generated by FI with 2, 3 and 4 branches.

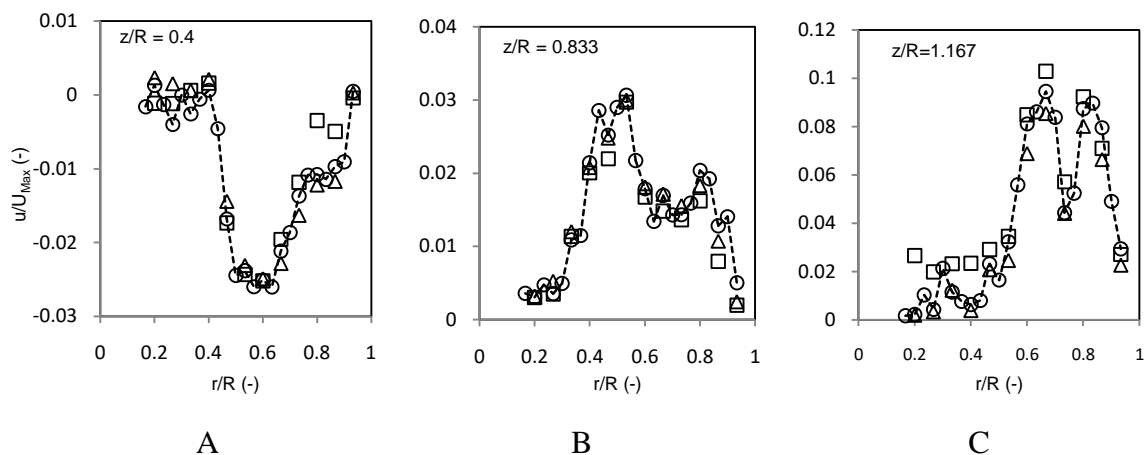


Figure 7.3: Radial profiles of radial mean velocity ( $u$ ) at different axial locations ( $z/R$ ) for different  $N$  ( $\square = 1$ ,  $\Delta = 1.5$ ,  $O = 2$ ) A)  $z/R=0.4$ , B)  $z/R=0.833$ , C)  $z/R=1.167$ . For all the plots, ordinate is  $u/U_{\max}$ .

### 7.3.1.2 Mean Velocity and Flow Patterns

The generated by the fractal impeller has already been explained in Chapter 5. In this work, the effect of a number of branches on the mean flow profiles will be discussed in details. The normalized radial, axial and tangential mean velocities at various locations in the tank are given in the Figures. 7.4, 7.5 and 7.6 respectively. From these Figures, it can be observed that the mean radial and axial velocity component has almost identical nature (both in the direction as well as in magnitude) for three different configurations of 2, 3 and 4 branches. Wu et al., (2001) have also reported similar results on the effect of a number of blades and blade thickness on the hydrodynamics and solid suspension in a stirred tank with PBT and RT. These authors have reported universal velocity profiles (radial and axial) irrespective of a number of blades. In the case of FI, the large difference was observed in mean tangential velocity component especially in the region occupied by the impeller. This is due to the periodicity of the branches and the overall flux pushed by the vertical blades at a given impeller rotation speed. In all the configurations of FI, the tangential velocity component was found to be 5 to 6 times higher than both radial and axial velocity components. This also can be explained on the basis of the structure of the FI. The FI is designed such that, it distributes energy over 80-90% volume of the tank and blades are

oriented in the horizontal and vertical direction in most of the region. FI generates a significant tangential movement locally, which is not the case with conventional impellers.

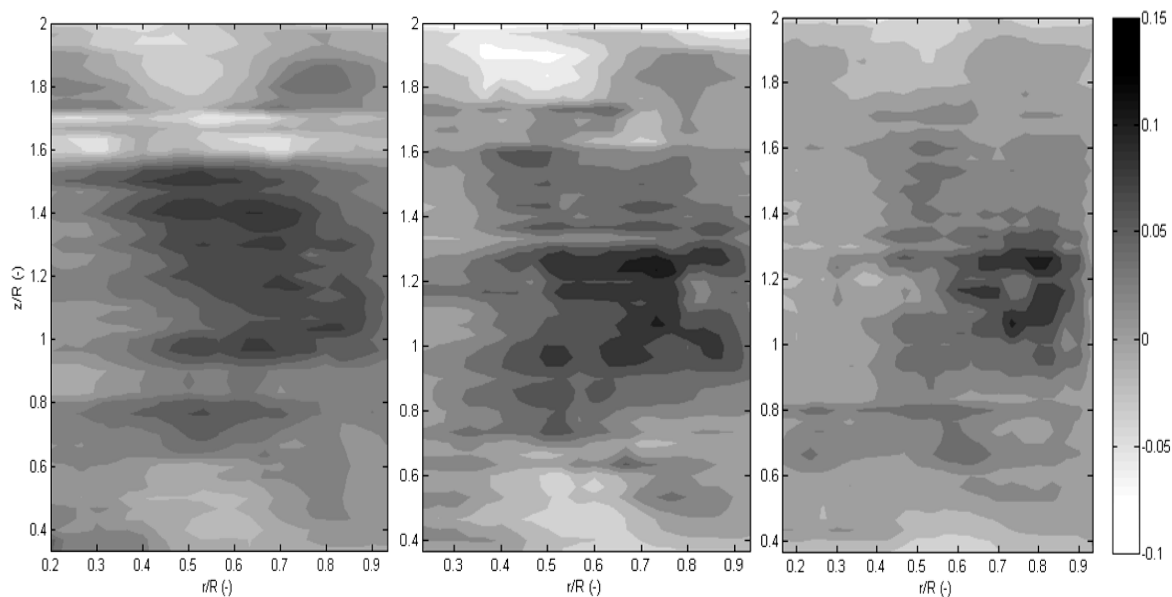


Figure 7.4: Contour plots of the measured normalized mean radial velocity in  $r$ - $z$  plane for three different configurations of FI (Left) 2 branches, (Middle) 3 branches, (Right) 4 branches

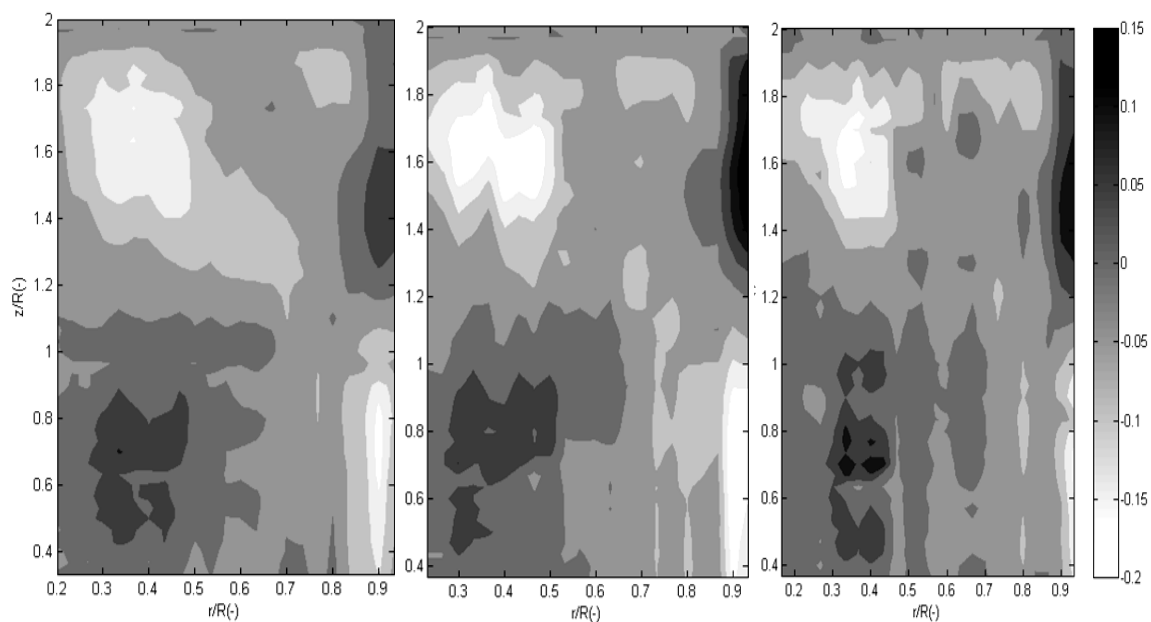


Figure 7.5: Contour plots of the measured normalized mean axial velocity in  $r$ - $z$  plane for three different configurations of FI (Left) 2 branches, (Middle) 3 branches, (Right) 4 branches

In order to support our findings, we normalized the tangential velocities with respect to local tip velocity ( $2\pi lN$ , where  $l$  is the distance of the blade from the centre) and the profiles are given in Fig. 7.7A. It was observed that the normalized velocities are 60-70% of the local tip velocities and the effect of number of branches was seen predominantly in the region unoccupied by FI in the stirred tank (Figure 7.7B).

A number of blades ensure the flow to remain tangential and hence the effect of a number of branches is evident mainly in the tangential velocities. The advantage of higher tangential velocity in a baffled vessel can be used to benefit the mixing of single phase as it helps to distribute the fluid throughout the reactor in relatively shorter time.

As explained in Chapter 5, Figure 7.4 shows the change in the direction of radial velocity component along the axial direction, which suggests the existence of two primary circulation loops. Similar observations can be made for axial velocity in the radial direction (Figure 7.5). The existence of outward flow from the center of the tank is due to the movement of vertical blades of  $B_{I2}$  branch. These blades were found to discharge a certain volume of the fluid toward radial and tangential directions. Due to the close clearance, the radially directed fluid hits the tank wall and gets divided into two vertically opposite streams (upward and downward). The stream along downward direction encounters the tank bottom and again gets redirected along the impeller axis. Similarly, upward stream along the wall encounters the free surface and pulled back towards the impeller axis. This generates low-pressure zone near the impeller axis at the middle plane of the stirred tank. The fluid coming from the bottom and free surface is drawn towards the shaft and redirected again. This continuous motion of the fluid leads to the formation of two primary loops. Similarly, vertical blades of  $B_{I1}$  and  $B_{I3}$  also help in maintaining and generating the radial flow. The overall flow structure remains the same for all configurations of FI with some minor transitions in the upper portion of the tank. The flow patterns obtained from the resultant velocity in an  $r$ - $z$  plane for all the three configurations of FI are given in Figure 7.8. These observations are consistent with all the configurations. However, for tangential mean velocities at different locations, the effect of a number of branches can be observed.

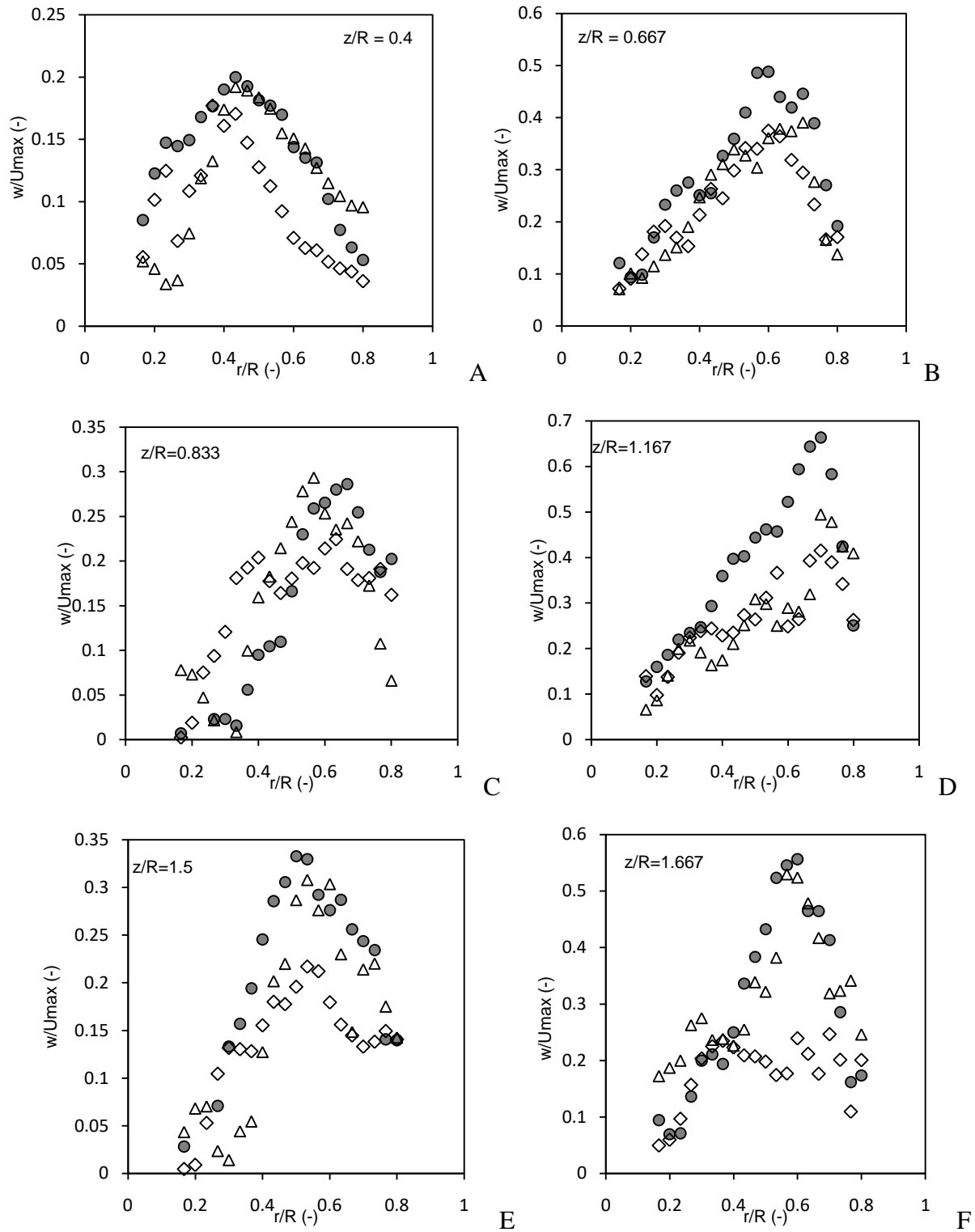


Figure 7.6: Radial profiles of normalized tangential mean velocity ( $w$ ) at different axial locations ( $\diamond$ -2 branches,  $\Delta$ -3 branches,  $\bullet$ -4 branches) A)  $z/R=0.4$ , B)  $z/R=0.67$ , C)  $z/R=0.83$ , D)  $z/R=1.167$ , E)  $z/R=1.5$ , F)  $z/R=1.67$ .



At a constant  $N$ , due to the higher tangential velocities, the transport of fluid between two successive  $r$ - $z$  planes is highest in case of FI with 4 branches and lowest in case of FI with 2 branches. This entire process leads circulation to happen very rigorously and hence this can lead to a difference in the mixing time for different impeller configurations at constant  $N$ . More details on the mixing time are given in next section.

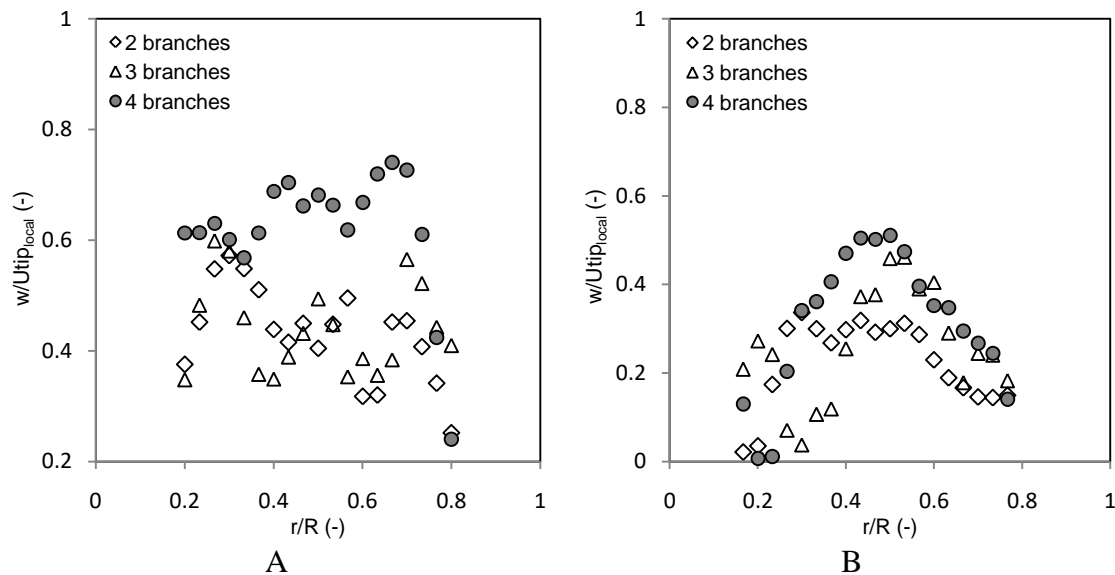


Figure 7.7: Tangential velocity normalized with local tip velocity at different axial locations (A)  $z/R=1.667$  (region occupied by FI) (B)  $z/R=1.5$  (region unoccupied by FI)

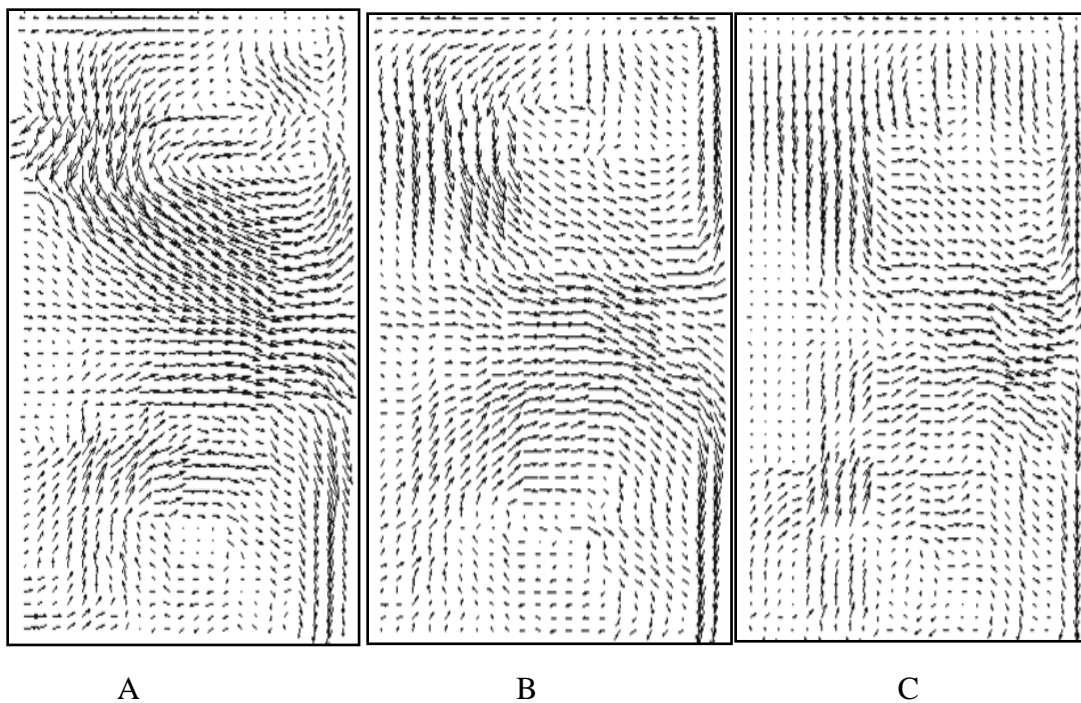


Figure 7.8: Flow Patterns in an  $r-z$  plane for three configurations of FI A) 2 branches, B) 3 branches, C) 4 branches.

The mean kinetic energy ( $k_m$ ) was estimated to see the effect of a number of branches on mixing by convection. Figures 7.9A-7.9D clearly illustrates the effect of a number of branches on  $k_m$ . Mean kinetic energy ( $k_m$ ) was found higher for FI with 4 branches, than other configurations. This confirms that local advection is achieved more rigorously by using a maximum number of branches and will be effective even at lower impeller rotational speeds.

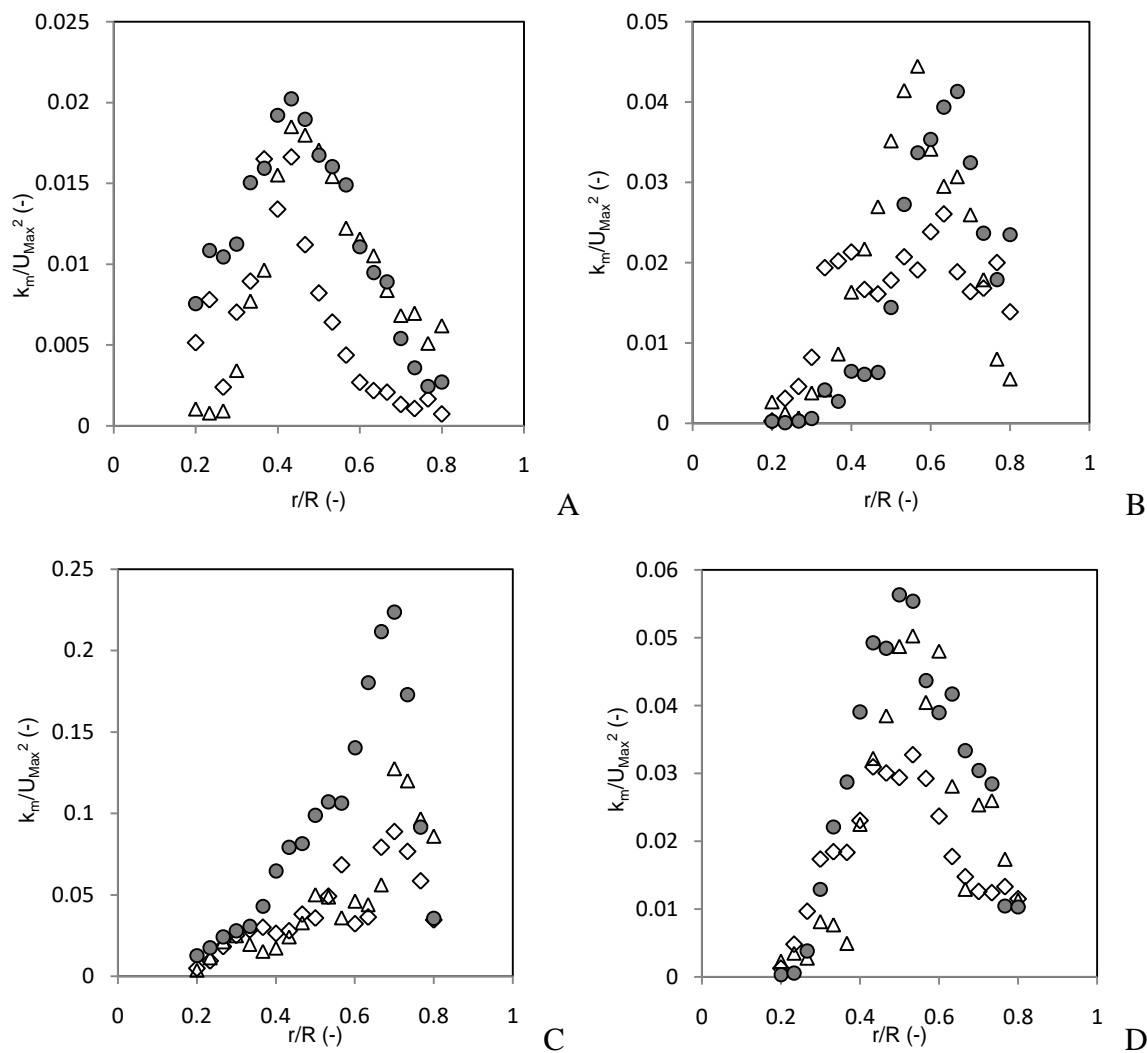


Figure 7.9: Normalized mean kinetic energy at different axial locations ( $\diamond$ -2 branches,  $\Delta$ -3 branches,  $\circ$ -4 branches) A)  $z/R=0.4$ , B)  $z/R=0.833$ , C)  $z/R=0.116$ , D)  $z/R=1.5$ .

### 7.3.2 Power consumption

The power consumption ( $P$ ) for all the three impeller configuration was estimated using the torque data ( $\tau$ ) at different rotational speeds as  $P = 2\pi N\tau$ , where  $N$  is the impeller rotational speed per second. Subsequently power consumption per unit mass  $P_W$  (W/kg) for each configuration were estimated. Figure 7.10A shows the power per unit mass ( $P_W$ ) for FI with respect to impeller  $Re$ , which shows a positive dependence of  $P_W$  on  $Re$ . It needs to be noted that for the FI with 2branches, 3branches and 4branches, it has 28, 40 and 54 blades respectively.

Therefore the variation in power consumption for individual impellers is intuitive. In general,  $\bar{\epsilon}$  (or  $P_W$ ) and  $N^3 D^2$  (also known as power draw scale) are used as a scaling parameter for local energy dissipation, among which the later one is believed to be more useful for exact scale-up (Baldi and Yianneskis, 2004). Figure 7.10B illustrates the variation in  $P_W$  with  $N^3 D^2$ . The plot signifies the dimensionless energy drawn at different  $Re$ . A first order linear dependence was observed for all three configurations over the entire range of  $N$ , with its slope proportional to the number of branches. It implies that the overall energy drawn by an impeller with 2 branches is less compared to other two configurations. In order to explore this observation further, the slope of the energy drawn was plotted as a function of the number of blades of a respective configuration (Fig. not shown). From the data a correlation for  $P_W$  in terms of number of blades, rotation speed and impeller diameter was obtained and is given as Eq. (7.1),

$$P_W = A_1 N_{BL} N^3 D_{FI}^2 \quad 7.1$$

, where  $A_1$  is a constant (0.003 in the present case);  $N_{BL}$  - number of blades;  $N$  - impeller rotational speed (in sec.) and  $D_{FI}$  is the impeller diameter. The total drag experienced by the impeller and hence the power consumption is expected to increase with increasing number of blades in a given configuration.

The variation of  $\log(P_W)$  as a function of  $\log(Re)$  showed the first-order variation for all the configurations. Whereas, the slope i.e.  $\log[P_W]/\log[Re]$  as a function of  $\log(Re)$  was found to go through maxima around  $\log(Re)=5$ . As explained in the previous Chapter, for working fluid as water, fractal impeller shows similar characteristics as that of the conventional impeller. In order to understand the associated flow pattern, the Power number ( $N_P$ ) was estimated and plotted as a function of impeller  $Re$  (Figure 10C). It can be observed that: (i) For  $30000 < Re < 60000$  (i.e.  $0.5 < N < 1$ ),  $N_P \propto Re^{-x}$  ( $x=1.64, 1.25$  and  $1.5$  for FI with 2, 3 and 4 branches, respectively), (ii) For  $N = 1$  to  $1.67$ ,  $N_P$  continued to vary and then reached a constant value beyond  $Re > 10^5$  and (iii) For  $Re > 10^5$  (i.e.  $N > 1.67$ )  $N_P = \text{constant}$ . The power characteristics of fractal impeller are different from that of the conventional. However, the constant power number can be referred as impeller power number which for FI with 4 branches was 1.67. The mixing efficiency of the fractal impeller is discussed in the next section.

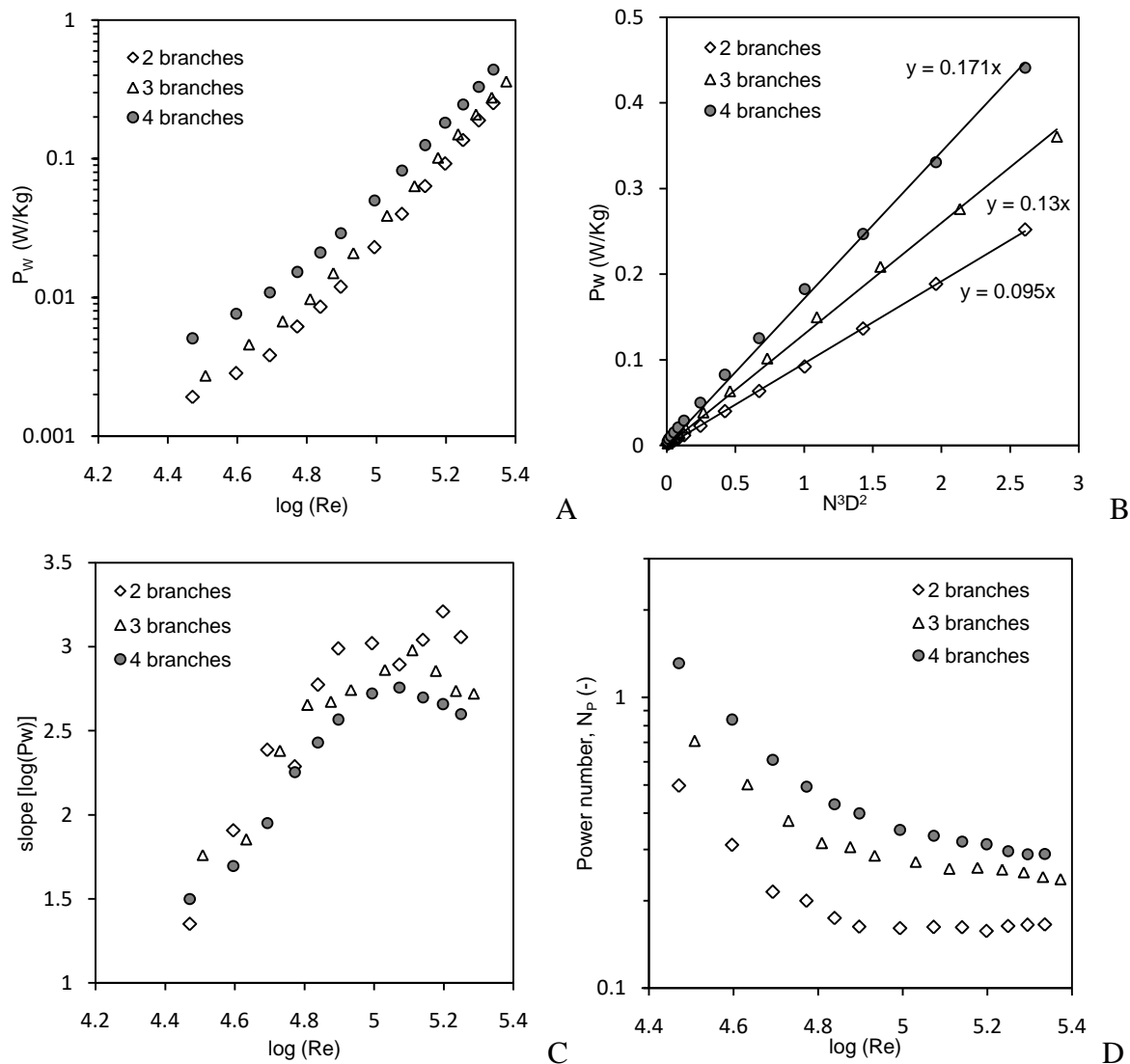


Figure 7.10: (A) Variation of the power consumption per unit mass ( $P_w$ ) with impeller  $Re$ , (B)  $P_w$  vs.  $N^3 D^2$ , (C)  $\log[P_w]/\log[Re]$  vs.  $\log(Re)$ , (D)  $N_p$  vs.  $\log(Re)$ .

### 7.3.3 Mixing time

Performance of an impeller largely depends upon its mixing characteristics. Many researchers have proposed correlations for mixing time ( $\theta_{mix}$ ) in a stirred tank with standard impellers. In general, if mixing is controlled by energy dissipation in the region of slowest mixing then  $N\theta_{mix}$  is proportional to  $N_p^{-1/3}(T/D)^2$ . On the other hand, if mixing is controlled by convection, then  $N\theta_{mix}$  is proportional to  $N_Q^{-1}(T/D)^3$  (Nienow, 1997; Patwardhan et al., 2003). This relationship indicates that the impellers with larger  $(T/D)$  ratio and lower  $N_p$  are more

appropriate for single phase mixing. Literature also reports the  $\theta_{mix}$  to depend on  $P_W^{1/3}$  for various impellers (Hass and Nienow, 1989; Nienow, 1997; Patwardhan and Joshi, 1999; Prochazka and Landau, 1961; Ruszkowski, 1994). Upon analyzing a comprehensive data from the literature on various (RT, PBDT, Lightnin A310, Scaba 6SRGT, Prochem Maxflow axial flow hydrofoil, etc.) impellers on mixing time, Ruszkowski (1994) and Nienow (1997) reported the following correlation:

$$\theta_{mix} = 5.9 T^{2/3} P_W^{-1/3} (D/T)^{-1/3} \quad 7.2$$

However, it needs to be tested for its applicability for FI. Mixing time was measured (as discussed in Chapter 3) and the results are analyzed with reference to the power consumption characteristics for FI with different configurations. The observations are shown in Figure 7.11A. It can be observed that the mixing efficiency per unit power consumed is almost identical for all the FI configurations. This observation indicates equal power consumption by all the impellers, i.e. all the three configurations give similar performance. However, at identical  $N$ , the FI with 4 branches performs much better than a design with 2 and 3 branches. With increase in the number of branches (and hence the number of blades) the overall amount of liquid displaced (in tangential direction) by the vertically oriented blades and the turbulence generated due to interaction with the fluid that gets separated over the horizontal blades was found to increase at particular  $N$  and hence the difference is intuitive.

Figure 7.11B shows the comparison of mixing performance with the data from the literature. Analysis of data from FI and propeller shows different behavior as a function of  $P_W$ , i.e.  $\theta_{mix} = 0.460 P_W^{-0.84}$  for FI and  $\theta_{mix} = 7.386 P_W^{-1/3}$  for the propeller. For identical  $P_W$  say 0.1, time requires for homogenization ( $\theta_{mix}$ ) for FI is 3.18 s, for propeller it is 15.81 s, and the calculations using Eq. 9 gives  $\theta_{mix} = 8.22$  s. This is an interesting observation as it confirms that at higher power consumption, FI needs lesser time than standard impellers to achieve homogenization (also see Figure 7.11B). This observation can be entirely attributed to the maximum energy dissipation by the impeller as well as its space-filling features. Since the FI is spread over the entire tank, it ensures that the flow gets distributed in at each part of the tank in a

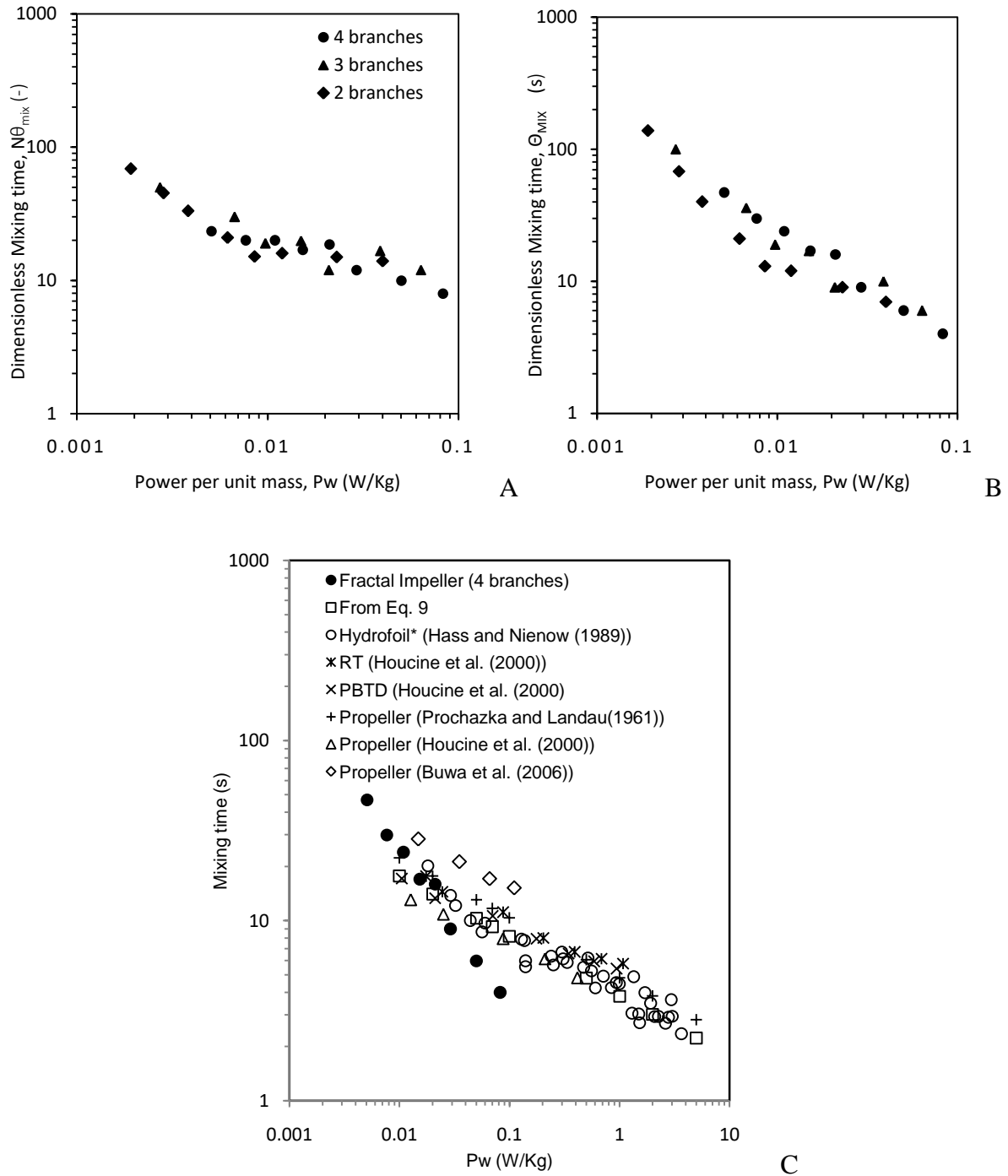


Figure 7.11: A) Dimensionless mixing time ( $N\theta_{mix}$ ) vs  $P_w$ , B) mixing time ( $\theta_{mix}$ ) vs  $P_w$ , C) comparison of mixing performance of FI with Propeller and Disc Grid impeller (mixing studies by (Buwa et al., 2006) were carried out with water in 0.3m diameter tank, \*Prochem Maxflow axial flow hydrofoil).

relatively shorter time. The hydrodynamics in the stirred tank explains the reason for lower mixing time. At a constant  $N$ , the transport of fluid between two successive  $r$ - $z$  planes is highest in case of FI with 4 branches and lowest in case of FI with 2 branches. This leads to rapid circulation and hence should be one of the reasons for FI with 4 branches to perform better than other two configurations at constant  $N$ .

Since  $P_W$  depends on impeller rotation speed ( $N$ ), number of blades ( $N_{BL}$ ) and impeller diameter ( $D_{FI}$ ),  $\theta_{mix}$  can also be correlated with the abovementioned parameters. Eq. (7.3) gives the correlation for mixing time:

$$\theta_{mix} = A_2 N_{BL}^{-0.84} N^{-2.52} D_{FI}^{-1.68} \quad 7.3$$

, where,  $A_2$  is a constant. These results indicate that the mixing process is roughly proportional to  $(1/D_{FI})^{1.7}$ . This slope (1.7) comes in the range that is reported for the standard impellers.

Above results on mixing show that, FI with any blade configuration (studied in present work) is a good alternative to standard impellers. Moreover, the performance of FI mainly depends on the impeller diameter, a number of blades and rotational speed and hence the right combination of these parameters would help to achieve the desired performance.

The analysis of data indicates that the quality of mixing per unit power consumed is same for all the FI configurations. However, among the different configurations, a slightly more power number of FI with 4 branches actually gives far better spatial distribution than the others configurations.

## 7.4 Conclusions

In this work, power consumption, mixing time and the flow patterns were measured to study the effect of a number of branches of a Fractal Impeller on the performance. Impellers having 2, 3, and 4 main branches were used. Mixing time studies were performed by monitoring the variation in local conductivity while local instantaneous velocity was measured using Ultrasonic velocity profiler (UVP). All the three velocity components were measured and used for mapping of the flow field in different planes. Based on the observations, the following conclusions can be drawn to understand the effect of the impeller configuration on its performance.



The power consumption was observed to increase with an increase in the number of blades. A correlation could be established for estimation of power consumption unit mass using the number of blades, impeller speed, and the impeller diameter.

Mixing efficiency per unit power consumed was almost identical for all the FI configurations. However, at identical  $N$ , FI with 4 branches was observed to perform better. The data on  $\theta_{mix}$  vs.  $P_W$  for all three configurations followed the identical trend and the slope of the plot was found to be  $-0.84$ , which is greater than  $-0.33$ , which is typically observed for conventional impellers. At equal power consumption, FI requires less time for homogenization compared to conventional impellers.

Normalized radial and axial velocity profiles were found similar for all the three configurations. However, the tangential component for 4 branches FI was having the highest magnitude among all.

The flow generated by the fractal impeller in a stirred tank was found to have a very large tangential velocity component. Moreover, two primary circulation loops were observed in an  $r$ - $z$  plane with a very strong tangential flow close to the wall. Strong tangential flow is seen to enhance the interaction of different mixing zones thereby achieving better mixing characteristics.

Overall, from a mixing point of view, any branch configuration can be practiced as long as FI retains the symmetry in the design. Since the power needed to achieve certain mixing strongly depends upon the number of blades if one has limitations on rotational speeds the FI with 4 branches is recommended.

**References**

Houcine, I., Plasari, E., David, R., 2000. Effects of the stirred tank's design on power consumption and mixing time in liquid phase. *Chemical Engineering & Technology* 23, 605-613.

Kresta, S., 1998. Turbulence in stirred tanks: Anisotropic, approximate, and applied. *The Canadian Journal of Chemical Engineering* 76, 563-576.

Kresta, S.M., Wood, P.E., 1993. The flow field produced by a pitched blade turbine: Characterization of the turbulence and estimation of the dissipation rate. *Chemical Engineering Science* 48, 1761-1774.

Kumaresan, T., Nere, N.K., Joshi, J.B., 2005. Effect of internals on the flow pattern and mixing in stirred tanks. *Industrial & Engineering Chemistry Research* 44, 9951-9961.

Nere, N.K., Patwardhan, A.W., Joshi, J.B., 2003. Liquid-phase mixing in stirred vessels: Turbulent flow regime. *Industrial & Engineering Chemistry Research* 42, 2661-2698.

Ng, K., Yianneskis, M., 2000. Observations on the distribution of energy dissipation in stirred vessels. *Chemical Engineering Research and Design* 78, 334-341.

Nienow, A.W., 1997. On impeller circulation and mixing effectiveness in the turbulent flow regime. *Chemical Engineering Science* 52, 2557-2565.

Patwardhan, A.W., Joshi, J.B., 1999. Relation between flow pattern and blending in stirred tanks. *Industrial & Engineering Chemistry Research* 38, 3131-3143.

**Nomenclature of Part-I**

$A$	proportionality constant of Eq. 2.17
$A_1$	proportionality constant of Eq. 7.1
$A_2$	proportionality constant of Eq. 7.3
$B$	baffle width (mm)
$C$	off bottom clearance (mm)
$c$	speed of sound, m/s
$C_0$	Concentration measured before addition of tracer
$C_\infty$	Concentration measured after the test is complete
$C_i$	instantaneous concentration
$C_i'$	normalized instantaneous concentration
$d_{NB}$	dia. neutrally buoyant particles ( $\mu\text{m}$ )
$D$	impeller diameter (m)
$D_{FI}$	fractal impeller diameter (m)
$E(\kappa)$	Energy spectrum
$f_D$	Doppler shift frequency, Hz
$f_0$	Doppler frequency, Hz
$H$	liquid height in the tank (m)
$k$	turbulent kinetic energy per unit mass ( $\text{m}^2/\text{s}^2$ )
$k_m$	mean kinetic energy ( $\text{m}^2/\text{s}^2$ )
$l$	characteristic length scale
$L$	length of the blade (m)
$N$	impeller rotational speed (1/s)
$N_{BL}$	number of blades
$N_P$	power number, ( $P_0/\rho N^3 D^5$ )
$r$	radial coordinate (m)
$r.p.m.$	rotational speed in min. (1/min)
$R$	Radius of the tank (m)
$Re$	Reynolds number ( $D^2 N \rho / \mu$ )
$R_{ij}$	Reynolds stresses ( $\text{m}^2/\text{s}^2$ )
$p'$	fluctuating pressure component
$P$	energy input by the impeller (Watt)
$P_V$	energy dissipated in the specified region (Watt)
$P_{Max}$	maximum penetration depth, m
$P_W$	power per unit mass ( $\text{m}^2/\text{s}^3$ )
$Q_{FI}$	discharge flow rate ( $\text{m}^3/\text{s}$ )

- $t_{urf}$  time period of pulse (s)  
 $t$ , time delay (s)  
 $T$  tank diameter (m)  
 $u, v, w$  mean radial, axial and tangential velocity components (m/s)  
 $U_{Max}$  maximum velocity in the stirred tank (m/s)  
 $U_x, U_y$  instantaneous velocities at x and y direction (m/s)  
 $U_{tip}$  tip velocity (m/s)  
 $u_i$  velocity in  $i$ th direction (m/s)  
 $u'_i$  fluctuating velocity component in  $i$ th direction (m/s)  
 $u_{iRMS}$  = RMS velocity in  $i$ th direction (m/s)  
 $\overline{u'_i u'_j}$  fluctuating velocity correlations or Reynolds stresses ( $m^2/s^2$ )  
 $V$  velocity measured by UVP (m/s)  
 $W$  height of blade (m)  
 $X$  distance measured by UVP (m)  
 $x_i$  x-direction coordinates (m)  
 $x, y$  coordinates in the x-axis and in the y-axis (m)  
 $z$  axial coordinate (m)

**Greek letters:**

- $\varepsilon$  dissipation rate ( $m^2/s^3$ )  
 $\varepsilon_{max}$  dissipation rate ( $m^2/s^3$ )  
 $\bar{\varepsilon}$  average dissipation rate ( $m^2/s^3$ )  
 $\kappa$  wave number (1/m)  
 $\rho$  density of the fluid ( $kg/m^3$ )  
 $\nu$  kinematic viscosity of the fluid ( $m^2/s$ )  
 $\rho_s$  density of the solid particles ( $kg/m^3$ )  
 $\lambda$  Taylor micro-scale  
 $\tau_r$  torque  
 $\theta_{mix}$  mixing time, s

**Subscripts**

- FI = fractal impeller  
 Max = maximum  
 RMS = root mean square  
 NB = neutrally buoyant

***Part II: Exothermic reactions in stirred tank reactor***

## **Chapter 8**

### **Assessment of Usefulness of CSTRs for Exothermic Nitration: Design aspects**

## 8.1 Introduction

In the industries such as pharmaceuticals, most of the exothermic reactions are carried out in the batch or semi-batch reactors. As in cases of fast and exothermic where the possibility of having run away reaction is more when the rate of heat generation due to reaction progress is greater than that of the rate of heat removal by the cooling (Cui et al., 2015). To avoid this scenario in industries nitration reactions are carried out in semi-batch mode, where the heat load is minimized by the slow addition of the nitric acid (Albright et al., 1996; Zaldivar et al., 1996). However, for the reaction involving multiple reactants, as the volume of the reaction vessel increases, mixing determines the rate of the reaction (Baldyga and Bourne, 1990; Bałdyga et al., 1997). Therefore, it can be safely said that mixing and reaction rate are related to each other. As discussed in the earlier chapter, mixing time increases as the volume of vessel increases. Hence, it limits the progress of the reaction which in the end results in prolongation of batch time. These issues can be addressed by reducing the volume of the reactors and carrying out the reaction in a continuous operation for maintaining the yield or the production as that of the batch.

However, to carry out fast and exothermic reactions reaction in continuous operation, it is very important to study the temperature rise in the reactor with changes in the input conditions. Most of the runaway events take place due to mischarging of the reactants, improper heat balance or lack of knowledge of reactions and physic-chemical properties of reactants or products. However, in recent times, researchers have shown the way for the continuous production of nitro derivatives using the concept of microreactors (Kulkarni, 2014; Kulkarni et al., 2009). Microreactors have a large surface area to volume ratio and hence heat can be removed more adequately and rapidly, therefore, can be operated at isothermal condition (Ehrfeld et al., 2000). Few researchers have also tried to carry out fast and exothermic reactions in continuous stirred tank reactors (CSTRs). For example, Veretennikov et al. (2001) reported the continuous production of nitrochlorobenzene using series of CSTRs. Authors used nitric acid as a nitrating reagent and showed that in this reaction system variation in stirring rate did not affect the reaction rate. On the contrary, Quadros and Baptista (2003) used nitric and the sulphuric acid mixture as a nitrating reagent for adiabatic nitration of benzene in pilot-scale single CSTR (1.06 L reactor volume). Authors reported mass transfer limitation and therefore successfully employed two-film theory to predict the benzene concentration in the outlet stream. Cui et al.

(2015) also tried to model the nonlinear dynamics of CSTR of alkylpyridines N-oxidation for the safe operation of CSTRs for the particular reaction.

As stated earlier, it is very important to know the heat generation in the reactor to operate the CSTRs in safe mode without compromising on the production rate. In a view of introduction, this chapter discusses all the possible routes of the safe operation without compromising on the production rate considering one case study by numerical simulations of CSTR(s). These safer routes can be CSTRs in parallel, CSTRs in series or combination of both or multipoint dosing. All these routes are explored by considering one case study.

## 8.2 Nitration of by-aryl compound

In a nitration reaction, a nitro group is introduced onto a carbon, nitrogen or oxygen of the organic compound when it is reacted with the nitrating reagent. A nitrating mixture of nitric acid and sulfuric acid is the most common nitrating agent used for aromatic nitration. Most of the aromatic reactions such as nitration of benzene or nitration of xylene are liquid phase reactions, therefore can be handled easily in continuous flow processes using micro-reactor concept. However, reactions involving solids are difficult to handle in such reactors. One of the examples is nitration of naphthalene (Olah et al., 1981). It is reported in the literature that the combination of solvent and nitrating reagent affect the selectivity for the case of naphthalene nitration. Along with the reagent the ratio of products viz. 1-Nitronaphthalene ( $\alpha$ ) and 2-Nitronaphthalene ( $\beta$ ) also depends on various factors such as temperature, reaction time, Naphthalene to Nitric acid mol ratio and solvent used for the reaction. 1-Nitronaphthalene ( $\alpha$ ) is the major product and has a commercial importance. In case of nitration of anthracene, same authors reported that at 0-5 °C, the nitronium salt ( $\text{NO}_2^+\text{BF}_4^-$ ) react with anthracene to give 9-Nitro-anthracene.

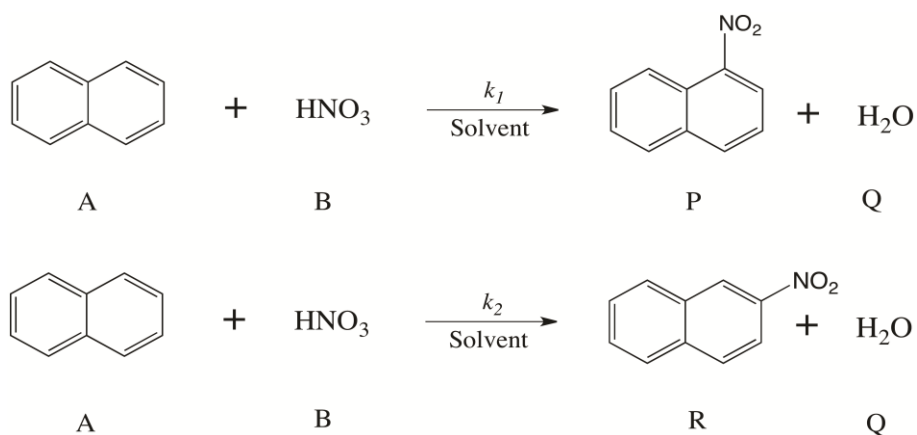
In this work, we present an analysis of the continuous production of 1-Nitro naphthalene using series of Continuous Stirred Tank Reactors (CSTRs), taking safety aspects into consideration. One of the reasons for choosing CSTRs over PFR (Plug Flow Reactor) is that naphthalene forms a solid suspension with the solvent. As mentioned, Naphthalene is in a solid state, and its solubility in the solvent at room temperature is approximately 5% w/v. Usage of this huge amount of solvent can lead to its loss during the process. Moreover, it diluted solution also slows the progress of the reaction. Therefore, it becomes a necessity to use a high



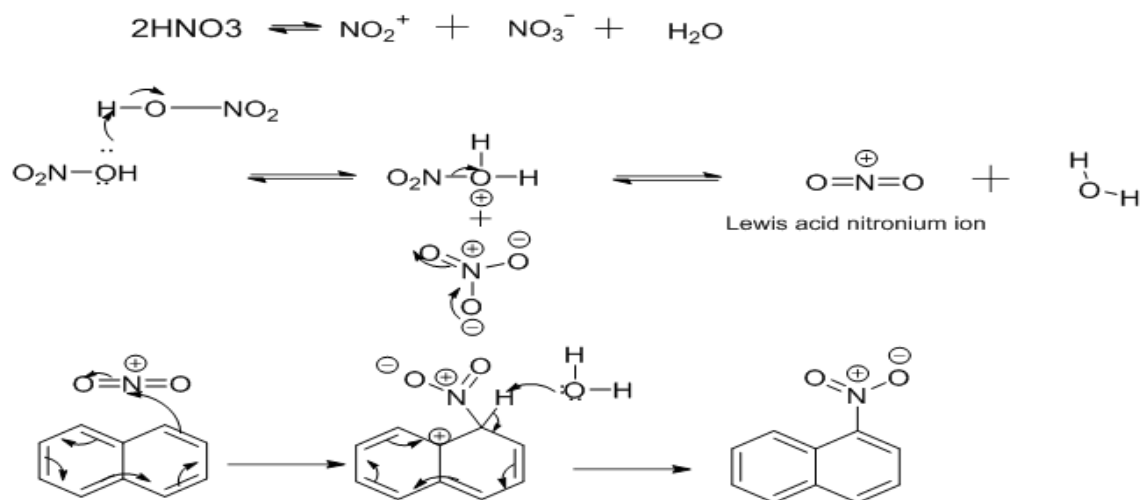
concentrated slurry of the naphthalene. It is very hard to make solid suspensions flow in small tubular reactors for higher inlet concentration as chances of PFR getting clogged are huge. Therefore, CSTR seemed to be the best option, as agitation helps in keeping solid particles suspended during the course of the reaction. It is important to realize that, numerical predictions play important role in optimizing the conditions for smooth and effective operation of any reactor. Therefore, numerical predictions using theoretical modeling were used to do the systematic study and observe the effect of various parameters on the overall production of the desired product.

### 8.2.1 Reaction

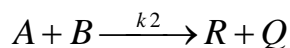
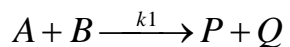
The synthesis of 1-nitro naphthalene is an aromatic electrophile substitution reaction. The naphthalene acts as a nucleophile and nitronium ion ( $+NO_2$ ) acts as an electrophile. Source of nitronium ion is a nitric acid. Two molecules of nitric acid give one molecule of nitronium ion and one molecule again gets back converted into nitric acid (Eberson and Radner, 1987). Nitronium ion is a Lewis acid (electron deficient) and naphthalene is a nucleophile (electron rich species). Nitration of Naphthalene is an electrophilic substitution reaction which on nitration forms 1-Nitronaphthalene ( $\alpha$ ) as a major product and 2-Nitronaphthalene ( $\beta$ ) as a minor product. Olah et al. (1981) reported that with nitronium salt ( $NO_2^+BF_4^-$ ) as reagent 1-Nitronaphthalene ( $\alpha$ ) at 25  $^{\circ}C$  and 20 minutes of batch time forms Di-nitronaphthalene. However, with other reagents, the formation of Di-nitronaphthalene takes place at very high temperature.



Mechanism-



In the chapter, hereafter, Naphthalene,  $\text{HNO}_3$  (69% w/w), 1-Nitro naphthalene, 4-Nitro naphthalene,  $\text{H}_2\text{O}$ , and solvent are referred as A, B, P, R, Q and S respectively. The reaction can now be given as follow:



here,  $k_1$  and  $k_2$  are rate constants and their ratio depends on the reaction temperature.

### 8.3 Experimental Section

#### 8.3.1 Set up for kinetics study

Separate experimental set up was arranged for kinetic measurements. The experimental set up consists of two syringe pumps for two reactants and the tubular reactor (see Figure 8.1). The tubular reactor has several outlets to collect the samples. The experiments were carried out at different flow rates and different residence time. Experiments were repeated several times and at different temperature and the samples were analyzed using Gas Chromatography (GC).

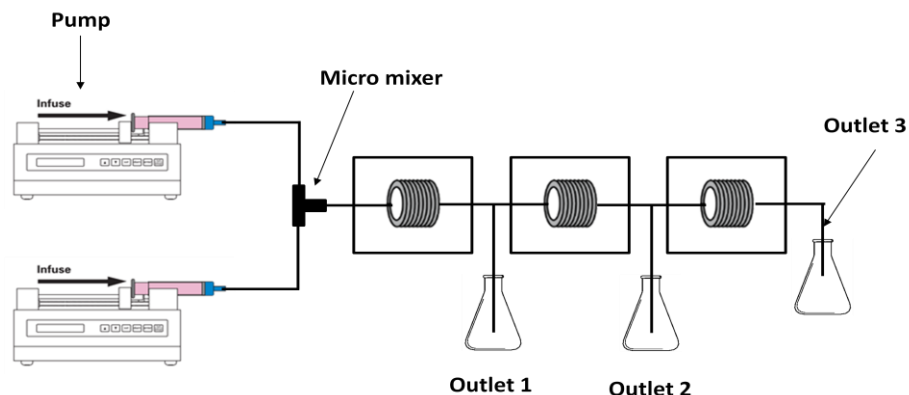


Figure 8.1: Experimental Set up for kinetics study

### 8.3.2 Experimental Set up of Continuous Stirred Tank Reactors (CSTRs)

All the experiments were carried out using series of 2 CSTRs of volume 150 ml each. The residence time ( $\tau$ ) was varied over a range of 6 to 15 minutes. The reactors used have a jacket for heat transfer. The coolant flow rate was maintained at 15 liters/min. Coolant temperature was maintained constant. The inlet concentration of 5.7 millimoles/ml of naphthalene (A) was maintained throughout the experiment and concentrated  $\text{HNO}_3$  (B) (69% w/w) was used as a nitrating reagent. The flow rate of each reactant was calculated considering the molar flow rate ratio ( $F_{B0}/F_{A0}$ ) as 2. Reactants were pumped using piston pumps. Since the boiling point of  $\text{HNO}_3$  (B) is 83 °C, it is advisable to operate the reactor at below 50-60 °C considering the safety aspects. The rate of any reaction, in general, is the highest at the beginning of the reaction and therefore the heat load is at peak at the start. To minimize the heat load in the reactor at the beginning of each experiment, CSTRs were initially filled with a solvent of volume 150 ml. The reaction was allowed to happen for 30 minutes and samples were collected at the outlet of CSTR1 and CSTR2. Collected samples were first given an acid wash to remove the acid traces and then organic phase and acid phase were separated. Samples were analyzed using GC and conversion and yield was recorded.

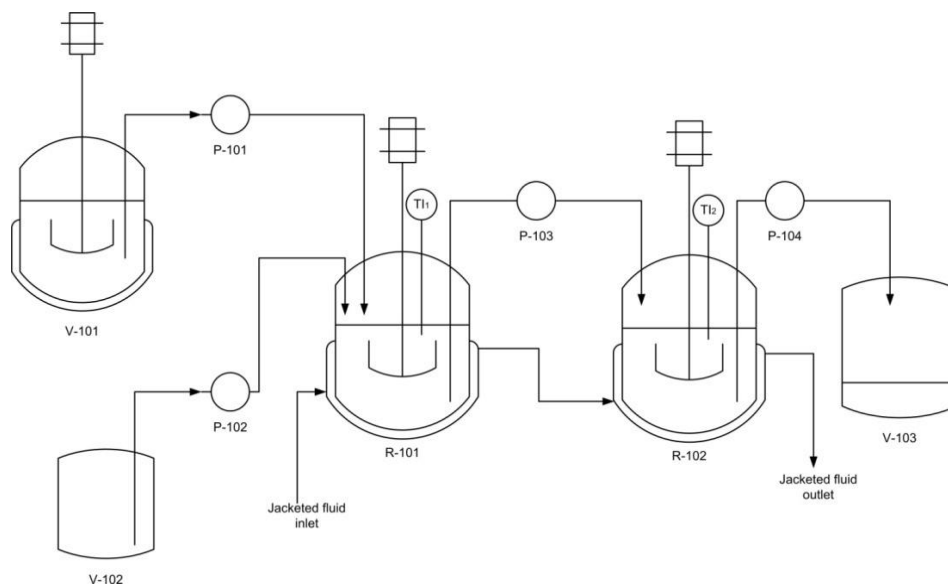


Figure 8.2: Experimental Set up for the production of 1-Nitro naphthalene (V-101 – stock solution naphthalene, V-102 – HNO<sub>3</sub> reservoir, P-101, 102, 103, 104 – Pumps used for the continuous operation, R-101 – CSTR1, R-102 – CSTR2, V-103 – Product container).

#### 8.4 Numerical Modelling

A dynamic continuous stirred tank reactor (CSTR) model is used in the present case to predict the behavior of CSTR(s). The model assumes constant inlet and outlet volumetric flow rates, constant coolant flow rate, constant coolant inlet temperature, and constant heat transfer area. Similarly, it also assumes that the physiochemical properties of the species to remain constant with the increase or decrease in the temperature of the reactor. The reaction is assumed to be pseudo-homogeneous. Therefore, the mass transfer effects can be neglected. The governing equations representing mass balance and energy balance for each species are given below (Fogler, 1999);

$$\frac{dC_A}{dt} = r_A + \frac{C_{A0} - C_A}{\tau} \quad 8.1$$

$$\frac{dC_B}{dt} = r_B + \frac{C_{B0} - C_B}{\tau} \quad 8.2$$

$$\frac{dC_P}{dt} = r_P + \frac{C_{P0} - C_P}{\tau} \quad 8.3$$

$$\frac{dC_Q}{dt} = r_Q + \frac{C_{Q0} - C_Q}{\tau} \quad 8.4$$

$$\frac{dC_R}{dt} = r_R + \frac{C_{R0} - C_R}{\tau} \quad 8.5$$

$$\frac{dC_S}{dt} = \frac{C_{S0} - C_S}{\tau} \quad 8.6$$

$$\frac{dT_{rx}}{dt} = \frac{Q_{RJ} + (r_A)V(-\Delta H_{Rx}) + F_{A0} \sum \phi_i C_{Pi}(T_{rx} - T_A)}{V \sum C_i C_{Pi}} \quad 8.7$$

$$\frac{dT_{Jout}}{dt} = \left\{ 1 - \exp\left(\frac{UA}{m_c C_{PC}}\right) \right\} \frac{dT_{rx}}{dt} + \left\{ \exp\left(-\frac{UA}{m_c C_{PC}}\right) \frac{dT_{Jin}}{dt} \right\} \quad 8.8$$

$$Q_{RJ} = m_c C_{PC} (T_{Jin} - T_{rx}) \left( 1 - \exp\left(\frac{-UA}{m_c C_{PC}}\right) \right) \quad 8.9$$

here,  $C_i$ ,  $r_i$ ,  $C_{Pi}$  and  $F_{Ai}$  are the concentration, rate expression, specific heat capacity and molar flow rate of the  $i$ th species.  $\Delta H_{Rx}$  is the heat of reaction,  $T_{rx}$  is the reactor temperature and  $Q_{RJ}$  is the heat removal rate using coolant.  $T_{Jin}$  is the inlet coolant temperature and  $m_c$  and  $C_{PC}$  are mass flow rate and specific heat capacity of the coolant, respectively. Detailed rate expression for each of the chemical species is given in the Appendix 1. Overall heat transfer coefficient ( $UA$ ) is calculated using heat transfer coefficient of process side and jacket side and conduction of material of reactor (MOC). The overall heat transfer coefficient can be given as follows:

$$\frac{1}{UA} = \frac{1}{h_i A_i} + \frac{1}{h_o A_o} + \frac{\left\{ \ln\left(\frac{D_{ji}}{2}\right) - \ln\left(\frac{T}{2}\right) \right\}}{2\pi H k_{MOC}} \quad 8.10$$

here,  $h_i$  and  $h_o$  are heat transfer coefficient of process side and jacket side, respectively.  $D_{ji}$  is the internal diameter of jacket,  $T$  is the reactor tank diameter and  $H$  is the height of reactant mixture in the reactor. All the process side, jacket side calculations are given in the Appendix 1.

## 8.5 Results and Discussions

### 8.5.1 Validation of numerical predictions

#### 8.5.1.1 Kinetics development

Results obtained from kinetics study experiments were analyzed as concentration vs. time data for each species for different temperatures. Both reactions (described above) were found to follow second order kinetics. The details on the kinetic parameters are given in Table 8.1. The reaction kinetics estimated in the present study are the lumped kinetics obtained under the assumption that the reaction rates are independent of interfacial mass transfer resistance. The heat of the reaction was estimated by Group Contribution Method (Joback Method) (Joback and Reid, 1987). The details on the Joback Method are given in Appendix 2. All the estimated parameters were used to accurately predict dynamic functioning of CSTR(s).

Table 8.1: Kinetic parameters of the given reaction scheme

Reaction	Pre-exponential frequency factor	Activation energy ( $E_a/R$ )
1	$2.5232 \times 10^5$	2271.71
2	$1.0067 \times 10^5$	2298.75

#### 8.5.1.2 Comparison of numerical results with experiments

Initial simulations were carried out for determining the operating conditions for lab scale experiments. The concentration of 'A' was chosen such that it forms a slurry in a solvent which is an advantage for stirred tank reactors over micro-reactors. Molar flow ratio ( $F_{B0}/F_{A0}$ ) was kept constant at 2. Simulations for different volume and different resident times were carried out to set the experimental conditions. Based on the initial simulation data, for 150 ml volume CSTR, the residence time of 10 to 15 minutes the temperature in the reactor found to be in the operating regime (50-60 °C). Hence, experiments in the CSTRs were carried out in the above temperature range. At this operating conditions, conversion at the end of a CSTR was found to be around 91%. Therefore, it was decided to carry out the experiments in CSTRs in series to achieve the complete conversion.

As mentioned earlier experiments were conducted in a series of glass reactors of volume 150 ml each and rise in the temperature with respect to time was recorded inside the first CSTR. Samples at the outlet of each CSTR were collected and analyzed to compare the conversion and yield of the product. Figure 8.3 gives the comparison between experiments and numerical predictions of temperature rise in the first CSTR. Numerical predictions show the steady state temperature in the reactor; however, it does not capture the initial trend. This can be attributed to the limitations of the model in considering the homogeneous model, as at the start the temperature in the reactor is less hence the operation can be termed as solid-liquid. In other words, it is due to the mass transfer limitations at the start of the process, which is not taken into account in the model. However, once it overcomes the temperature limitations, the numerical results found to predict the temperature profiles as that of experimental. The effect of the presence of an aromatic substrate in the solvent at the start-up of CSTR can be seen next section (Start-up of CSTR). Table 8.2, gives the steady state comparison of conversion and yield percentage at the outlet of CSTR1. From Figure 8.3 and Table 8.2, it can be observed that numerical results are good in agreement with that of experimental. Experiment 1 and Experiment 2 are repeat experiments at the same condition. Results suggest that numerical modeling can be used to optimize the overall process of continuous production  $\alpha$ -nitro derivative using series of CSTRs.

Table 8.2: Comparison of experimental results with that of numerical predictions

	Experiment 1	Experiment 2	Numerical Predications
Conversion	0.87	0.91	0.902
Yield (P)	0.85	0.89	0.86

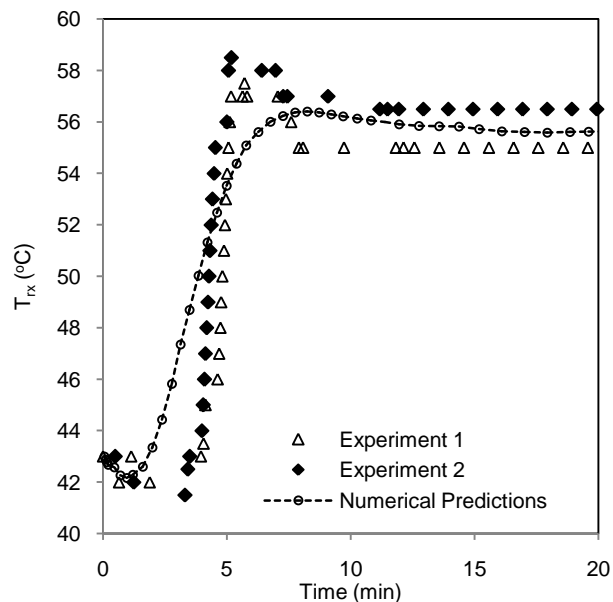


Figure 8.3: Temperature profile of CSTR1 with respect to time.

### 8.5.2 Dynamics of start-up of CSTR

The most critical part of the operation in CSTRs is the start-up procedure. The concentrations of the reactants are high at the beginning of the reaction and hence the heat load is maximum. This scenario can be handled properly by having a CSTR filled with solvent or water before start-up. Figure 8.4, shows the effect of different reacting fluid or solvent filled in the reactor before start-up. The figure clearly shows that, before start-up, if the reactor has some amount of aromatic substrate in the solvent, the temperature will first shoot up and comes down to steady state (same can be observed from experimental temperature data). A similar thing can be observed for nitric acid, however, the specific heat capacity of nitric acid is lower compared to the substrate and solvent and hence the heat load is minimal. On the other hand, if we have reactor filled with water or solvent, at first temperature drops down by 1 or 2 degrees and then shoots up as the reaction progresses and then comes down to steady state. The time at which system reaches steady state depends on the fluid used to fill the reactor before start-up. In general, the steady of the system reaches after passing 2-3 fold volume of the reaction mixture



through the reactor. In present work, all the further simulations were done considering solvent filled in the reactor before start-up.

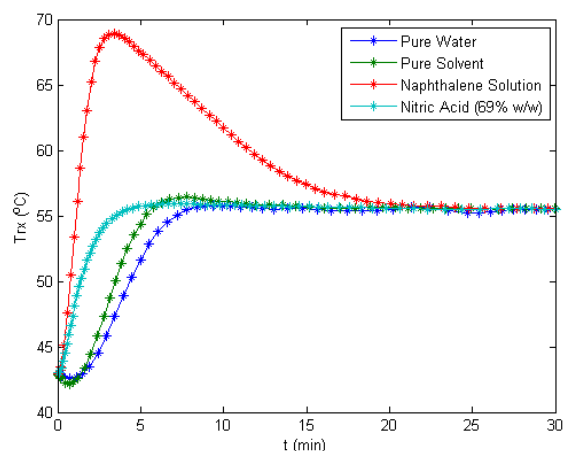


Figure 8.4: Temperature variation in CSTR1 with respect to time.

### 8.5.3 Effect of various parameters on the production

In general, production of the desired product depends on several parameters such as residence time ( $\tau$ ), volume of the reactor ( $V$ ), temperature of the reactor ( $T_{rx}$ ), molar flow ratio of the reactants ( $F_{B0}/F_{A0}$ ), inlet concentration of the reactants ( $C_{A0}$ ,  $C_{B0}$ ) and coolant temperature ( $T_{j_{in}}$ ). It becomes important to study the effect of these parameters to come up with better-operating conditions.

#### 8.5.3.1 Inlet concentration ( $C_{A01}$ ) and molar flow rate ratio ( $F_{B0}/F_{A0}$ )

Keeping the volume of the reactor as same as experimental the effect of inlet concentration of  $A$  ( $C_{A01}$ ) and molar flow ratio was studied using numerical simulations. Figure 8.5 (A-C) illustrates the effect on the temperature. From the figures, it can be observed that for a fixed initial concentration of  $A$ , the temperature in the reactor goes down with an increase in  $F_{B0}/F_{A0}$ . Similar observations can be made by low inlet concentration at fixed  $F_{B0}/F_{A0}$ . This is entirely attributed to the dilution in the system. With constant residence time and volume of the reactor, the total volumetric flow rate gets fixed. Therefore, at higher  $F_{B0}/F_{A0}$  the concentration of  $A$  in the well-mixed reactor is much lesser compared that at lower  $F_{B0}/F_{A0}$ . However, the conversion at higher  $F_{B0}/F_{A0}$  is higher compared to that at lower  $F_{B0}/F_{A0}$ , which almost attains

plateau after  $\frac{F_{B0}}{F_{A0}} = 2$  (see Figure 8.5E). In addition, the production is fairly high at  $\frac{F_{B0}}{F_{A0}} = 2$  (see Figure 8.5F). These studies reveal that  $\frac{F_{B0}}{F_{A0}} = 2$  with  $C_{A01} = 5.7$  milimoles/ml are the optimized operating conditions for CSTRs.

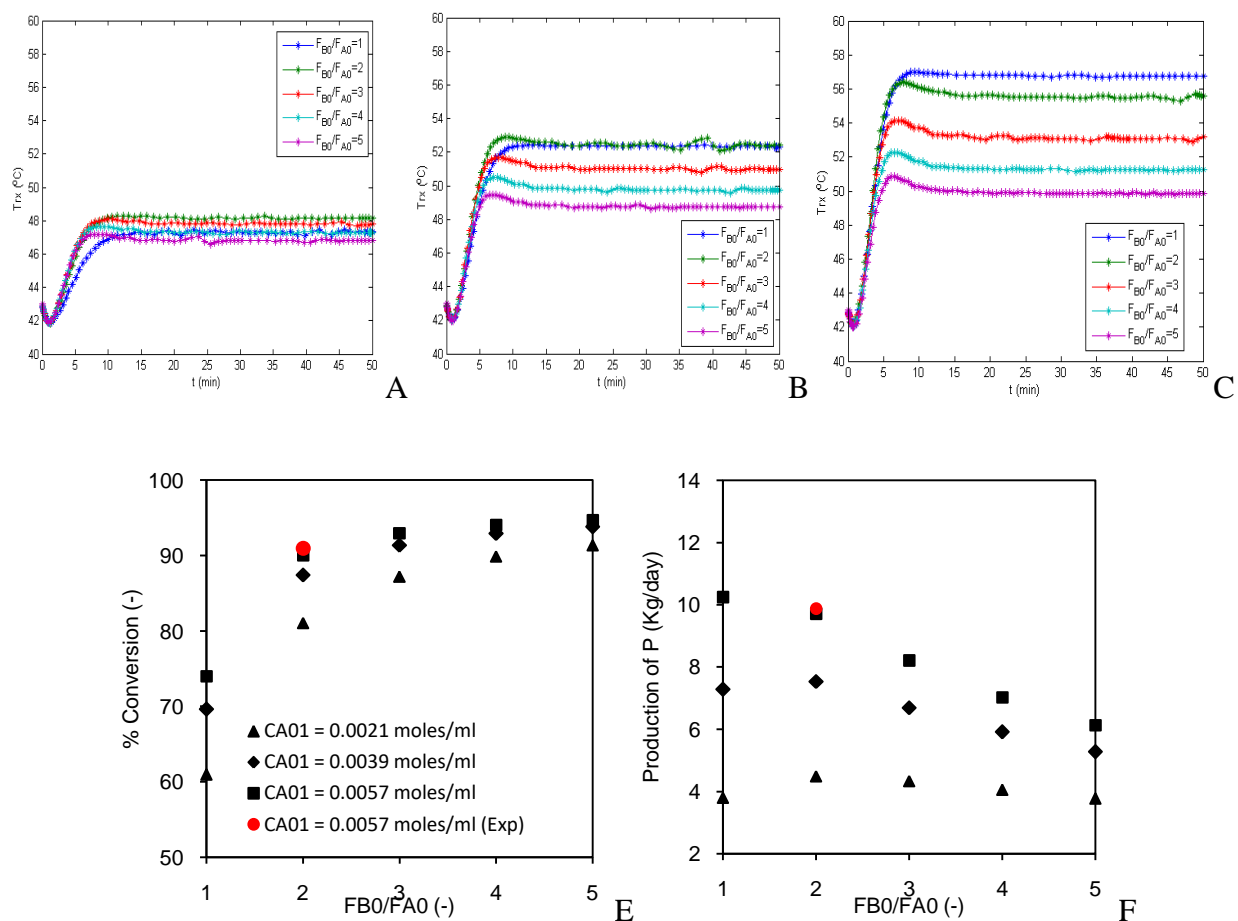


Figure 8.5: Reactor temperature profiles at different molar ratio A)  $C_{A01}=2.1$  milimoles/ml, B)  $C_{A01}=3.9$  milimoles/ml, C)  $C_{A01}=5.7$  milimoles/ml, E) Conversion vs Molar flow ratio ( $F_{B0}/F_{A0}$ ), F) Production (kg/day) vs Molar flow ratio ( $F_{B0}/F_{A0}$ ).

### 8.5.3.2 Effect of volume of the reactor ( $V$ ) and Residence time ( $\tau$ )

Results from the last section were taken into consideration for studying the effect of volume of the reactor ( $V$ ) and the residence time ( $\tau$ ). The inlet concentration of A ( $C_{A01}$ ) was maintained at 5.7 milimoles/ml and molar flow rate ratio ( $F_{B0}/F_{A0}$ ) as 2. The calculations were done considering glass jacketed reactors where jacket inlet ( $T_{j,in}$ ) temperature was set at 27 °C. It

should be noted that all the scale up guidelines were followed and scale up related equations are given in Appendix 1.

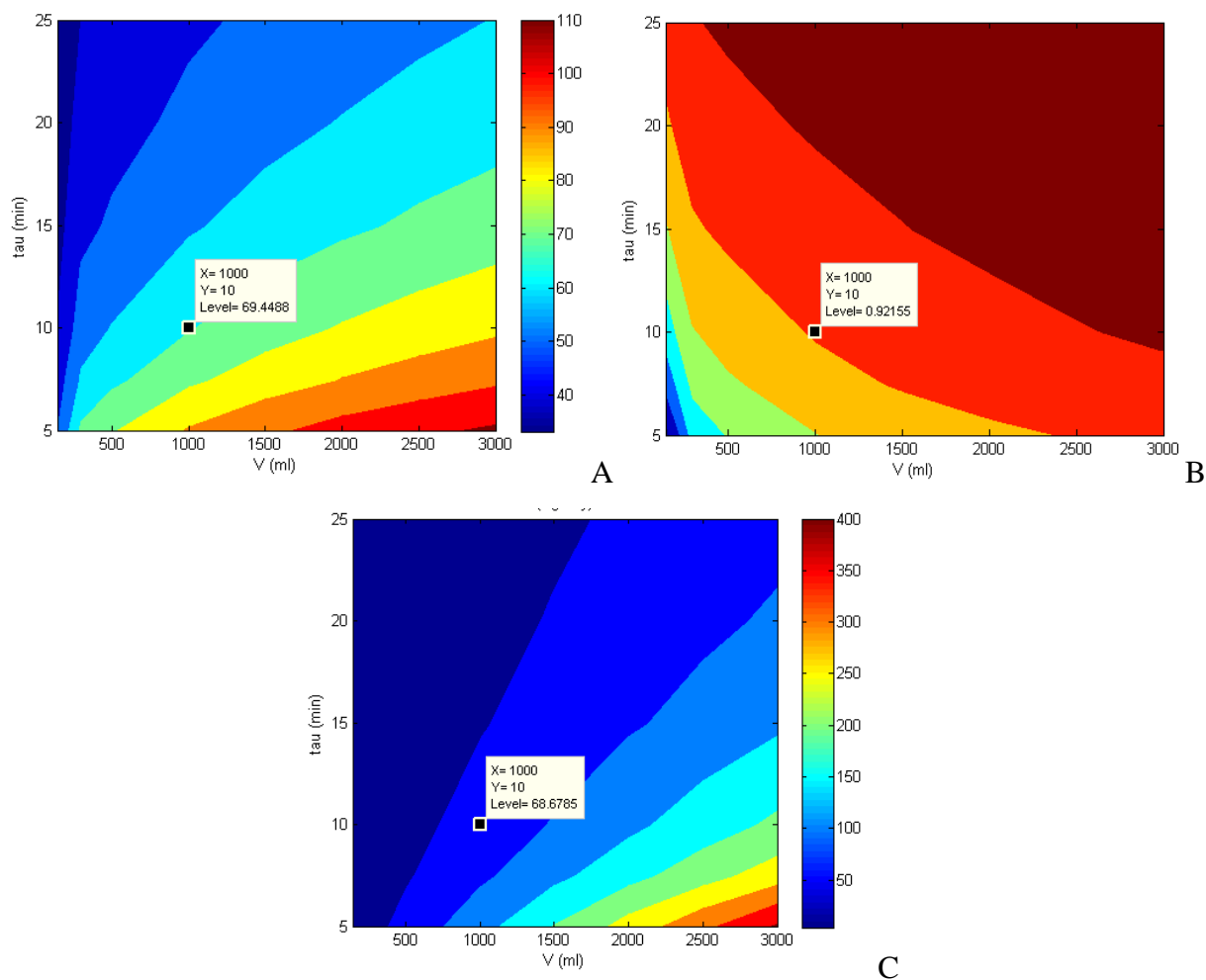


Figure 8.6: Effect of volume of the reactor and residence time on A) Temperature ( $T_{rx}$ ) in the reactor, B) Percent conversion, C) Production (kg/day).

It is clear from the Figure 8.6 (A-B) that the CSTR can be operated at higher residence time and at a larger volume of the reactor, as the temperature in the reactor for this range is  $60 \pm 10$  °C. Also, the percent conversion of reactant 'A' is on the higher side. However, the production at this range of  $\tau$  and  $V$  is the minimum. Therefore, by considering all the three requirements ( $T_{rx}$ , conversion and highest production), the acceptable operating point is  $V = 1000$  ml and  $\tau = 10$  minutes. The effect of other parameters such as coolant inlet temperature and

coolant flow rate were studied considering the reactor volume of 1000 ml and residence time of 10 minutes.

### 8.5.3.3 Effect of coolant inlet temperature ( $T_{J_{in}}$ ) and coolant mass flow rate ( $m_c$ )

The effect  $T_{J_{in}}$  of and  $m_c$  on the steady state operation was studied using the energy balance equation. The steady state point of CSTR operation is said to be achieved when heat-generated curve intersects with that of heat-removal (see Figure 8.7). The equations equation for both the curves are given below;

$$Q_R = m_c C_{P_C} (T_{rx} - T_{J_{in}}) \left( 1 - \exp\left(\frac{-UA}{m_c C_{P_C}}\right) \right) + F_{A0} \sum \phi_i C_{P_i} (T_{rx} - T_A) \quad 8.11$$

$$Q_G = (r_A)V(-\Delta H_{Rx}) = -F_{A0}X_A(-\Delta H_{Rx}) \quad 8.12$$

here,  $Q_R$  and  $Q_G$  are heat removal and heat generation curves respectively. The heat generation curve is plotted against the temperature using mole balance. However, the heat removal curve is plotted against the temperature using flow and heat exchange. A careful observation of Figure 8.7A, suggest that one would observe more than one steady state if parameters changed slightly. However, the operation conditions for such scenario is ruled out in the present study as to minimize the operating cost by feeding coolant above 15 °C. In this case only a single intersection point between  $Q_R$  and  $Q_G$  can be observed (Figure 8.7B). Hence the effect of coolant inlet temperature and coolant flow rate on steady state operation was studied. From Figure 8.7, it can be observed that the increase in the coolant inlet temperature shifts the steady state towards unsafe operation. On the other hand, increase in the coolant flow rate more than 5 Ltr/min does not result in much change in the operating conditions (see Figure 8.7C). This is attributed to the term  $\exp\left(\frac{-UA}{m_c C_{P_C}}\right)$  in the energy balance equation.

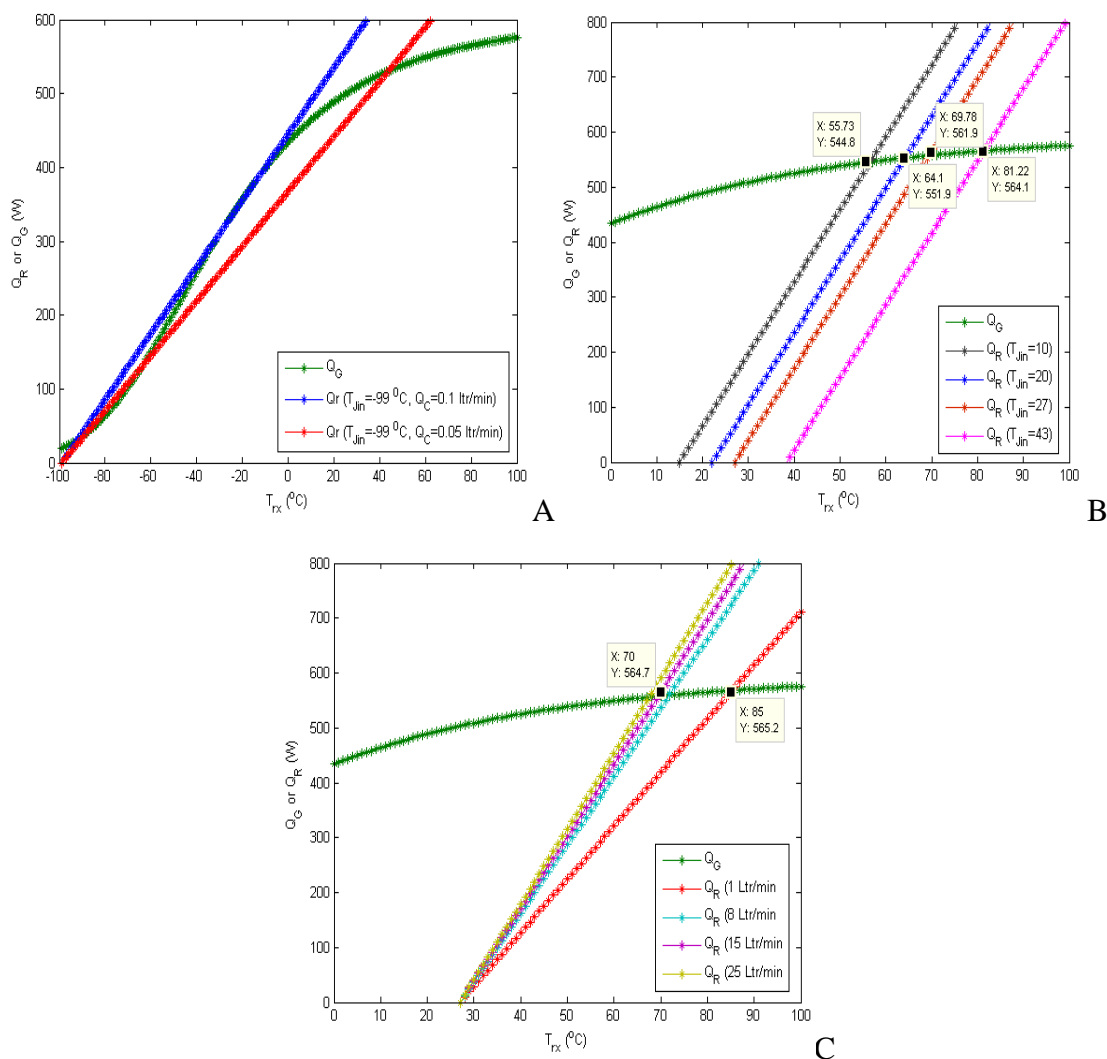
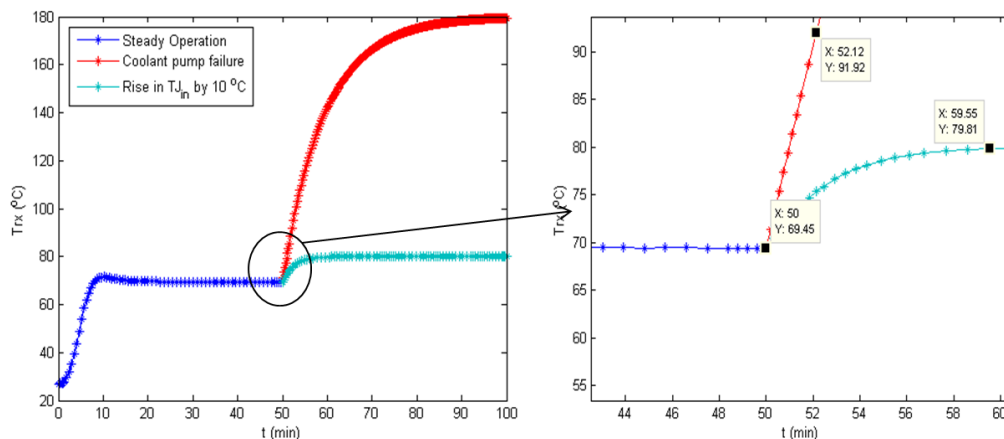


Figure 8.7: Effect coolant parameters A) Multiple steady states, B) Coolant inlet temperature, C) Coolant flow rate.

### 8.5.4 Safety aspects of the operation in CSTRs

It is important to look at the safety aspects of the operation in CSTR as a slight change in the inlet condition can lead to a rise in the temperature instantly. Two cases have been discussed in the present case where the problems while operating the CSTRs can be faced. For an instant, if the cooling pumps stop working or there is a power shutdown, in no time the temperature in the reactor shoots and reaches to the adiabatic temperature. Same can be observed in Figure 8.8. Whereas, rise in the coolant temperature by  $10^{\circ}\text{C}$ , shifts the steady state of the operation by  $10^{\circ}\text{C}$ .



A

Figure 8.8: Safety aspects related to the operation of CSTRs

### 8.5.5 Scale-up Strategies

Safety concerns are more noticeable in the large volume CSTRs to meet the desired production per day. Therefore, it is essential to discuss various strategies related to scale up of CSTRs. For the conviction, it was decided of the setting of a plant of minimum 150 Kg/day of  $\alpha$ -nitro derivative. It should be noted that the feasible operating range should be around 65 - 70 °C to avoid un-necessary events related to safety. The temperature in the reactor depends on the various parameters such as  $T_{J_{in}}$ , operating volume ( $V$ ), inlet concentration of Aromatic substrate ( $C_{A0}$ ), residence time ( $\tau$ ) molar flow rate ratio ( $F_{B0}/F_{A0}$ ) and thermal conductivity material of construction of the vessel. As per the scale up guidelines, the residence time and molar flow rate ratio have been maintained as that of lab scale (experimental). The effect of all these parameters was studied to come up with best scale-up strategies. To minimize the operating cost, simulations for scale-up strategies were carried out for  $T_{J_{in}} = 27$  °C. All the results are compiled and discussed in the later part of the section.

#### 8.5.5.1 Scheme I: Thermal conductivity ( $k_{MOC}$ ) = 1.06 W/m.K

Initially, conversion and operating temperature at different reactor volume and residence were simulated and studied (see Figure 8.9). Based on the observation it was evident that at a residence time of 10 minutes, operating volume less than 1000 ml (1 Ltr) as feasible for the

scale-up, however, it can produce only 69 Kg/day of the Nitro-aromatic substrate (Figure 8.9B). Moreover, it gives 92.5% conversion only (Figure 8.9C).

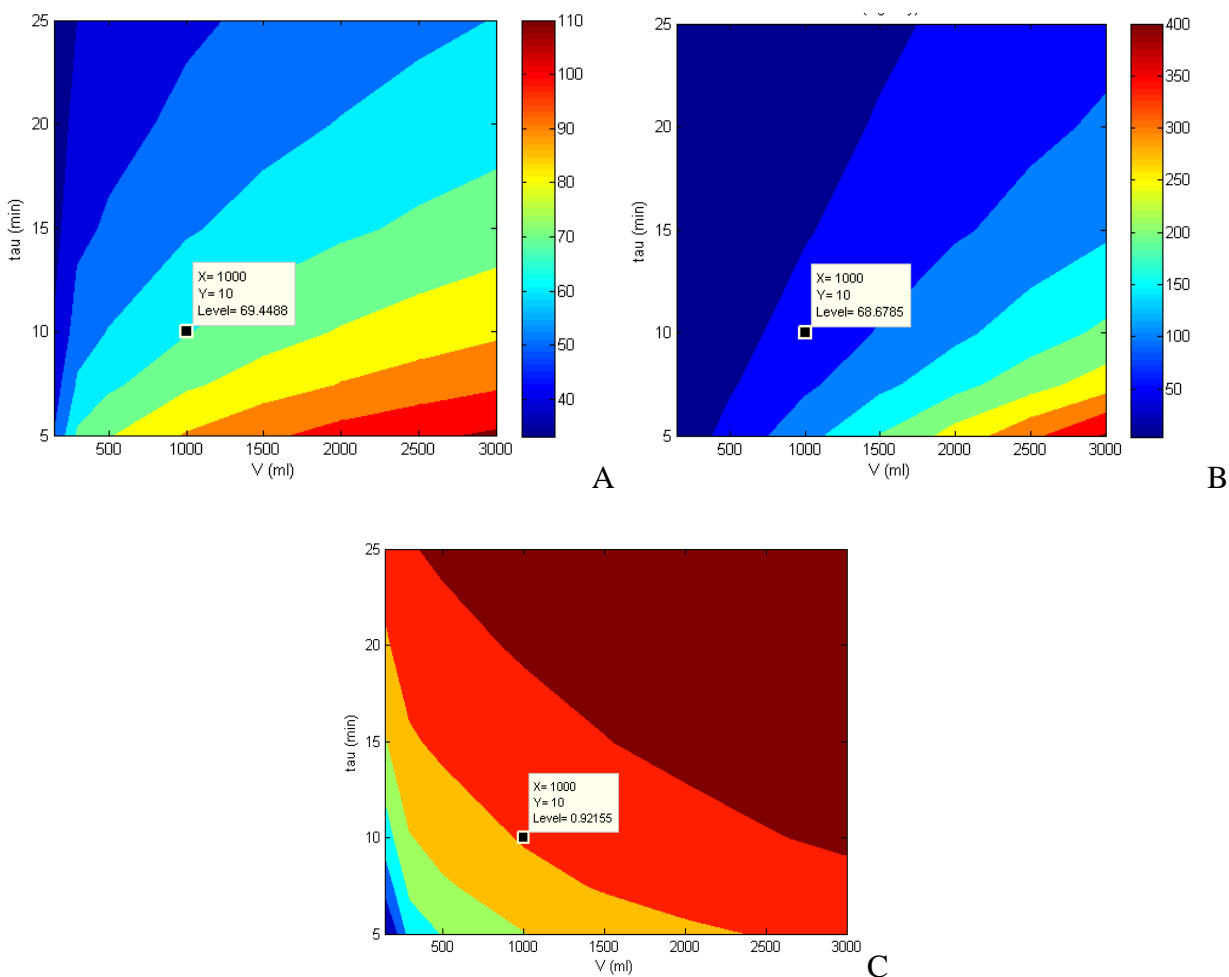


Figure 8.9: Effect of residence time and operating volume on various parameters for  $k_{MOC} = 1.06$  W/m.K. A) Temperature in the reactor, B) Production, C) Conversion.

Required production can be achieved by numbering-up and 100% conversion can be achieved by carrying out an operation in series of CSTRs. Keeping in mind the feasibility of operation, two parallel CSTRs of 1000 ml each followed by a CSTR of 2000 ml found to be the best choice for achieving the production of 150 Kg/day. The outline of the configuration is given in the Figure 8.10A. The temperature profiles of the reactors are given in the Figure 8.10B. The input streams of individual reactants are distributed equally in the two parallel CSTRs and the outlets of these two reactors are combined and serve input to the third CSTR in series. The

conversion and yield from two parallel reactors is 92% and 87% respectively. However, the third reactor in series helps to achieve 98% conversion of the substrate with 92% yield of desired product. The production of the desired product can be achieved as close to 148 Kg/day (Table 8.3).

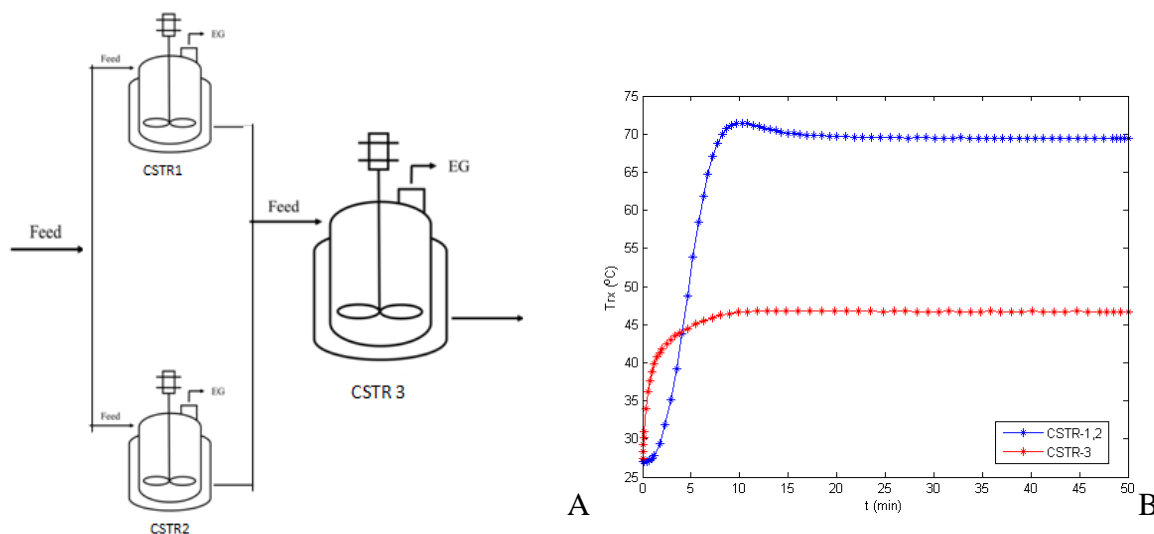


Figure 8.10: A) Reactor assembly for scale-up, B) Temperature in the reactors ( $k_{MOC}=1.06$  W/m.K).

Table 8.3: Production of  $\alpha$ -nitro derivative using material of thermal conductivity 1.06 W/m.K

Reactors/Results	CSTR-1 (Parallel)	CSTR-2 (Parallel)	CSTR-3 (Series)
Volume (ml)	1000	1000	2000
Distribution of reactants	50 %	50 %	-
Temperature ( $^{\circ}$ C)	70	70	46.5
Conversion ( $X_A$ )	92 %	92 %	98 %
Yield	87 %	87 %	92 %
Production (Kg/day)	68.5	68.5	148

#### 8.4.5.2 Scheme II: Thermal conductivity ( $K_{MOC} = 16.3$ W/m.K)

Similar to an earlier part, initially study for single CSTR of different volume at different residence time was carried out for higher thermal conductivity material. When results were compared with that of the reactor of lower thermal conductivity, it was observed that reactors



with higher thermal conductivity withstand the exothermic reactions at higher volume due to higher heat transfer rate which helps in withdrawing heat generated by reaction at a higher rate. (see Figure 8.9A and Figure 8.11A). The results showed that reactor volume up to 3000 ml can be used with MOC of thermal conductivity of 16.3 W/m.K. The single CSTR made up of this MOC can produce up to 203 Kg/day, however, it achieves the conversion of 90% (see Figure 8.11). Therefore, an additional CSTR in series can help in achieving the nearly complete conversion. The configuration is presented in Figure 8.12.

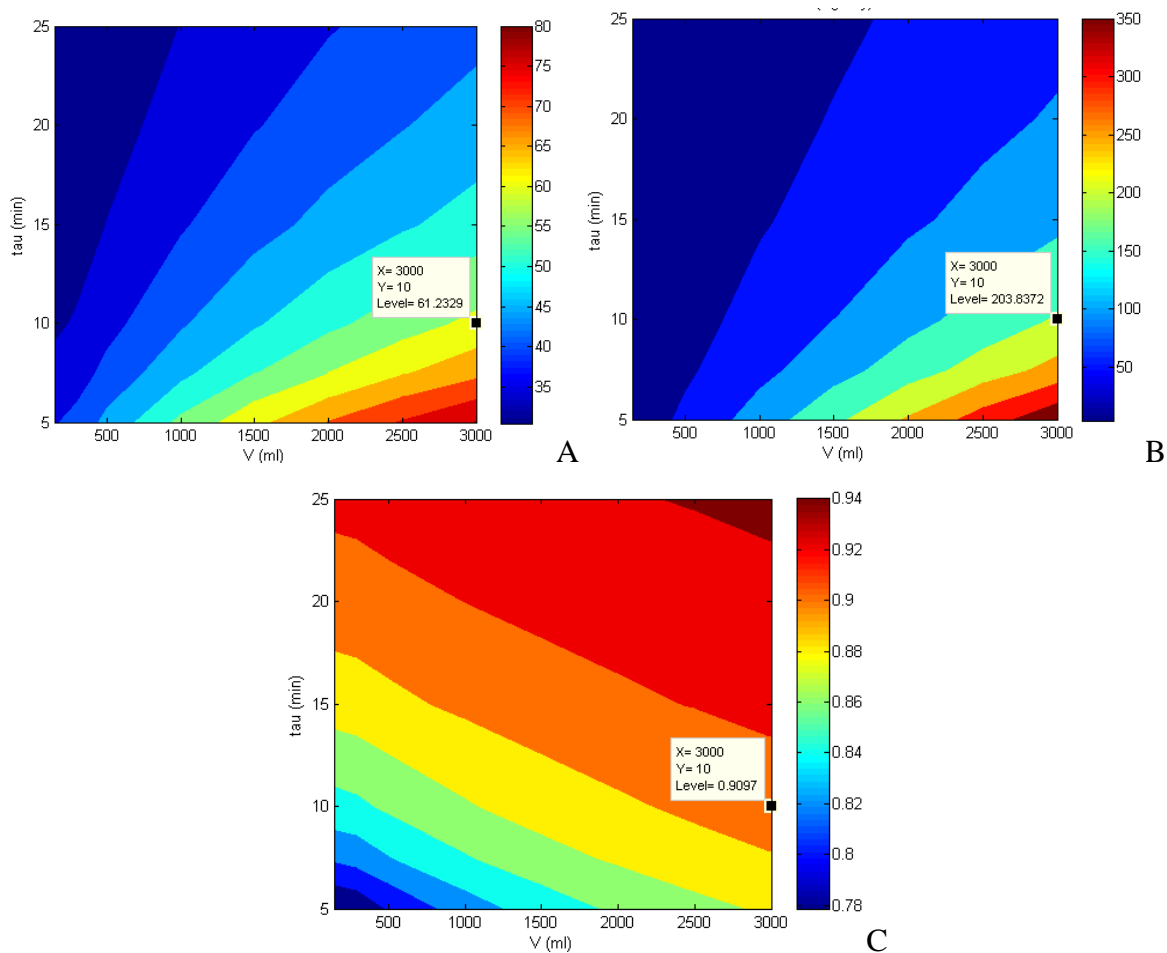


Figure 8.11: Effect of residence time and operating volume on various parameters for  $k_{MOC} = 16.3$  W/m.K. reactors A) Temperature in the reactor, B) Production, C) Conversion.

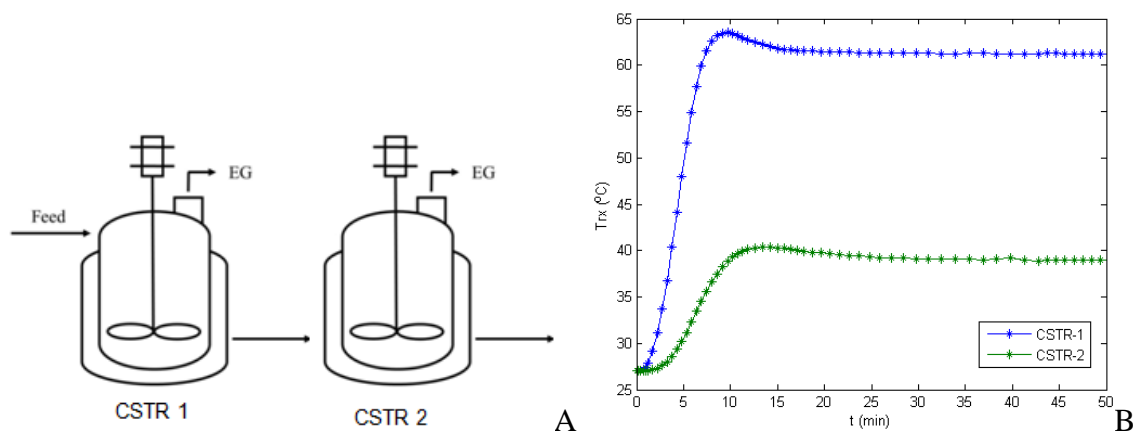


Figure 8.12: A) Reactor assembly for scale-up ( $k_{MOC} = 16.3 \text{ W/m.K}$ ), B) Temperature in the reactors

Table 8.4: Production of  $\alpha$ -nitro derivative using material of thermal conductivity  $16.3 \text{ W/m.K}$

Reactors/Results	CSTR-1	CSTR-2 (Series)
Volume (ml)	3000	3000
Distribution of reactants	100%	-
Temperature ( $^{\circ}\text{C}$ )	62	46.5
Conversion ( $X_A$ )	90%	98.64%
Yield	86.5%	92.75%
Production (Kg/day)	204	218

#### 8.4.5.3 Scheme III: Reactors configuration with multipoint dosing

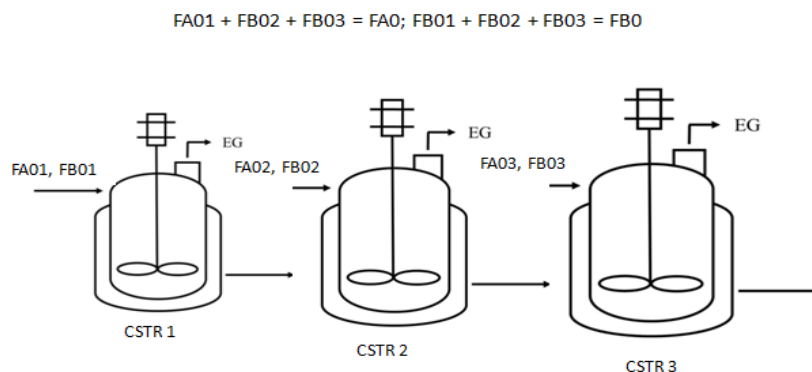


Figure 8.13: Schematic of multipoint dosing in CSTRs in series.

The distribution of two reactants in series of CSTRs play important role in operating a CSTR in a controlled manner. For example, if we have three CSTRs in series of different volume, the general practice has been to feed all the reactants in the first reactors. However, instead of feeding everything in first CSTRs, if the initial moles of A and B reactants is distributed in all CSTRs, it would have an impact on overall conversion as well as throughput. In the present case, we have explored the impact of distribution on production, operational temperature and conversion (yield) by considering three CSTRs in series of volume 3000 ml, 5000 ml, and 7000 ml respectively of higher thermal conductivity material ( $k_{MOC}=16.3$  W/m.K.). The total inlet molar flow rate has been kept constant for all the cases. The schematic of the arrangement is shown in Figure 8.13. The results are tabulated in Table 8.5.

Table 8.5 illustrates the effect of different multipoint dosing strategies in CSTRs with an objective of maximum production with safe operation. Among all the different options, Case-IIIB and Case-IIID found to be the appropriate choice. In these above two cases, the third CSTR is mostly been used to get near 100% conversion and hence the maximum production. The temperature profiles of each configuration are given in Figure 8.14.

Different scale-up approaches show that small change in operations or selection of the reactors can alter the overall throughput. For comparison, Case-I gives 150 Kg/day of production, Case-II 222 Kg/day and Case-III 522 Kg/day. This study shows that exothermic reactions can be handled in CSTRs if studied thoroughly. Numerical studies play an important role in covering every aspect regarding scale-up and safe operation.

Table 8.5: Multipoint dosing operations and respective results

		CSTR-1 (3000 ml)	CSTR-2 (5000 ml)	CSTR-3 (7000 ml)	Conversion (%)	Yield (%)	Production (Kg/day)
Case IIIA	Distribution (A)	100%	-	-	99.74	94.8	522.1
	Distribution (B)	100%	-	-			
	Temperature in reactor (°C)	85.16*	56.57	40.4			
	Residence time ( $\tau$ ) (min)	4.3	7.2	10			
Case IIIB	Distribution (A)	50%	50%	-	99.25	94.8	522.04
	Distribution (B)	100%	-	-			
	Temperature in reactor (°C)	69	70	46			
	Residence time ( $\tau$ ) (min)	5.93	7.14	10			
Case IIIC	Distribution (A)	100%	-	-	99.5	94.7	521.5
	Distribution (B)	50%	50%	-			
	Temperature in reactor (°C)	83.12*	63.5	43.8			
	Residence time ( $\tau$ ) (min)	5.5	7.2	10			
Case IIID	Distribution (A)	50%	50%	-	99.3	94.7	521.5
	Distribution (B)	50%	50%	-			
	Temperature in reactor (°C)	65	71.5	47.5			
	Residence time ( $\tau$ ) (min)	8.57	7.14	10			
Case IIIE	Distribution (A)	33.33%	33.33%	33.33%	96.3	92.2	507.7
	Distribution (B)	100%	-	-			
	Temperature in reactor (°C)	50	56	57			
	Residence time ( $\tau$ ) (min)	6.8	8.8	10			

\*unsafe operation

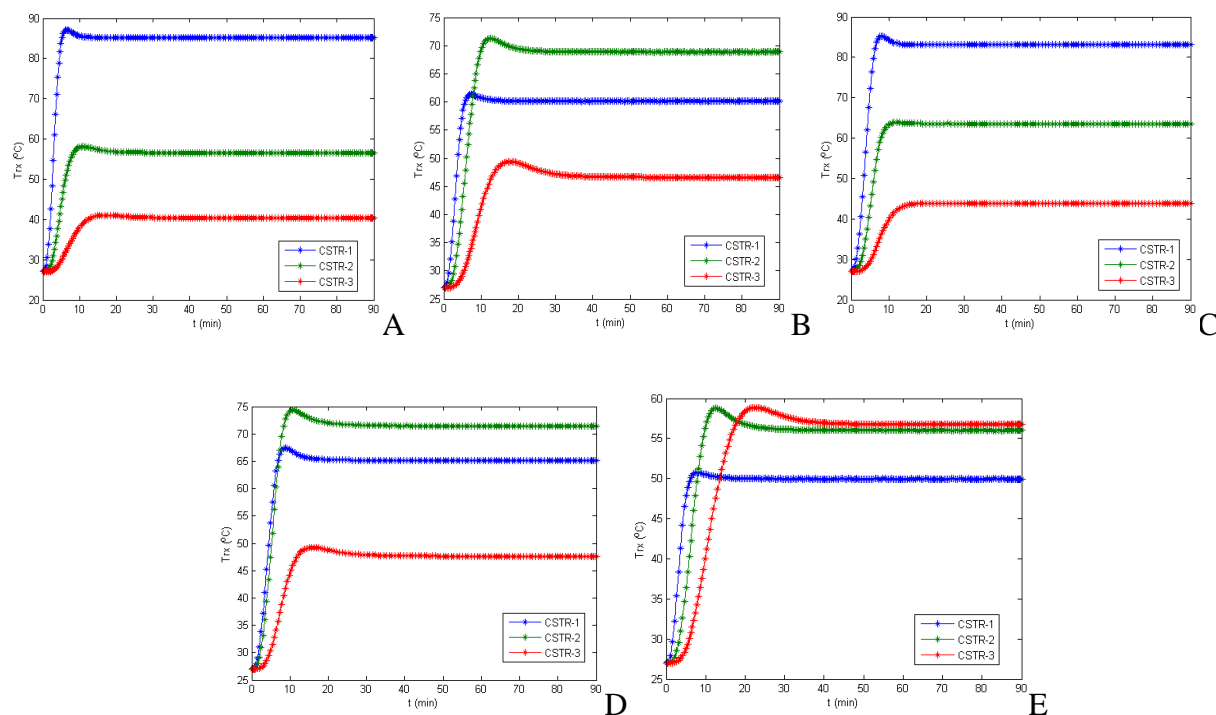


Figure 8.14: Temperature profiles of CSTRs A) Case-III A, B) Case-III B, C) Case-III C, D) Case-III D, E) Case-III E.

## 8.5 Conclusions

In this work, how CSTRs can be used for exothermic nitration reactions has been demonstrated. First, kinetics of reactions have been determined and were used to model the CSTR operation. Lab scale experiments were performed and results were compared with that of numerical. Numerical results found to predict the nature of the temperature profile in CSTR and conversion (yield). Effect of different parameters such as mole ratio, inlet concentration, jacket temperature, the volume of the reactor and residence time on the overall process has been discussed in details.

Different scale-up strategies have been adopted to maximize the production such as parallel CSTRs, Series of CSTRs and Multipoint dosing (minimum 150 Kg/day).

- i) Glass reactors configuration (two CSTRs of volume 1 liter in parallel followed by CSTR of volume 2 liter): The production of the desired product can be achieved as close to 148 Kg/day.

- ii) SS316L reactors configuration (two CSTRs of volume 2 liter each): The production of the desired product can be achieved as close to 218 Kg/day.
- iii) Multipoint dosing (three CSTRs of volume 3 liters, 5 liters and 7 liters in series): With the variable distribution of feed in three different reactors, different throughput can be achieved. The production of the desired product can be achieved as close to 522 Kg/day.

The simulations indicate that the multipoint dosing with variable volume reactors can be used for maximizing the production with safe operation. The numerical results show some promising performance of CSTRs for exothermic reactions and can be taken forward as the new tool for developing continuous flow process.

### Nomenclature

$A$	Naphthalene
$B$	Nitric Acid
$C_{i0l}$	inlet concentration of reactants or products
$C_{i0}$	initial concentration of reactants or products
$C_i$	concentration of $i$ th species
$C_{Pi}$	specific heat capacity of $i$ th species
$D$	diameter of the impeller
$D_{Ji}$	jacket internal diameter
$F_{i0}$	molar flow rate of reactants
$H$	height of the liquid in the tank
$h_i$	heat transfer coefficient of the process side
$h_o$	heat transfer coefficient of the jacket side
$\Delta H_{Rx}$	heat of reaction
$k$	thermal conductivity
$m_c$	mass flow rate of coolant
$N$	impeller speed
$Nu$	Nusselt number (-)
$P$	1-Nitronaphthalene (alfa)
$Pr$	Prandtl number (-)
$R$	2- Nitronaphthalene (beta)
$Re$	Reynolds number (-)
$Q$	water
$Q_R$	heat removal rate
$Q_G$	heat generation rate
$S$	solvent
$T$	tank diameter
$T_{rx}$	temperature in the reactor ( $^{\circ}$ C)
$TJ_{in}$	jacket inlet temperature ( $^{\circ}$ C)

$UA$	overall heat transfer coefficient
$V$	volume of the CSTR (ml)
$X_A$	conversion

### Greek letters

$\tau$	residence time
$\mu$	viscosity of the reacting mixture
$\rho$	density of the reacting mixture

### Appendix 1

#### *Process-side heat transfer ( $h_i$ ) calculations:*

The process side heat transfer coefficient can be calculated using correlations provided. The correlations are in the form of dimensionless numbers

$$Re = \frac{D^2 N \rho}{\mu} \quad A1$$

$$Pr = \frac{C_p \mu}{k} \quad A2$$

$$Nu = \frac{h_i T}{k} = a Re^{\frac{2}{3}} Pr^{\frac{1}{3}} \left( \frac{\mu}{\mu_w} \right)^{0.14} \quad A3$$

#### *Jacket side heat transfer ( $h_i$ ) calculations:*

Similar to process side calculations, jacket side correlations are also provided in the heat transfer book. However, the physical properties used in this case are of coolant fluid (water in the present case).

$$Re = \frac{(T_{Jo} - T_{Jin}) u \rho_w}{\mu_w} \quad A4$$

$$Pr = \frac{C_{pW} \mu_w}{k} \quad A5$$

for  $Re \leq 800$ ;

$$Nu = \frac{h_i T}{k} = 1.02 Re^{0.45} Pr^{\frac{1}{3}} \left( \frac{\mu}{\mu_w} \right)^{0.14} \left( \frac{T_{Jo} - T_{Jin}}{H} \right)^{0.4} \left( \frac{T_{Jo}}{T_{Jin}} \right)^{0.8} \quad A6$$

for  $Re \geq 4000$

$$Nu = \frac{h_i T}{k} = 0.027 Re^{0.8} Pr^{\frac{1}{3}} \left( \frac{\mu}{\mu_w} \right)^{0.14} \left( 1 + 3.5 \frac{(T_{Jo} - T_{Jin})}{(T_{Jo} + T_{Jin})/2} \right) \quad A7$$

for  $Re \geq 800$  and  $Re \leq 4000$

mean of above two equations has been taken to calculate the heat transfer coefficient.

## Appendix II

### Joback Method:

This is a well known method to predict the important and commonly used thermodynamic properties of a compound from its molecular structure. In other word, it is a group contribution method. The method uses basic structural information of a chemical molecule like a list of simple functional groups, adds parameters to these functional groups, and calculates thermophysical and transport properties as a function of the sum of group parameters. The method assumes that there are no interactions between the groups and therefore only uses additive contributions and no contributions for interactions between groups.



## References

Albright, L.F., Carr, R.V., Schmitt, R.J., 1996. Nitration: recent laboratory and industrial developments. ACS Publications.

Baldyga, J., Bourne, J., 1990. The effect of micromixing on parallel reactions. *Chemical Engineering Science* 45, 907-916.

Baldyga, J., Bourne, J., Hearn, S., 1997. Interaction between chemical reactions and mixing on various scales. *Chemical Engineering Science* 52, 457-466.

Cui, X., Mannan, M.S., Wilhite, B.A., 2015. Towards efficient and inherently safer continuous reactor alternatives to batch-wise processing of fine chemicals: CSTR nonlinear dynamics analysis of alkyipyridines N-oxidation. *Chemical Engineering Science* 137, 487-503.

Eberson, L., Radner, F., 1987. Electron-transfer mechanisms in electrophilic aromatic nitration. *Accounts of Chemical Research* 20, 53-59.

Ehrfeld, W., Hessel, V., Haverkamp, V., 2000. *Microreactors*. Wiley Online Library.

Fogler, H.S., 1999. *Elements of chemical reaction engineering*.

Joback, K.G., Reid, R.C., 1987. Estimation of pure-component properties from group-contributions. *Chemical Engineering Communications* 57, 233-243.

Kulkarni, A.A., 2014. Continuous flow nitration in miniaturized devices. *Beilstein Journal of Organic Chemistry* 10, 405.

Kulkarni, A.A., Kalyani, V.S., Joshi, R.A., Joshi, R.R., 2009. Continuous flow nitration of benzaldehyde. *Organic Process Research & Development* 13, 999-1002.

Olah, G.A., Narang, S.C., Olah, J.A., 1981. Nitration of naphthalene and remarks on the mechanism of electrophilic aromatic nitration. *Proceedings of the National Academy of Sciences* 78, 3298-3300.

Quadros, P.A., Baptista, C.M., 2003. Effective interfacial area in agitated liquid-liquid continuous reactors. *Chemical Engineering Science* 58, 3935-3945.

Veretennikov, E., Lebedev, B., Tselinskii, I., 2001. Nitration of chlorobenzene with nitric acid in a continuous installation. *Russian Journal of Applied Chemistry* 74, 1872-1876.

Zaldivar, J., Molga, E., Alós, M., Hernández, H., Westerterp, K., 1996. Aromatic nitrations by mixed acid. Fast liquid-liquid reaction regime. *Chemical Engineering and Processing: Process Intensification* 35, 91-105.

***Part III: Flow Past Objects in Small Channels***

**Chapter 9**  
**Effect of Shape of Microstructured Post on the  
Flow in Small Channels**

## 9.1 Introduction

Flow past object is an extensively studied phenomenon as it has many applications in aerodynamics, wind energy, fluid mechanics, heat transfer, impeller design for mixing etc. Recently, physics of flow past object also found to be applicable in microfluidics and microscale devices for various purposes. For example, the microstructured catalysts are used to fabricate the posts of different shapes within a reactor to create a large catalytic surface area (Losey et al., 2002; Ni et al., 2005). These microstructured catalytic posts are reported to perturb the flow and enhance the mixing (Deshmukh and Vlachos, 2005). Moreover, the built-in obstacle in the microchannels reported enhancing heat transfer and mixing in the microchannels (Jung et al., 2012; Meis et al., 2010). In addition, the sequence of micropillars in channels is used to engineer the fluid flow to achieve enhanced mixing and heat transfer (Amini et al., 2013; Stoecklein et al., 2016; Stoecklein et al., 2014). Most of the studies on this topic are limited to 2D geometries, where it is assumed that the variations in the third direction are minimal. However, considering microreactors and microstructures it becomes important to evaluate the effect of channel depth on the hydrodynamics of the given system.

The wake dynamics past different geometries is expected to be different due to the different flow separation points. For example, flow separation points are time dependent for circular cylinders, while they are fixed for the square cylinder at rear edges. In general, for a given object, different flow regimes can be observed by changing the upstream velocity (or Reynolds number ( $Re$ )). In the creeping flow regime (i.e.  $Re \leq 1$ ) viscous forces dominate the flow and boundary layer separation does not take place on the surface of the object. However, with an increase in  $Re$  flow starts to separate and forms a recirculation region consisting of two steady symmetric vortices behind the object. With further increase in  $Re$ , the steady flow appears to become unstable to small disturbances. These small disturbances eventually give rise to oscillation of the wake. The nature of vortices and their dynamics vary significantly depending upon the shape and  $Re$  and a detailed analysis can be found in (Zdravkovich, 1996) and (Williamson, 1996). Moreover, in case of flow past object in a straight channel, it also depends on blockage ratio.(Chakraborty et al., 2004; De and Dalal, 2007; Wham et al., 1996). In addition, if the channel is made up of arrays of such micropillars the interaction between wakes of two nearby pillars also changes the overall flow pattern in the channel. In a view of the above

discussion, the selection of structure of the micropillars and its arrays in the channel in the channel is critical and hence needs to be addressed. In addition, the effect of channel depth on the flow past objects also needs to be studied to identify the depth beyond which 2D flow simulations show features similar to simulations of a 3D geometry.

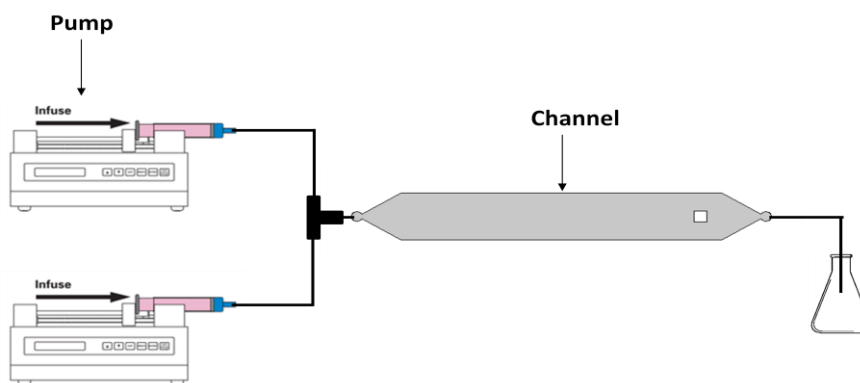
In the present work, we studied the numerical simulations for understanding the flow past object of different geometries in a small confined channel within a range of  $Re$  ( $0.1 \leq Re \leq 150$ ), where  $Re$  is based on the projected length. The geometries considered in this work are cylindrical posts of following cross-sectional shapes: elliptical, rectangular, triangular cylinders (with the base perpendicular to the flow and apex points upstream) and some fractal objects generated from square and triangle. Initially, experiments in a specially designed channel were carried out to observe the hydrodynamics of the channel. Experiments were followed by CFD simulations to get the details on the depth of the channel. In view of this, the objective of this work is to illustrate the effect of the shape of an object on corresponding wake dynamics in a channel. It also aims to use the results to suggest the most suitable post shape that would enhance mixing in the channel.

In view of the above introduction, this Chapter is organized as follows: after Introduction, we discuss the experimental work (Section 9.2) followed by the details of the model, geometries and simulation approach (Section 9.3). In the subsequent Section, we compare the simulation results with the data from literature and then present the findings from the current work. Finally, observations are summarized.

## 9.2 Experimental Section

Experiments were carried out in a channel (10 mm x 75 mm x 0.58 mm) to study hydrodynamics and mixing therefore to validate the CFD simulation. Liquids of two different colors were chosen and pumped using Syringe pumps as a step input to observe the wake formation behind the object. Videos of all the experiments were captured and analyzed using ImageJ software to get the wake length for each object at a different flow rate. Schematic of the experimental set-up is given in the Figure 9.1A. To study the effect of shapes of the geometries on flow properties the ratio of projected length to the channel diameter ( $L_p/D$  or  $\lambda$ ) was

maintained at 0.222. The details on the choice of this ratio are provided in the Supporting Information. The aspect ratio of 0.2 to 0.3 provides flow past an object without significant channel wall effects and also to mimic the flow in microchannels and minichannels where the obstacle is used to perturb the flow.



A



B

Figure 9.1: A) Schematic of the experimental setup, B) Photograph of the channel with square micropillar

### 9.3 Modelling and simulations

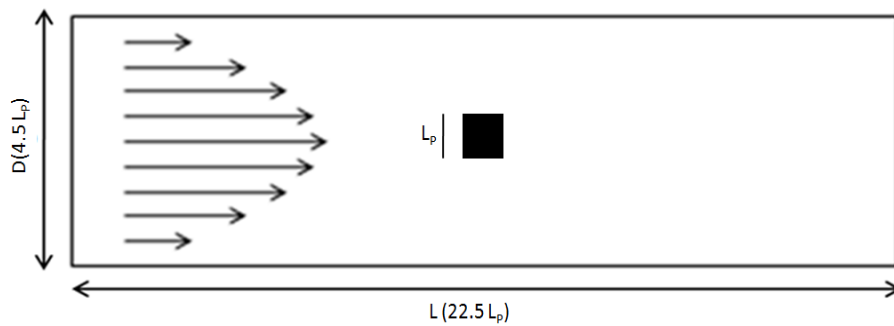
#### 9.3.1 Geometries, computational domain

To replicate the flow in the channel, geometry with same dimensions was constructed in COMSOL Multiphysics geometry builder (see Figure 9.2A). Initially, 3D simulations were carried out to explore the effect of channel depth on the flow. Subsequently, only 2D simulations were carried out for objects having different geometrical shapes placed at the center (Figure 9.2C). As mentioned previously, the ratio of projected length to channel width ( $L_p/D$ ) was kept

constant in all simulations. A few simulations for flow past square cylinder were also carried out using large channel size (viz.  $L_p/D = 0.125$ ) to compare the results with the literature data to support the simulation approach. The details on different geometries are given in Figure 9.2C. The selection of the different sets of geometry was done on the basis of identical upstream facing side.

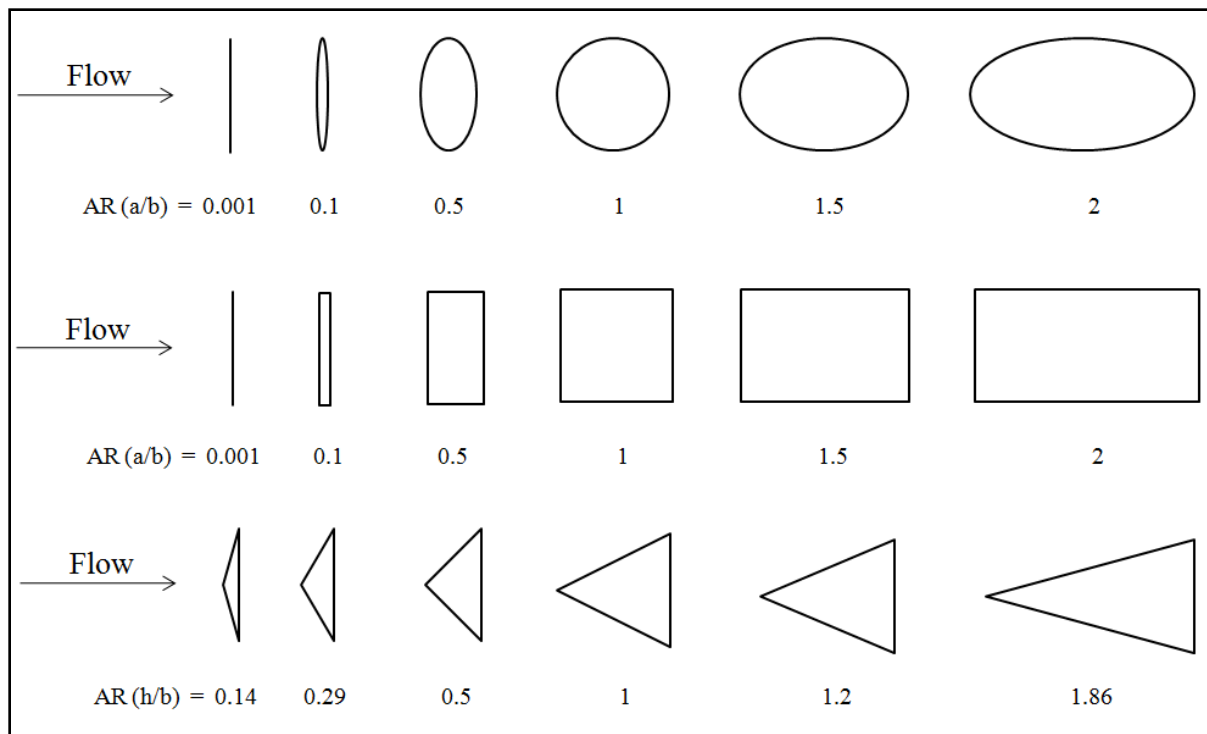


A

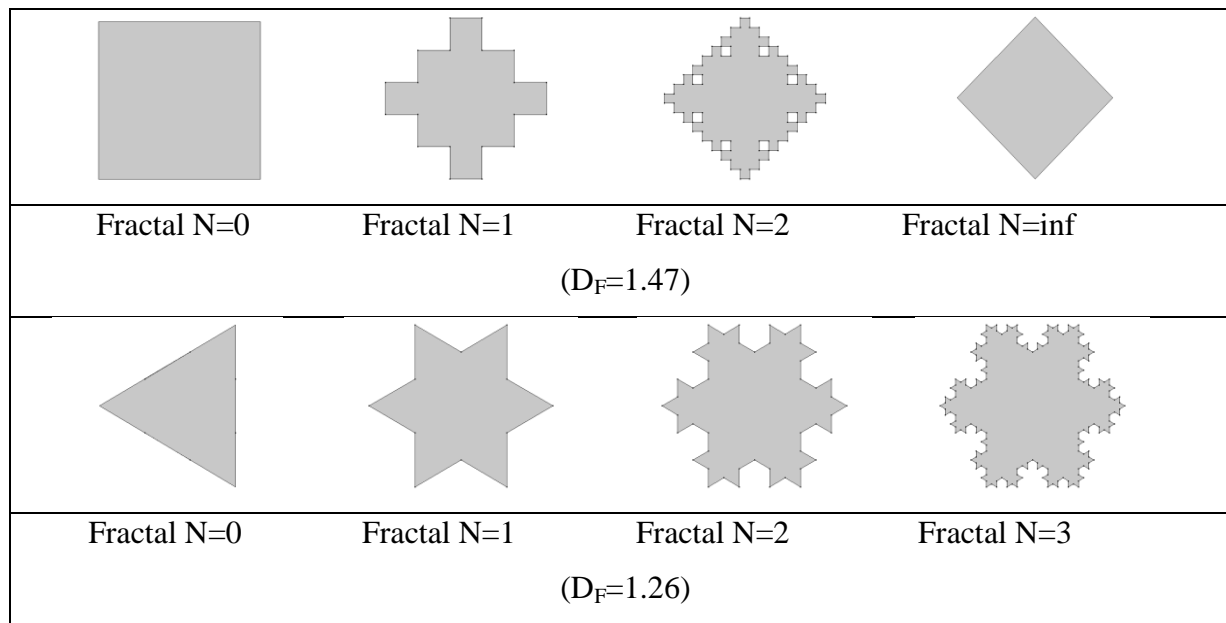


B





C



D

Figure 9.2: A) 3D geometry for flow in a micro-channel B) 2D geometry for flow in a microchannel, C) Different conventional 2D cross-sectional geometries, D) Fractal 2D cross-sectional geometries considered in this work

### 9.3.2 Governing equations

The equation of continuity and Navier-Stokes equations for non-compressible flow were solved simultaneously to simulate the 3D and 2D flow in a channel for the steady and unsteady state. Continuity equation describes the transport of the fluid, whereas, Navier-Stokes equation describes the motion of the viscous substances. Finite Element Method (FEM) based Comsol Multiphysics® was used for these simulations. Velocity vector values were used to solve for vorticity and streamlines. Backward differentiation formula was used for a time stepping in the unsteady state simulation. The absolute tolerance of values  $10^{-5}$ ,  $10^{-6}$  and  $10^{-7}$  for the relative difference of pressure and velocity values between two successive iterations were set and respective drag coefficient values were analyzed. From the analysis value of  $10^{-6}$  was found to be sufficient to consider convergence of the solution and it was set as convergence criteria for both steady and unsteady state simulations reported here.

$$\frac{\partial u_i}{\partial x_i} = 0 \quad 9.1$$

$$\rho \frac{\partial u_i}{\partial t} + \rho u_j \frac{\partial u_i}{\partial x_j} = - \frac{\partial P}{\partial x_i} + \mu \frac{\partial^2 u_i}{\partial x_j^2} \quad 9.2$$

$Re$  was estimated using the projected length ( $L_P$ ) of the object and the maximum velocity ( $U_{max}$ ) in the channel inlet and the fluid properties of water were used from COMSOL Multiphysics® materials library.

### 9.3.3 Boundary conditions

For a confined 2D and 3D geometries under consideration, no slip and no penetration conditions were set to all the wall boundaries (channel as well as the object), which mean fluid will have zero velocity relative to wall ( $u_i, u_j = 0$ ) and fluid will not penetrate in the solid wall. The inlet boundary condition was of parabolic velocity profile (maximum velocity,  $U_{max}$ ). However, in 3D simulations, the flowrate at the inlet was set such that the average velocity in the

channel before reaching to the micropillar is compared to that of 2D case at the particular  $Re$ . At the outflow boundary, no pressure and no viscous stresses condition was used ( $T:nn = 0$ ) with a positive vent coefficient, which ensured that vortices can approach and pass the outflow boundary without significant disturbance to the inner domain without any reverse flow at the exit.

### 9.3.4 Parameters studied

#### 9.3.4.1 Wake Length ( $L_W$ )

The wake length is defined as the distance between rear stagnation point and wake stagnation point. The wake stagnation point is defined as the point on the streamwise rear axis where the magnitude of streamwise velocity ( $u_i$ ) is zero. In present work, dimensionless wake length ( $L_W$ ) is calculated by Eq. (9.3).

$$L_W = \frac{l - c}{L_P} \quad 9.3$$

, where  $l$  is the length of wake stagnation point,  $c$  is half of the minor axis for the elliptical cylinder, half of the length for rectangular cylinder and 0 for the triangular cylinder. And  $L_P$  is the projected length.

#### 9.3.4.2 Drag coefficient ( $C_D$ ) and Lift coefficient ( $C_L$ )

Drag force ( $F_D$ ) and lift force ( $F_L$ ) was estimated by integrating the forces over the surface of the object. In general, these surface forces are studied as dimensionless parameters as these parameters depend on  $Re$  and object's shape not on object size. The drag coefficient ( $C_D$ ) and the lift coefficient ( $C_L$ ) are estimated by Eq. (9.4) and Eq. (9.5) respectively.

$$C_D = \frac{F_D}{0.5\rho U_{Max}^2 L_P} \quad 9.4$$

$$C_L = \frac{F_L}{0.5\rho U_{Max}^2 L_P} \quad 9.5$$

, where  $\rho$  is the fluid density,  $U_{Max}$  is the maximum velocity at channel inlet and  $L_P$  is the appropriate length scale.

#### 9.3.4.3 Pressure coefficient ( $C_P$ )

The pressure coefficient represents the dimensionless pressure distribution over the surface of the object and is given by the Eq. (9.6)

$$C_P = \frac{p_s - p_{oulet}}{0.5\rho U_{Max}^2} \quad 9.6$$

#### 9.3.4.4 Vorticity in a channel ( $\Omega$ )

The dimensionless surface velocity at the surface of the object is calculated from the relation given in Eq. (9.7)

$$\Omega = -\frac{\Omega_0 L_P}{U_{Max}} \quad 9.7$$

#### 9.3.4.5 Critical Reynolds number ( $Re_C$ ) for the onset of vortex shedding

The transition from steady state to periodic oscillations is characterized by a Hoff bifurcation (Schumm et al., 1994; Sohankar et al., 1998) and can be described by Stuart-Landau equation:

$$\frac{dA}{dt} = \sigma A - l |A|^2 A \quad 9.8$$

, where,  $A(t)$  is a characteristic complex amplitude associated with fundamental frequency component,  $\sigma = (\sigma_r + i\sigma_i)$  is the linear growth rate and  $l = (l_r + il_i)$  is the first Landau

constant. After linearizing the Eq. (9.8) around  $Re_C$ , where  $\sigma = 0$ , the instantaneous growth rate at  $Re > Re_C$  is given as:

$$S = |A|^{-1} \frac{d|A|}{dt} = \sigma_r - l_r |A|^2 = \sigma_r \left( 1 - \frac{|A|^2}{|A|_{sat}^2} \right) \quad 9.9$$

, where,  $|A|_{sat}$  is the amplitude in a saturated state (Schumm et al., 1994). At small departure from the onset the real part,  $\sigma_r$  is a linear function of  $(Re - Re_C)$ ,

$$\sigma_r = K (Re - Re_C) \quad 9.10$$

, where,  $K$  is a positive constant. Eqs. (8) and (9) are only valid for  $Re$  close to the onset value. In the present study lift coefficient ( $C_L$ ) as  $A(t)$  was monitored. Using viscous scaling for time,  $\sigma_r$  is calculated for different  $Re$  and using Eq. (9). After getting  $\sigma_r$  for particular  $Re$ ,  $Re_C$  can be calculated by interpolating Eq. (9.10). A Matlab code was developed to obtain the values of  $Re_C$ .

### 9.3.5 Mesh independence

In general, a numerical solution depends on the mesh used in the computational domain. The accuracy of a numerical solution usually increases with increase in the number of elements. In this work, the number of elements, as well as number of nodes, was varied to meet this requirement for individual geometry. For every geometry under consideration (circular cylinder, square cylinder and triangular cylinder ( $\theta^\circ=60$ )), several meshes, with increasing element density, were studied to ensure that the solution was independent of the mesh used. Drag coefficient ( $C_D$ ) values and wake length ( $L_W$ ) values at  $Re = 30$  were monitored and compared for the various mesh sizes. Table 1 gives the details on the mesh independence study. From the Table 9.1 it can be observed that for each of the geometry,  $C_D$  and  $L_W$  values do not vary for finer, extra fine and extremely fine meshes. In order to capture the flow features near the boundaries of the object with better accuracy, the extremely fine mesh was used in the domain. Figure 9.3 shows the extremely fine mesh used for a square cylinder in a flow domain. All the results reported here are for simulations using extremely fine mesh in the computational domain.

Table 9.1. Mesh independence study for the different geometries considered in this work for 2D geometries. ( $N_E$  – number of elements,  $C_D$  – drag coefficient) at  $Re = 30$ .

Cross-section (2D) Object/Mesh		Coarse	Normal	Fine	Finer	Extra fine	Extremely fine
Circular cylinder	$N_E$	2910	4304	7498	17300	42202	78326
	$C_D$	2.21	2.22	2.23	2.23	2.22	2.22
	$L_w$	0.75	0.81	0.78	0.82	0.85	0.85
Square cylinder	$N_E$	2226	3412	6390	11776	22526	65356
	$C_D$	3.22	3.19	3.18	3.16	3.15	3.15
	$L_w$	0.99	1.02	1.05	1.05	1.06	1.06
Triangular cylinder ( $\theta=60^\circ$ )	$N_E$	3364	5134	9017	20251	47899	85409
	$C_D$	2.14	2.15	2.14	2.14	2.14	2.14
	$L_w$	1.4	1.42	1.44	1.45	1.5	1.5

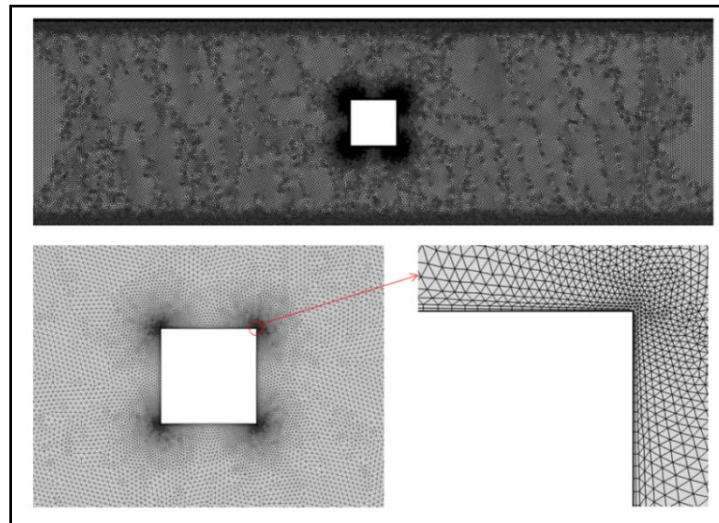


Figure 9.3. Mesh structure in computational domain A) 2D square channel (top), B) near object (bottom left), C) at the corner of the object (bottom right).

## 9.4 Results and Discussions

Simulations were carried out by changing the inlet velocity (water as fluid) such that the  $Re$  (based on the projected length ( $L_P$ ) of the object) ranged from 0.1 to 150. In order to confirm the suitability of approach, we have compared our results with that of published in the literature and then our findings are presented.

### 9.4.1 Validation of model

#### 9.4.1.1 Comparison with Experimental data

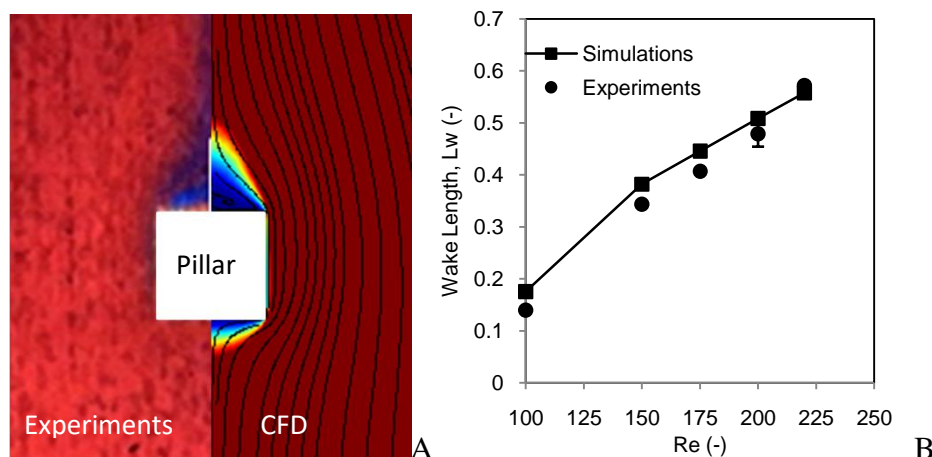


Figure 9.4: A) Estimation of wake length ( $L_W$ ) from experimental data, B) Comparison of CFD results with that of experimental

Experiments at different  $Re$  to estimate the wake-length ( $L_W$ ) and compared with that of CFD values. The comparison can be seen in Figure 9.4. A slight deviation from the experimental values can be attributed to the experimental errors. To further validate our model, we decided to compare CFD results with that of literature and same as provided in the next section.

#### 9.4.1.2. Comparison with literature data

Effect of channel depth on the hydrodynamics was analyzed using wake dynamics. From the CFD results, it was evident that wake dynamics of channel depth greater than 5 mm show similar results as that of 2D channel. Hence, 2D simulations were studied and analyzed henceforth. 2D geometry was modified slightly as to get the detailed study of the effect of space filling nature on the hydrodynamics of the system. To verify the 2D simulation, initial simulations were carried out for a square cylinder having its sides perpendicular to the flow and

with the ratio of projected length to diameter ( $\lambda$ ) ranging from than 0.1 to 0.5. Data for flow past square cylinder and circular cylinder in a channel is widely available in the literature. Figure 9.5 shows the comparison of drag coefficient (Figure 9.5A) and wake length (Figure 9.5B) at different  $Re$ . Results from present work show an excellent comparison with the data from the literature.

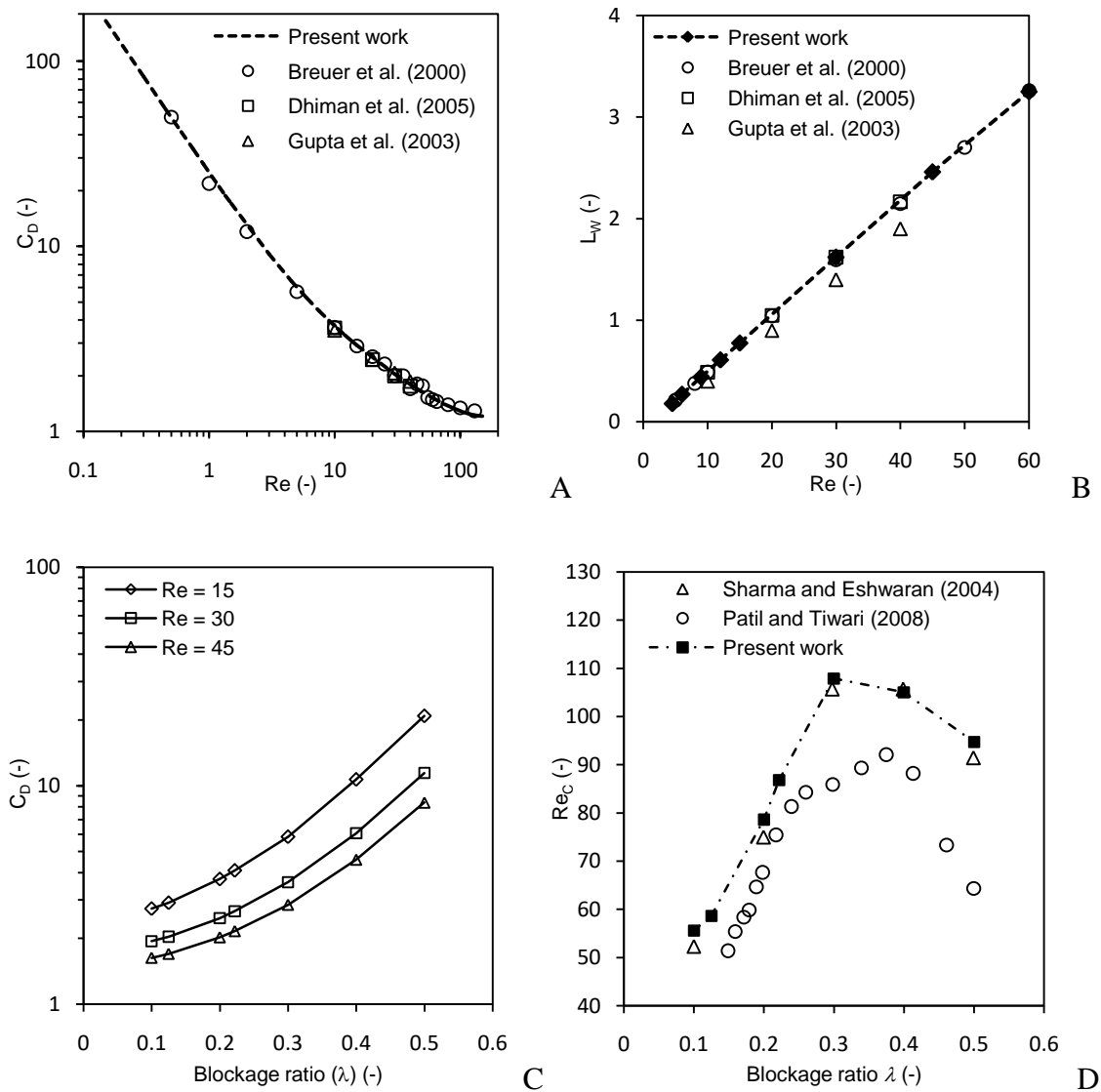


Figure 9.5: Comparison with literature data A) drag coefficient ( $C_D$ ) vs  $Re$  B) wake length ( $L_W$ ) vs  $Re$  for a square cylinder at blockage ratio ( $\lambda$ ) 0.125 C) Effect of blockage ratio (walls) on drag coefficient. D) critical Reynolds number for flow oscillations ( $Re_C$ ) for a square cylinder [(Sharma and Eshwaran, 2004) and (Patil and Tiwari, 2008) calculated  $Re$  based on mean velocity at the channel inlet and hence are recalculated on the basis of maximum velocity for comparison.]



In addition to this, effect of blockage ratio or wall proximity on drag coefficient and critical Reynolds number for oscillation was also studied for square cylinder. As indicated in Figure 9.5C drag coefficient increases as the wall proximity increases. This is attributed to the channel wall drag on observed on the square cylinder. This results in suppression of wake length for a particular Reynolds number. Similarly, the critical Reynolds number ( $Re_C$ ) for flow oscillations was found to be around  $\sim 60$  for  $\lambda=0.125$ , which is in good agreement with the results from the literature (Breuer et al., 2000). Comparison for critical  $Re$  of flow oscillation was also carried out at different blockage ratio ( $\lambda$ ). The variation in  $Re_C$  with respect to  $\lambda$  for square cylinder has an interesting trend (see Figure 9.5D) as  $Re_C$  goes through maxima. This trend is also reported as well as explained in the literature (Patil and Tiwari, 2008; Sharma and Eswaran, 2004). This comparison motivated us to go for further studies on various objects given in Figure 9.2.

#### 9.4.2 Flow patterns (streamline contour plots)

Deformation of the fluid stream takes place when flow approaches micropillar (object) in the channel. With the increase in the fluid velocity, these deformation creates eddies or recirculating flow in the microchannels. At low  $Re \leq 1$ , the creeping steady state flow past an object continues to be without separation. The dominance of inertia force over viscous force increases with increase in  $Re$  which results in boundary layer separation. The  $Re$  at which first transition (recirculation region formation) occurs, however, varies from object to object. For example, for circular cylinder, a recirculation region has been shown to exist at  $Re \geq 6$  (Faruquee et al., 2007) while for a streamlined body such as an elliptic cylinder, it occurs at  $Re \geq 10$ . For streamline bodies ( an object that offers least possible resistance to flow), fluid adheres to the surface and delays the separation of the boundary layer as a consequence shows a minimum recirculation region. On the other hand for a square cylinder the wake/recirculation region can be observed for  $Re \geq 5$ , (Breuer et al., 2000; Yoon et al., 2011) and for a sharp-edged body such as plate recirculation region is observed at much lower  $Re$  ( $1.5 \leq Re \leq 3$ ). It should be noted that the boundary layer separation in all the objects mentioned above takes place in a different manner and at different points. Therefore, we observe the difference in the wake dynamics. In the present work, due to high blockage ratio, it was observed that for a circular and a square cylinder the wake formation or recirculating flow starts at a slightly greater value of  $Re$ . It is known that, for

any given object, the recirculation region (wake length,  $L_W$ ) grows linearly with respect to  $Re$ . However, the slope at which it grows varies from one object to another. Therefore it becomes necessary to evaluate their performance for the better selection of the shape of the object. The wake length ( $L_W$ ) at  $Re=30$  for circular cylinder, square cylinder and triangular cylinder ( $\theta=90^\circ$ ) found to be 0.85, 1.06 and 1.425 respectively. This shows that, for a given  $Re$  and aspect ratio, triangular cylinders has the highest recirculation region. The boundary layer separation points for triangular cylinder were found to be fixed for all  $Re$  studied in present work. Whereas, for the square cylinder, the flow separates first at the points on rear edge till  $Re=90$  and then at the points on the upstream edge. On the other hand, the boundary layer separation points are  $Re$  dependent for circular

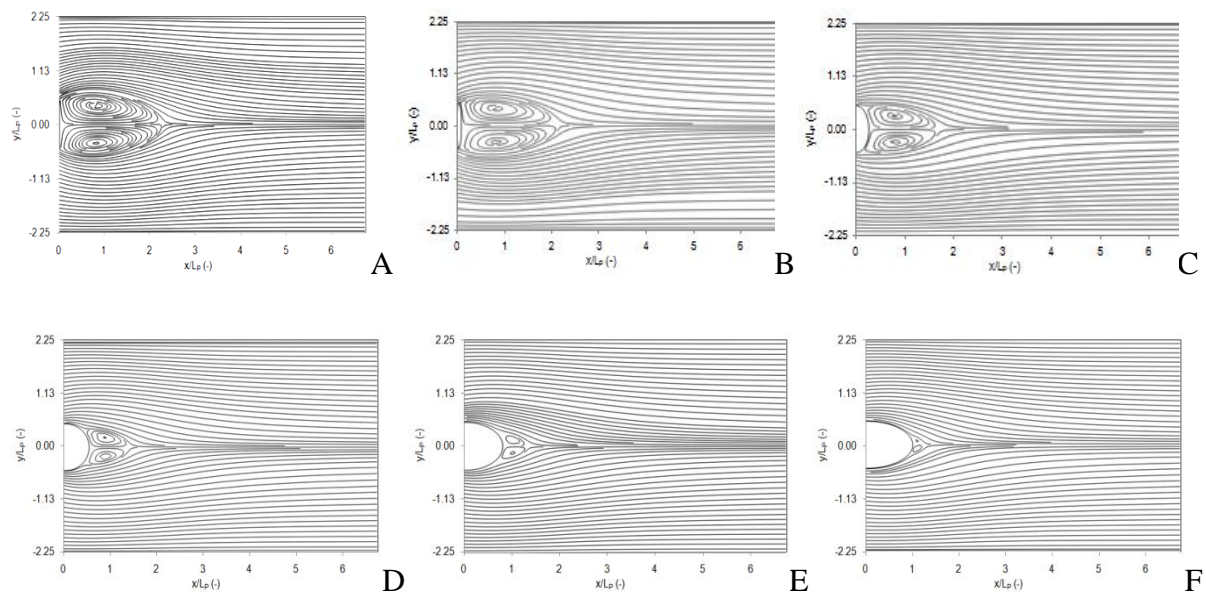


Figure 9.6: Streamlines contour plots of elliptical cylinders of different aspect ratio (AR) at  $Re=30$  A) 0.001, B) 0.1, C) 0.5, D) 1 or circular cylinder, E) 1.5, F) 2.

cylinder. More details on the wake length ( $L_W$ ) are given in the supporting information. Figs. 5, 6 and 7 show the streamlines contour plot for elliptical, rectangular and triangular cylinders respectively. From the Figs. it can be observed that for all the three cases the wake region decreases with increase in aspect ratio.

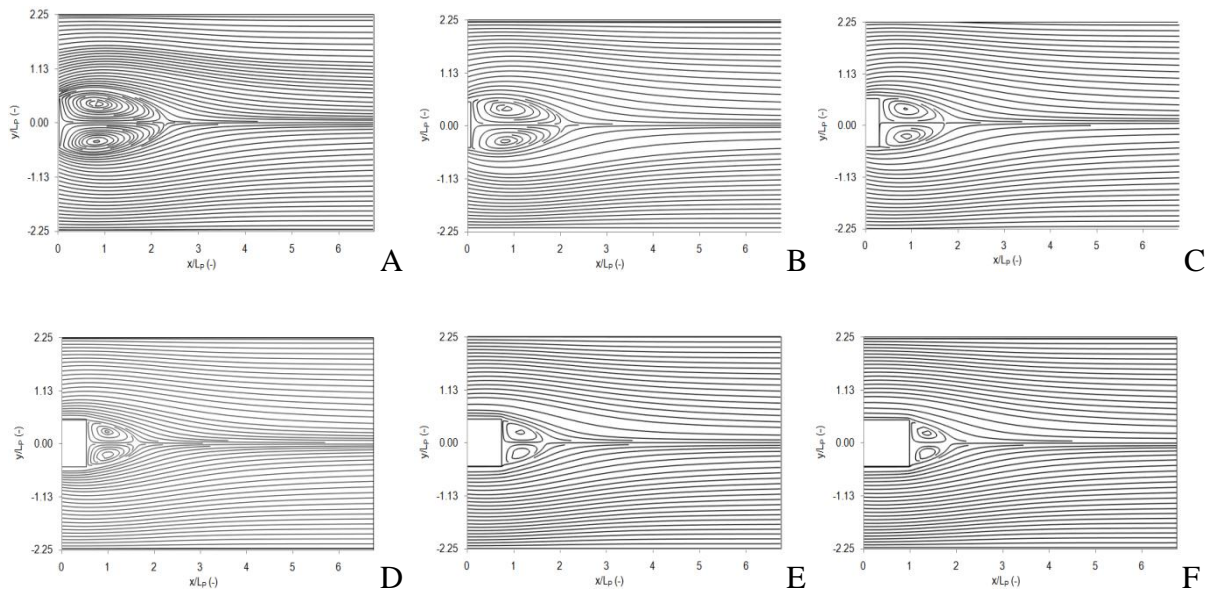


Figure 9.7: Streamlines contour plots of rectangular cylinder of different aspect ratio (AR) at  $Re=30$  A) 0.001 or plate, B) 0.1, C) 0.5, D) 1 or square cylinder, E) 1.5, F) 2.

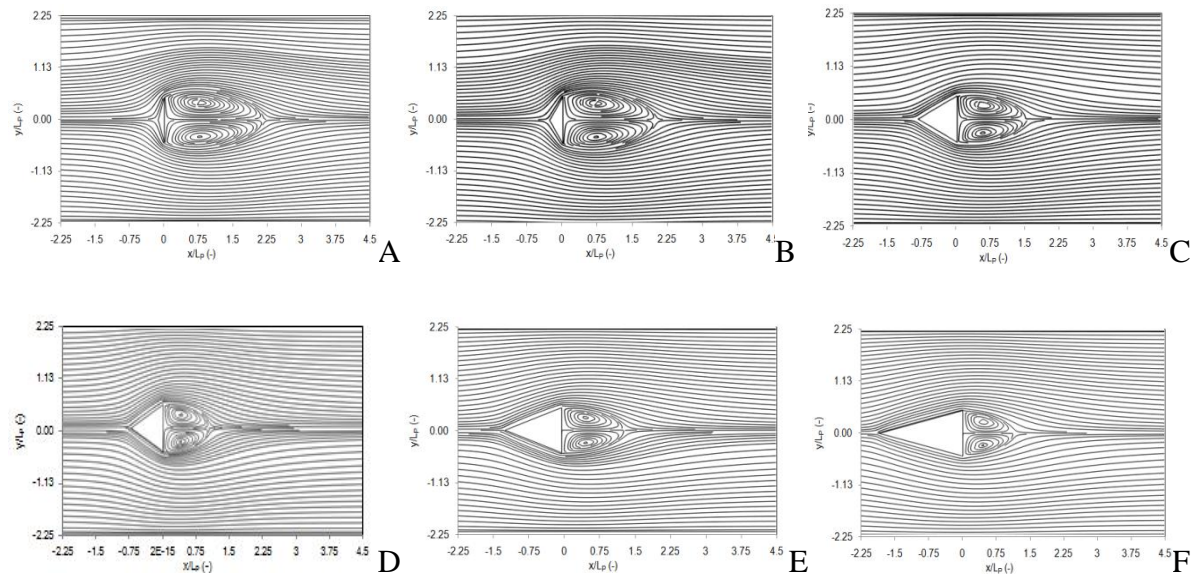


Figure 9.8: Streamlines contour plots of triangular cylinders of different aspect ratio (AR) at  $Re=30$  A) AR = 0.14 or  $\theta = 150^\circ$ , B) AR = 0.29 or  $\theta = 120^\circ$ , C) AR = 0.5 or  $\theta = 90^\circ$ , D) AR = 1 or  $\theta = 53.13^\circ$ , E) AR = 1.20 or  $\theta = 45^\circ$ , F) AR = 1.87 or  $\theta = 30^\circ$ .

For circular and square cylinder the extended surface area in the streamline direction delays the boundary layer separation and hence we observe a difference in the recirculation region ( $L_W$ ). On the other hand, in case of the triangular cylinder the upstream flow after reaching to the point joining two upstream edges accelerates at a certain angle (for example for  $AR = 0.5$ , flow accelerates at  $45^\circ$ ; for  $AR = 0.866$ , at  $30^\circ$  etc.). The separation of two parallel streams at various angles results in different pressure distribution on the walls and leads to different wake dynamics. Pressure distribution over the surface of the objects is discussed subsequently. The flow was found to become unsteady at  $Re_C$  and beyond this  $Re$ , well-known vortex street was observed for all the objects studied in the present work.

The effect of space filling nature on the wake characteristics can be observed more distinctly in fractal geometries. The fractal geometries generated from a square and triangle initiator have self-similar features which continue to increase the complexity and yet fill more and more space with further iterations. These structures upon magnification indicate the presence of steps on the edges and the length scales of these steps decreases with increasing number and continues to smoothen the edges. The flow patterns behind the fractal object (Figure 9.9) were observed to be quite different from that of the conventional geometries. Even at creeping flow we observe small eddies (cavities) behind the object for fractal  $N = 1, 2$  originated from the square initiator. Energy loss in keeping up the acceleration at the downstream and upstream edges results in the boundary layer separation which leads to the formation of small eddies at the corners. These eddies are well known as shear driver cavities which can be observed in step flow as well. With increasing  $Re$ , from 6 to 13.5, initially merging of the small eddies into a larger one happens because of an increase in the adverse pressure at the back of the object, which eventually shows only two vortices behind the fractal objects, which is similar to the observation for conventional objects. Similar observations were made in flow around fractal objects generated from triangle initiators in Figure 9.10. However, due to the structural difference in the objects, different flow patterns were observed. Unlike the other objects where the flow separation occurs due to the rear edges, in case of fractal  $N = 1$  flow separation occurs due to counter-rotating eddies. Moreover, unlike the fractal  $N = 1$  of square initiator, the merging of eddies was not observed even at high  $Re$ , which results in enhanced drag. These eddies get smaller and

smaller with fractal iteration, and the interaction of these eddies leads to different flow pattern which normally is not seen in case of flow past conventional objects.

Another noticeable feature can be observed when analyzing the flow behind the objects of fractal  $N = 2$ , generated from the square initiator. In the open spaces (refer Appendix 1), small sequence of trailing eddies in the corners are observed get oriented due to the shape of the object. These observations match with the observations by Moffat, (1964), where it has been stated that the flow near the corner must consist of a sequence of eddies of decreasing intensity. Similar observations can be made in those open spaces as the fractal objects have several such corners due to its space-filling nature.

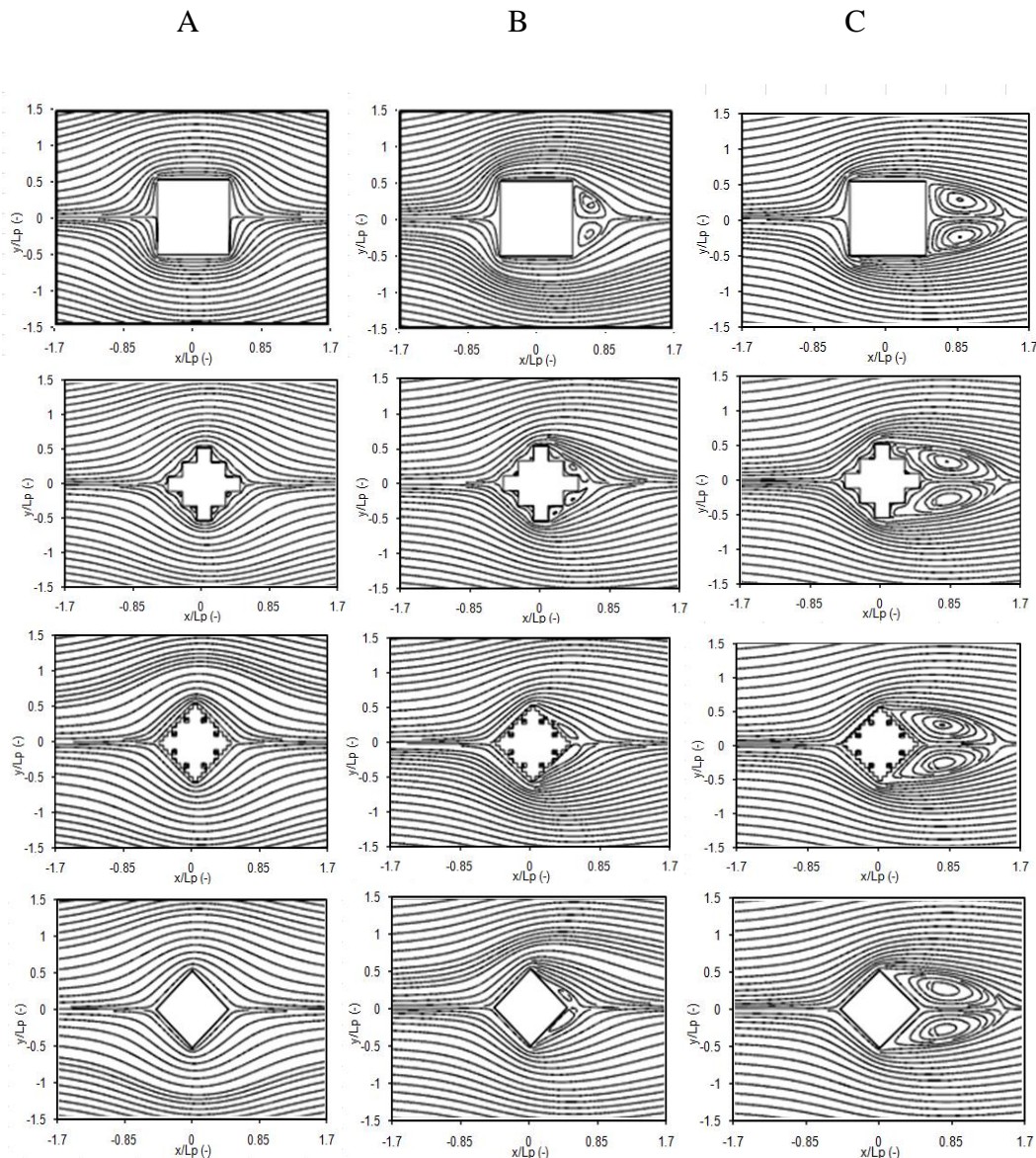


Figure 9.9: Streamline contour plots of flow around fractal objects of square initiator A)  $Re=1$ , B)  $Re=12$ , C)  $Re=30$ .

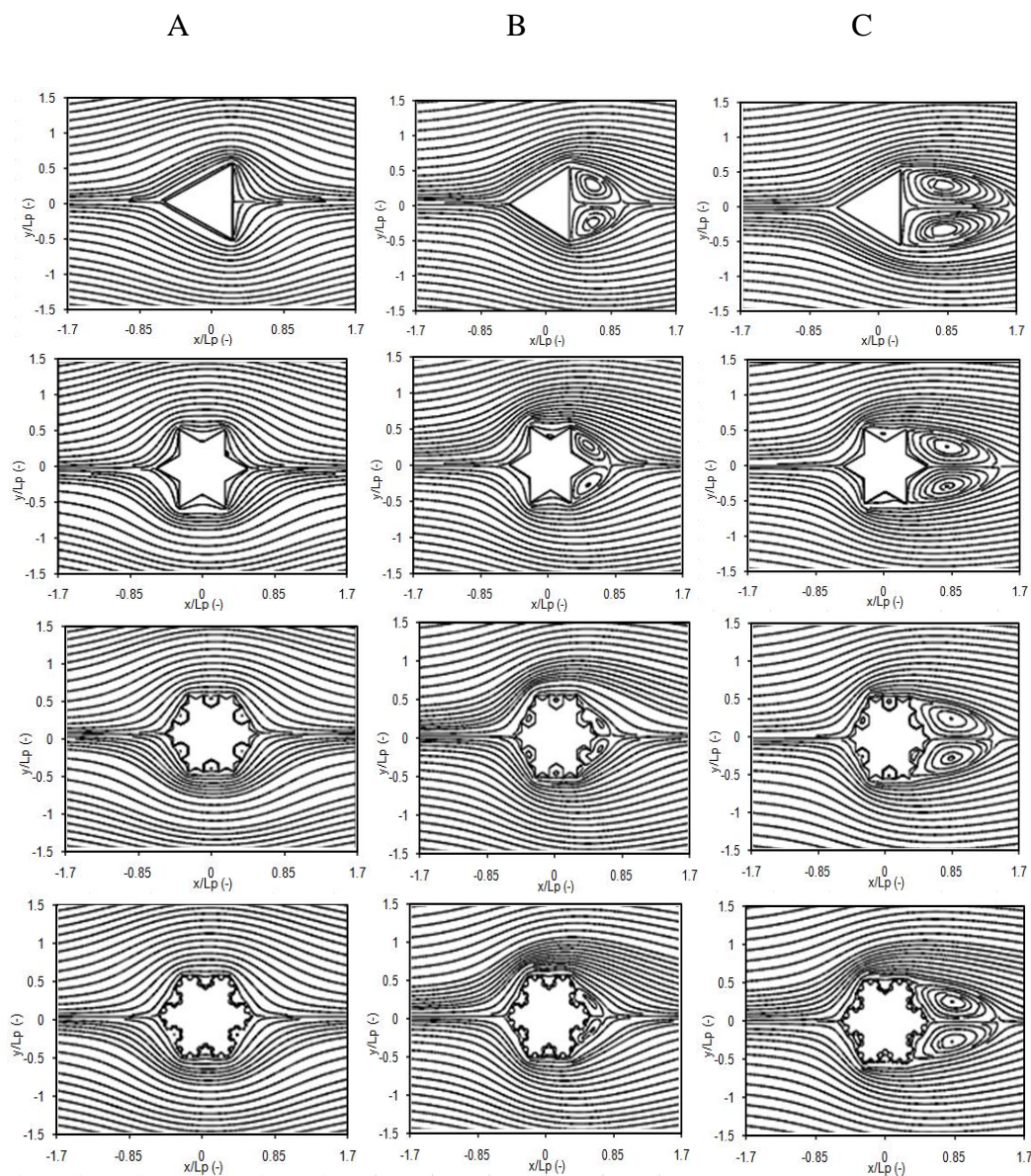
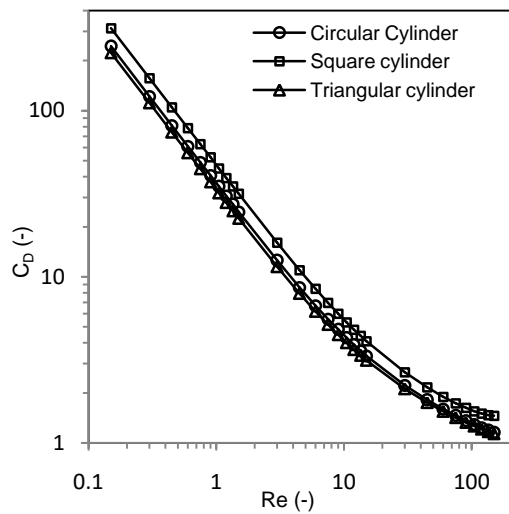


Figure 9.10: Streamline contour plots of flow around fractal objects of triangle initiator A)  $Re=1$ , B)  $Re=12$ , C)  $Re=30$ .

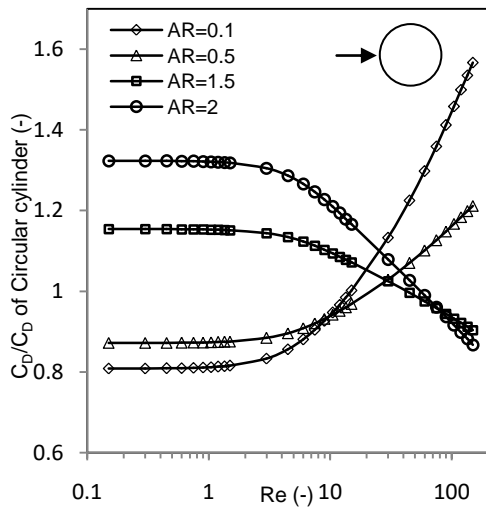
### 9.4.3 Flow-induced forces

The pressure drop across the channel is related to drag experienced by the micropillars or objects in the channel. Drag coefficient ( $C_D$ ) values for reference objects (circular cylinder, square initiator and triangle initiator) are shown in Figure 9.11A. The difference in the  $C_D$  can be entirely attributed to the different pressure distribution over the surface of the object (given in supporting information). The variation in the ratio of  $C_D$  of elliptical cylinders to the  $C_D$  of a circular cylinder with respective  $Re$  is given in Figure 9.11B. For  $Re \leq 1$ , the drag force is dominated by viscous stresses and hence it is expected to have more drag at the surface of the bodies having a more cross-sectional area or wetted perimeter. A similar trend can be observed from the Figure 9.11B. However, at high  $Re$ , the flow observed past these objects shows very different features. The object with smaller AR tends to have a relatively larger low-pressure zone (recirculation region) behind the object due to the dominance of inertial forces over viscous forces. Elliptical cylinders with higher AR, help in prolonging the boundary layer separation and further reducing the drag. Therefore, the drag coefficient at  $Re \geq 60$  increase with a decrease in AR. Similar trends have been observed for rectangular cylinders and triangular cylinders. These results signify that extended surface contributes significantly to  $C_D$  for the particular object.

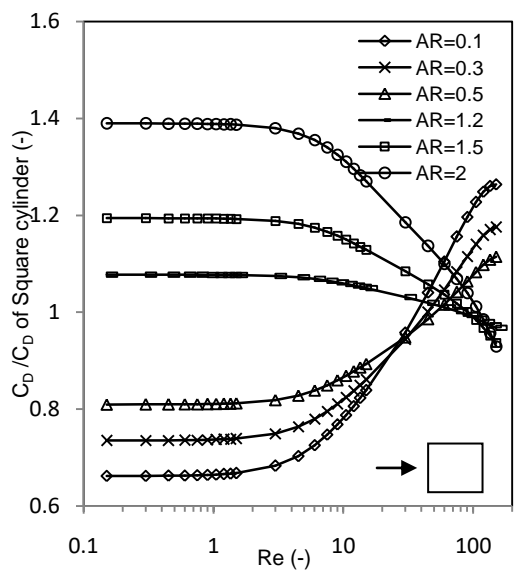
Based on the trends of the drag coefficient for conventional geometries, at low  $Re$ , the drag force should increase with an increase in cross-sectional area. Similar trends were observed for fractal objects generated from triangle initiator. In addition to the effect of cross-sectional area, the flow separation over counter-rotating eddies adds drag force which can be observed in Figure 9.11C. However, this trend does not hold true for the fractal objects. At low  $Re$ , small size shear driven eddies at the corners of Fractal structures with  $N = 1$ ,  $N = 2$  generated from the square initiator, contribute significantly to the total drag. The effect of small eddies was only observed for  $Re < 15$ , while beyond this range, the smaller eddies merge with the large vortices that get formed behind the objects and the wake structure is similar to that of the conventional geometries. In general, the drag coefficient was seen to decrease with increasing perimeter of the wetted surface area, with a region where the drag coefficient goes through a minimum over a narrow range of the ratio of perimeter to projected length  $\sim 2.8$  to  $3.2$  and this range is independent of  $Re$ .



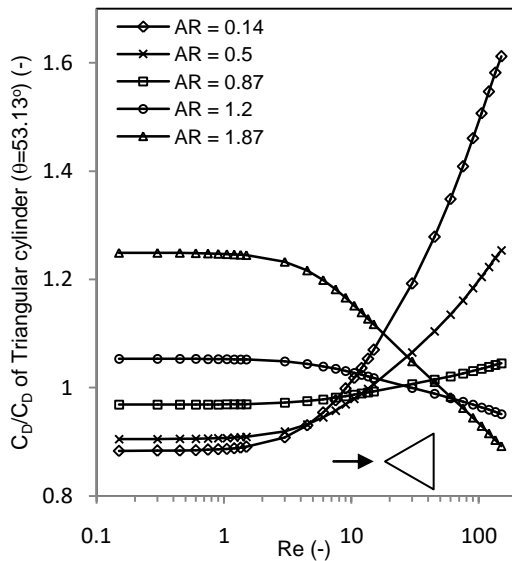
A



B



C



D



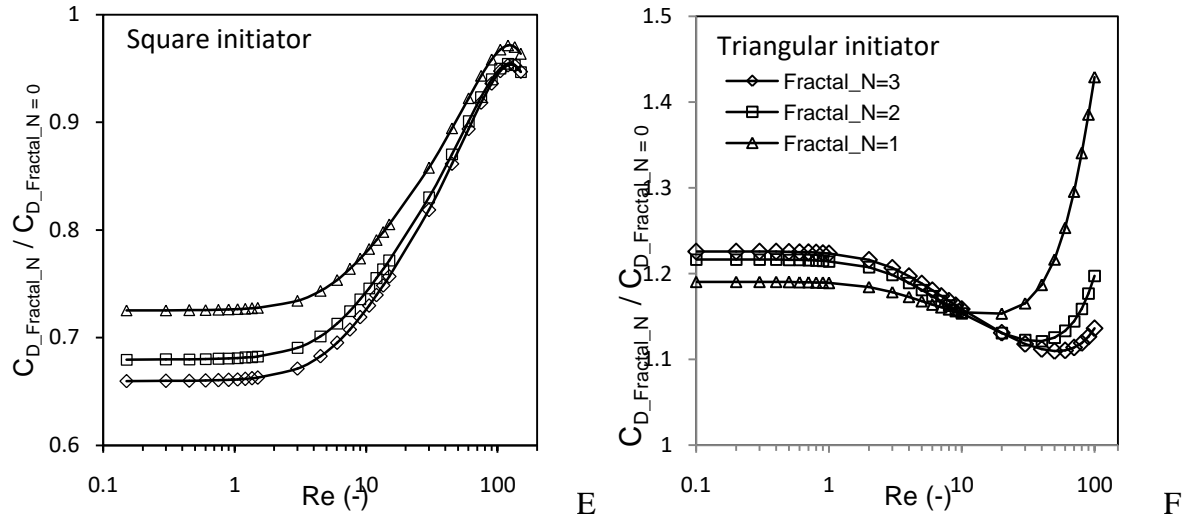


Figure 9.11: A) Drag coefficient ( $C_D$ ) vs  $Re$ , B) ratio of  $C_D$  for elliptical cylinders vs  $Re$ , C) ratio of  $C_D$  for rectangular cylinders vs  $Re$ , D) ratio of  $C_D$  for triangular cylinders vs  $Re$ , E) ratio of  $C_D$  for square cylinders fractals vs  $Re$ , F) ratio of  $C_D$  for triangular cylinders fractals vs  $Re$ .

#### 9.4.4 Onset of vortex shedding

At higher  $Re$ , steady flow behind the object becomes unstable to small disturbances. The instability first affects the tail of the wake, at some distance from the object. This results in the slow oscillations of the wake. This eventually leads to well known "Von-Karman" vortex street. The  $Re$  at which slow oscillations start is termed as critical Reynolds number of flow oscillations ( $Re_C$ ). It is extremely important to know the  $Re_C$  for the given object as to set the inflow conditions in the microscale devices to achieve vortex shedding or otherwise. Literature reports  $Re_C$  values for circular cylinder, square cylinder and triangular cylinder for bounded as well as unbounded flow past object (Dhiman et al., 2005; Jackson, 1987; Srikanth et al., 2010). In general, it is known that the  $Re_C$  for unbounded flow past object is always lower than the flow in a confined channel. For any system,  $Re_C$  can be estimated by monitoring the lift coefficient ( $C_L$ ) at various Reynolds number. In the present work,  $Re_C$  for each object studied in the present work was estimated by using the linearized SL equation as outlined in Section 2 and results are presented in Figure 9.12.

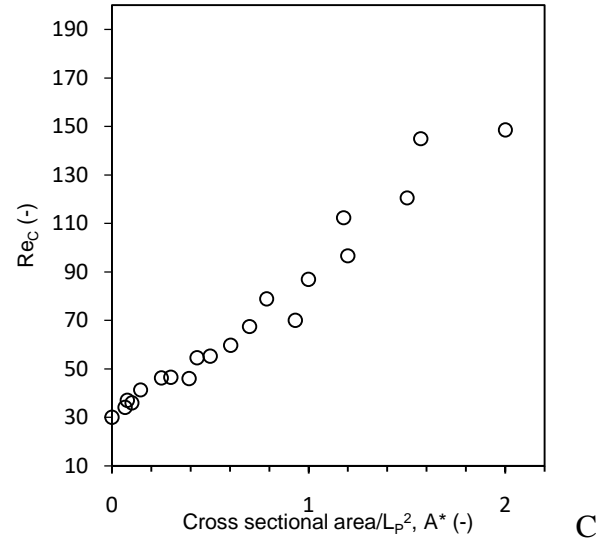
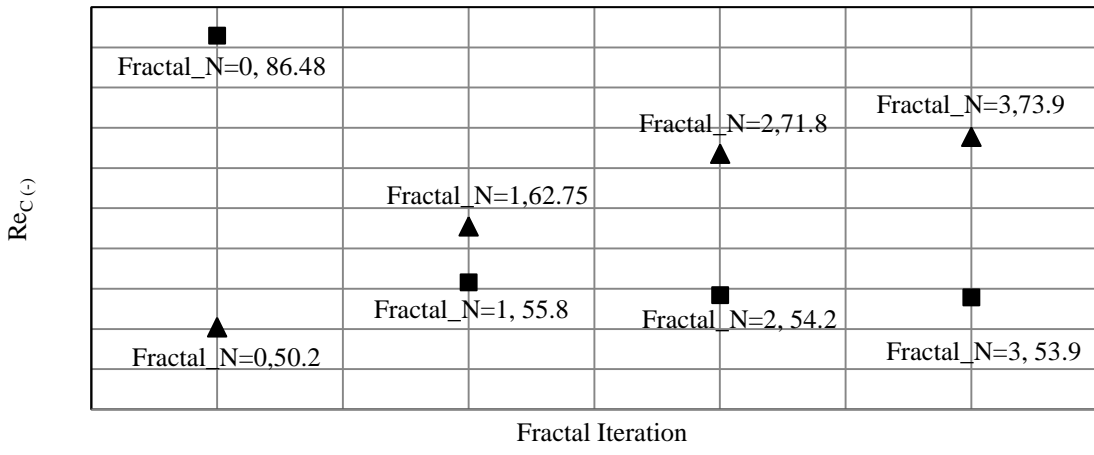
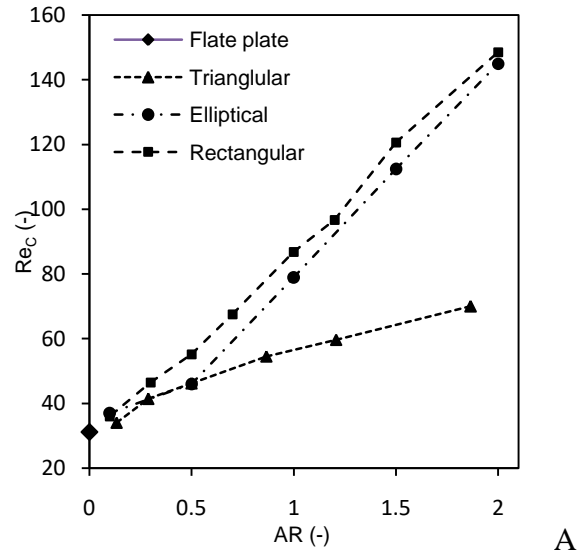


Figure 9.12: Critical Reynolds number ( $Re_c$ ) for the onset of vortex shedding A) with respect to the aspect ratio (AR) for different cylindrical objects, B) with respect of fractal iteration, C) with respect to cross-sectional area.

For any cylindrical object flat plate perpendicular to flow represents the object with  $AR = 0$  and flat plate parallel to flow represents the object with  $AR = \infty$ . In case of flat plate with  $AR = 0$ , the flow separation takes place at two vertices and vortices are shed alternatively in a downward direction at higher  $Re$ . Since there is no support at downstream to damp out the oscillations, the  $Re_C$  found to be minimum (see Fig. 8). At  $0.1 \leq AR \leq 0.5$ , all the three cylindrical objects found to behave identically. This is expected as geometrical differences disappear in this limit. At  $AR > 0.5$   $Re_C$  found to increase almost linearly with  $AR$  for all the three cylinders considered in the present work. However, at same  $AR$ , flow oscillations start at relatively lower  $Re$  for triangular cylinder than for rectangular and circular cylinder. The triangular cylinders are most streamlined objects for upstream flow, and rectangular cylinders are most blunt. Therefore, the  $Re_C$  is minimum for triangular cylinders, whereas maximum for rectangular cylinders and in between for elliptical cylinders at equal  $AR$  (see Figure 9.12A). Similar observations were also reported by Jackson (1987). This shows that upstream sides play an important role in vortex shedding. In case of fractal objects generated from the square initiator, with higher fractal iterations the  $Re_C$  was found to decrease linearly. Fractal objects generated from square initiator tend approach Square ( $\theta = 45^\circ$ ) shape with smoothening rear edges on successive iteration. Therefore, the results justify as typically sharp edges of the objects contribute to flow separation and vortex shedding. On the other hand, Fractal objects generated from triangle initiator tend to approach hexagon shape with similar orientation, therefore, the  $Re_C$  found increasing with the fractal iteration. To see the effect of cross-sectional area on the vortex shedding we also plotted the  $Re_C$  with respect to cross-sectional area. Fig. 8B shows the linear relationship between  $Re_C$  and cross-sectional area. To support this, we also carried out some additional simulations for Hexagonal cylinder and Octagonal cylinder. And results were found encouraging as  $Re_C$  for mentioned objects also found to be on the linear plot. The linear relationship is given below;

$$Re_C = 62.6A^* + 27.67 \quad 9.11$$

, where,  $A^*$  is cross-sectional area normalized with  $L_P^2$ . From the results, it can be said that, for a given projected length,  $Re_C$  increases with an increase in cross-sectional area of the object (i.e. increase of the size parallel to flow). This is an interesting observation as this can be helpful in predicting the  $Re_C$  for an obstacle on the basis of its cross-sectional area. This will also allow

setting the operating conditions for microchannels to achieve the higher vortex strength in a channel.

### 9.5 Effect of arrays of object on mixing

Three different arrangements of different geometries were selected to study the effect of arrays on the mixing in the small channel. Conventional geometries such as circles, triangles, and squares were adopted to investigate the nature of the flow and hence mixing. Residence time distribution (RTD) analysis was carried out to study the mixing in small channels and compared with different geometries. The geometrical arrangement is given in the Figure 9.13.

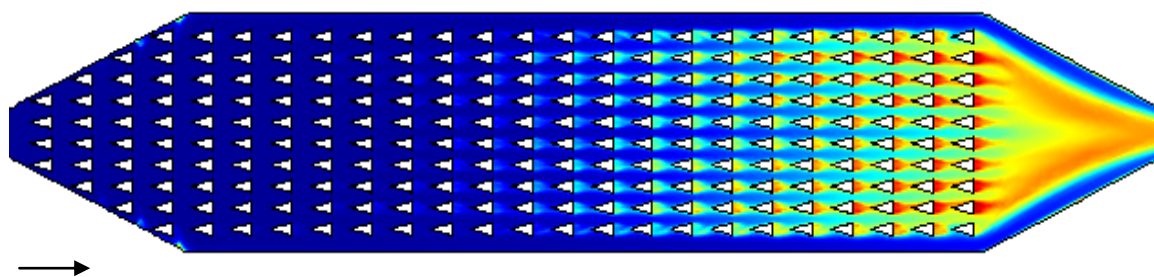


Figure 9.13A: Symmetrical arrays with triangular cylinders (movement of the tracer).

As shown in the Figure 9.13, first Geometry of each shape is of the symmetric type in which many posts of single shape is arranged one behind other exactly. The horizontal distance between the centers of the post of a different shape is maintained such that the wake form behind the one post is in constructive interference of the wake behind the post of next column. The vertical distance of the post is also maintained such that the two posts start preventing them to behave like a single post. Hence total 10 rows and 25 columns of posts are built in the microreactor. For different shape, only the shape of post used is changed but the basic configuration is same for all shapes.

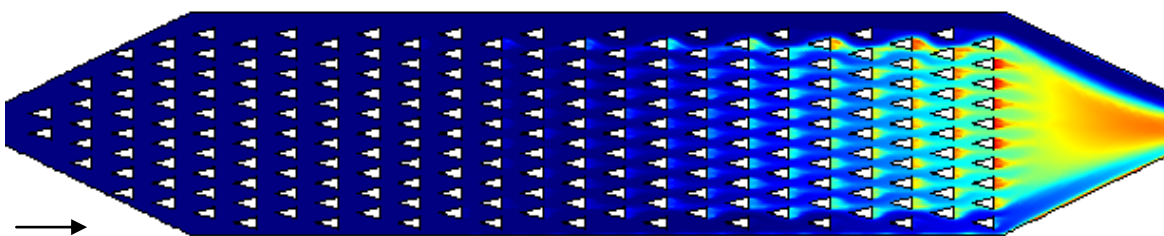


Figure 9.13B: Asymmetrical arrays with triangular cylinders (movement of the tracer).

On the other hand, second geometry (Figure 9.13B) of each shape is of the asymmetric type in which many posts of a single shape is arranged such a way that the post of the second column is just in between the two post of front column. The horizontal distance between the centers of the post of a different shape is so maintained that the wake formed behind the one post is in constructive interference of the wake behind the post of next column. The vertical distance of the post is also maintained to that the two posts start preventing them to behave like a single post. Hence total 10 rows and 25 columns of posts are built in the microreactor. For different shape, only the shape of post used is changed but the basic configuration is same for all shapes.

Third Geometry of each shape is of the random type in which many posts of a single shape is arranged in random order. In this pattern, each column's vertical height is changed by one unit upper side from the lower boundary and after reaching the upper boundary again one unit of downward shift is done. Means if the first column is mid to the channel next 2nd column is shifted one unit downward and next again by one unit. After reaching the lowest boundary again the shift is done in an upward direction. The horizontal distance between the centers of the post of a different shape is so maintained that the wake formed behind the one post is in constructive interference of the wake behind the post of next column. The vertical distance of the post is also maintained to that the two posts start preventing them to behave like a single post. Hence total 10 rows and 25 columns of posts are built in the microreactor. For different shape, only the shape of post used is changed but the basic configuration is same for all shapes.

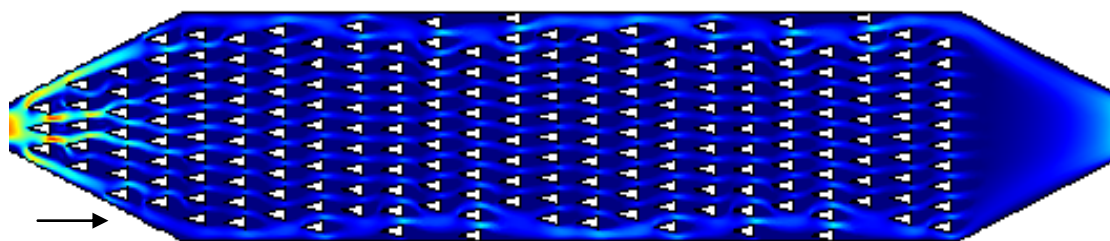


Figure 9.13C: Random arrays with triangular cylinders (movement of the tracer).

At first, flow was simulated for the different geometries as described above. The contour plot analysis of streamlines indicated the convergence and divergence of the streamlines in case of asymmetric and random arrangements. In these geometries fluid element constantly changes its direction before it comes out of the channel. This principle can be explained by observing the tracer movement in the channel by RTD studies. Therefore, RTD analysis was done to see the effect of different array geometry on the mixing in a small channel. On analyzing the RTD data mean residence time and variance was calculated for each case. Figure 9.14A shows the effect of different geometrical structure on the mean residence time. Results show that the random arrangement of any geometry shows higher mean residence time at particular Reynolds number. In another sense, mixing in the different channel can be compared by using tank-in-series model for the variance of the system. Where, more number of CSTR indicates more mixing in the system. Similar things can be observed in Figure 9.14B. The overall observation from the hydrodynamics and RTD analysis shows that the flow in an array work on the principle of diverging and converging of the fluid element and hence good mixing can be achieved with random arrangement of small posts.

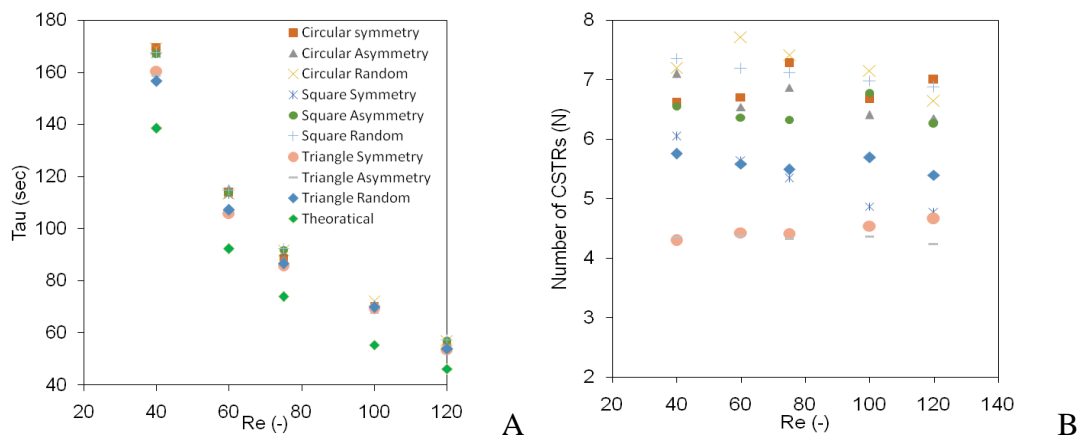


Figure 9.14: A) Residence time ( $\tau$ ) vs Reynolds number, B) Number of CSTRs vs Reynolds number. Here Reynolds number is calculated on the basis of the diameter of the channel.

## 9.6 Conclusion

2D and 3D numerical simulations of the flow past single micropillars of different known (elliptical, rectangular and triangular) and some fractal geometries over a range of  $Re$  ( $0.1 \leq Re \leq 150$ ) were carried out to find a better geometry for the posted microreactor to enhance mixing and heat transfer in micro or minichannels. Wake length ( $L_w$ ) was estimated through experimental investigation at different  $Re$  and compared with that of simulations. To support the data of 2D simulations, the drag coefficient simulated for a square cylinder having its sides perpendicular to the flow at different  $Re$  was also compared and showed good agreement with the published data and hence the analysis was extended for other geometries. At identical  $Re$ , the recirculation region behind a 2D plate was maximum while it was very small for the elliptical bodies. With increasing aspect ratio of the objects, the recirculation region behind the object was seen to get reduced (due to delayed boundary layer separation). However, for the fractal objects smaller eddies at the corners were also found to exist even at low  $Re$  which contributes to the total drag. The space filling nature of objects in the direction of flow contributes to the wake characteristics and influences the  $Re_c$ . For a similar flow approaching side, the linear relationship of  $Re_c$  found to exist with cross-sectional area. Lack of supporting surface for the wake or streamlined surfaces resulted in high-frequency vortex shedding which is good from heat transfer point of view. However, it comes with the penalty of higher pressure drop. Triangular cylinders found to be the best obstacle among all three which can be considered for enhancement of

mixing and heat transfer in a channel. In terms of selection of arrays in the channels shows that any geometry with random arrangement shows better mixing in the channel compared to other arrangements.

## Nomenclature

$A$	characteristic complex amplitude
$A^*$	dimensionless cross-sectional area (-)
$A_{sat}$	amplitude in a saturated state
$AR$	aspect ratio
$C_D$	drag coefficient (-)
$C_L$	lift coefficient (-)
$C_p$	dimensionless pressure distribution over the surface (-)
$D$	diameter of the channel (m)
$N_E$	number of elements (-)
$F_D$	drag force per unit length (N/m)
$K$	positive constant (-)
$L$	length of the channel (m)
$L_P$	projected Length (m)
$L_W$	wavelength (m)
$Re$	Reynolds number (-)
$Re_C$	critical Reynolds number for onset of vortex shedding (-)
$u_i$	velocity in $i$ th direction (m/s)
$U_{max}$	maximum velocity (m/s)
$Y$	coordinates in 'y' direction

## Greek Letters

$\rho$	density of the fluid ( $\text{kg/m}^3$ )
$\mu$	viscosity of the fluid (Pa.S)
$\sigma$	fundamental frequency component
$\lambda$	blockage ratio (-)
$\Omega$	dimensionless vorticity (-)
$\Omega_o$	vorticity (1/s)



## References

Amini, H., Sollier, E., Masaeli, M., Xie, Y., Ganapathysubramanian, B., Stone, H.A., Di Carlo, D., 2013. Engineering fluid flow using sequenced microstructures. *Nature communications* 4, 1826.

Breuer, M., Bernsdorf, J., Zeiser, T., Durst, F., 2000. Accurate computations of the laminar flow past a square cylinder based on two different methods: lattice-Boltzmann and finite-volume. *International Journal of Heat and Fluid Flow* 21, 186-196.

Chakraborty, J., Verma, N., Chhabra, R., 2004. Wall effects in flow past a circular cylinder in a plane channel: a numerical study. *Chemical Engineering and Processing: Process Intensification* 43, 1529-1537.

De, A.K., Dalal, A., 2007. Numerical study of laminar forced convection fluid flow and heat transfer from a triangular cylinder placed in a channel. *Journal of Heat Transfer* 129, 646-656.

Deshmukh, S., Vlachos, D., 2005. Novel micromixers driven by flow instabilities: Application to post-reactors. *AIChE Journal* 51, 3193-3204.

Dhiman, A., Chhabra, R., Eswaran, V., 2005. Flow and heat transfer across a confined square cylinder in the steady flow regime: effect of Peclet number. *International Journal of Heat and Mass Transfer* 48, 4598-4614.

Faruquee, Z., Ting, D.S., Fartaj, A., Barron, R.M., Carriveau, R., 2007. The effects of axis ratio on laminar fluid flow around an elliptical cylinder. *International Journal of Heat and Fluid Flow* 28, 1178-1189.

Jackson, C., 1987. A finite-element study of the onset of vortex shedding in flow past variously shaped bodies. *Journal of Fluid Mechanics* 182, 23-45.

Jung, J., Kuo, C.-J., Peles, Y., Amitay, M., 2012. The flow field around a micropillar confined in a microchannel. *International Journal of Heat and Fluid Flow* 36, 118-132.

Losey, M.W., Jackman, R.J., Firebaugh, S.L., Schmidt, M., Jensen, K.F., 2002. Design and fabrication of microfluidic devices for multiphase mixing and reaction. *Microelectromechanical Systems, Journal of* 11, 709-717.

Meis, M., Varas, F., Velázquez, A., Vega, J., 2010. Heat transfer enhancement in micro-channels caused by vortex promoters. *International Journal of Heat and Mass Transfer* 53, 29-40.

Moffatt, H.K., 1964. Viscous and resistive eddies near a sharp corner. *Journal of Fluid Mechanics* 18, 1-18.

Ni, Z., Seebauer, E., Masel, R.I., 2005. Effects of microreactor geometry on performance: differences between posted reactors and channel reactors. *Industrial & Engineering Chemistry Research* 44, 4267-4271.

Patil, P.P., Tiwari, S., 2008. Effect of blockage ratio on wake transition for flow past square cylinder. *Fluid Dynamics Research* 40, 753-778.

Schumm, M., Berger, E., Monkewitz, P.A., 1994. Self-excited oscillations in the wake of 2-dimensional bluff-bodies and their control. *Journal of Fluid Mechanics* 271, 17-53.

Sharma, A., Eswaran, V., 2004. Heat and fluid flow across a square cylinder in the two-dimensional laminar flow regime. *Numerical Heat Transfer, Part A: Applications* 45, 247-269.

Sohankar, A., Norberg, C., Davidson, L., 1998. Low-Reynolds-number flow around a square cylinder at incidence: Study of blockage, onset of vortex shedding and outlet boundary condition. *International Journal for Numerical Methods in Fluids* 26, 39-56.

Srikanth, S., Dhiman, A., Bijjam, S., 2010. Confined flow and heat transfer across a triangular cylinder in a channel. *International Journal of Thermal Sciences* 49, 2191-2200.

Stoecklein, D., Wu, C.-Y., Kim, D., Di Carlo, D., Ganapathysubramanian, B., 2016. Optimization of micropillar sequences for fluid flow sculpting. *Physics of Fluids (1994-present)* 28, 012003.

Stoecklein, D., Wu, C.-Y., Owsley, K., Xie, Y., Di Carlo, D., Ganapathysubramanian, B., 2014. Micropillar sequence designs for fundamental inertial flow transformations. *Lab on a Chip* 14, 4197-4204.

Wham, R.M., Basaran, O.A., Byers, C.H., 1996. Wall effects on flow past solid spheres at finite Reynolds number. *Industrial & Engineering Chemistry Research* 35, 864-874.

Williamson, C.H.K., 1996. Vortex dynamics in the cylinder wake. *Annual Review of Fluid Mechanics* 28, 477-539.

Yoon, D.H., Yang, K.S., Choi, C.B., 2011. Flow past a square cylinder with an angle of incidence. *Physics of Fluids* 22.

Zdravkovich, M.M., 1996. Different modes of vortex shedding: An overview. *Journal of Fluids and Structures* 10, 427-437.

## **Chapter 10**

### **Conclusions and Recommendations**

## 10.1 Conclusions

The work focuses on the mixing studies in stirred tank reactors and in small channels. As mentioned, the thesis was divided into three parts. In the first part, a fractal impeller for stirred tank reactors and its applicability has been discussed by carrying out mixing and hydrodynamics studies. The second part of the thesis is focused on the use of CSTRs for exothermic reactions and the third part is on mixing in small channels.

In Chapter 5, the flow generated by fractal impeller was studied experimentally using Ultrasonic velocity profiler (UVP) for a range of impeller rotation speeds and compared with the flow pattern generated from CFD simulations. Various simulation strategies were adopted to come up with better comparison with that of experimental results. Among all, a laminar model with sliding mesh approach found to be the best choice for CFD simulation of stirred tank with the fractal impeller. All the three velocity components were mapped in the entire stirred tank. Mean flow obtained from CFD simulations found to be comparable with experimental, however, turbulent kinetic energy was under-predicted by various RANS models. The flow generated by the fractal impeller in a stirred tank was found to have a very large tangential velocity component. Several interacting mixing zones were observed in the  $r$ - $z$  plane, which gets generated from two primary and a few secondary circulation loops. Strong tangential flow is seen to enhance the interaction of different mixing zones thereby achieving better mixing characteristics. Large deviations in the RMS velocity components were found in the most of the region in the tank which suggests the non-isotropic nature of the turbulence. Based on the experimental evidence, the distribution of turbulent kinetic energy throughout the stirred tank was seen to be better than in the stirred tank with conventional impellers.

To study the applicability of fractal impeller achieving mixing of viscous liquids, in Chapter 6, power consumption, mixing time and velocity measurements were performed in a stirred tank filled with fluids of different viscosities. The power consumption per unit mass measured at different impeller rotation speeds of the FI showed trends similar to the conventional impellers. However, it was not necessary as well as possible to operate the impeller at high  $Re$  to achieve  $N_P$  independent of  $Re$ . Mixing time for the viscous liquids was found to be a function of power consumption per unit mass and showed power law dependence. The measured mixing time was significantly lower than the conventional impellers and hence the Fractal Impeller can

be a good option for mixing of viscous liquids. Mean radial velocity profiles were found to be unaffected by the fluid viscosities in the laminar region.

It was necessary to study the design aspects of the fractal impeller in order to understand the effect of the space-filling nature of the impeller. Therefore, in Chapter 7, power consumption, mixing time and the flow patterns were measured to study the effect of a number of branches of a Fractal Impeller on the performance. Impellers having 2, 3, and 4 main branches were used. Mixing time studies were performed by monitoring the variation in local conductivity while local instantaneous velocity was measured using Ultrasonic velocity profiler (UVP). All the three velocity components were measured and used for mapping of the flow field in different planes. Based on the observations, the following conclusions can be drawn to understand the effect of the impeller configuration on its performance. The power consumption was observed to increase with an increase in the number of blades. A correlation could be established for estimation of power consumption unit mass using the number of blades, impeller speed, and the impeller diameter. Mixing efficiency per unit power consumed was almost identical for all the FI configurations. However, at identical  $N$ , FI with 4 branches was observed to perform better. The data on  $\theta_{mix}$  vs.  $P_w$  for all three configurations followed the identical trend and the slope of the plot was found to be  $-0.84$ , which is greater than  $-0.33$ , which is typically observed for conventional impellers. At equal power consumption, FI requires less time for homogenization compared to conventional impellers. Normalized radial and axial velocity profiles were found similar for all the three configurations. However, the tangential component for 4 branches FI was having the highest magnitude among all. The flow generated by the fractal impeller in a stirred tank was found to have a very large tangential velocity component. Moreover, two primary circulation loops were observed in an  $r$ - $z$  plane with a very strong tangential flow close to the wall. Strong tangential flow is seen to enhance the interaction of different mixing zones thereby achieving better mixing characteristics. Overall, from a mixing point of view, any branch configuration can be practiced as long as FI retains the symmetry in the design. Since the power needed to achieve certain mixing strongly depends upon the number of blades if one has limitations on rotational speeds the FI with 4 branches is recommended.

Mixing and reaction rate are related to each other and mixing time increases as the volume of vessel increases. Therefore increase in mixing time limits the progress of the reaction,

which in the end results in prolongation of batch time. These issues can be addressed by reducing the volume of the reactors and carrying out the reaction in a continuous operation for maintaining the yield or the production as that of the batch. In the second part of the thesis (Chapter 8), how CSTRs can be used for exothermic nitration reactions has been demonstrated. First, kinetics of reactions have been determined and were used to model the CSTR operation. Lab scale experiments were performed and results were compared with that of numerical. Numerical results found to predict the nature of the temperature profile in CSTR and conversion (yield). Effect of different parameters such as mole ratio, inlet concentration, jacket temperature, the volume of the reactor and residence time on the overall process has been discussed in details. Mole ratio (Nitric acid to Naphthalene) 2 and residence time of 10 minutes found to be the optimal range for the operation. Different scale-up strategies have been adopted to maximize the production such as parallel CSTRs, Series of CSTRs and Multipoint dosing.

Different scale-up strategies have been adopted to maximize the production such as parallel CSTRs, Series of CSTRs and Multipoint dosing (minimum 150 Kg/day).

- i) Glass reactors configuration (two CSTRs of volume 1 liter in parallel followed by CSTR of volume 2 liter): The production of the desired product can be achieved as close to 148 Kg/day.
- ii) SS316L reactors configuration (two CSTRs of volume 2 liter each): The production of the desired product can be achieved as close to 218 Kg/day.
- iii) Multipoint dosing (three CSTRs of volume 3 liter, 5 liters and 7 liters in series): With variable distribution of feed in three different reactors, different throughput can be achieved. The production of the desired product can be achieved as close to 522 Kg/day.

In the third part of the thesis (Chapter 9), mixing in small channels and issues related to it are discussed. In recent time, flow past object phenomenon has been used to enhance mixing in the small channels. In this work, 2D and 3D numerical simulations of the flow past single micropillars of different known (elliptical, rectangular and triangular) and some fractal geometries over a range of  $Re$  ( $0.1 \leq Re \leq 150$ ) were carried out to find a better geometry for the posted microreactor to enhance mixing and heat transfer in micro or minichannels. Wake length ( $L_w$ ) was estimated through experimental investigation at different  $Re$  and compared with that of

simulations. To support the data of 2D simulations, the drag coefficient simulated for a square cylinder having its sides perpendicular to the flow at different  $Re$  was also compared and showed good agreement with the published data and hence the analysis was extended for other geometries. At identical  $Re$ , the recirculation region behind a 2D plate was maximum while it was very small for the elliptical bodies. With increasing aspect ratio of the objects, the recirculation region behind the object was seen to get reduced (due to delayed boundary layer separation). However, for the fractal objects smaller eddies at the corners were also found to exist even at low  $Re$  which contributes to the total drag. The space filling nature of objects in the direction of flow contributes to the wake characteristics and influences the  $Re_C$ . For a similar flow approaching side, the linear relationship of  $Re_C$  found to exist with cross-sectional area. Lack of supporting surface for the wake or streamlined surfaces resulted in high-frequency vortex shedding which is good from heat transfer point of view. However, it comes with the penalty of higher pressure drop. Triangular cylinders found to be the best obstacle among all three which can be considered for enhancement of mixing and heat transfer in a channel. In terms of selection of arrays in the channels shows that any geometry with random arrangement shows better mixing in the channel compared to other arrangements.

## 10.2 Recommendations

Fractal Impeller (FI) for stirred tank reactors has shown some promising results in terms of mixing and hydrodynamics. However, the scale-up studies related to this are still unexplored. Scale-up studies/guidelines of the Fractal Impeller will provide the insight for its applicability at a larger scale in the industry.

In case of mixing in small channels, channels with the arrays of small objects need to get fabricated to get a better understanding of mixing in the small channels. The RTD analysis using experimental data should be carried out to study the effect of dispersion in the system.

---

### List of Publications

1. **Mule, G.M., Lohia, R., Kulkarni A.A., 2016. Effect of number of branches on the performance of fractal impeller in a stirred tank: Mixing and hydrodynamics.** Chemical Engineering Research and Design, 108, pp., 164-175
2. **Mule, G.M., Kulkarni A.A., 2016. Mixing of medium viscosity liquids in a stirred tank with fractal impeller.** Theoretical Foundations of Chemical Engineering, 50 (6), pp., 914-921.
3. **Mule, G.M., Kulkarni A.A., 2017. Flow patterns in a stirred tank with fractal impeller: Experiments and CFD simulations.** Chemical Engineering Research and Design, (*submitted*)
4. **Mule, G.M., Kulkarni A.A., 2015. New Impellers for Stirred Tank Reactor: A Brief Review from Recent Literature.** Chemical Industry Digest, July 2015, pp., 58-64
5. **Mule, G.M., Kulkarni S., Kulkarni A.A., Assessment of usefulness of CSTRs in exothermic nitration: Lab scale to plant scale studies.** (*in preparation*)
6. **Mule, G.M., Kulkarni, A.A., Effect of fractal objects on mixing in small channels: Experiments and CFD simulations.** (*submitted*)

### Conference presentations

1. **Mule, G.M., Kulkarni A.A., 2015. Flow patterns generated by fractal impeller in a stirred tank.** In: Proceedings of 15<sup>th</sup> European Conference of Mixing, Saint Petersburg, Russia, pp, 252-257
2. **Mule, G.M., Kulkarni A.A., 2014. Flow generated by fractal impeller in stirred tank: CFD simulations,** In: Proceedings of the 2014 COMSOL conference, Bangalore, India.
3. **Mule, G.M., Doshi, P., Kulkarni A.A., 2013. Understanding the flow past fractal objects.** In: Proceedings of Chemcon-2013, Mumbai, India.